Label-free Monitoring of Photolipid Bilayer Isomerization with Single Gold Nanoprobes

Jinhua Zhang

Munich, 2024

Label-free Monitoring of Photolipid Bilayer Isomerization with Single Gold Nanoprobes

Dissertation

to obtain the doctoral degree of natural sciences (Dr. rer. nat.)

at the Faculty of Physics

of the Ludwig-Maximilians-Universität München

submitted by

Jinhua Zhang

from Anhui

Munich, 30th September, 2024

First referee:	PD. Dr. Theobald Lohmüller
Second referee:	Prof. Dr. Andreas Tittl
Date of oral examination:	25th November 2024

Markerlose Überwachung der Isomerisierung von Photolipiddoppelschichten durch Einzelne Gold-Nanosonden

Dissertation

zur Erlangung des Doktorgrades der Naturwissenschaften (Dr. rer. nat.)

an der Fakultät für Physik

der Ludwig-Maximilians-Universität München

vorgelegt von

Jinhua Zhang

aus Anhui

München, 30.09.2024

Erstgutachter:	PD. Dr. Theobald Lohmüller
Zweitgutachter:	Prof. Dr. Andreas Tittl
Tag der mündlichen Prüfung:	25.11.2024

Publications, Conferences, and Awards

Scientific Publications of Results Presented in This Work

- Jinhua Zhang, Francis Schuknecht, Ludwig Habermann, Alexander Pattis, Jonathan Heine, Stefanie D. Pritzl, Dirk Trauner, Theobald Lohmüller
  Label-Free Time-Resolved Monitoring of Photolipid Bilayer Isomerization by Plasmonic Sensing
  Advanced Optical Materials 2302266 (2024)

- Jinhua Zhang, Paul Vosshage, Francis Schuknecht, Theobald Lohmüller
  Optothermal Printing of Gold Nano-Lemons for SERS on Photolipid Bilayer Membranes
  Manuscript preparation

- Jinhua Zhang, Benedikt Baumgartner, Theresa Kehler, Stefanie D. Pritzl, Dirk Trauner, Oliver Thorn-Seshold, Theobald Lohmüller
  Photosensitization and Photomodulation of Fluorescence in Azobenzene Bilayer Membranes
  Manuscript preparation

Additional Publications

- Maria-Ana Huergo, Francis Schuknecht, Jinhua Zhang, Theobald Lohmüller
  Plasmonic Nanoagents in Biophysics and Biomedicine
  Advanced Optical Materials 10 (14), 2200572 (2022)

- Thorsten Gölz, Enrico Baù, Jinhua Zhang, Korbinian Kaltenecker, Dirk Trauner, Stefan A Maier, Fritz Keilmann, Theobald Lohmüller, Andreas Tittl
  Resolving the Millisecond Photoswitching Dynamics of Nanoscale Lipid Vesicles Using in-situ Infrared Nanoscopy
  arXiv preprint Submitted

- Benedikt Baumgartner, …, Jinhua Zhang, …, Oliver Thorn-Seshold
  A General Method for Near-Infrared Photoswitching in Biology, Demonstrated by the >700 nm Photocontrol of GPCR Activity in Brain Slices
  ChemRxiv Submitted

Conferences and Workshops

- *PhoG Day (Talk)*
  Rapid Isomerization of Photolipid Membranes Triggered via Photosensitization with Red Light
  Munich, October 2021

- *PhoG Chair workshop on Optical Spectroscopy of New Materials (Talk)*
  Plasmonic Sensing of Photoswitchable Supported Lipid Bilayer Membranes
  Fall-Lenggries, July 2022

- *SFB1032 Annual Workshop (Talk)*
  Plasmonic Nanosensors for Monitoring Photoswitchable Supported Lipid Bilayer Membranes
  Munich, October 2022

- *LMU - CSC Poster Session (Poster)*
  Plasmonic Nanosensors for Monitoring Photoswitchable Supported Lipid Bilayer Membranes
  Munich, October 2022

- *DPG-Frühjahrstagungen 2023 (Talk)*
  Monitoring the Switching Dynamics of Photolipid Membranes with Plasmonic Nanorods
  Dresten, March 2023

- *Molecular Plasmonics 2023 (Poster)*
  Monitoring Photolipid Bilayer Membrane Switching with Plasmonic Nanorods
  Jena, May 2023

Zusammenfassung

Das Photolipid *azo*-**PC** ist ein photoschaltbares Derivat von Phosphatidylcholin, das eine Azobenzolgruppe in einem seiner Lipidschwänze enthält.[1] Es kann durch Beleuchtung mit ultraviolettem (UV) und blauem Licht reversibel zwischen seiner *trans*- und *cis*-isomeren Form geschaltet werden. Wenn *azo*-**PC** in synthetische Lipidmembranen[2] oder Zellmembranen integriert wird,[3] ist es möglich, durch das optische Schalten der *azo*-**PC**-Konformation spezielle Lipidmembraneigenschaften[4,5] wie beispielsweise die Biegesteifigkeit,[6] Fluidität,[7] Permeabilität,[8,9] Membranfusion[10] und die Bildung von Lipiddomänen[11] mit Licht zu steuern. Zur Untersuchung dieser physikalischen Eigenschaften von Lipidsystemen kommt häufig die Fluoreszenzmikroskopie zum Einsatz.[10,8,11] Dabei ist die mögliche Wechselwirkung zwischen fluoreszierenden Molekülen und der Photoisomerisierung von azobenzol-modifizierten Lipiden in Membranen von Vesikeln oder oberflächengebundenen Lipidmembranen bisher weitestgehend unerforscht. Starke Effekte sind jedoch zu erwarten, da Azobenzol häufig als Fluoreszenzquencher in Lösung und in Polymersystemen zum Einsatz kommt.

Ein Ziel dieser Arbeit war es, den Einfluss von fluoreszenzmarkierten Lipiden auf die Photophysik von *azo*-**PC** in Lipidmembransystemen zu untersuchen. Dabei konnte insbesondere gezeigt werden, dass durch die Dotierung von Photolipidmembranen mit Fluoreszenzfarbstoffen, die im roten Bereich des sichtbaren Spektrums angeregt werden, wie beispielsweise Rhodamin, die *cis*-zu-*trans*-Schaltrate von *azo*-**PC** in diesem Wellenlängenbereich um mehrere Größenordnungen beschleunigt werden kann. Rotes Licht ist für biologische Anwendungen besonders geeignet, da es eine größere Eindringtiefe in Gewebe hat als Licht mit kürzeren Wellenlängen. Die Möglichkeit, Azobenol-lipide mithilfe von Fluoreszenzfarbstoffen zu photosensibilisieren, eröffnet daher neue Perspektiven für den Einsatz von Photoschaltern in biologischen Systemen. Gleichzeitig führt die Wechselwirkung der *azo*-**PC** auch zu einer Modulation der Farbstoffemission. Die Fluoreszenzlöschung für verschiedene Fluorophore in Abhängigkeit von der Photolipidkonzentration und -konformation wurde ebenfalls charakterisiert, und es wurde eine deutlich effizientere Fluoreszenzlöschung für die *cis*-Isomere im Vergleich zur *trans*-Form festgestellt.

Die starken Wechselwirkungen zwischen Fluoreszenzfarbstoffen und azobenzol-basierten Photolipiden begründen die Notwendigkeit der Entwicklung markierungsfreier Methoden zur Untersuchung des Schaltverhaltens in Photolipidmembranen. Im Rahmen dieser Arbeit wurden zwei komplementäre Methoden entwickelt um dieses Ziel zu erreichen. Die erste Methode basiert auf der Untersuchung photoschaltbarer, oberflächengebundener Lipidmembranen mittels plasmonischer Sensoren. Dazu wurden Gold-Nanostäbchen auf einem Glassubstrat

mit einer Photolipid-Doppelschicht bedeckt, deren Moleküle durch wechselnde Beleuchtung mit UV und blauem Licht zwischen der *trans*- und *cis*-Form geschaltet wurden. Die lichtgesteuerte Veränderung der Membraneigenschaften, insbesondere die Veränderung der Membrandicke, -dichte und die Konformationsänderung der Azobenzol-Gruppe, führt zu einer Veränderung der dielektrischen Umgebung der Nanopartikel und damit zu einer Verschiebung der Plasmonresonanzfrequenz. Die Anwendung dieses Verfahrens zur Messung des Membranschaltdynamik und zur Analyse der Membranfluidität konnte mittels zeitabhängiger Messungen der Streuspektren an einzelnen Nanostäbchen gezeigt werden.

Als zweites Verfahren wurde die Möglichkeit der oberflächenverstärkten Raman-Streuung (surface enhanced Raman scattering, SERS) von Photolipiden auf Gold-Nanoellipsoiden untersucht. Der Vorteil der Raman-Spektroskopie im Vergleich zur plasmonischen Sensorik liegt darin, dass in den Spektren auch Informationen über die chemische Struktur der *azo*-**PC**-Isomere enthalten sind. Zur Entwicklung einer Einzelpartikel-SERS-Plattform wurde eine Methode entwickelt, um Gold-Nanostäbchen durch die Kombination von optischen Kräften und plasmonischem Heizen auf ein Glassubstrat zu drucken. Dabei wurde beobachtet, dass bei einer bestimmten Laserintensität die kontrollierte Verformung der Nanostäbchen zu Nanoellipsoiden erzielt werden kann. Diese Ellipsoide zeigen schärfere Spitzen an den Partikelenden und dadurch eine erhöhte elektromagnetische Feldverstärkung, die SERS-Messungen der Schaltvorgänge von Photolipiden in einer Lipidmembran ermöglicht.

Abstract

The photolipid *azo*-**PC** is a photoswitchable derivative of phosphatidylcholine, containing an azobenzene group in one of its lipid tails.[1] It can be reversibly switched between its *trans*- and *cis*-isomeric forms by illumination with ultraviolet (UV) and blue light, respectively. When *azo*-**PC** is integrated into synthetic lipid bilayer membranes[2] or biological (cell-) membranes,[3] it is possible to control specific lipid membrane properties[4,5] such as bending rigidity,[6] fluidity,[7] permeability,[8,9] membrane fusion,[10] and the formation of lipid domains[11] by optical switching of its conformation. Fluorescence microscopy is widely used to investigate these physical properties of lipid bilayer systems, i.e. of liposomes or supported lipid bilayers (SLBs).[10,8,11] However, the interaction between fluorescent molecules and azobenzene-modified photolipids in a bilayer assembly remains largely unexplored. Strong effects are expected, as azobenzenes have been reported as efficient fluorescence quencher in solution or in polymer systems.

One aim of this work was to investigate the influence of fluorescence-labeled lipids on the photo-physics and isomerization behavior of *azo*-**PC** in lipid bilayer membranes. In particular, it was analyzed how doping of photolipid membranes with fluorescently labelled lipids that are excited in the red region of the visible spectrum, such as Rhodamine, can accelerate the *cis*-to-*trans* switching rate of *azo*-**PC** by several orders of magnitude. Red light in particular is favorable for biological applications of photolipids because it penetrates deeper into tissue than light with shorter wavelengths. Therefore, the demonstrated ability to photosensitize *azo*-**PC** isomerization with fluorescent dyes opens up new perspectives for the use of photoswitches in biological systems. At the same time, the switching of *azo*-**PC** photolipids also leads to a modulation of dye emission. The dependence of fluorescence quenching on photolipid concentration and conformation was also characterized for different fluorophores, revealing significantly more efficient quenching for the *cis* compared to the *trans* isomer.

The strong interactions between fluorescent dyes and azobenzene-based photolipids emphasize the need for the development of label-free methods to study switching behavior in photolipid membranes in real time. In this work, two complementary methods were developed and characterized. The first approach is based on the investigation of photoswitchable SLB membranes using plasmonic sensors. For this purpose, Gold nanorods (AuNRs) adsorbed on a glass substrate were coated with a supported photolipid bilayer. The molecules were switched between *trans* and *cis* by alternating irradiation with UV and blue light using light-emitting diodes (LEDs). The light-driven changes in membrane properties, associated with changes in membrane thickness, -density, and the conformational changes of the azobenzene lipid tails,

lead to alterations in the dielectric environment of the nanoparticles and, consequently, to a measurable shift in the plasmon resonance frequency. The applicability of this approach for analyzing membrane photoisomerization and fluidity was demonstrated through time-dependent measurements of scattering spectra from individual nanorods.

Secondly, an approach to conduct surface enhanced Raman scattering (SERS) spectroscopy of photolipids bilayers on gold nanoellipsoids was developed. The advantage of Raman spectroscopy compared to plasmonic sensing lies in the fact that the SERS spectra contain information about the chemical nature and, therefore, the conformation of *azo*-**PC** within the bilayer. To develop a single-particle SERS platform, a method was devised to print AuNRs onto a glass substrate by combining optical forces and plasmonic heating. It was observed that at a certain laser intensity, controlled deformation of the nanorods into nanoellipsoids could be achieved. These ellipsoids exhibit sharper tips at the particle ends, resulting in increased electromagnetic field enhancement, enabling SERS measurements of the switching behavior of photolipids in a bilayer.

Table of Contents

Zusammenfassung vii

Abstract ix

1 Introduction to Photoswitchable Lipid Bilayer Membranes 1

2 Fundamentals of *Azo*-PC and AuNPs 5

2.1 The Light-sensitive Phospholipid *Azo*-**PC** . . . 6

2.1.1 Phospholipids in Nature . . . 6

2.1.2 The Light-sensitive Phospholipid *Azo*-**PC** . . . 7

2.1.3 Physical Properties of *Azo*-**PC** Lipid Membranes . . . 9

2.2 Interactions between Azobenzene and Fluorophores . . . 15

2.2.1 Mechanism of Fluorescence Quenching . . . 16

2.2.2 Mechanism of Sensitized Photoisomerization . . . 19

2.3 Interactions of Gold Nanoparticles and Light . . . 22

2.3.1 The Particle Plasmon . . . 22

2.3.2 Gold Nanoparticles as Plasmonic Sensors . . . 27

2.3.3 Optical Forces . . . 28

2.3.4 Melting of Gold Nanorods . . . 29

2.4 Surface Enhanced Raman Scattering . . . 31

2.4.1 The Principle of SERS . . . 31

2.4.2 SERS Substrates . . . 34

2.4.3 Raman Spectra of Azobenzene . . . 35

3 Preparation and Characterization of Lipid Membranes and AuNRs 37

3.1 Preparation and Characterization of Lipid Membranes . . . 38

3.1.1 Lipid Molecules . . . 38

3.1.2 Preparation of Photolipid Membranes . . . 40

3.1.3 Characterization of Photolipid Membranes . . . 41

3.2 Characterization and Simulation of AuNRs . . . 46

3.2.1 AuNRs Dropcasting and Ligand Removal . . . 46

3.2.2 Dark-field Scattering and Raman Spectroscopy . . . 47

3.2.3 Scanning Electron Microscopy . . . 49

3.2.4 Finite Difference Time Domain Simulations . . . 50

4 Photosensitization and -modulation between Photolipids and Dyes 51
4.1 Sensitized *Cis*-to-*trans* Isomerization of *Azo*-**PC** . . . 52
4.1.1 Direct *Cis*-to-*trans* Isomerization of *Azo*-**PC** . . . 52
4.1.2 Sensitized *Cis*-to-*trans* Isomerization of *Azo*-**PC** . . . 53
4.1.3 Effects of Dye Concentration . . . 56
4.1.4 Reversibility . . . 57
4.2 *Azo*-**PC** Protects Methylene Blue from Photobleaching . . . 59
4.3 Fluorescence Modulation of Dyes by *Azo*-**PC** Photoisomerization . . . 61
4.4 Mechanism Discussions . . . 65
4.5 Other Azobenzene-containing Lipids . . . 67

5 Plasmonic Sensing of Photolipid Bilayer Isomerization 69
5.1 Nanorods Selction . . . 70
5.2 Plasmonic Sensing of Membrane Deposition . . . 72
5.3 Plasmonic Sensing of *Azo*-**PC** Bilayer Isomerization . . . 73
5.4 Effects of Ligands on Plasmonic Sensitivity . . . 78
5.5 FDTD Simulations of *Azo*-**PC** Bilayer Photoswitching . . . 79
5.6 Plasmonic Sensing of Membrane Diffusion . . . 81
5.7 Plasmonic Sensing by An AuNRs Array . . . 84

6 Optothermal-printed AuNRs for SERS of Photolipid Bilayer Isomerization 87
6.1 Optical Printing of Gold Nanorods . . . 88
6.2 SERS on Ellipsoid Nanoparticles . . . 92
6.3 SERS of Photolipid *Azo*-**PC** . . . 96
6.4 SERS of Photolipid Bilayer Isomerization . . . 99

7 Conclusions and Outlook 101

References I

List of Figures XXII

List of Tables XXIII

List of Abbreviations XXV

Acknowledgments XXVII

1

Introduction to Photoswitchable Lipid Bilayer Membranes

Light as a stimulus offers great advantages for applications in biophysics, synthetic biology, and nanomedicine, as it is contact-free and can be applied with high temporal and spatial precision. By incorporating a photoswitch molecule - azobenzene into one tail of a phospholipid, the photoswitchable lipid *azo*-**PC** can be synthesized. *Azo*-**PC** can be switched between two isomers *trans* and *cis* with ultraviolet (UV) and blue light. Embedding *azo*-**PC** into lipid bilayer membranes enables one to control a wide range of biophysical membrane properties, such as bending rigidity,[6] fusion,[10] permeability,[8] fluidity,[7] and domain formation,[11] in a fast and reversible manner. These changes in membrane properties are solely resulting from *azo*-**PC** conformation changes due to photoisomerization. For example, a lipid bilayer assembled with pure *trans azo*-**PC** lipids is approximately 4 nm thick. Small-angle X-ray scattering (SAXS) has shown that photoswitching leads to a decrease in bilayer thickness (head-to-head) by just 5 to 10 Å, depending on the photostationary states (PSSs) of the membrane.[12] Furthermore, it was shown that the *cis*-isomers of azo-PC are arranged less orderly within a lipid bilayer, and that the lipid cross-section increases 8.7 $Å^2$ upon *trans*-to- *cis* photoisomerization.[8] These changes may appear small, despite their significant impact on the membrane's physical properties. It becomes evident, however, that analyzing such minute changes in photolipid membrane isomerization is of great importance for applications in synthetic biology or photopharmacology.

Arguably, the most widely used approaches to study biological systems in general, and biomembranes in particular, are fluorescence-based. This is also true for photolipid systems.

For example, light-controlled shape changes and domain formation in giant unilamellar vesicles (GUVs) have been visualized with epifluorescence microscopy by doping the photolipid membrane with a small amount of fluorescent lipid (<1 mol %). Fluorescence recovery after photobleaching (FRAP)[13] and fluorescence correlation spectroscopy (FCS)[14] have been used to analyze the diffusivity of dyes within supported lipid bilayers (SLBs).

However, there are two important considerations before using fluorescence-based methods to study photolipid bilayers. Firstly, the light used to excite the dyes should not interfere with the photoisomerization process itself. Like regular azobenzenes, *azo*-**PC** can be isomerized at wavelengths in the UV/blue spectral range. Consequently, only fluorophores excited by and emitting in the orange/red infrared range are suitable for photolipid applications. Secondly, fluorescent dyes may affect the photoisomerization of *azo*-**PC** via photosensitization. It has been reported that azobenzene can be dye-sensitized in solution, polymer blends, and dyads, but many details about dye/azobenzene sensitization and fluorescence modulation in lipid bilayer membranes remain enigmatic as these systems are scarcely explored.

The investigation and characterization of the photophysical interactions between synthetic *azo*-**PC** phospholipids and fluorescent dyes embedded in lipid systems such as liposomes or SLBs are presented in this thesis. In particular, it was found that dyes can be applied to expand the wavelength range for photolipid isomerization to the red/near-IR spectral region within the biological window of tissue. The observed sensitivity of *azo*-**PC** photolipids to fluorophores justifies the need for developing label-free methods for membrane analysis. Two complementary approaches have been devised to achieve this aim: membrane photoisomerization analysis by plasmonic sensing and by surface enhanced Raman scattering (SERS).

This thesis is structured as follows. Chapter 2 presents the theoretical framework for the experimental approaches and the interpretation of the results obtained in this thesis. The chapter introduces fundamental principles of azobenzene isomerization and reviews concepts and mechanisms for photosensitization and energy transfer between azobenzene photoswitches and fluorophores from literature. This is followed by an introduction to localized surface plasmons, optical forces on plasmonic nanoparticles, and plasmonic heating. Finally, the general principles of Raman spectroscopy, particularly SERS, are introduced.

Chapter 3 provides an overview of all the sample preparation protocols, spectroscopic and microscopic setups, as well as theoretical models used for data analysis.

The influence of fluorescence-labeled lipids on the photoisomerization of *azo*-**PC** in lipid bilayer membrane assemblies is presented in Chapter 4. It is demonstrated that *cis*/*trans*

photoisomerization of *azo*-**PC** bilayer membranes can be achieved with red light by doping the bilayer with red-fluorescent dyes. The efficiency of this azobenzene photosensitization process is analyzed for different dyes, and potential photophysical processes are discussed. The chapter concludes by presenting the fluorescence quenching capabilities of *azo*-**PC** isomers in a lipid bilayer system and by discussing potential applications for fluorescence imaging and spectroscopy.

The notion that lipid dyes sensitize photoswitching highlights the need for developing label-free methods for photolipid membrane analysis. The application of plasmonic sensing to monitor *azo*-**PC** photoswitching by single-nanorod dark-field scattering spectroscopy is presented in Chapter 5. A method to form *azo*-**PC** SLBs on top of gold nanorods (AuNRs) sitting on a glass substrate was developed. Bilayer formation was confirmed by real-time monitoring of membrane deposition. The high sensitivity of this approach for monitoring the switching dynamics of the SLB was demonstrated by time-resolved measurements. Finally, the obtained experimental results were compared with theoretical values to interpret the origin of the observed plasmon shift and benchmark the sensitivity of the approach for analyzing membrane changes.

In Chapter 6, the idea of using plasmonic nanoparticles to study bilayer membranes was taken one step further by developing an approach for SERS on *azo*-**PC** SLBs using gold nanoellipsoids. Arrays of nanoellipsoids can be generated on a glass substrate using optothermal printing of gold nanorods. This approach takes advantage of both optical forces and plasmonic heating, which emerge due to light-particle interactions between nanorods and a focused laser beam in solution. It is shown that controlled nanoparticle reshaping by plasmonic heating results in rod-to-ellipsoid transformations. These ellipsoids display sharper tips at their ends and hence a higher electromagnetic field enhancement. The superior SERS performance of the ellipsoids in comparison to nanorods and nanospheres is demonstrated by SERS measurements on *azo*-**PC** SLBs.

Finally, Chapter 7 summarizes the main findings of this thesis and provides an outlook on potential future applications.

2

Fundamentals of *Azo*-PC and AuNPs

This chapter provides an overview of the fundamental concepts relevant for this thesis. In Section 2.1, the light-sensitive phospholipid *azo*-**PC** is introduced. As a synthetic lipid with an azobenzene group in one of its lipid tails, *azo*-**PC** retains specific phospholipid properties such as self-assembly and lateral diffusion, and inherits photochromic properties of azobenzene group. Fluorescent dyes are the most common tools to study lipid membranes. But it was reported that fluorophores can interact with azobenzene. Isomerization of azobenzene and fluorescence of dyes are affected by each other. The possible mechanism leading to this indirect azobenzene isomerization and fluorescence modulation are discussed in Section 2.2. Then, Section 2.3 focuses on the interaction between light and gold nanoparticles (AuNPs), starting with the introduction of particle plasmons which are the basis for plasmonic sensing. The optical forces acting on AuNPs and the plasmonic heating are discussed. Finally, Section 2.4 describes the principle of SERS, provides an overview on typical SERS substrates and introduces the SERS spectra of azobenzene molecules.

2.1 The Light-sensitive Phospholipid *Azo*-PC

2.1.1 Phospholipids in Nature

The plasma membrane is one of the most important cell structures, which separates a cell's interior from the exterior environment.[15] It mainly consists of a double layer of lipid molecules, that is phospholipids and cholesterol, as shown in Figure 2.1a. Furthermore, membrane proteins and sugars (including glycoproteins and glycolipids) are embedded in or attached to the lipid bilayer.[15,16]

Three types of lipids are mainly found in cell membranes: phospholipids, glycolipids, and sterols.[17,18] Their composition varies in membrane or cell types.[17,19] Phospholipids are characterized by a hydrophilic head and hydrophobic tails.[20] There are two main classes of phospholipids: glycerophospholipids and sphingophospholipids, with glycerophospholipids being the most abundant lipids among all types.[19] Glycerophospholipids are formed by attaching two hydrophobic chains of fatty acids to a glycerol and phosphate group. Figure 2.1b depicts a glycerophospholipid that contains a choline molecule in the head group, referred as phosphatidylcholine (PC). Other molecules such as serine and ethanolamine can replace the choline in this position, so that phosphatidylserine (PS) and phosphatidylethanolamine (PE) are obtained.[17,19,20] Not only the head group, but the tails vary in number, length and degree of saturation. The high lipid diversity in structure or composition is significant for the physical

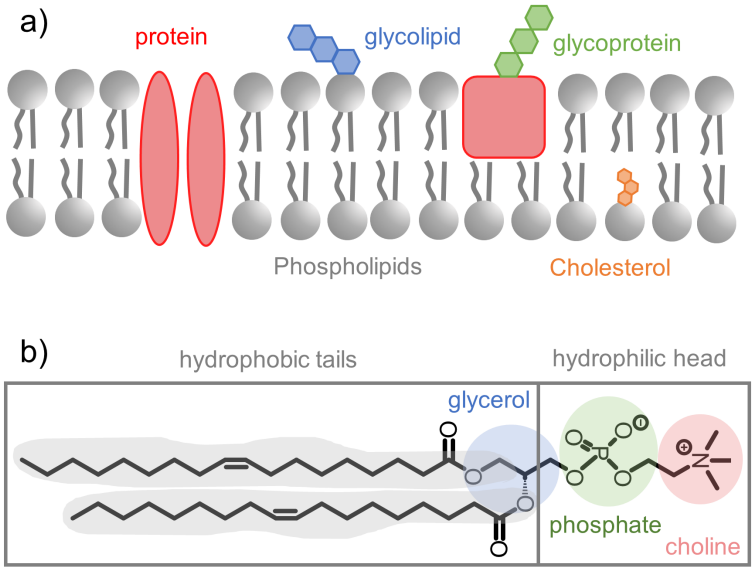

Figure 2.1: Phospholipids are building blocks of cell membranes. (a) Cell membrane model. The cell membrane is composed of a phospholipid bilayer with cholesterol, proteins and sugar (glycoprotein and glycolipid). **(b)** An example of glycerophospholipid: 1,2-dioleoyl-sn-glycero-3-phosphocholine (DOPC). DOPC contains a hydrophilic phosphocholine headgroup and two hydrophobic unsaturated chains.

properties and functions of the cell membranes.[21]

Cell membranes are involved in a variety of processes such as cell signaling, ion conductivity, and cell activity (adhesion, migration, proliferation, differentiation, and death).[22] These are often dependent on the physical properties of the lipid bilayer including elasticity (bending, stretching, thickness change, shearing),[19] fluidity,[23] permeability,[24] phase,[25,26] and domain formation.[27,28] Many factors can affect and modulate the physical properties of a lipid membrane such as lipid composition,[21,29] temperature,[30] pH,[31] and ion/molecule concentration.[32]

Various approaches have been investigated to control membrane properties for medical or pharmaceutical applications, for example, by applying an electric field,[33] introducing temperature gradients[34] or by changing the pH.[35] However, these methods are slow and lack target specificity. Light as a stimulus can provide control with high temporal and spatial precision. If a lipid molecule is light sensitive, this allows for tuning membrane properties with high accuracy. In the following, the light-sensitive phospholipid *Azo*-**PC** is introduced.

2.1.2 The Light-sensitive Phospholipid *Azo*-PC

Azobenzene as a photoswitch was first reported by Harley in 1937.[36] It consists of two phenyl rings linked by an N=N bond (Figure 2.2a), which has two isomeric states: a more thermally stable *trans* state and a meta-stable *cis* state. *Trans* azobenzene shows a planar configuration while the *cis* form adopts a twisted geometry. These two isomers of azobenzene can be reversibly switched by irradiation of UV and visible light. Since the trans conformation is

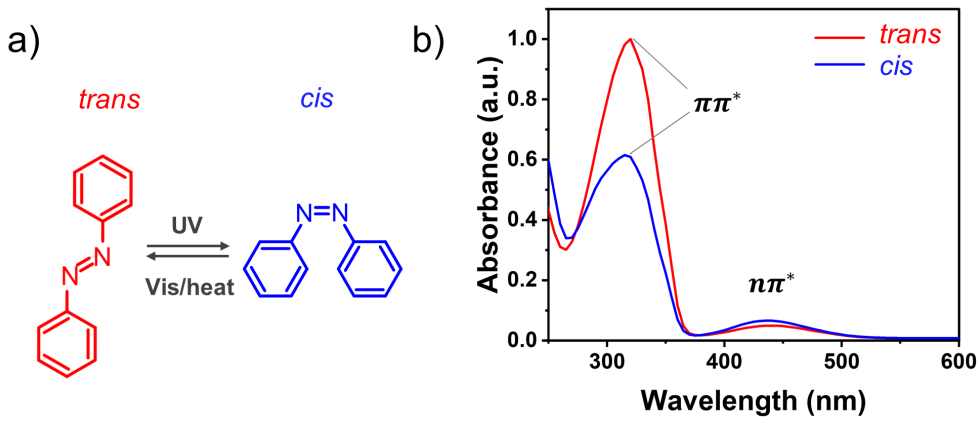

Figure 2.2: Azobenzene isomers and their absorption spectra. (a) *Trans* azobenzene is planer while *cis* azobenzene shows a twisted geometry. Reversible switching between two azobenzene isomers can be achieved by illumination of UV and visible light or by heat. **(b)** Two electronic bands are shown in the absorption spectra of both azobenzene isomers (dissolved in chloroform): a strong band at 320 nm due to $\pi\pi^*$ transition and a weaker band at 440 nm due to $n\pi^*$ transition.

thermodynamically more stable, *cis*-to-*trans* isomerization can occur thermally in the dark.

The absorption spectrum of *trans* azobenzene (measured in chloroform) exhibits two bands, a strong band at 320 nm and a weaker band at 440 nm (Figure 2.2b). The strong UV band corresponds to the symmetry allowed $\pi\pi^*$ transition, from the ground state S_0 to the excited state S_2.[37] The weaker band corresponds to the symmetry forbidden $n\pi^*$ transition (S_0 to S_1) according to selection rules.[37] Compared to *trans* azobenzene, the $\pi\pi^*$ transition of the *cis* isomer is weaker, and $n\pi^*$ transition is stronger.

Azobenzene is excited to both S_1 to S_2 states during its *trans*-to-*cis* or *cis*-to-*trans* isomerization. However, the quantum yield of isomerization is different for each state that azobenzene is excited to,[38] which suggests different isomerization pathways.[39] By applying ultrafast time-resolved absorption/fluorescence[40,41] or Raman spectroscopy[42] and performing theoretical calculations,[43,44,45] several mechanisms have been proposed as possible isomerization pathways of azobenzene, including rotation, inversion, inversion-assisted rotation and concerted inversion.[37] The detailed mechanism is still not fully understood and the most recent studies assume that multiple pathways are involved during isomerization.[46]

Due to the excitation to both S_1 and S_2 states, different PSSs (ratio between *trans* and *cis* isomer) are observed. Thermal *cis*-to-*trans* relaxation can produce 100 % of the *trans* isomer. Thus, an azobenzene sample kept in the dark for days (called the dark-adapted sample) is almost 100 % trans. However, UV or visible irradiation typically results in a PSS of 80 % cis or 95 % trans at maximum.[47]

Due to its photoisomerization property, azobenzene has been used for optical data-storage devices[48,49,50] and sensors.[51,52,53] It also shows potential as a photo-mechanical material, which converts photonic energy to mechanical motion.[54,55,56,57] By incorporating azobenzene in a variety of materials such as polymers,[58,59] gels,[60,61] crystals[62,63] and thin films,[64] it can achieve photoinduced motions,[65,66] photo-patterning/-morphing[67] and surface modification.[68] Furthermore, it meets the requirements to be applied to biological systems.[69] First, azobenzene has high extinction coefficients in the visible range. Second, its isomerization occurs in picoseconds, which is faster than most biological processes.[70] Most importantly, the activity or function of a molecule coupled to azobenzene can be effectively changed. Azobenzene photoswitches have shown wide application for photocontrol of biomolecules such as proteins,[71,72] lipids,[73,74] peptides,[75,76] nucleic acids[77,78] and carbohydrates.[79,80]

Azo-**PC** is a phosphatidylcholine derivative that contains an azobenzene group in the sn2 acyl chain (Figure 2.3a). *Azo*-**PC** retains the photochromic property from the azobenzene group.

Therefore, it can be switched back and forth between *trans* and *cis* states by illumination of UV and blue light. Figure 2.3b shows the absorption spectra of *azo*-**PC** membrane in water, which is similar to the absorption spectra of azobenzene. A strong peak at 315 nm is shown for *trans azo*-**PC**, corresponding to the S_0 to S_2 transition. At the *cis* state, the peak at 440 nm is stronger, corresponding to the S_0 to S_1 transition. Noting that for *azo*-**PC** bilayer membranes, a hypsochromic shift of the main absorption peak is observed due to the formation of H-aggregates.[11]

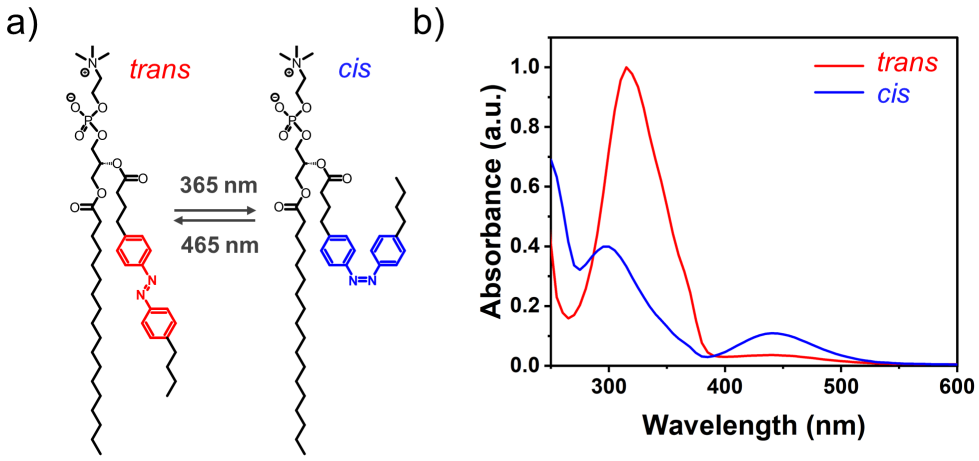

Figure 2.3: Photoswitchable lipid *azo*-PC (a) Molecular structure of *azo*-**PC** in *trans* and *cis* states. **(b)** The absorption spectra of *azo*-**PC** membrane in *trans* and *cis* states, measured in water.

2.1.3 Physical Properties of *Azo*-PC Lipid Membranes

As a phospholipid, *azo*-**PC** has a hydrophilic head and a hydrophobic tail. This amphiphilic nature leads to the self-assembly of *azo*-**PC** in an aqueous environment. *Azo*-**PC** membranes are fluid, which was revealed by analyzing the diffusion of *azo*-**PC** lipid molecules. Benefiting from the photoswitchable property of *azo*-**PC**, membrane diffusivity as well as thickness,[7] density,[8] bending rigidity[6] and domains[11] could be controlled by illumination of appropriate wavelengths. In this section, these properties will be discussed.

Self-assembly of phospholipids

Lipid self-assembly into well-defined structures is driven by two *opposing forces*.[81] The hydrophobic effect of the hydrocarbon chains causes molecular association. The hydrophilic head group maintains contact with water.[82] These two interactions compete with each other at the interfacial region: the hydrophobic attraction tends to decrease the interfacial area a per molecule while the hydrophilic repulsion tends to increase it.

The free energy per molecule in aggregates μ_N^0 can be described by taking these two effects into account. Hydrophobic attraction, arising from interfacial tension γ, contributes to μ_N^0 as γa. The contribution of hydrophilic repulsion can be given by C/a, where C is a constant. Therefore, the free energy per molecule in aggregates can be written as

$$\mu_N^0 = \gamma a + C/a. \tag{2.1}$$

The minimum free energy is thus given by expressing Equation 2.1 as

$$\mu_N^0 = 2\gamma a + \frac{\gamma}{a}(a - a_0)^2, \tag{2.2}$$

where $a_0 = \sqrt{C/\gamma}$, a_0 is referred to as the *optimal surface area per molecule* (Figure 2.4), which is an important parameter to determine the shape and size of lipid aggregate.

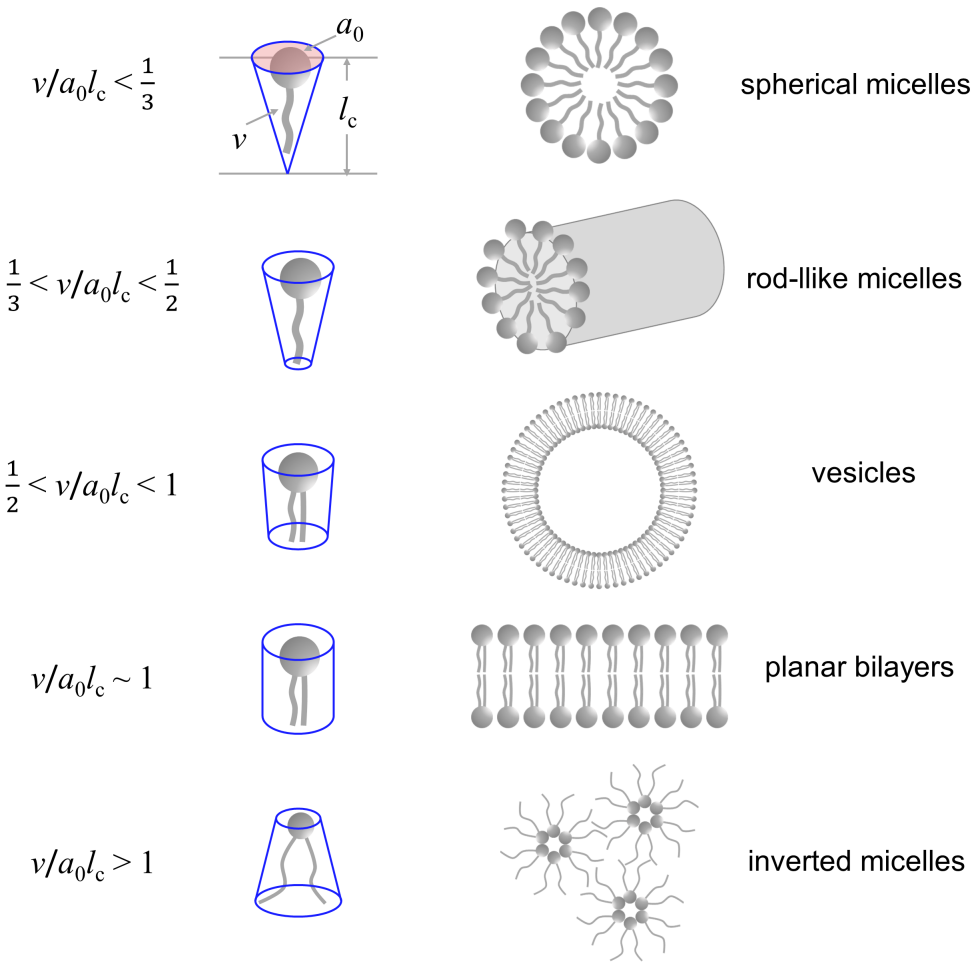

Figure 2.4: Self-assembly of phospholipids. The packing properties depend on the packing parameter v/a_0l_c, where v, a_0 and l_c are the volume of the hydrophobic chain, optimal surface area and critical chain length, respectively. Lipids will assemble into spherical micelles ($v/a_0l_c < 1/3$), rod-like micelles ($1/3 < v/a_0l_c < 1/2$), bilayers ($1/2 < v/a_0l_c < 1$) and inverted micelles ($v/a_0l_c > 1$). (adapted from ref[82])

Except for the optimal surface area a_0, the geometry or packing of lipid aggregates also depends on the *volume of hydrophobic chain* v and the maximum or *critical chain length* l_c (Figure 2.4). The *Packing parameter* is defined as $v/a_0 l_c$.[83,84,85] As depicted in Figure 2.4, if the packing parameter is $v/a_0 l_c < 1/3$, which normally means that lipid molecules have a single chain and large head-group area, spherical micelles will be assembled. Lipids with smaller head-group areas so that $1/3 < v/a_0 l_c < 1/2$ will assemble into rod-like micelles rather than spherical micelles. Bilayer-forming lipids possess double chains and large head-group areas so that $1/2 < v/a_0 l_c < 1$. If $v/a_0 l_c > 1$, lipids will pack into inverted micelles since their head group is too small. Other factors such as lipid composition and solvent type affect the shape and size of aggregates as well.[82]

As a synthetic phospholipid, the packing parameter of *azo*-**PC** has not been reported. *Azo*-**PC** maintains a bilayer even at 100 % of concentration, which suggest a packing diameter of ~ 1. It was reported that *azo*-**PC** can form GUVs with a diameter above 1 μm, small unilamellar vesicles (SUVs) with a diameter below 100 nm and SLBs.[7,11] Figure 2.5 shows GUVs that consist of 50% of DOPC plus 50% of *azo*-**PC** (and 1% of TexasRed-DHPE, Figure 2.5a) and GUVs formed from pure *azo*-**PC** (and 1% of TexasRed-DHPE, Figure 2.5b).

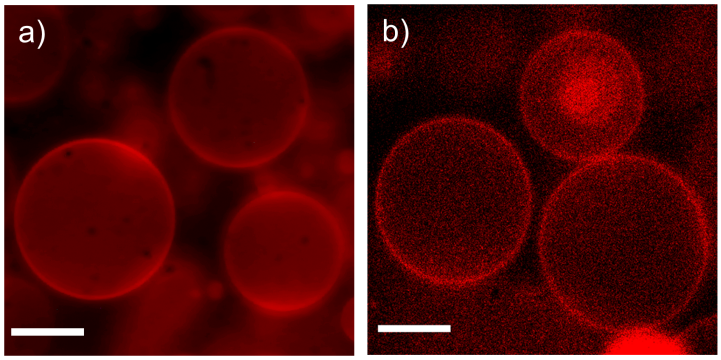

Figure 2.5: GUVs. GUVs consist of **(a)** 50% of DOPC, 50% of *azo*-**PC** plus 1% of Rhodamine dyes and **(b)** pure *azo*-**PC** plus 1% of TexasRed-DHPE. Scale bar: 10 μm. Images were taken under fluorescent microscopy with **(a)** a CMOS camera and **(b)** a CCD camera.

Lateral lipid diffusion

In a two-dimensional bilayer membrane, lipid molecules are oriented perpendicular to the membrane plane. Due to the thermal agitation, lipids move rotationally or translationally within the bilayer sheet.[86] However, translational diffusion is the most important, which is referred as to lateral lipid diffusion.

In a homogeneous membrane, lateral diffusion is described by the diffusion equation[87]

$$\frac{\partial c(r,t)}{\partial t} = D\nabla^2 c(r,t), \tag{2.3}$$

where $c(r, t)$ is the density distribution dependent on location r and time t. D represents the *diffusion coefficient*. The solution to the diffusion equation is

$$c(r, t) = \frac{1}{4\pi Dt}\exp(-\frac{r^2}{4Dt}). \tag{2.4}$$

The diffusion coefficient then can be linked to the mean square displacement of a randomly moving tracer

$$r^2 = \int_0^\infty r^2 c(r, t) 2\pi r \mathrm{d}r = 4Dt. \tag{2.5}$$

For a homogeneous two-dimensional bilayer system, the diffusion coefficient D can be derived from free-area theory, which is an extension of free-volume theory.[87]

$$D = \int_{A^*}^\infty D(A)P(A)\mathrm{d}(A), \tag{2.6}$$

where A^* represents the critical free area, which is the minimum area useful for diffusion. $D(A)$ is a constant for diffusion in an area A. P(A) is the probability for finding such a free area with size A, that can be given by

$$P(A) = \eta/A_\mathrm{f}\exp(-\frac{\eta A}{A_\mathrm{f}}), \tag{2.7}$$

where η is a parameter related to the overlap of free areas, and A_f is the mean free area. Equation 2.6 can be calculated as

$$D = D(A^*)\exp(-\frac{\eta A}{A_\mathrm{f}}). \tag{2.8}$$

By taking the repulsive interaction that the neighbors or surrounding fluid exerted on lipid molecules into account, parameter E_A is introduced to the equation

$$D = D'\exp(-\frac{\eta A}{A_\mathrm{f}} - \frac{E_A}{kt}). \tag{2.9}$$

The D' here represents the unhindered diffusion coefficient.

Several experimental methods can be used to measure diffusion, such as FRAP and[88] single particle tracking (SPT).[89] For FRAP, fluorescent lipids in a small area of the membrane are bleached, by measuring the fluorescence intensity recovery kinetics due to back-diffusion of unbleached fluorescent lipids, the diffusion coefficient can be calculated. (Figure 2.6a, b) Urban et al.[7] measured the diffusion coefficient of *azo*-**PC** SLBs with FRAP. It was shown that the diffusion coefficient in the *cis* state is approximately twice as large compared to the *trans*

state (Figure 2.6c). By changing the intensity of the UV illumination, membrane diffusivity can be reversibly controlled. Not only the diffusivity, but other physical properties can also be reversibly controlled by photoisomerization of *azo*-**PC**, which will be introduced in the following.

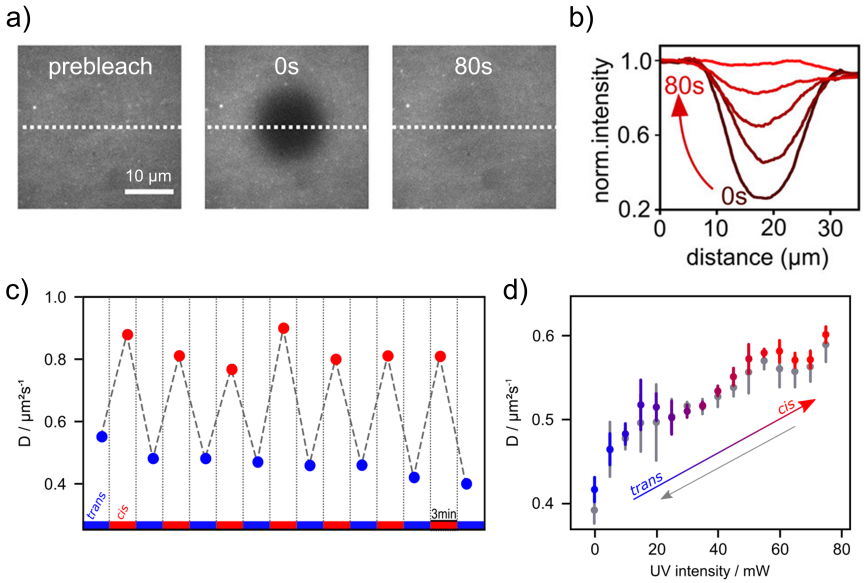

Figure 2.6: Diffusion of *azo*-PC SLBs. (a)(b) FRAP measurements of *azo*-**PC** SLBs. **(c)** The diffusion coefficient of *azo*-**PC** SLBs in the *cis* state is larger than that in the *trans* state. **(d)** Membrane diffusivity can be reversibly controlled by tuning the illumination intensity. (adapted from ref[7])

Optical control of photolipid membrane properties

The different configurations of *azo*-**PC** in *trans* and *cis* states determine the different ways the molecules form a membrane. By applying SAXS, the membrane thickness (head-to-head distance of the bilayer) can be measured. Urban et al.[7] found that in DI water, the thickness for trans and cis bilayer is 3.9 nm and 3.4 nm, respectively. A 5 Å reduction was observed (Figure 2.7a). In buffer solution, this thickness reduction due to photoisomerization increases to 8 to 10 Å.[12] This is because a higher PSS of *cis* isomers can be obtained in buffer solution.

With a Langmuir–Blodgett (LB) device, the surface tension can be measured and thus the cross-section area per lipid can be calculated. It was revealed that the area per lipid of *cis* *azo*-**PC** is 8.7 Å^2 larger than the area of *trans* *azo*-**PC**.[8,90] This area change enables photo-control of vesicles' permeability (Figure 2.7a).[91] Pritzl et al.[8] showed the fluorescence dye leakage from GUVs of *azo*-**PC** after irradiation with UV-A and visible light. Incorporating *azo*-**PC** into a lipid nanoparticle system, Chander et al. demonstrated that drug release can be triggered by switching photolipids to the *cis* state.[9]

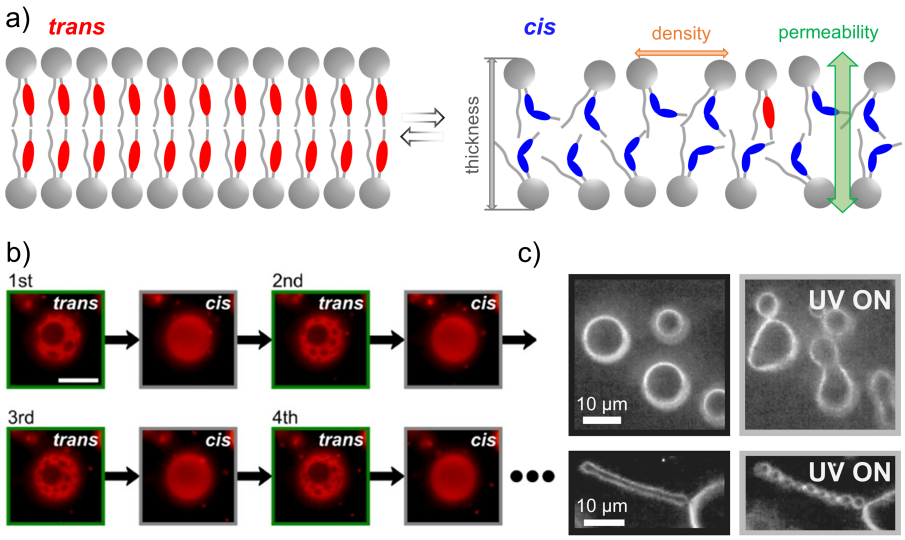

Figure 2.7: Controlling membrane properties with photolipids. (a) Lower thickness and lipid density of *cis azo*-**PC** bilayer compared to *trans* membrane. **(b)** Ternary-mixture GUVs containing 40 % of *azo*-**PC**, 40 % of DPhPC and 20 % of cholesterol. Domains reversibly form in *trans* state and disappear in *cis* state. Scale bar: 20 μm.(taken from ref[11]) **(c)** Mechanical properties and shape of GUVs composed of pure *azo*-**PC** were controlled with light. Shape transitions such as budding and pearling occurred by UV illumination. Scale bar: 10 μm. (taken from ref[6])

Figure 2.7c shows light-controlled domain formation in ternary-mixture GUVs prepared with *azo*-**PC**, 1,2-diphytanoyl-sn-glycero-3-phosphocholine (DPhPC) and cholesterol (lipid ratio 4:4:2, vesicles are labeled by 1 mol % of TR-DHPE). Upon illumination with UV and blue light, the membrane domains disappeared and recovered reversibly.[11] This was explained, since illumination changed the ratio between *trans* and *cis* photolipids. Thus the phase separation between *trans azo*-**PC** and DPhPC was dynamically tuned, leading to the assembly and disassembly of domains.

Furthermore, Pernpeintner et al.[6] presented that the mechanical properties of photolipid bilayer membrane can be controlled with light. They measured the bending rigidity of pure *azo*-**PC** GUVs and found a decrease by almost two orders from *trans* $\kappa = (1.0 \pm 0.6) \times 10^{-17}$ J to *cis* $\kappa = (5.4 \pm 1.8) \times 10^{-19}$ J. Based on this, vesicle shape transitions such as budding, fission, pealing and tube formation were induced in photolipid GUVs by controlling the time and intensity of illumination (Figure 2.7d).[92]

2.2 Interactions between Azobenzene and Fluorophores

Azobenzene, as a photochrome with two isomers, is non-fluorescent in both forms. In combination with a fluorophore, azobenzene molecules offer a means for photomodulation of the fluorophore emission.[93,94,95,96] As depicted in Figure 2.8, when azobenzene is in the *trans* state, the nearby fluorophore molecules emit fluorescence upon excitation. After switched to the *cis* state, azobenzene can act as an acceptor. Due to energy transfer (ET) or photoinduced electron transfer (PET) from the fluorophore to azobenzene, the fluorescence emission of fluorophore is quenched. Fluorescence on and off can thus be reversibly modulated by photoisomerizing the azobenzene molecules.

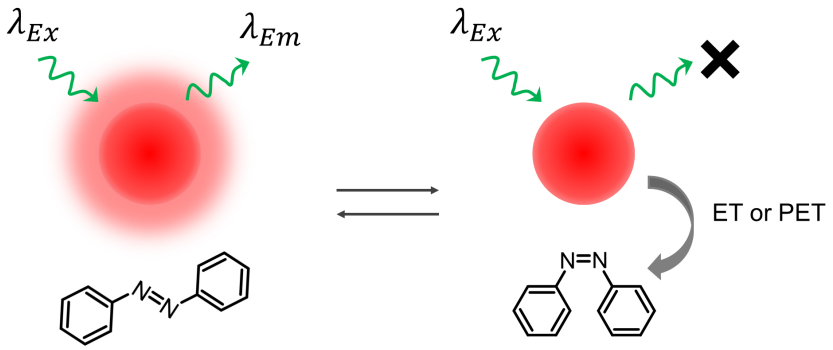

Figure 2.8: A system combining azobenzene and fluorophore molecules. The influence of azobenzene states on fluorophores: the fluorescence of fluorophore is on when azobenzene is in the *trans* state, while it is off after switching azobenzene to the *cis* state due to the ET or PET interaction. The presence of fluorophores to azobenzene states: by exciting the fluorophores, azobenzene molecules can switch from *cis* to *trans* state.

Fluorescence modulation describes the influence of the azobenzene states on fluorophores. In addition, it was reported that fluorophores can catalyze azobenzene isomerization.[97,98,99,100] Instead of switching azobenzene using direct UV and blue light radiation, excitation of fluorophore molecules is able to switch azobenzene from the *cis* to *trans* state via photosensitization. This indirect switching offers the possibility to isomerize azobenzene molecules with red light and even NIR light by choosing appropriate fluorophores, which are not harmful to biological samples and are of great interest for biomedical applications.

To better understand the interaction between azobenzene and fluorophores, one should understand the mechanism behind fluorescence quenching and sensitized azobenzene photoisomerization, which will be introduced in the following.

2.2.1 Mechanism of Fluorescence Quenching

Once a fluorophore is excited, it usually goes to higher vibrational levels of excited electronic states S_1 or S_2. The molecule then relaxes to the lowest vibrational level of S_1 through internal conversion (IC). The molecule in S_1 can return to ground state S_0 by emitting fluorescence. It can also convert to first triplet state T_1 via intersystem crossing (ISC) and then return to S_0 by emitting phosphorescence. Fluorescence and phosphorescence emission are radiative processes while IC and ISC are non-radiative pathways. Various mechanisms can cause fluorescence quenching including induced intersystem crossing, resonance energy transfer, Dexter energy transfer (DET), and photoinduced energy transfer.[101]

Intersystem crossing

Heavy atoms like halogens and triplet oxygen induce fluorescence quenching by intersystem crossing.[101,102] For example, the triplet oxygen can interact with some of the singlet excited fluorophore so that the fluorophore goes to its triplet state and singlet oxygen is produced (Figure 2.9). Triplet fluorophore then can continue to react with triplet oxygen to the ground state or return to the ground state by non-radiative decay. The interaction between triplet fluorophore and oxygen is Dexter triplet energy transfer,[103] which will be discussed later in this section. Fluorophores that have high ISC efficiency can be used as triplet sensitizers, including Methylene Blue, Fluorescein, Rose Bengal, and Eosin Blue.[104] Such fluorophores often requires the exclusion of oxygen to prevent photobleaching.

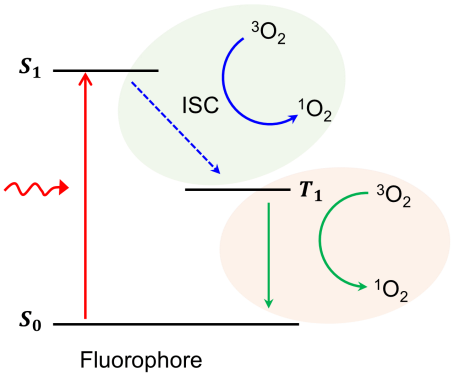

Figure 2.9: Fluorescence quenching by intersystem crossing.

Förster resonance energy transfer

Förster resonance energy transfer (FRET) is an energy transfer process from an excited donor D to an acceptor A due to dipole-dipole interactions so that the acceptor molecule is left in the excited state (Figure 2.10a). It is a non-radiative process, which means it does not involve the emission of the donor D being absorbed by the acceptorA. Three main factors determine FRET and influence its efficiency, which are the spectral overlap of D emission and A absorption, the distance between D and A, and the orientation of D and A dipoles.[101,105]

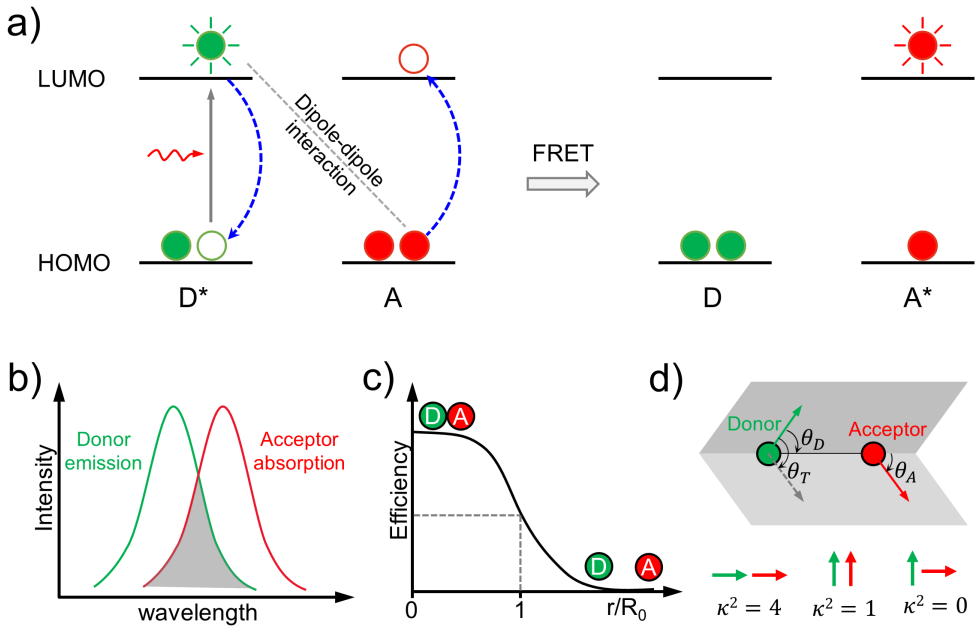

Figure 2.10: Förster resonance energy transfer. **(a)** FRET occurs due to dipole-dipole interaction between excited donor D and acceptor A. **(b)** FRET requires a spectral overlap of the donor emission and acceptor absorption. **(c)** The relationship between FRET efficiency and donor-acceptor distance r. R_0 represents Förster radius. When $r = R_0$, FRET efficiency equals 50%. **(d)** Orientation factor κ^2 can be calculated through the direction of donor and acceptor dipole. (adapted from refs[101,105])

The overlap integral is used to describe the degree of the spectral overlap of donor emission and acceptor absorption (Figure 2.10b), which is defined as a function of wavelength λ

$$\mathcal{J} = \int_0^\infty F_D(\lambda)\varepsilon_A(\lambda)\lambda^4 d\lambda, \tag{2.10}$$

where $F_D(\lambda)$ is the normalized emission spectrum of the donor and $\varepsilon_A(\lambda)$ is the normalized absorption spectrum of the acceptor. The rate of energy transfer $k_{\mathrm{ET}}(r)$ is dependent on overlap integral $\mathcal{J}$, donor-acceptor distance r (Figure 2.10c) and orientation factor κ^2 (Figure 2.10d)

$$k_{\mathrm{RET}}(r) = \frac{\phi_D \kappa^2}{\tau_D r^6 n^4} \frac{9000 \ln 10}{125\pi^5 N_A} \mathcal{J}, \tag{2.11}$$

with ϕ_D being donor fluorescence quantum yield, τ_D the lifetime of the donor, N_A the Avogadro constant, and n the refractive index of the medium. By defining the Förster radius R_0, which equals the distance between donor and acceptor where 50% of the energy gets transferred, $k_{\mathrm{RET}}(r)$ can be given by

$$k_{\mathrm{RET}}(r) = \frac{1}{\tau_D}\left(\frac{R_0}{r}\right)^6, \tag{2.12}$$

$$R_0^6 = \frac{\phi_D \kappa^2}{n^4} \frac{9000 \ln 10}{125\pi^5 N_A} \mathcal{J}. \tag{2.13}$$

The efficiency of the energy transfer can be derived as

$$E = \frac{k_{\mathrm{RET}}(r)}{\tau_D^{-1} + k_{\mathrm{RET}}(r)} = \frac{R_0^6}{R_0^6 + r^6}. \tag{2.14}$$

Dexter energy transfer

Dexter energy transfer is also called electron exchange energy transfer. As its name indicates, it involves the exchange of two electrons between the donor and acceptor. An electron in the lowest unoccupied molecular orbital (LUMO) of excited donor D is transferred to the acceptor A, and then A transfers another electron from the highest occupied molecular orbital (HOMO) to D (Figure 2.11). The results of electron exchange is that the excited D returns to the ground state and A goes to an excited state.[106] One DET type is triplet energy transfer (TET), with the interaction of $^3\mathrm{D}^* + \mathrm{A} \rightarrow \mathrm{D} + {}^3\mathrm{A}^*$.[107] In this case, both the excited-state energy and spin multiplicity are transferred. The D returns from the triplet state to ground state, while the A goes to the excited triplet state. DET occurs when the donor and acceptor are close enough (within 15 Å) so that their orbitals overlap. The DET rate also depends on the spectral overlap of D and A, but it could occur even if the overlap is small. For DET, if the triplet energy of the donor is higher than that of the acceptor, the rate of TET is fast (exothermic energy transfer). The TET could also happen when the reaction is endothermic. The rate for DET is given by[105,108]

$$k_{\mathrm{DET}}(r) = K\mathcal{J}\exp(-2r/\mathrm{L}), \tag{2.15}$$

where K denotes orbital overlap, $\mathcal{J}$ is the normalized spectral overlap integral, r is the donor-acceptor distance and L is the van der Waals radii between donor and acceptor.

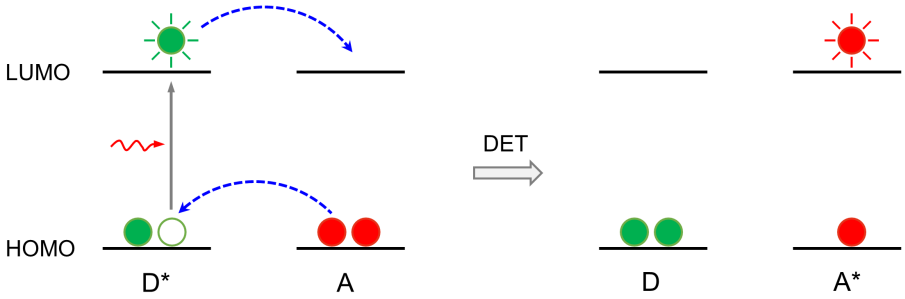

Figure 2.11: Dexter energy transfer.

Photoinduced electron transfer

Different from DET, only one electron is transferred between donor D and acceptor A for PET. If the transfer of a single electron happens involving LUMO of D and A, it is referred as to electron transfer (Figure 2.12a). It is hole transfer if the electron is transferred involving HOMO of D and A (Figure 2.12b). $(\mathrm{D}^+\mathrm{A}^-)^*$ and $(\mathrm{D}^-\mathrm{A}^+)^*$ are obtained after electron transfer and hole transfer, respectively.[106]

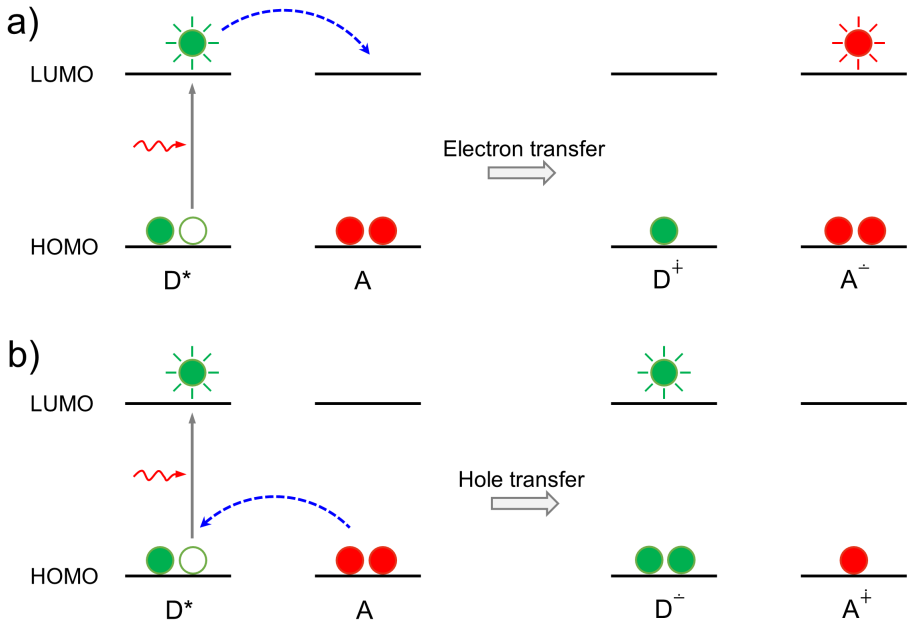

Figure 2.12: Photoinduced electron transfer. (a) Electron transfer: the single electron is transferred from the LUMO of donor D to acceptor A, forming $(D^+A^-)^*$. **(b)** Hole transfer: the single electron is transferred from the HOMO of A to D, forming $(D^-A^+)^*$. (adapted from ref[106])

The energy change for the PET process is described by the Rehm-Weller equation. For electron transfer, it is given by[106]

$$\Delta G_{et} = E^{ox}(D) - E^{red}(A) - E_{exc}(A) + \Delta E_{Coulombic}, \tag{2.16}$$

with $E^{ox}(D)$ being the oxidation potential of D, $E^{red}(A)$ being the reduction potential of A. $E_{exc}(A)$ represents the energy of $S_0 \rightarrow S_1$ transition for A, and $\Delta E_{Coulombic}$ is the electrostatic interaction between D and A ions. The energy change for hole transfer is[106]

$$\Delta G_{ht} = E^{ox}(A) - E^{red}(D) - E_{exc}(D) + \Delta E_{Coulombic}. \tag{2.17}$$

ΔG must be negative for PET to occur.

Almost all the fluorescence quenching of fluorophores by azobenzene (and its derivatives) was reported through the FRET mechanism in an azobenzene-fluorophore system,[109,110,111] which has been applied for analytes detection and bioimaging.[112]

2.2.2 Mechanism of Sensitized Photoisomerization

Indirect Photoisomerization of azobenzene can be induced with the assistance of sensitizers such as fluorophores, which is also called sensitized photoisomerization in this thesis. Instead

of absorbing light by azobenzene itself, sensitizers are excited by light and then trigger the azobenzene switching. The reported mechanisms for indirect *cis*-to-*trans* azobenzene isomerization are triplet energy transfer and photoinduced electron transfer.[113]

Triplet energy transfer

When a triplet sensitizer is excited from the ground state S_0 to singlet excited state S_1, it relaxes to its triplet state T_1 via ISC. If this sensitizer is close to azobenzene molecules, TET interaction yields azobenzene to its triplet excited state (Figure 2.13a). As early as 1965, by studying *cis*-to-*trans* isomerization of azobenzene by triplet sensitizer triphenylene, 3-acetonaphthone, and 3-acetylpyrene, Hammond and Jones[114] proposed that the mechanism following

$$^3\mathrm{S}^* + \mathit{trans} - \mathrm{Azo} \xrightarrow{k_{\text{TET-t}}} \mathrm{S} + {}^3\mathrm{Azo}^*, \tag{2.18}$$

$$^3\mathrm{S}^* + \mathit{cis} - \mathrm{Azo} \xrightarrow{k_{\text{TET-c}}} \mathrm{S} + {}^3\mathrm{Azo}^*, \tag{2.19}$$

$$^3\mathrm{Azo}^* \xrightarrow{k_{\text{ISC-t}}} \mathit{trans} - \mathrm{Azo}, \tag{2.20}$$

$$^3\mathrm{Azo}^* \xrightarrow{k_{\text{ISC-c}}} \mathit{cis} - \mathrm{Azo}. \tag{2.21}$$

It showed azobenzene in the triplet excited state returns to the ground state in both *trans* and *cis* form with rates of $k_{\text{ISC-t}}$ and $k_{\text{ISC-c}}$. The photostationary state is determined by

$$\frac{[\mathit{trans}]}{[\mathit{cis}]} = \frac{k_{\text{TET-c}} k_{\text{ISC-t}}}{k_{\text{TET-t}} k_{\text{ISC-c}}}. \tag{2.22}$$

They stated that $k_{\text{TET-c}}/k_{\text{TET-t}}$ is unity, so PSS is determined by $k_{\text{ISC-t}}/k_{\text{ISC-c}}$. The value of $k_{\text{ISC-t}}$ was measured 60 times higher than $k_{\text{ISC-c}}$, and 98 % of *trans* isomer was achieved. Later in 1979,

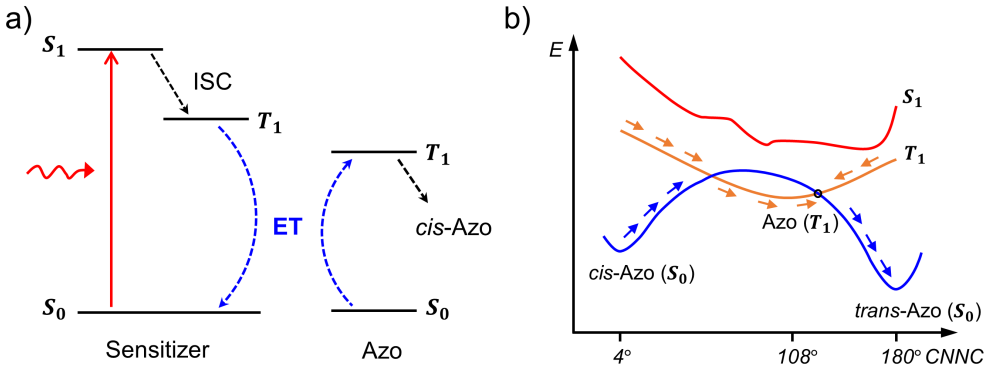

Figure 2.13: (a) *Cis*-to-*trans* isomerization of azobenzene by sensitizer via Triplet energy transfer. **(b)** Potential energy surface of azobenzene ground state S_0, singlet excited state S_1 and triplet excited state T_1. (adapted from ref[45]) Black circle represents the lowest energy cross of S_0 and T_1 potential energy surface.

Bortolus and Monti[115] measured the same process using 4,4'-dimethylaminobenzophenone, benzil and acridine as sensitizers. They obtained a TET-PSS of 98 % to 99 % *trans* azobenzene. Isokuortti et al.[116] reported that Pt/Pd porphyrins as sensitizers lead to 99 % of tera-ortho-fluorinated azobenzene via exothermic or endothermic TET upon excitation up to 770 nm. From the studies about the triplet energy of azobenzene,[45,117,118,119] TET-assisted *cis*-to-*trans* isomerization can be better understood. Cembran et al. calculated the minimum energy path and potential energy surface (PES) of azobenzene ground state S_0, singlet excited state S_1 and triplet excited state T_1 (Figure 2.13b). They found that the minimum of T_1 PES is at the twisted geometry and below the S_0 barrier. The lowest energy cross of S_0 and T_1 is on the *trans* side and close to the T_1 PES minimum, which explains why the decay rate from triplet azobenzene to *trans* isomer is much greater than to *cis* isomer.

Fluorophores as triplet sensitizers have also been studied for *cis*-to-*trans* isomerization of azobenzene. Early in 1987, Shimomura and Kunitake[97] applied cyanine dye to the switching of azobenzene-containing lipids via TET. Jacques[98] et al showed that rose Bengal, eosin Y, fluorescein, and methylene blue can achieve sensitized photoisomerization with high efficiency.

Photoinduced electron transfer

Recently, Stefan Hecht proposed that *cis*-to-*trans* isomerization of azobenzene can be achieved via electron or hole catalytic process by choosing the proper reductant and oxidant (redox potential should meet the requirement Equation 2.16, Equation 2.17). By obtaining an electron from the excited sensitizer, the *cis* isomer can be reduced to the *cis* radical anion, which immediately converts to the corresponding *trans* radical. The *trans* radical then reacts with another neutral *cis* isomer catalytically to form *trans* isomer (Figure 2.14, electron transfer).[120]

In addition, the *cis* isomer can also transfer a hole to the excited sensitizer to form a radical cation, which immediately converts to the *trans* radical cation to initiate a chain reaction with another neutral cis azobenzene (Figure 2.14, hole transfer).[100]

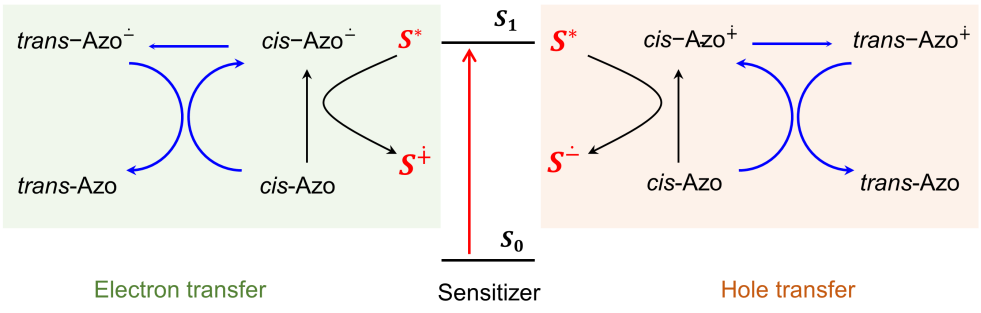

Figure 2.14: *cis*-to-*trans* isomerization of azobenzene via electron or hole transfer. (adapted from ref[100,120])

2.3 Interactions of Gold Nanoparticles and Light

The noble metal gold (Au) has an electronic configuration of $[Xe]4f^{14}5d^{10}6s^1$. It has completely filled 5d bands, where ten electrons are tightly bound. The 6s (sp-hybridized) band can hold two electrons at maximum, which is hall-filled up to the Fermi energy. Electrons in this 6sp band behave more like free electrons and determine the metallic and characteristic optical properties of gold.[121]

2.3.1 The Particle Plasmon

When light is incident on a gold nanoparticle, plasmons are generated, which are oscillations of conduction band electrons confined to the particle.[122] Therefore, to understand the interaction of AuNPs with light, one needs to characterize the motion of conduction band electrons while exposed to an external electromagnetic field. The conduction band electrons for AuNPs are electrons in the 6sp band. Since these electrons can be regarded as free electrons, they can be described by the Drude model.[122] The Drude model leads to descriptions of the dielectric properties of gold. With this dielectric function, plasmons of AuNPs can be described and understood.

Dielectric properties of gold

In the Drude model, electrons are modeled as ideal gases that will be accelerated by an external electric field. Electrons also undergo collisions after a mean scattering time τ. The motion of the displacement $\boldsymbol{x}$ for such an electron is given by:[121,122]

$$\mathrm{m}_e \frac{\partial^2 \boldsymbol{x}}{\partial t^2} + \mathrm{m}_e \Gamma \frac{\partial \boldsymbol{x}}{\partial t} = -e\boldsymbol{E}(t) = -e\boldsymbol{E}_0 \mathrm{e}^{-\mathrm{i}\omega t}, \tag{2.23}$$

where m_e is the electron mass and e is the magnitude of the electron charge. The damping rate is $\Gamma = \tau^{-1}$. The electric field of the incident electromagnetic wave is $\boldsymbol{E}(t) = \boldsymbol{E}_0 \mathrm{e}^{-\mathrm{i}\omega t}$ with ω being the angular frequency. In Equation 2.23, the terms from left-hand to right-hand side represent acceleration, damping, and the driving force respectively. The electric field of incident light will drive electrons to oscillate at the same frequency ω, thus

$$\boldsymbol{x} = \boldsymbol{x}(0)\mathrm{e}^{-\mathrm{i}\omega t}. \tag{2.24}$$

By substituting Equation 2.24 into Equation 2.23, the solution can be obtained

$$\boldsymbol{x}(\omega) = \frac{e\boldsymbol{E}_(\omega)}{\mathrm{m}_e(\omega^2 + \mathrm{i}\Gamma\omega)}. \tag{2.25}$$

This displacement of the electron induces a dipole moment $\boldsymbol{p}(\omega) = -e\boldsymbol{x}(\omega)$. Thus the polarization of the medium is generated, which is the dipole moment per unit volume[121,122]

$$\boldsymbol{P}(\omega) = N\boldsymbol{p}(\omega) = -Ne\boldsymbol{x}(\omega) = \frac{-Ne^2\boldsymbol{E}(\omega)}{\mathrm{m}_e(\omega^2 + \mathrm{i}\Gamma\omega)}, \tag{2.26}$$

with N being the number of electrons per unit volume. The electric displacement of the medium is dependent on electric field and polarization and can be expressed by:

$$\boldsymbol{D}(\omega) = \varepsilon_0\boldsymbol{E}(\omega) + \boldsymbol{P}(\omega) = \varepsilon_0\varepsilon(\omega)\boldsymbol{E}(\omega), \tag{2.27}$$

where ε_0 represents vacuum permittivity. Combining Equation 2.26 and Equation 2.27, the dielectric function of free electron gas can be derived[121,122]

$$\varepsilon(\omega) = 1 - \frac{\omega_\mathrm{p}^2}{\omega^2 + \mathrm{i}\Gamma\omega}, \tag{2.28}$$

where ω_p is the *plasma frequency* of the free electron gas

$$\omega_\mathrm{p} = \sqrt{\frac{Ne^2}{\varepsilon_0\mathrm{m}_e}}. \tag{2.29}$$

This complex dielectric function can be also expressed as $\varepsilon(\omega) = \varepsilon_1(\omega) + \mathrm{i}\varepsilon_2(\omega)$. Its real and imaginary parts are given as:[121,122]

$$\mathrm{Re}[\varepsilon(\omega)] = \varepsilon_1(\omega) = 1 - \frac{\omega_\mathrm{p}^2}{\omega^2 + \Gamma^2}, \tag{2.30}$$

$$\mathrm{Im}[\varepsilon(\omega)] = \varepsilon_2(\omega) = \frac{\omega_\mathrm{p}^2\Gamma}{\omega(\omega^2 + \Gamma^2)}. \tag{2.31}$$

It is shown that the dielectric function $\varepsilon(\omega)$ is only relying on the plasma frequency ω_p and the damping rate Γ. If $\omega >> \Gamma$, the damping is negligible. In this case, $\varepsilon(\omega)$ is mainly real, and Equation 2.28 can be simplified to

$$\varepsilon(\omega) = 1 - \frac{\omega_\mathrm{p}^2}{\omega^2}. \tag{2.32}$$

Until now all the descriptions are for ideal free electrons, the positive background due to the ion core in real metal has been ignored. This can be solved by adding a background polarization term $\boldsymbol{P}_\infty = \varepsilon_0(\varepsilon_\infty - 1)\boldsymbol{E}$ to Equation 2.27. The dielectric function thus becomes[122]

$$\varepsilon(\omega) = \varepsilon_\infty - \frac{\omega_\mathrm{p}^2}{\omega^2 + \mathrm{i}\Gamma\omega}. \tag{2.33}$$

The Drude model only describes the optical response of free conduction electrons in gold, which includes the intraband transitions meaning the excited electrons remain in the 6sp conduction band. In reality, electrons experience interband transitions from 5d bands to 6sp bands when excited by light with high frequencies. This inaccuracy due to interband transitions can be corrected by taking the resonance frequency ω_0 the same as for bound electrons into account. This means a Lorentz-oscillator term is added to the dielectric function from the Drude model.[122]

Plasmons of single nanospheres

All these discussions above are general descriptions of gold crystals. For gold nanoparticles, the most important characteristic is that the generated plasmon is confined in the particle structures and can not propagate. Therefore, this kind of plasmon is called *localized surface plasmon*.[122]

If the dimension of the nanoparticle (size below 100 nm) is much smaller than the wavelength of the incident electromagnetic field, the *quasi-static approximation* can be applied. In this case, the oscillation of the incident field phase is neglected and considered to be a constant.[122] Figure 2.15 depicts the most simple case: a nanosphere with radius a and dielectric function $\varepsilon(\omega)$ in a uniform static electric field $\mathbf{E} = \mathrm{E}_0\hat{\mathbf{z}}$, with ε_m being the permittivity of the surrounding medium. The electric field is related to potential by $\mathbf{E} = -\nabla\Phi$. After solving the Laplace equation $\nabla^2\Phi = 0$, Legendre Polynomial $P_l(\cos\theta)$ is used to express the potential[122]

$$\Phi(r,\theta) = \sum_{l=0}^{\infty}[A_l\, r^l + B_l\, r^{-(l+1)}]P_l(\cos\theta). \tag{2.34}$$

By applying boundary conditions, the potentials inside ($r < a$) and outside the nanosphere

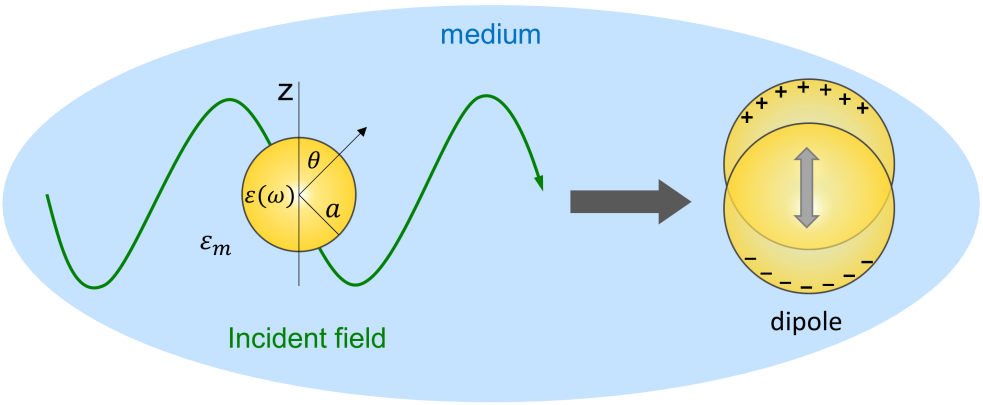

Figure 2.15: Exposure of a gold nanosphere to an electromagnetic field. The electromagnetic wave propagating through the gold nanoparticle induces the conduction band electrons to oscillate. The nanoparticle behaves like a dipole.

($r > a$) are:[122]

$$\Phi_{in} = -\frac{3\varepsilon_m}{\varepsilon + 2\varepsilon_m} E_0 r \cos\theta, \tag{2.35}$$

$$\Phi_{out} = -E_0 r \cos\theta + \frac{\varepsilon - \varepsilon_m}{\varepsilon + 2\varepsilon_m} E_0 a^3 \frac{\cos\theta}{r^2}. \tag{2.36}$$

Equation 2.36 shows that Φ_{out} originates from a superposition of the exerted field and the field of a nanosphere dipole. Hence by introducing the dipole moment $\mathbf{p}$, Equation 2.36 can be rewritten as[122]

$$\Phi_{out} = -E_0 r \cos\theta + \frac{\mathbf{p} \cdot \mathbf{r}}{4\pi\varepsilon_0\varepsilon_m r^3}, \tag{2.37}$$

$$\mathbf{p} = 4\pi\varepsilon_0\varepsilon_m a^3 \frac{\varepsilon - \varepsilon_m}{\varepsilon + 2\varepsilon_m} \mathbf{E}_0. \tag{2.38}$$

This means when exposed to an external field, a dipole moment inside the nanoparticle is generated. Since the dipole moment $\mathbf{p}$ is related to polarizability α by $\mathbf{p} = \varepsilon_0\varepsilon_m\alpha\mathbf{E}_0$, the polarizability is obtained as[122]

$$\alpha = 4\pi a^3 \frac{\varepsilon - \varepsilon_m}{\varepsilon + 2\varepsilon_m}. \tag{2.39}$$

It is clear when $|\varepsilon + 2\varepsilon_m| \to 0$, the polarizability or dipole moment of the nanoparticle has its resonance enhancement. For the case that damping is negligible so that $\varepsilon(\omega)$ is mainly real (Equation 2.32), the resonance condition becomes

$$\mathrm{Re}[\varepsilon(\omega)] = -2\varepsilon_m, \tag{2.40}$$

which is called Fröhlich condition.[122] It is very important for the application of plasmonic sensing since it indicates that the plasmonic resonance depends on the dielectric environment. As the permittivity of surrounding medium ε_m increases, the plasmonic resonance red-shifts. For a nanoparticle located in the air, its resonance is at $\omega = \omega_p/\sqrt{3}$.

Combining Equation 2.35, Equation 2.36 and formula $\mathbf{E} = -\nabla\Phi$, the electric field inside and outside the nanosphere can be derived as:

$$\mathbf{E}_{in} = \frac{3\varepsilon_m}{\varepsilon + 2\varepsilon_m} E_0, \tag{2.41}$$

$$\mathbf{E}_{out} = E_0 + \frac{3}{r^3} \frac{3\mathbf{n}(\mathbf{n} \cdot \mathbf{p}) - \mathbf{p}}{4\pi\varepsilon_0\varepsilon_m}, \tag{2.42}$$

with $\mathbf{n}$ being the direction of the interested point. It indicates at the plasmonic resonance, the field inside and the outside dipolar field get resonantly enhanced. This significant field enhancement is the basis for many applications of gold nanoparticles such as SERS, which will be discussed in section 2.3.

From the polarizability (Equation 2.39), the scattering and absorption cross section can thus be calculated through[122]

$$\sigma_{\text{sca}} = \frac{k^4}{6\pi}|\alpha|^2 = \frac{8\pi}{3}k^4a^6|\frac{\varepsilon-\varepsilon_{\text{m}}}{\varepsilon+2\varepsilon_{\text{m}}}|^2, \tag{2.43}$$

$$\sigma_{\text{abs}} = k\,\text{Im}[\alpha] = 4\pi ka^3\text{Im}[\frac{\varepsilon-\varepsilon_{\text{m}}}{\varepsilon+2\varepsilon_{\text{m}}}], \tag{2.44}$$

$$\sigma_{\text{ext}} = \sigma_{\text{abs}} + \sigma_{\text{sca}} \tag{2.45}$$

The extinction cross section is the sum of the scattering cross section and the absorption cross section. Equation 2.43 and Equation 2.44 show that at the plasmon resonance, absorption, scattering and thus extinction get resonantly enhanced.

Plasmons of single anisotropic nanoparticles

Spherical metal nanoparticles that have been discussed above are the simplest case. In this thesis, AuNRs and ellipsoid are used. The difference in nanoparticle morphologies has an influence on the plasmonic properties. First, it will affect the position and shape of the plasmonic resonance.

For example, the geometry of ellipsoids is defined by three different axes a_1,a_2 and a_3

$$\frac{x^2}{a_1^2}+\frac{y^2}{a_2^2}+\frac{z^2}{a_3^2}=1. \tag{2.46}$$

Similar to Equation 2.39, the polarizabilities α_i (i = 1, 2, 3) along axes of ellipsoid is[122]

$$\alpha_i = 4\pi a_1a_2a_3\,\frac{\varepsilon-\varepsilon_{\text{m}}}{3\varepsilon_{\text{m}}+3L_i(\varepsilon-\varepsilon_{\text{m}})}, \tag{2.47}$$

where L_i is the geometry factor and satisfies $L_1+L_2+L_3=1$. Assuming $a_1=a_2$ or $a_2=a_3$, a spheroid can be obtained. In this case, two plasmonic resonance peaks are exhibited by solving Equation 2.47. These two resonances correspond to the transversal and longitudinal plasmon modes respectively. The transversal resonance is similar to that of a sphere with comparable diameter. The longitudinal resonance is red-shifted due to the increased dipole length.

Gold nanorods have gained the most attention among all anisotropic morphologies. AuNRs also present two plasmon resonances. The much weaker transversal mode is located between 510-540 nm while the strong longitudinal mode can be tuned in a wide spectral range from visible (550 nm) to near-infrared region (up to 1400 nm) by tuning the particle's aspect ratio (length-width ratio).[123,124]

Not only does the plasmon resonance change, but the geometry differences also affect the field enhancement properties. In principle, nanoparticle geometries with sharper tips feature higher field enhancement[125] due to lightning rod effect.[126] Compared to nanospheres, the field enhancement at nanorods tips is higher. Compared to nanorods, the field enhancement at ellipsoid tips is higher. Benefiting from chemical synthesis, other geometries such as nanotriangles and nanostars have been synthesized, to take advantage of the so-called lightning rod effect. These geometries feature sharp tips are good probes for SERS measurements (in Subsection 2.4.2).

2.3.2 Gold Nanoparticles as Plasmonic Sensors

The Fröhlich condition shows that plasmonic resonance is strongly dependent on the local environment. The plasmon resonance shifts as the refractive index of the surrounding medium changes. Based on this, gold nanoparticles can be used as plasmonic sensors. Single gold nanoparticles are sensitive enough to detect local environment changes,[127,128,129] which have been applied in biological systems to monitor events including local absorption,[130] desorption, dynamics of molecules (such as MinDE protein oscillations[131,132]), molecular switching[133,134] (such as azobenzene switching[135]), chemical reactions[136] and binding[137,138](such as protein-protein[139,140] or lipid-protein interaction[141]). This method avoids the use of fluorescence labeling and is non-destructive to biomolecules. In addition, plasmonic AuNPs allow for measurements with high spatial resolution on the nanometer scale.

Plasmonic nanoparticles can be analyzed by a dark field microscope and spectroscopy (will be discussed in Subsection 3.2.2). To apply AuNPs as plasmonic sensors, firstly, nanoparticles need to be functionalized so that interested molecules can bind to them (Figure 2.16 a, top). Then a scattering spectrum of a single NPs is obtained (solid red line in Figure 2.16 b). When interested molecules are added to interact with the nanoparticles, or chemicals are added

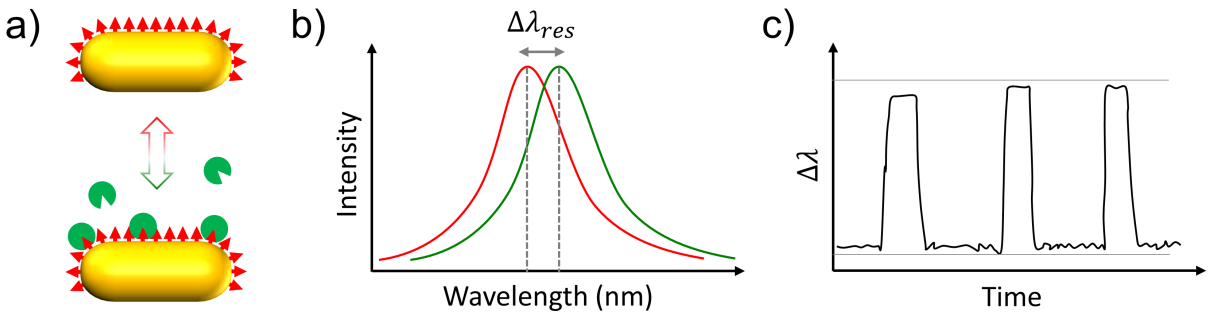

Figure 2.16: Principle of plasmonic sensing with single nanoparticles. (a) Interactions happen on the surface of the nanoparticles, which induces a refractive index change. **(b)** This change could be detected by measuring the plasmon resonance shift. **(c)** Real-time monitoring could be achieved by continuously measuring the plasmon resonance shift.

to trigger a reaction (Figure 2.16 a, bottom), the scattering spectrum should be measured again after changing the dielectric environment (solid green line in Figure 2.16 b). Plasmon resonance shift can be calculated by comparing the scattering spectra. The plasmon resonance shift $\Delta\lambda_{res}$ is thereby dependent on the refractive index of the surrounding medium (Δn) and the thickness of the adsorbate layer (d), which is given by[142,143,144]

$$\Delta\lambda_{res} = m\Delta n(1 - e^{-2d/l_d}), \tag{2.48}$$

with l_d being the electromagnetic field decay length and m being the sensitivity factor that relies on the size, shape and composition of the used particle. By continuously measuring the plasmon resonance shift, real-time monitoring can be achieved. (Figure 2.16 c).

2.3.3 Optical Forces

Another important aspect of light-AuNP interactions is the optical forces that light exerts on a nanoparticle. Optical forces have been used to manipulate individual nanoparticles for trapping,[145] printing[146,147] and patterning.[148]

The optical force can be split into two components: the gradient force and the scattering force.[149] The gradient force attracts the particle into the area of highest light intensity. The scattering force results from the momentum conservation law. When an incident photon is absorbed or scattered by a particle, the change of the photon momentum must be transferred to the mechanical momentum of the particle. Thus this scattering force pushes the particle to move along the direction of light propagation.

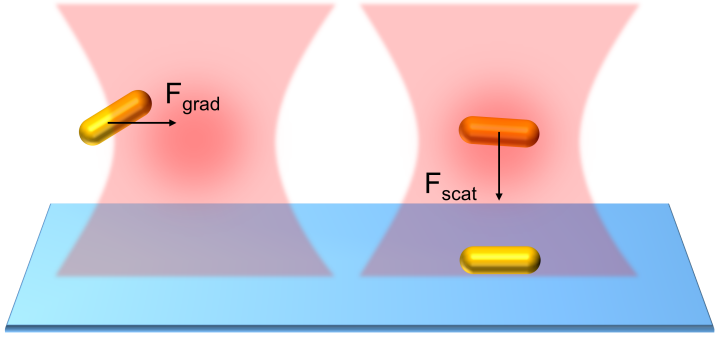

Figure 2.17: Illustration of optical forces The gradient force pulls the particle into the position with the highest intensity (left). The scattering force pushes the particle to move along the light propagation direction (right).

For A nanoparticle with dimension much smaller than the wavelength of the incident light, THE Rayleigh approximation (or quasi-static approximation) is satisfied. As discussed in section 2.2.1, nanoparticles can be considered as a dipole. In this case, the optical forces can

be calculated using the Lorentz force. The Lorentz force acting on the dipole is

$$\mathbf{F} = (\mathbf{p} \cdot \nabla)\mathbf{E} + \frac{\partial \mathbf{p}}{\partial t} \times \mathbf{B}, \tag{2.49}$$

where $\mathbf{p} = \alpha \mathbf{E}$ is the polarization of the dipole, and $\mathbf{E}$ and $\mathbf{B}$ are the electric field and magnetic flux density. With polarizability $\alpha = \alpha' + i\alpha''$, the Lorentz force can be derived as[150]

$$< \mathbf{F} >= \underbrace{\frac{1}{4}\varepsilon_0 \varepsilon_m \alpha' \nabla(E_j E_j^*)}_{<\mathbf{F}_{grad}>} + \underbrace{\frac{1}{2}\varepsilon_0 \varepsilon_m \alpha'' \mathrm{Im}(E_j^* \nabla E_j)}_{<\mathbf{F}_{scat}>}, \tag{2.50}$$

where j denotes Cartesian coordinates. Two terms in Equation 2.50 describes the gradient force $\mathbf{F}_{grad}$ and the scattering force $\mathbf{F}_{scat}$, which depend on the real part and the imaginary part of the polarizability, respectively.

2.3.4 Melting of Gold Nanorods

Gold nanoparticles are efficient in converting optical energy into thermal energy. Significant heating of NPs is generated under laser irradiation.[151] This heating results from the internal plasmonic decay processes.

An excited plasmon can decay through two pathways, as shown in Figure 2.18, radiative and non-radiative decay.[152] The radiative decay process does not lead to the heating of NPs since in this case the dipole energy is lost via re-emission of photons. The non-radiative decay finally induces thermalization. The non-radiative decay occurs via creating electron-hole pairs. Electron-hole pairs are formed by exciting the electrons inside the sp-band (intraband decay) or from the d-band to the sp-band (interband decay). Then the excited electrons can

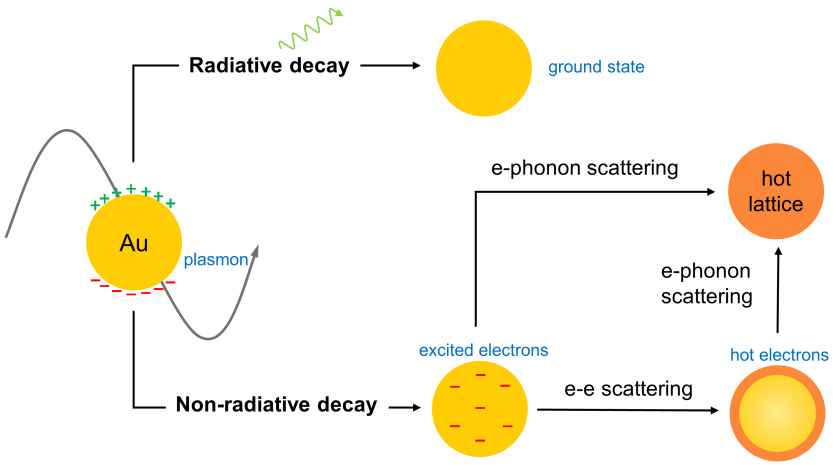

Figure 2.18: Internal non-radiative plasmonic decay induces heating of AuNPs.

scatter with electrons or with phonons. Both of the scatterings finally will thermalize the lattice and homogeneously heat the whole NPs.

Plasmonic heating can lead to shape and size changes, that is the photo-thermal melting of AuNPs. For non-spherical nanoparticles such as gold nanorods, once the melting temperature is reached, a transfermation to a spherical shape is observed, since spheres provide the highest surface-to-volume ratio.[153] It was shown that compared to bulk materials, the melting point of nanoparticles is significatly decreased.[154] The melting point of nanoparticles is dependent on radius and shape.[155]

Link et al. investigated the morphology changes of gold nanorods in solution during the melting process.[156] From the high-resolution transmission electron microscopy (TEM) images, they revealed the transition from a gold nanorod to nanodot starts in the interior of the rod by creating point and line defects (Figure 2.19b). These point defects then form twins (multiple) and stacking faults (planar defects), as shown in Figure 2.19d. Finally, melting occurs after the surface diffusion of gold atoms from the tips to the rod center (Figure 2.19c). Melting was found to be dependent on laser-pulse width and energy.

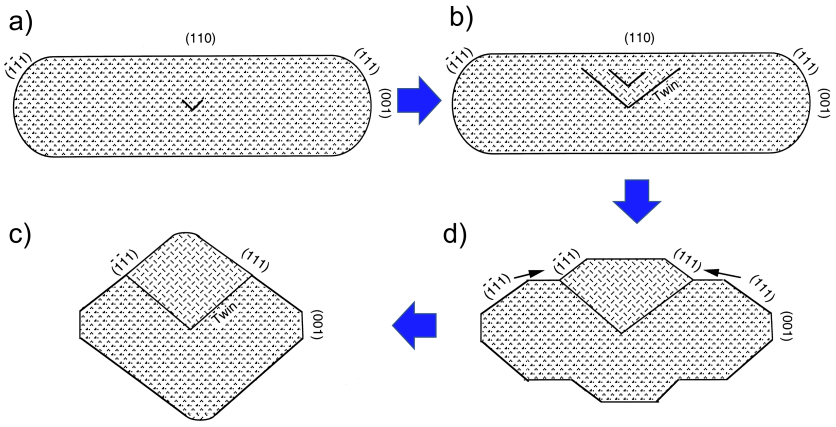

Figure 2.19: Melting process from a gold nanorod to nanodot. (taken from ref[156])

Different shapes[157,158] were observed such as dumbells, ϕ-shaped, banana-shaped, and sickle-shaped during the intermediate steps of gold nanorods melting. Combining plasmonic heating and optical forces, Babynina et al.[159] showed that single nanorods can be bent and printed onto a substrate. They demonstrated that the bending angle and orientation depend on the laser intensity and polarization. Furthermore, Schuknecht et al.[160] found that by continuing to increase the laser power after nanorods get bent, single gold nanorods can be split into dimers and printed on the substrate. This nanorod splitting was explained by a combination of plasmonic heating, optical forces, surface tension and inhomogeneous hydrodynamic pressure. The gap between dimers was found to be within 1 nm, which was highly suitable for SERS.

2.4 Surface Enhanced Raman Scattering

One of the most exciting applications of plasmonics is SERS, which combines Raman spectroscopy and the field enhancement properties of plasmonic nanoantennas for the strong amplification of the Raman scattering signal of molecules close to the surface of a metallic nanostructure.[161] As discussed in section 2.2.1, at the plasmonic resonance, the scattering cross section increases (Equation 2.43) and the local fields get highly enhanced (Equation 2.42), so that the excitation laser fields and the scattered Raman will be enhanced. Both the increased cross section and enhanced fields of excitation and radiation give rise to an amplified Raman signal.

2.4.1 The Principle of SERS

Before introducing the theory of SERS, first the Raman effect is briefly discussed. When a photon is incident on a molecule, it can be spontaneously scattered. If the scattered photon has the same energy as the incident photon, this process is elastic scattering, referred to as Rayleigh scattering (Figure 2.20 b). Raman scattering is an inelastic scattering process. The energy of the incident photon $h\nu_0$ is shifted by the transition energy of the molecular vibrational and rotational level $h\nu_m$. It is Stokes scattering if the scattered photon loses energy and anti-Stokes scattering when the photon gains energy of $h\nu_m$ (Figure 2.20 c). Therefore, the Raman scattered photon has frequencies of (Stokes ν_S, anti-Stokes ν_{AS})[122,162]

$$\nu_S = \nu_0 - \nu_m, \tag{2.51}$$

$$\nu_{AS} = \nu_0 + \nu_m. \tag{2.52}$$

Note that no absorption and emission of photons are involved in the scattering process. Thus the shifted energy level of scattered photons may not exist, represented by an intermediate virtual state. If the incident photon is not in resonance with any molecular transitions so that the virtual state is away from the real electronic states of the molecule, this process is non-resonance Raman scattering. If the virtual state coincides with one of the real states, this is so-called resonance Raman scattering (RRS). In the case of RRS, scattering efficiency increases by several orders of magnitude.[163]

In comparison, fluorescence is a two-step process including first the absorption of a photon and then the emission of another photon (Figure 2.20 d). Fluorescence spectra are typically broad due to the non-radiative relaxation of electrons to lower vibrational levels within the same electronic state. Different from fluorescence spectra, Raman spectra show sharp peaks, which provide structure information of the molecule.

IR spectroscopy is also a technique providing molecular vibrational and rotational information. It is based on the absorption of IR radiation (Figure 2.20 a). The main difference between IR and Raman spectroscopy is that IR measures the vibration that changes the dipole moment and Raman detects the vibration that changes the polarizability.[164]

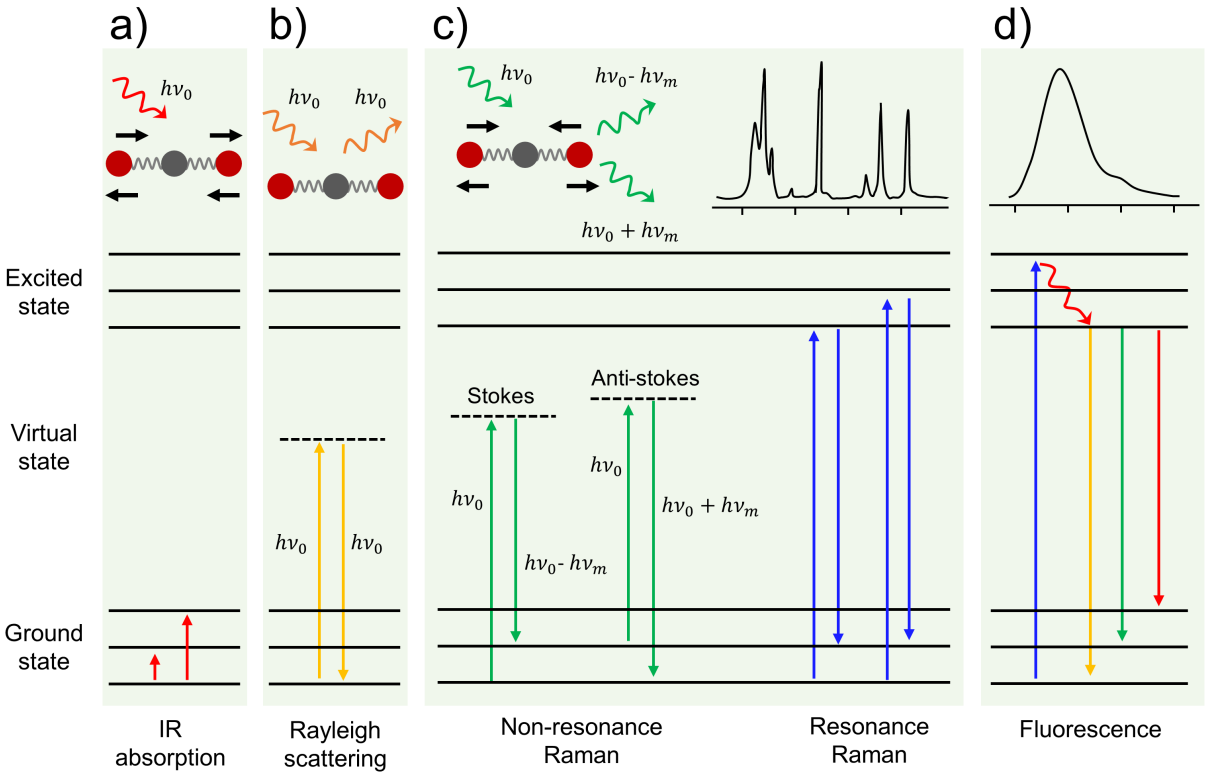

Figure 2.20: Illustration of IR, Rayleigh scattering, Raman scattering and fluorescence.[165,166] **(a)** IR spectra are based on absorption of IR irradiation. It measures the vibrations of molecules that cause dipole moment change. **(b)** Rayleigh scattering is an elastic scattering. **(c)** Raman scattering is an inelastic scattering. It has two bans, Stokes and anti-Stokes. If the incident photon is in resonance with the electronic transitions, it is resonance Raman scattering. Raman spectra show sharp peaks, which provide information on molecular vibrations that cause a change in polarizability. **(d)** Absorption and emission of photons are involved in the fluorescence process. Its spectrum is broad.

Enhancement factors of SERS

The intensity of the Stokes Raman signal P_{RS} is dependent on the Raman cross section σ_{RS}, the excitation intensity $I(\nu_L)$ and the number of molecules that scatter N. It is given by[122]

$$P_{\mathrm{RS}}(\nu_L) = N\sigma_{\mathrm{RS}}\, I(\nu_L). \tag{2.53}$$

For SERS, the molecule must be in the vicinity of the metal nanostructure (with distance d)(Figure 2.21). As briefly mentioned at the beginning of this section, the enhancement of the Raman signal is primarily based on two effects:[122,167]

(i) Compared to the Raman cross section σ_{RS} of a free molecule, the SERS cross section σ_{SERS} (molecule close to the metallic nanostructure) is increased, this is called chemical enhancement.[168,169] This kind of enhancement relies on the chemical nature of the molecule and exhibits a strong molecular selectivity. Different mechanisms are proposed to explain the origin of chemical enhancement, such as electronic coupling[167] or change transfer.[170] It can contributes to an enhancement on the order of 10-100.[171]
(ii) From Equation 2.42, the local optical field $\boldsymbol{E}_m$ is enhanced due to the formation of a dipole field $\boldsymbol{E}_{dp}$:

$$\boldsymbol{E}_m = \boldsymbol{E}_0 + \boldsymbol{E}_{dp} = \boldsymbol{E}_0 + \frac{a^3}{(a+d)^3}\frac{\varepsilon - \varepsilon_m}{\varepsilon + 2\varepsilon_m}\boldsymbol{E}_0. \tag{2.54}$$

So that the field enhancement factor $A(\nu)$ is:

$$A(\nu) = \frac{|\boldsymbol{E}_m(\nu)|}{|\boldsymbol{E}_0(\nu)|} \sim \frac{a^3}{(a+d)^3}\frac{\varepsilon - \varepsilon_m}{\varepsilon + 2\varepsilon_m}. \tag{2.55}$$

Considering these two effects, the power of SERS Stokes is

$$P_{SERS}(\nu_L) = N'\,\sigma_{SERS}\,|A(\nu_L)|^2|A(\nu_S)|^2 I(\nu_L), \tag{2.56}$$

with $A(\nu_L)$ and $A(\nu_s)$ as the enhancement factors for the excitation and scattered light. Therefore, the total field enhancement becomes[167,172]

$$R = |A(\nu_L)|^2|A(\nu_S)|^2 \sim \frac{|\boldsymbol{E}_m(\nu)|^4}{|\boldsymbol{E}_0(\nu)|^4} \sim |\frac{\varepsilon - \varepsilon_m}{\varepsilon + 2\varepsilon_m}|^4 (\frac{a}{a+d})^{12}. \tag{2.57}$$

This formula shows that SERS enhancement is approximately equal to the fourth power of the field enhancement. At the resonance of localized plasmons, the excitation and scattered field get enhanced and accordingly the Raman signal. In addition, the Raman intensity strongly depends on the distance between molecule and metal according to the formula due to a drop of the near field intensity with distance.

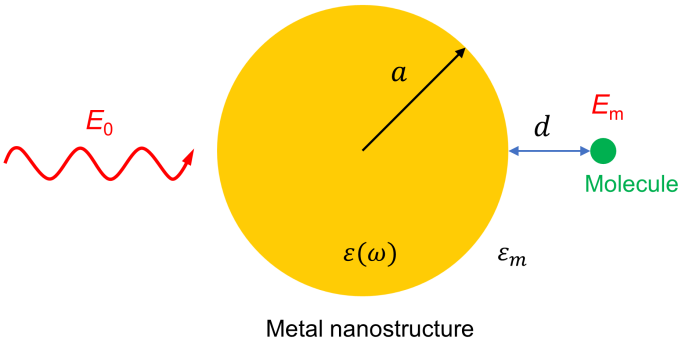

Figure 2.21: Schematic to calculate the field enhancement of SERS. The molecule is in the near field of a metal nanostructure at a distance of *d*. (adapted from ref[167,172])

2.4.2 SERS Substrates

It was reported that SERS can achieve an enhancement factor up to 10^{14}-10^{15},[173,174] which could be applied for ultrasensitive detection such as single-molecule SERS.[175] The greatest enhancement factors are acquired within the so-called hot spot regions,[172] including sharp tips or vertices in single nanostructures, gaps between two or multi-nanoparticles, and junctions or crevices in nanoparticle aggregates. This provides strategies for the design of SERS substrates.

In general, SERS substrates can be divided into two types: periodic nanostructures[176] and single SERS nanoantennae.[177] Controlled deposition and lithographic/template synthesis are the most common methods used for the fabrication of periodic 2D nanostructures (Figure 2.22 a and b).[178] In some examples, organic layers such as CTAB[179] and inorganic shells (such as silica)[180] have been used to control the distance between the periodically deposited nanoparticles. Figure 2.22 b illustrates an example of triangle array synthesized by nanosphere lithography,[181,182,183] in which a monolayer of polystyrene spheres is spin-coated and then removed from the substrates after metal deposition to control the spacing and dimensions of the gold triangles.

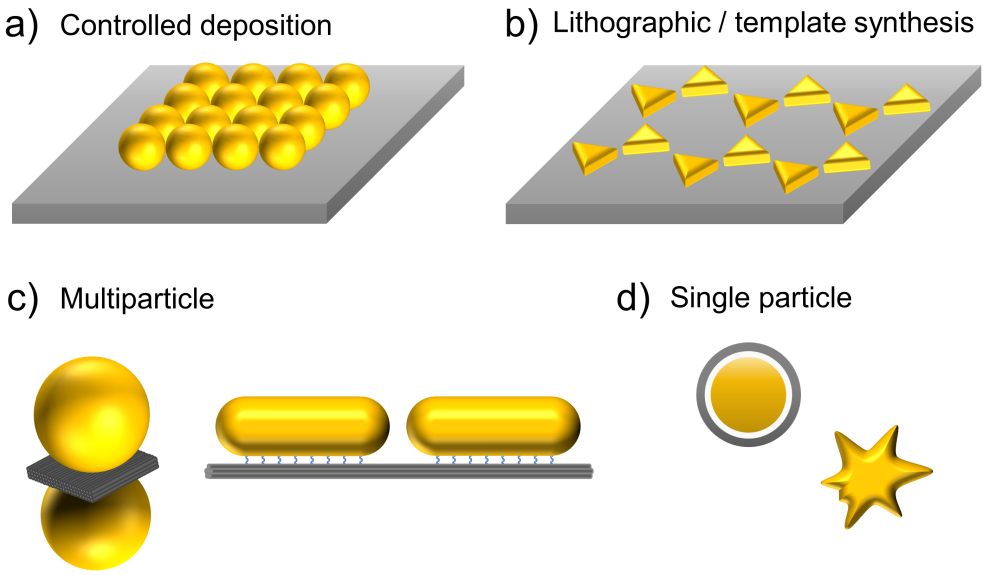

Figure 2.22: Typical SERS substrates. **(a)** Nanostructure arrays formed by controlled deposition. **(b)** Periodic metallic triangles prepared by nanosphere lithography. **(c)** gold NP dimers and bi-rods assembled with DNA origami. **(d)** Metallic core-shell structures and nanoparticles with sharp tips.

The field enhancement of single gold nanospheres is generally too weak for SERS. Nanorods provide greater enhancement, but single gold nanorods are still weak for a reliable SERS except for resonance molecules.[184] Anisotropic paricles with shapes displaying sharp tips

were synthesized to obtain higher enhancement for SERS such as nanotriangles[185,186] and nanostars[187,188,189] (Figure 2.22 d). Single core-shell structures are shown to be able to create hot-spots as well.[190] In addition, dimers or aggregates of nanoparticles were designed as a single SERS antenna. DNA strands have been used as a scaffold for the assembly of nanoparticle aggregates.[191,192] This method can produce aggregates of different shapes such as dimers, quadramers and pyramidal structures with high yield.[193] DNA origami also enables the tuning of gap size between nanoparticles and provides a binding site for the analytes at the position of the highest field enhancement. Gold NP dimers[194,195] and bi-rods[160,196] shown in Figure 2.22 c have been assembled with DNA origami to achieve even single-molecule SERS.

2.4.3 Raman Spectra of Azobenzene

Raman scattering, which is sensitive to molecular vibrations, has been applied for the detection of changes in the structure and conformation of molecules. Furthermore, the reversible photoisomerization of azobenzene molecules could be monitored by Raman spectroscopy. Different Raman sensors have been used to obtain the Raman spectra of azobenzene, such as gold nanohole arrays,[197] colloid gold nanoprisms,[198] nanoparticle aggregates,[199,200] and metal tips.[201,202]

The Raman spectra of azobenzene measured with different nanoprobes are similar,[197,203,204] as shown in Figure 2.23. Typically, seven peaks are observed at 1130 cm^{-1} (P1), 1180 cm^{-1} (P2),

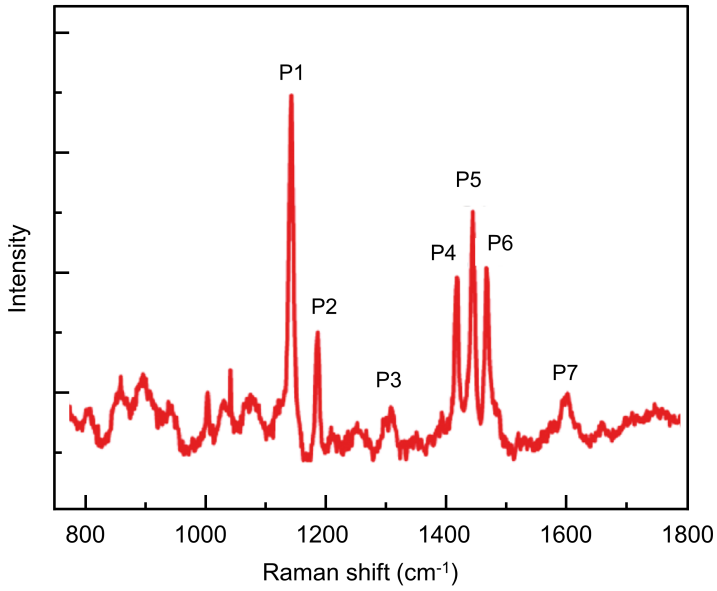

Figure 2.23: Typical Raman spectra of azobenzene molecules. The spectrum shows seven peaks at1130 cm^{-1} (P1), 1180 cm^{-1} (P2), 1310 cm^{-1} (P3), 1420 cm^{-1} (P4), 1450 cm^{-1} (P5), 1470 cm^{-1} (P6) and 1600 cm^{-1} (P7). (Adapted from ref[197])

1310 cm^{-1} (P3), 1420 cm^{-1} (P4), 1450 cm^{-1} (P5), 1470 cm^{-1} (P6) and 1600 cm^{-1} (P7). By performing simulations and DFT calculations, the mode descriptions corresponding to each peak were reported in literature.[197,204] The peaks at 1130 cm^{-1} and 1180 cm^{-1} are due to C-N stretching. Small peaks at 1310 cm^{-1} (C-C in-plane bending) and 1600 cm^{-1} (C-C stretching) are related to motions with the phenyl rings. The peaks at 1420cm^{-1} and 1450 cm^{-1} are in-plane ring bending modes coupled to N=N stretching and 1470 cm^{-1} peak is attribute to N=N stretching (Table 2.1).

Table 2.1: Raman peaks for azobenzene[197,198,204]

Peaks	Raman shifts(cm^{-1})	Mode descriptions
P_1	1130	CN stretching
P_2	1180	CN stretching
P_3	1310	CC in plane bending
P_4	1420	NN stretching in-plane ring bending
P_5	1450	NN stretching in-plane ring bending
P_6	1470	NN stretching
P_7	1600	CC stretching

Switching kinetics of azobenzene molecules can be analyzed by changes of Raman modes due to a change in the molecule's configuration. The Raman spectra for *trans* and *cis* azobenzene look similar. However, differences in peak intensity[198,204] and peak ratio[197,198,203] or the appearance of new peaks[202] are indicative for the switching between *trans* and *cis* states. Stuart et al.[204] showed that the Raman intensity of azobenzene solution in the *trans* state is higher than in the *cis* state. Later, Zheng et al.[197] measured SERS of a single azobenzene layer on a Au nanohole array, and got one order of magnitude higher Raman signal intensity for the *trans* compared to the *cis* isomer. They also found reversible changes in the peak ratio of P4/P5 by UV and blue exposure. However, Joshi et al.[198] observed a totally opposite trend in Raman intensity and peak ratio. This reverse trend was discussed to be caused by the use of a different nanostructure geometry (nanoprism) and electronic interaction between azobenzene and substrate.

3

Preparation and Characterization of Lipid Membranes and AuNRs

For the experiments presented in this thesis, sample preparation methods, spectroscopic and microscopic techniques used as well as analytical methods are essential, which will be introduced in this chapter. In Section 3.1, all the lipids and dyes used in all experiments are summarized. For the study of photolipids isomerization and its interaction with dye-lipid molecules, bilayer membrane samples including SUVs, GUVs and SLBs have been synthesized and the preparation protocols are described. The setups and methods used for sample characterization including fluorescence microscopy, UV-Vis spectroscopy, steady-state PL and time-resolved PL are also introduced. Finally, plasmonic sensing and SERS experiments on single gold nanoparticles were performed using dark-field scattering spectroscopy and Raman spectroscopy. These setups are discussed in Section 3.2. Furthermore, the scanning electron microscopy (SEM) setup used to characterize AuNPs and the numerical methods applied to calculate the plasmonic electrodynamical response are introduced.

3.1 Preparation and Characterization of Lipid Membranes

3.1.1 Lipid Molecules

Photolipids. *Azo*-**PC** molecules were synthesized and provided by the research group of Prof. Dr. Dirk Trauner (Department of Chemistry, University of Pennsylvania). *Oxy-azo*-**PC**, an *azo*-**PC** derivative with oxygen in para-position of the phenyl rings, was used for control experiments, which was synthesized by Dr. Benedikt Baumgartner from the research group of Dr. Oliver Thorn-Seshold (Department of Pharmacy, LMU). Molecular structures of these lipids are shown in Figure 3.1.

Non-photoswitchable lipids. Non-photoswitchable lipids DOPC (**18:1(Δ9-Cis)PC**, Avanti polar Lipids) was also used for control experiments since it has the same head group and similar chain length as *azo*-**PC**.

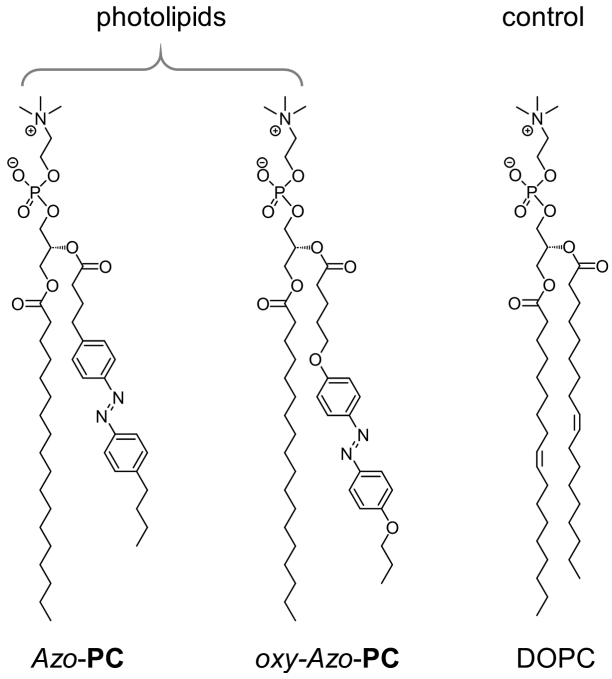

Figure 3.1: Chemical structure of lipid molecules. Photoswitchable lipids *azo*-**PC**, *Oxy-azo*-**PC** and non-photoswitchable lipids DOPC: 18:1(Δ9-Cis)PC.

Dye-labeled lipids. Several dye-labeled lipids were applied for the study of sensitized *azo*-**PC** photoisomerization, including TexasRed-DHPE (1,2-dihexadecanoyl-sn-glycero-3-phosphoethanolamine, ThermoFisher), Atto633-DPPE (1,2-dipalmitoyl-sn-glycero-3- phosphoethanolamine, AttoTec), Rhodamine-, Nile blue- and Methylene Blue-lipids (were synthesized and provided by Dr. Benedikt Baumgartner from Dr. Oliver Thorn-Seshold's group). Molecular structure, photoluminescence (PL) and photoluminescence excitation (PLE) spectra of all dye-labeled lipids are shown in Figure 3.2.

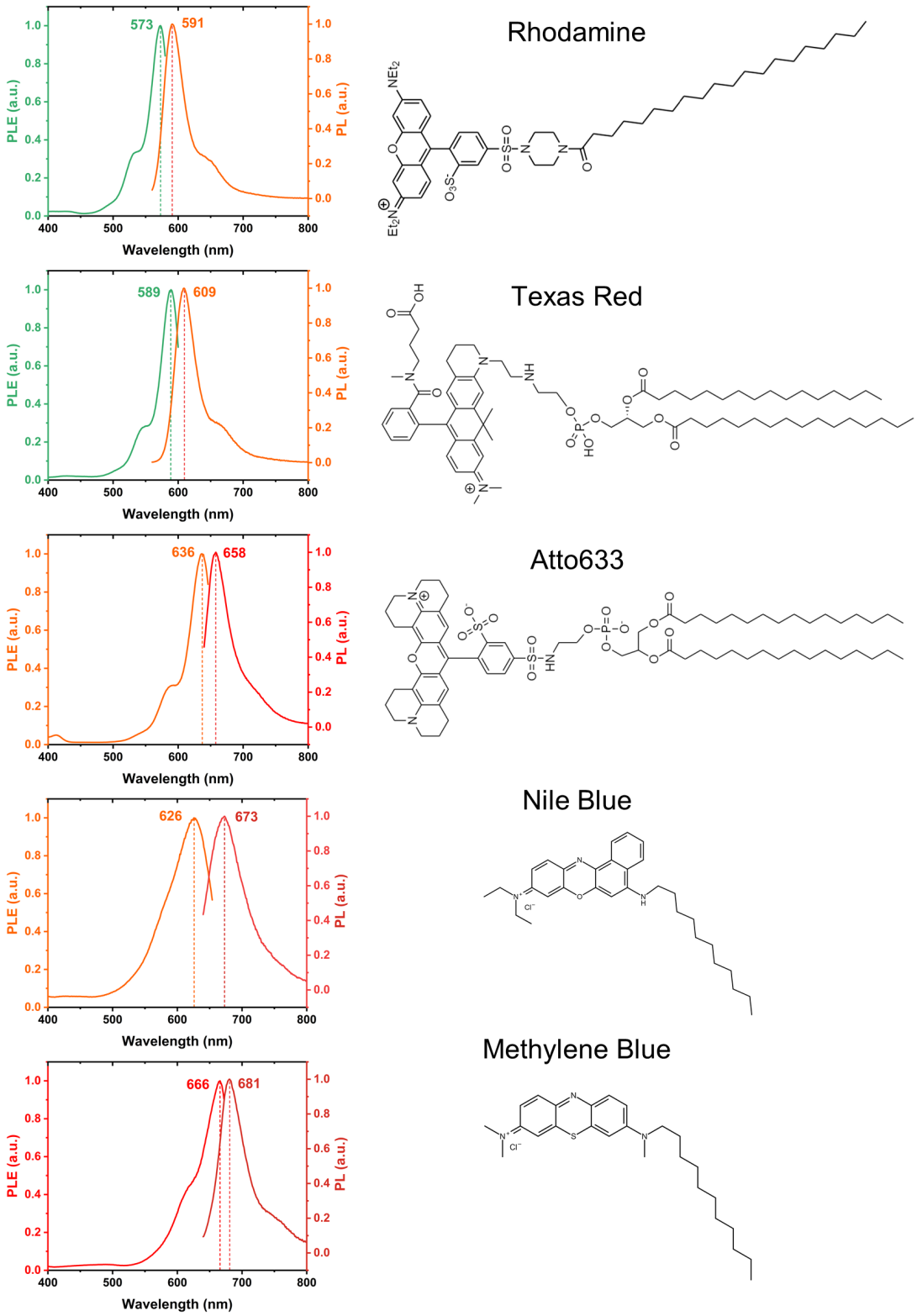

Figure 3.2: PL/PLE spectra and chemical structure of dye-labeled Lipids. Rhodamine: PLE_{max} = 573 nm, PL_{max} = 591 nm. Texas Red: PLE_{max} = 589 nm, PL_{max} = 609 nm. Atto633: PLE_{max} = 636 nm, PL_{max} = 658 nm. Nile blue: PLE_{max} = 626 nm, PL_{max} = 673 nm. Methylene Blue: PLE_{max} = 666 nm, PL_{max} = 681 nm.

3.1.2 Preparation of Photolipid Membranes

Small unilamellar vesicles. SUV samples were prepared by tip sonication[205] as shown in Figure 3.3. Firstly, lipids and dye-labeled lipids were dissolved in chloroform at a concentration of 6.36 mM and 0.636 mM, respectively. Then 100 uL of the lipids solution or a mixture solution of lipids and dyes (dye concentration of 1 mol %) were added to a 4 mL glass vial. After drying under a stream of air, the formed lipid film was rehydrated by adding 1.5 mL deionized water (Milli-Q, Merck) or phosphate-buffered saline (PBS) solution (1X, Sigma Aldrich). Mild sonication (Elmasonic P, 30 s) was applied to form multilamellar vesicles. Afterwards, the milky lipid solution was tip sonicated (BANDELIN electronic GmbH & Co.KG, amplitude 30 %, with tip MS 73) on ice twice for 30 s, until the solution was clear. Finally, the solution was centrifuged (mini Spin, Eppendorf AG) for 10 min at 8000 rpm. The supernatant containing SUVs was collected and stored at 4 °C for further use.

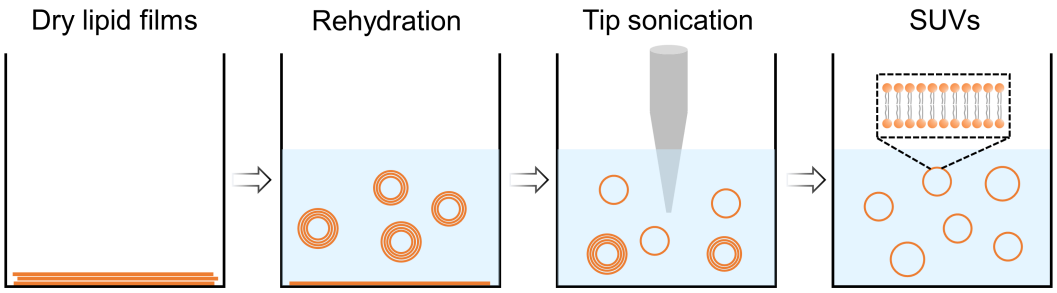

Figure 3.3: Preparation of SUVs by tip sonication. Dry lipid films on the glass surface were rehydrated to a milky solution by mild sonication. Then strong tip sonication induces the multilamellar vesicles to homogeneous SUVs.

Giant unilamellar vesicles. GUVs were prepared based on electroformation using vesicle prep pro device (Nanion technologies).[206] The electroformation chamber of this device is a sandwich-constructed structure, consisting of two Indium-Tin-Oxide (ITO) glass slides separated by an O-ring, as shown in Figure 3.4. The conductive sides of the two ITO substrates were facing toward each other in the chamber. 20 μL of the lipid sample dissolved in chloroform at a concentration of 10 mM was then spread on the conductive side of the bottom ITO slide. After the chloroform evaporation, a lipid film formed. Next, 250 μL of sucrose solution at a concentration of 300 mM was added to the chamber. By applying an alternating electric field (5 Hz, 3 V) to the ITO substrates and heating the chamber at 37 °C for 120 min, GUVs were formed. GUVs were stored at 4 °C for further use. The GUVs prepared with this protocol are highly concentrated and can be diluted with a 300 mM sucrose solution for experimental use.

Supported lipid bilayers. SLBs are prepared by vesicle fusion on clean glass slides following a previous protocol.[207] Borosilicate microscopy glass slides were used and cleaned by rinsing

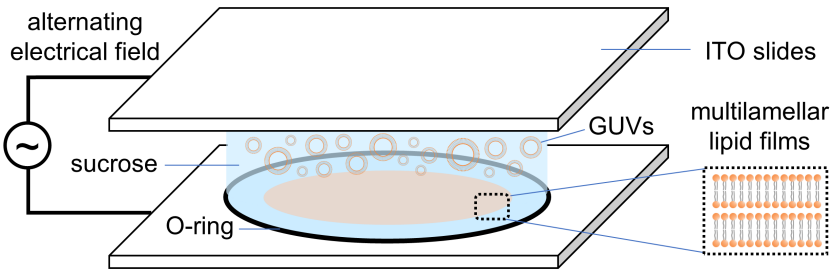

Figure 3.4: Preparation of GUVs by electroformation. The electroformation chamber is constructed by separating two ITO slides by O-ring with the conductive sides facing toward the chamber. Dry lipid films were rehydrated with high-concentration sucrose solution in the chamber. The applied alternating electric field (5 Hz, 3 V) and heating (37 °C) assisted the GUVs forming.

and sonicating the substrates in 50 % ethanol and 50 % deionized water solution twice for 30 min. Then the substrates were treated by air plasma (Harrick Plasma) at a high RF power setting for 1 min. 100 μL of SUV and 100 μL of PBS solutions (1X, Sigma Aldrich) were added on the clean glass substrate. Due to the fusion and rupture of the SUVs, a homogeneous supported bilayer forms within minutes. The remaining SUVs were removed by rinsing with PBS (1X) several times.

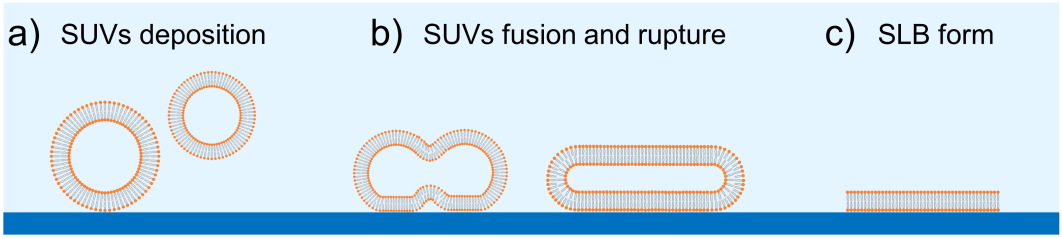

Figure 3.5: Preparation of SLBs by vesicle fusion. Adding SUV and PBS solution on a clean glass substrate results in vesicle fusion and rupture. After several minutes, a SLB is formed.

3.1.3 Characterization of Photolipid Membranes

Fluorescence microscopy. Fluorescence microscopy is a common technique used to image biological samples including cells and synthetic vesicles. In this work, by adding a small percentage of dye-labeled lipids, fluorescence microscopy enables us to image GUVs of photolipids (see Figure 2.5). The diffusivity of supported bilayer membranes was measured with FRAP (see Subsection 2.1.3) using this setup.[208]

Figure 3.6a shows the schematic of the fluorescence microscopy setup. It is a conventional inverted microscope (IX 81, Olympus) equipped with a mercury lamp (100 W, Olympus), filter cubes, and 100X air objective (NA=1.35, UPlanSApo, Olympus). Camera (Canon EOS 550D) and CCD (Andor iXon 897) was used for imaging. Filter cubes used in experiments are listed

in Table 3.1. Furthermore, light-emitting diodes (LEDs) (Prizmatix, UV and blue LEDs at wavelengths of 365 nm and 465 nm) were coupled into the microscope through an optical fiber for the switching of photolipids.

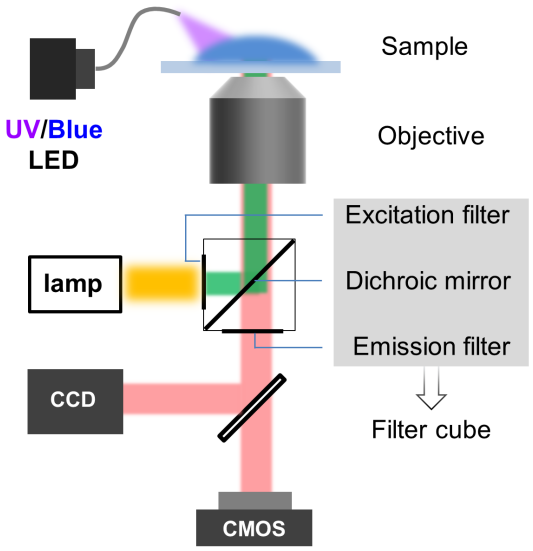

Figure 3.6: Fluorescence microscopy. The white light from the lamp is filtered by an excitation filter so that only the interested fluorophore is excited. The excitation light and emission light are separated by the dichroic mirror. With another emission filter, only the photoluminescence of the sample is detected by the camera.

Table 3.1: Filter cubes

filter cube	excitation filter(nm)	emission filter(nm)
blue	470-490	>520
green	510-550	>590
red	600-645	660-680

UV-vis spectroscopy. The switching of photolipid membranes was characterized by absorbance measurement. A Cary 60 UV-vis spectrophotometer (Agilent Technologies) was employed to obtain the absorption spectra. The schematic of the setup is shown in Figure 3.7a. A monochromator allows for a step-wise scanning of the desired spectral range. The transmitted attenuated signal I_t of SUV samples of photolipid in quartz cuvettes is measured compared to excitation signal I_0. Photostationary states of photolipid samples were controlled by the illuminating the sample with LEDs (Prizmatix, wavelength at 365 nm, 465 nm, 550 nm, 590 nm, 630 nm) from the top.

To measure the switching kinetics of photolipid membranes, time-lapse absorption spectra were recorded in cycle mode with time steps of 15 s upon LED illumination. Figure 3.8a shows the absorption spectra changes every 15 s during *cis*-to-*trans* switching, where the black solid line represents the spectrum of photolipids in dark-adapted state (100 % *trans*).

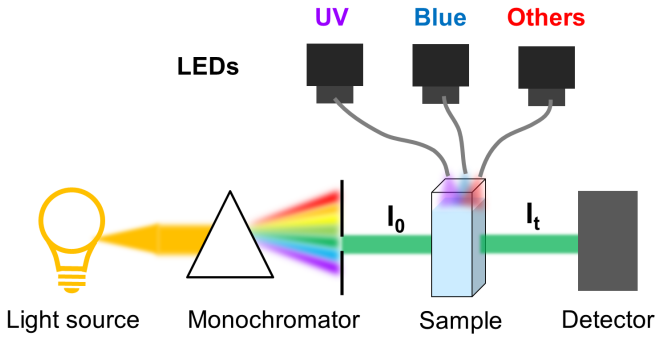

Figure 3.7: UV-vis absorption spectroscopy. The monochromator composed of a prism and a slit enables scanning of spectra range. The transmitted attenuated signal of sample I_t is obtained compared to the excitation signal I_0 by the detector.

The spectra was obtained after the sample was stored in darkness for days. By plotting the time-dependent intensity changes of the absorption at 315 nm, the switching kinetics of photolipid samples can be obtained (Figure 3.8a, figure on the right). Absorption intensity changes were normalized according to[203,209,210]

$$\mathrm{Abs\,(a.u.)} = \frac{A_\infty - A_t}{A_\infty - A_0}, \tag{3.1}$$

where A_0, A_t and A_∞ represents the absorption intensity at 315 nm before switching, at the time t, and at the reached PSS, respectively. Note that $\mathrm{Abs\,(a.u.)}_0 = 1$ and $\mathrm{Abs\,(a.u.)}_\infty = 0$. The normalized absorbance is shown in Figure 3.8b. Since this switching is triggered by direct blue illumination (465 nm), the switching rate k can be calculated by fitting the switching

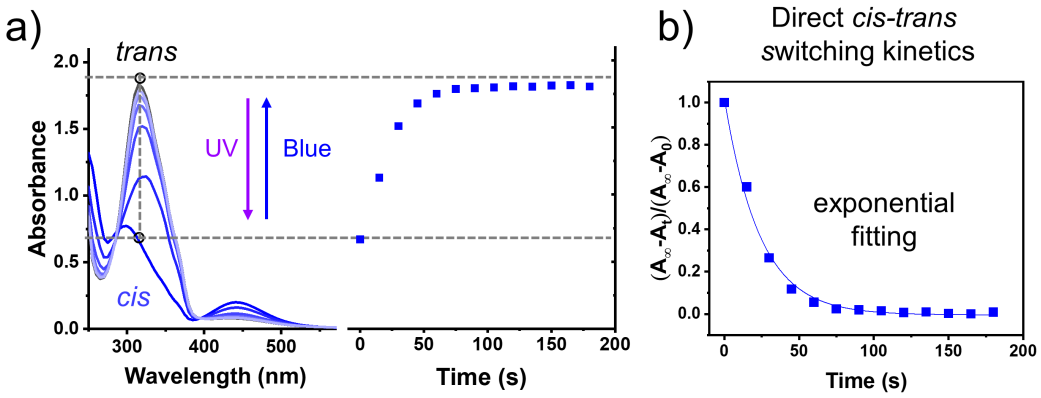

Figure 3.8: Calculating switching rate through time-lapse absorption spectra. (a) (left) Absorption spectra of *azo*-**PC** membrane were recorded every 15 s during *cis*-to-*trans* isomerization until PSS was reached. (right) Absorption intensity changes at 315 nm along time during *cis*-to-*trans* isomerization. **(b)** Normalized absorption intensity changes can be fitted with a mono-exponential function to obtain the switching rate for isomerization by direct UV or blue illumination.

kinetics with a mono-exponential function[209,211]

$$y = A * e^{-kt}. \tag{3.2}$$

Steady-state PL spectroscopy. Steady-state fluorescence of dye-labeled lipids (Figure 3.2) was measured with a spectrometer (Fluorolog-3 FL3-22 spectrofluorometer, Horiba Jobin Yvon GmbH). Photolipids were switched with fiber-coupled LEDs to investigate the effects of the photolipid PSS on the dye fluorescence.

Time-resolved PL spectroscopy. As discussed in Subsection 2.2.1, fluorophores in the excited state relax to the ground state via radiative and non-radiative decay processes. Suppose the excited fluorophores have initial population of N_0, the decays follows[212]

$$\frac{dN(t)}{dt} = (k_r + k_{nr})N(t), \tag{3.3}$$

where $N(t)$ denotes the population of excited fluorophores at time t, k_r and k_{nr} represents the rate constants of the radiative decay and the non-radiative decay, respectively. The lifetime τ is determined by the decay rate by $\tau = (k_r + k_{nr})^{-1}$. Since emission is a spontaneous process, each excited fluorophore has the same probability of emitting a photon during a given time interval. The excited-state population of fluorophores decays exponentially according to

$$N(t) = N_0 \exp(-t/\tau), \tag{3.4}$$

which can be observed in experiments by the exponential decay of fluorescence intensity

$$I(t) = I_0 \exp(-t/\tau). \tag{3.5}$$

This is because the fluorescence intensity $I(t)$ is proportional to the number of excited fluorophores $N(t)$. By measuring the fluorescence intensity decay over time after a short pulse excitation, the fluorescence lifetime can be determined, which is called time-domain lifetime measurement.

The most popular method to do time-domain lifetime measurement is using time-correlated single photon counting (TCSPC).[212] Figure 3.9 depicts the principle of TCSPC. The samples are excited by a laser pulse with a pulse width much smaller than the lifetime τ of the sample. As discussed above, excited-state depopulation is a random event, which means some fluorophores can emit at an earlier time, while other emits at a later time. The detector of TCSPC is set to detect not more than one photon per laser pulse. The time delay between the excitation laser pulse and the first-detected single photon is calculated and stored in the

histogram. By obtaining statistics, histograms are plotted with the time difference as x-axis and photon counts as y-axis. This histogram represents the waveform of PL decay.

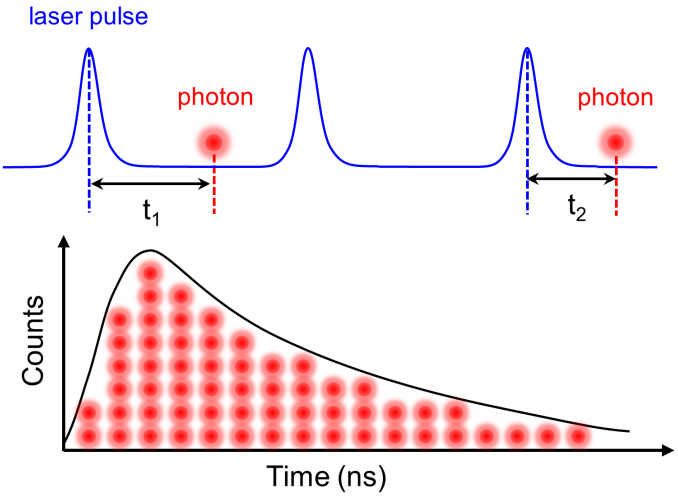

Figure 3.9: Principle of TCSPC. Once the laser pulse hits the sample, many fluorophores are excited so that photons are emitted. Since emission is a random event, fluorophores emit photons at different times. The detector is set to detect only one photon after every pulse excitation. The time delay of the detected photon is recorded versus photon counts in a histogram, which represents the waveform of PL decay.

PL decay measurement could be applied to resolve the multi-deactivation process. For the case of multiple luminescence centers with overlapped absorption and emission spectra where steady-state PL can not differentiate between different processes, the PL decay plays a role by resolving the different decay times by fitting using a multi-exponential function

$$I(t) = A_1 e^{-t/\tau_1} + A_2 e^{-t/\tau_2} + A_3 e^{-t/\tau_3} .... \tag{3.6}$$

PL lifetime measurement can also be used to study the interaction between a donor and an acceptor molecule. Aspects including the percentage of donor quenched by acceptor and different energy transfer mechanisms involved can be distinguished.

In this work, the fluorophore lifetime was measured via a home-built TCSPC setup.[213] A pulsed white light laser (SuperK EXTREME EXR-20, NKT Photonics, 0.12-78 MHz repetition rate with 30-90 ps pulse length) coupled with an extend UV unit (SuperK EXTEND-UV, NKT Photonics) or a modulator (SuperK SELECT, NKT Photonics) was used as the excitation beam which enables selected wavelength from 330 nm to 1100 nm. The laser beam was directed and focused on the sample via a dichroic mirror and an objective. The PL decay was obtained using a TCSPC unit (Timeharp 260p, Pico Quant).

3.2 Characterization and Simulation of AuNRs

3.2.1 AuNRs Dropcasting and Ligand Removal

During the synthesis of gold nanoparticles in solution, stabilizing agents (or capping agents) are added to control the size and morphology of the particles, prevent aggregation, and maintain stability.[214] The most common stabilizers are cetyltrimethylammonium bromide (CTAB) and citrate.[215] In this work, both CTAB-capped and citrate-capped AuNRs (Nanopartz Inc., Part # A12-40-650, OD=1) have been used (Figure 3.10).

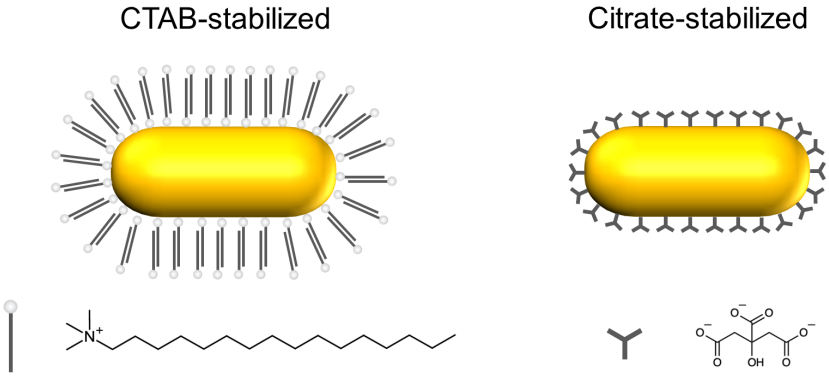

Figure 3.10: AuNRs stabilized with different ligands. CTAB molecule forms a positively charged bilayer on the surface of the AuNRs. Citrate is negatively charged.

In order to perform experiments on single AuNRs, the easiest way to prepare samples is by dispersing and dropcasting AuNRs on a glass substrate. Glass slides of fused silica have a negatively-charged surface due to the dissociation of silanol groups.[216] As shown in Figure 3.10, the CTAB layer is positively charged while the citrate is negatively charged. The CTAB-capped particles can be dropcasted onto the glass substrates and are adsorbed due to electrostatic interaction while citrate-capped AuNRs are repelled by the surface charge. However, citrate-capped AuNRs can be printed by a laser onto the substrates if the optical force overcomes electrostatic repulsion (Subsection 2.3.3). Figure 3.11 shows the dark-field image of dropcasted and optically printed AuNRs.

To dropcast CTAB-stabilized AuNRs onto the substrate, the glass slides were cleaned prior to use by rinsing and sonicating with 50 % ethanol and 50 % deionized (DI) water (Milli Q) twice for 30 min. First, the gold nanorod solution was sonicated for 30 s to avoid aggregation. Then 5 μL of gold nanorod solution and 100 μL of DI water were added to the clean glass substrate. After around 5 min waiting to allow the AuNRs to adsorb onto the substrate, the remaining AuNRs were removed by rinsing with DI water several times.

It was reported that the thickness is approximately 3.6 nm for the CTAB bilayer[217] and

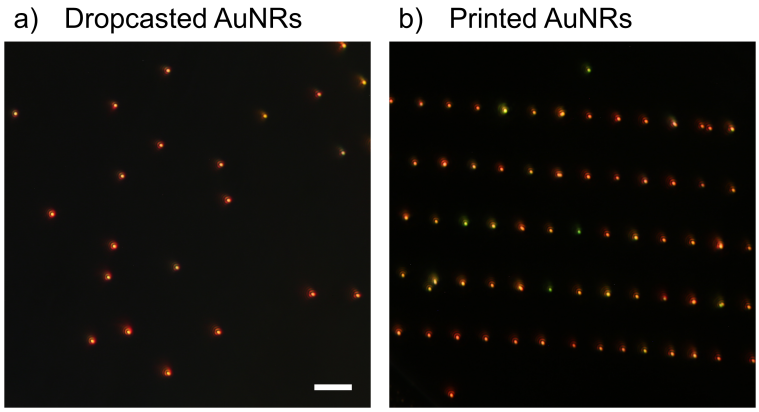

Figure 3.11: Dark-field image of dropcasted and printed AuNRs. AuNRs (length 80 nm, width 40 nm) are coated by **(a)** CTAB and **(b)** citrate layer. Scale bar: 10 μm.

between 0.38 nm and 0.7 nm for the citrate shell.[218] The presence of a capping agent especially the thicker CTAB bilayer will lower the sensitivity of AuNRs for plasmonic sensing or SERS due to the increased distance between AuNRs and analytes (see Equation 2.48 in Subsection 2.3.2 and Equation 2.57 in Subsection 2.4.1). It can be necessary to remove the CTAB coating for a higher sensitivity. Literature shows that appropriate plasma treatment of gold nanoparticles can effectively remove the CTAB.[219] Martinsson et al.[143] measured the thickness reduction of an adsorbed CTAB layer on a planar gold substrate after oxygen plasma treatment using atomic force microscopy (AFM). They found a thickness reduction of 3.6 nm after 60 s plasma cleaning indicating a complete CTAB removal. Alba et al. proved the effectiveness of CTAB removal by plasma treatment with SERS.[220] In this thesis, the dropcasted AuNRs on the substrate were plasma cleaned for 75 s with air plasma to remove the CTAB coating (Harrick, high power setting).

3.2.2 Dark-field Scattering and Raman Spectroscopy

Both single-particle scattering spectroscopy and SERS were performed with a dark field microscope (DFM). Dark field microscopy is an imaging technique that only allows the scattered light from the sample to be collected while blocking the directly transmitted light. DFM is ideal for imaging strong light scatters such as noble metal nanoparticles since it provides a dark background. As shown in Figure 3.12a, DFM was realized by using a dark field condenser (DFC). White light from a halogen lamp (100 W, Zeiss) past the DFC (Zeiss 445323, 1.2-1.4, oil immersion) and became a hollow light cone. The scattered light of single AuNRs was then collected with a water objective (100X, NA=1, Zeiss). Dark-field images were acquired with a digital camera (Canon EOS 6D). Under a dark field microscope, single AuNRs (40 nm $\times$ 80 nm) were identifiable as bright spots in a dark background (Figure 3.12b, scale bar 10 μm).

The dark-field setup was also equipped with a spectrometer and a charge-coupled diode (CCD)

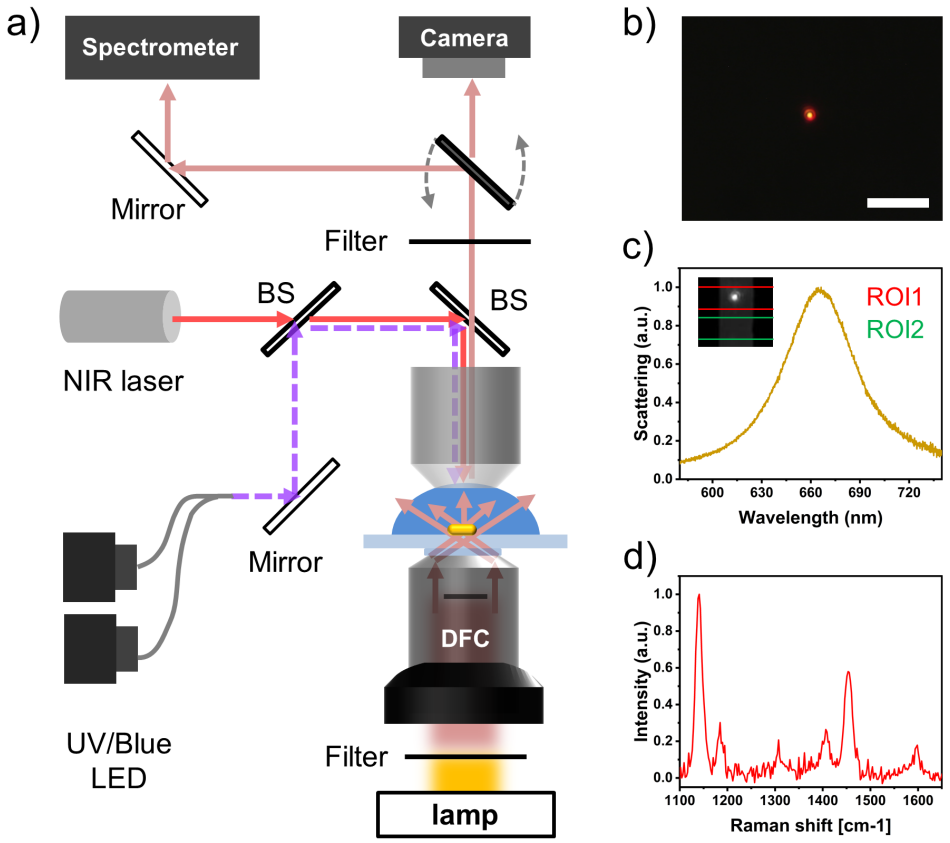

Figure 3.12: Microscope setup for dark field imaging, scattering spectroscopy, optical printing and SERS measurements. **(a)** Schema of the setup. The dark-field condenser blocks the directly transmitted light from the lamp so that only the scattered light of measured nanoparticles can pass through the objective to the camera and spectrometer, allowing the acquisition of **(b)** dark field image and **(c)** scattering spectra of AuNPs. The coupling of a NIR laser enables optical printing of AuNPs and **(d)** SERS measurement.

camera (Princeton Instruments SpectraPro2500 with a Spec-10:2k CCD), which enables to record scattering spectra of single AuNRs. In the image mode of the spectrometer, two regions of interest (ROI) are selected where scattered light is collected in ROI1 and in ROI2 the background (Figure 3.12c, inset). After switching to spectrum mode, both the spectrum of AuNRs and the background are simultaneously obtained. By subtracting the background, as well as the spectrum from the light source, the scattering spectrum of single nanoparticle is obtained (Figure 3.12c). For plasmonic sensing measurements of *azo*-**PC** membranes on single AuNRs, two LEDs were coupled into the microscope to control photoswitching. In addition, a filter was added to block a wavelength range from the lamp where unwanted photoswitching would occur(details about the measurements will be presented in Chapter 5).

A NIR laser (Novanta Gem 671, solid state, 671 nm, 500 mW) was used for the optical printing and SERS measurements. For SERS measurements, the 671 nm laser was focused with the objective to target the particle to be analyzed. The enhanced Raman scattered light was

acquired by the spectrometer. The back-reflected laser light was blocked using a appropriate filter.

3.2.3 Scanning Electron Microscopy

The gold nanoparticles used in this work had sizes below 100 nm, which is far beyond the resolution of a standard optical microscope. As discussed in Subsection 3.2.2, single AuNPs with the size of 40 nm × 80 nm appear as bright spots in the DFM. However, no details on the particle shape are obtained. SEM can achieve resolution down to 1 nm, and has been used to obtain morphology details of AuNPs.

A schematic of the SEM is depicted in Figure 3.13. Electrons emitted from the field emission gun are accelerated in an electric field and focused by the condenser on the sample surface. Due to electron-sample interactions, both the primary backscattered electrons (elastically scattered) and secondary generated electrons (inelastically scattered) can be detected. By scanning the electron beam across the sample, the surface topography can be imaged. A Gemini Ultra Plus field emission SEM from Zeiss was used in this thesis to collect SEM images. The SEM is equipped with two detectors, an Inlens and a SE2 (Everhart-Thornley) for detecting secondary electrons. The Inlens detector provides the highest spatial resolution while the SE2 is good for topological measurements. For AuNPs deposited on the non-conductive glass substrate, the sample needs to be coated with a 1 nm conductive layer of gold-palladium. This was obtained with a Leica EM SCD005 sputtering coater. A typical SEM image of single AuNRs was also shown in the inset of Figure 3.13.

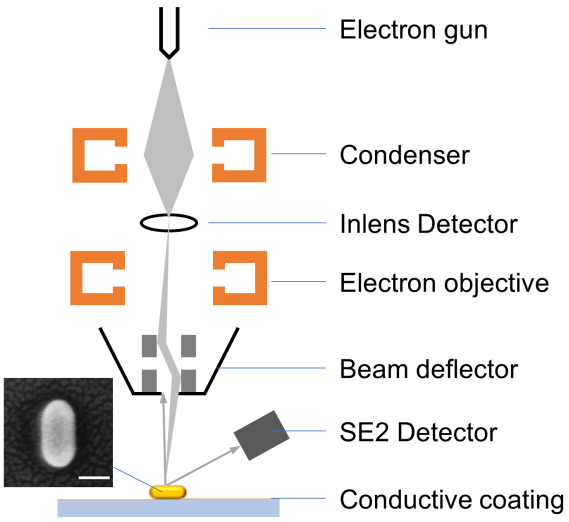

Figure 3.13: Schematic of Scanning electron microscopy. The AuNRs on the glass substrate are coated with a 1 nm conductive layer. Inset: typical SEM image of single AuNRs, scale bar 50 nm.

3.2.4 Finite Difference Time Domain Simulations

Finite difference time domain (FDTD) is a common method to calculate the absorption and scattering spectra as well as the field enhancements of plasmonic nanoparticles, especially for nanoparticles with complex geometries like nanorods.[221] In this thesis, FDTD simulations (Ansys Lumerical) have been used for the verification of the experimental results.

FDTD, proposed by Kane S. Yee in 1966,[222] is a grid-based differential numerical analysis method to solve time-dependent Maxwell's differential equations. The simulation space is divided into a grid of unit cells known as Yee cells, where the electric field cells and magnetic field cells are staggered (Figure 3.14a). When the electric field forms the border of the cube, the magnetic field is perpendicular to the surface of the electric field cell, and vice versa. The calculation of electric and magnetic fields over time is also staggered. Therefore, Maxwell's equations are solved in a discretized way spatially and temporally, determining electric fields $E(r, t)$ and magnetic fields $H(r, t)$.

To perform the FDTD simulation, the first step is to build up the model. For example, Figure 3.14b shows the model of single gold nanorods coated by an adsorbate layer deposited on a glass substrate in a water circumstance. Then, the information about the complex refractive index of materials including water, adsorbate, gold, and glass should be provided according to literature values. The electromagnetic wave source also needs to be defined in the software. Here, a self-subtracting light source cube (total field scattering field) was used. Other parameters like the mesh density should also be defined as needed. Finally, the electromagnetic fields and absorption/scattering spectra can be calculated as an output.

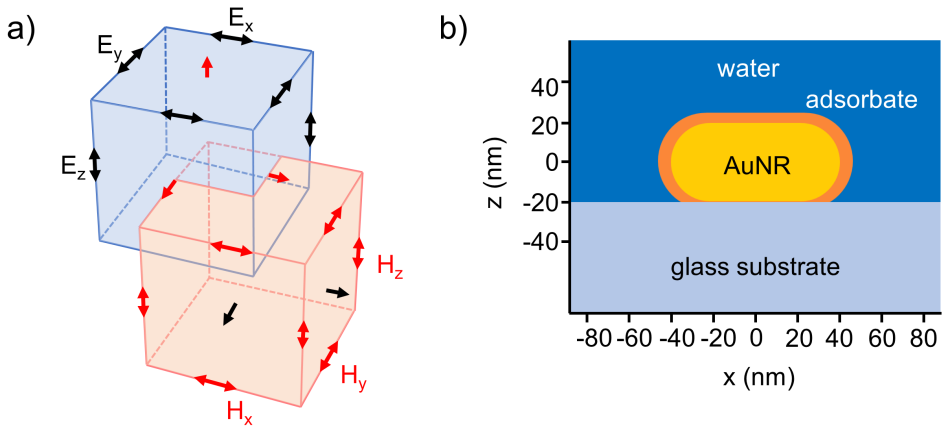

Figure 3.14: Finite-difference time-domain methods. (a) Sketch of the grid for FDTD: staggered electric field and magnetic field. **(b)** Modeling of single gold nanorods in water on a glass substrate for FDTD.

4

Photosensitization and -modulation between Photolipids and Dyes

As introduced in Section 2.1, photoswitchable lipid *azo*-**PC** provides optical means to reversibly control physical properties of synthetic bilayer membranes. It was reported that *azo*-**PC** can achieve light-triggered drug release[9] and manipulate cell membrane fluidity,[3] demonstrating its potential for application in biological or medical systems. However, the wider application of *azo*-**PC** in the biomedical field is restricted by its excitation wavelength. UV and blue light, both have poor penetration depth for biological tissues. Inspired by the interaction between azobenzene molecules and sensitizers, as discussed in Section 2.2, I explore the possibility of sensitized *cis*-to-*trans* isomerization of *azo*-**PC** with different lipid-dyes including Rhodamine (Rho), Texas Red (TR), Nile blue (NB), Methylene blue (MB) and Atto633 using green, orange and red light (Section 4.1). Notably, different from azobenzene and sensitizers in solution, *azo*-**PC** and lipid dyes are assembled together in the membrane, ensuring proximity.

In addition, the impact of *azo*-**PC** on dye fluorescence is explored. On one hand, in Section 4.2, I will present how *azo*-**PC** protects triplet sensitizers like MB from photobleaching by oxygen. On the other hand, the modulation of lipid-dyes' fluorescence by *azo*-**PC** isomerization will be discussed in Section 4.3. Finally, the possible mechanism involved in the process will be discussed in Section 4.4 and an outlook will be given by showing the results between lipid dyes and other azobenzene-containing lipids in Section 4.5.

The results presented in this chapter are currently being prepared for publication as *"Photosensitization and Photomodulation between Azobenzene Photolipids and Dyes in Bilayer Membranes"* by J. Zhang, B. Baumgartner, T. Kehler, S.D. Pritzl, D. Trauner, O.T. Seshold and T. Lohmüller.

4.1 Sensitized *Cis*-to-*trans* Isomerization of *Azo*-PC

4.1.1 Direct *Cis*-to-*trans* Isomerization of *Azo*-PC

First, the *cis*-to-*trans* switching rates of the *azo*-**PC** membrane by direct visible light illumination were measured. SUV solutions of pure *azo*-**PC** lipids was prepared following the protocol described in Subsection 3.1.2. SUV samples were switched to *cis* state with 365 nm LED. Then samples in the *cis* state were exposed under illumination of different wavelengths including blue light at 465 nm, green light at 550 nm, orange light at 590 nm and red light at 630 nm. The spectra of corresponding LEDs are plotted in Figure 4.1. Since illumination intensity can strongly affect the switching rate, the output power of all LEDs was set to 20 mW. By performing time-lapse absorption measurements, absorption intensity changes over time were obtained for all illumination wavelengths (see Figure 3.8). *Cis*-to-*trans* switching rates was calculated by fitting the normalized absorbance with an exponential function.

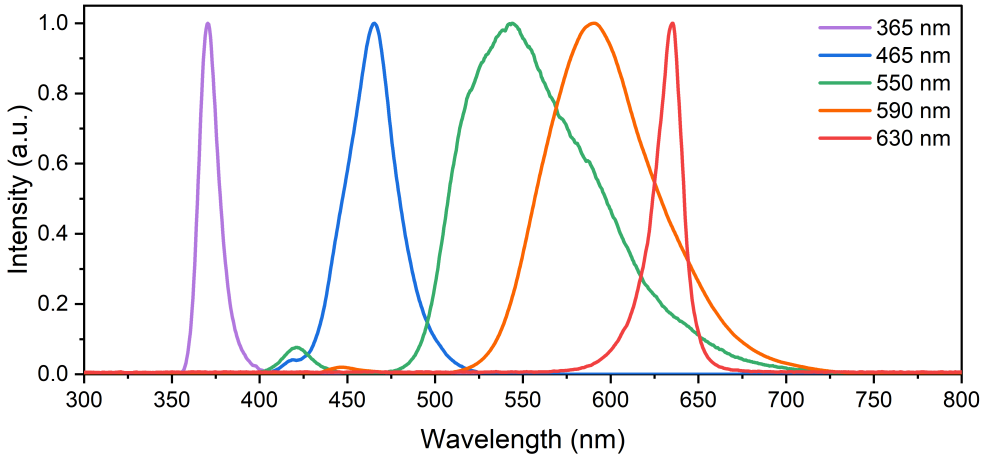

Figure 4.1: Emission specification of used LEDs. 5 different LEDs have been applied including UV LED at 365 nm, blue LED at 465 nm, green LED at 550 nm, orange LED at 590 nm and red LED at 630 nm. Among these, 550 nm and 590 nm LEDs have a relatively broad emission. Data are taken from https://www.prizmatix.com/MicLED/Mic-LEDs.aspx?NETID=68.

As shown in Figure 4.2, the *cis*-to-*trans* switching rate for 465 nm illumination was calculated to be $k_{465nm} = 2.52\ min^{-1}$. With 550 nm illumination, the switching rate decreased to $k_{550nm} = 0.36\ min^{-1}$, which is still effective. This is because the green LED has a broad emission up to the blue range (green line in Figure 4.1). The switching rate for the 590 nm LED of $k_{590nm} = 4.76 \times 10^{-2} min^{-1}$ was very small in comparison. Almost no *cis*-to-*trans*

switching was observed for 630 nm illumination, with an extremely low switching rate of $k_{630nm} = 3.30 \times 10^{-3} min^{-1}$, which shows that red light can not switch photolipids.

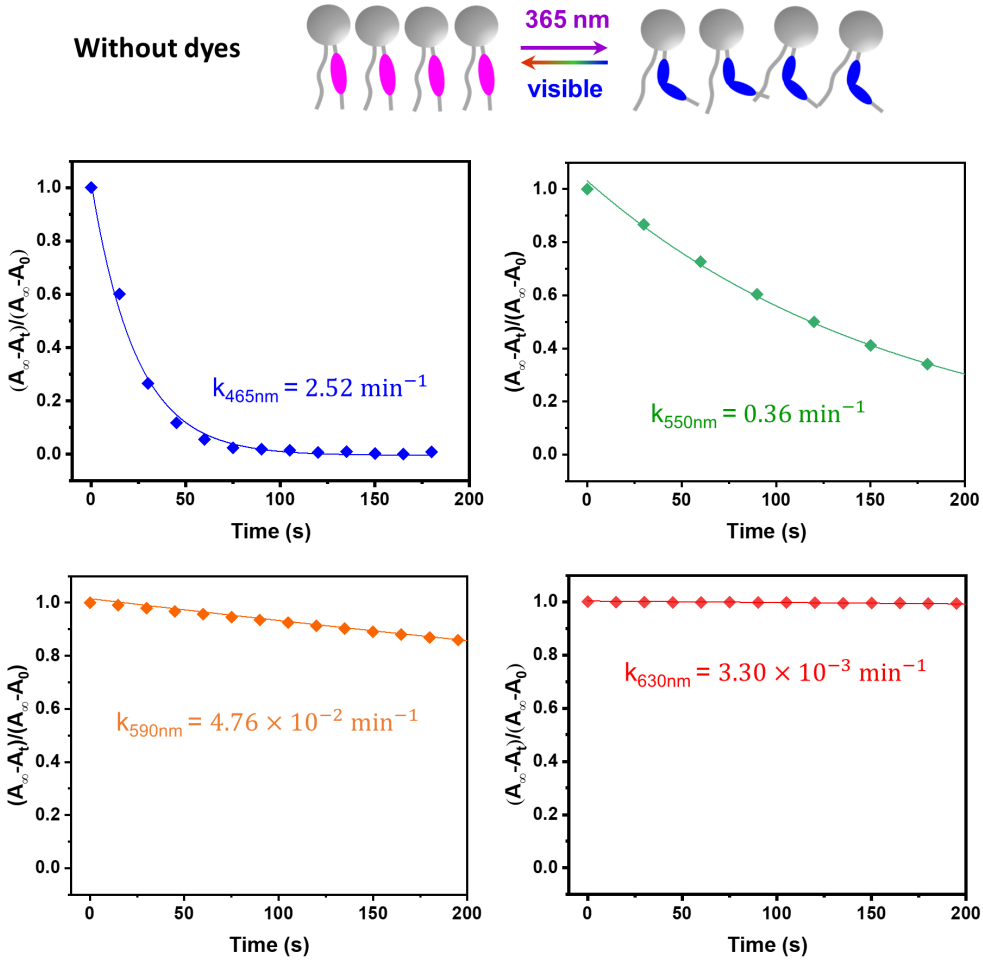

Figure 4.2: *Cis*-to-*trans* isomerization of *azo*-PC by direct illumination. Pure *azo*-**PC** membrane in the *cis* state was switched back with different wavelengths including 465 nm, 550 nm, 590 nm and 630 nm. Square dots in each plot represent normalized absorbance change over time. Solid lines are exponential fittings. Calculated *cis*-to-*trans* switching rates for different visible wavelengths are $k_{465nm} = 2.52\ min^{-1}$, $k_{550nm} = 0.36\ min^{-1}$, $k_{590nm} = 4.76 \times 10^{-2} min^{-1}$ and $k_{630nm} = 3.30 \times 10^{-3} min^{-1}$.

4.1.2 Sensitized *Cis*-to-*trans* Isomerization of *Azo*-PC

Next, five different SUV samples were prepared by doping with 1 % Rho, TR, NB, MB and Atto633 labeled lipids, respectively (Figure 4.3a). In the presence of the five different dyes, the switching rate for 465 nm illumination remains the same (Figure 4.3b). This is because 465 nm light does not excite dyes efficiently but controls *azo*-**PC** isomerization. With 550 nm excitation, the *cis*-to-*trans* switching rate of 1% Rho-doped membrane is 5.31 min^{-1}, which is more than 10 times faster than pure *azo*-**PC** membranes (Figure 4.3c). While the switching of pure *azo*-**PC** was inefficient with 590 nm illumination,

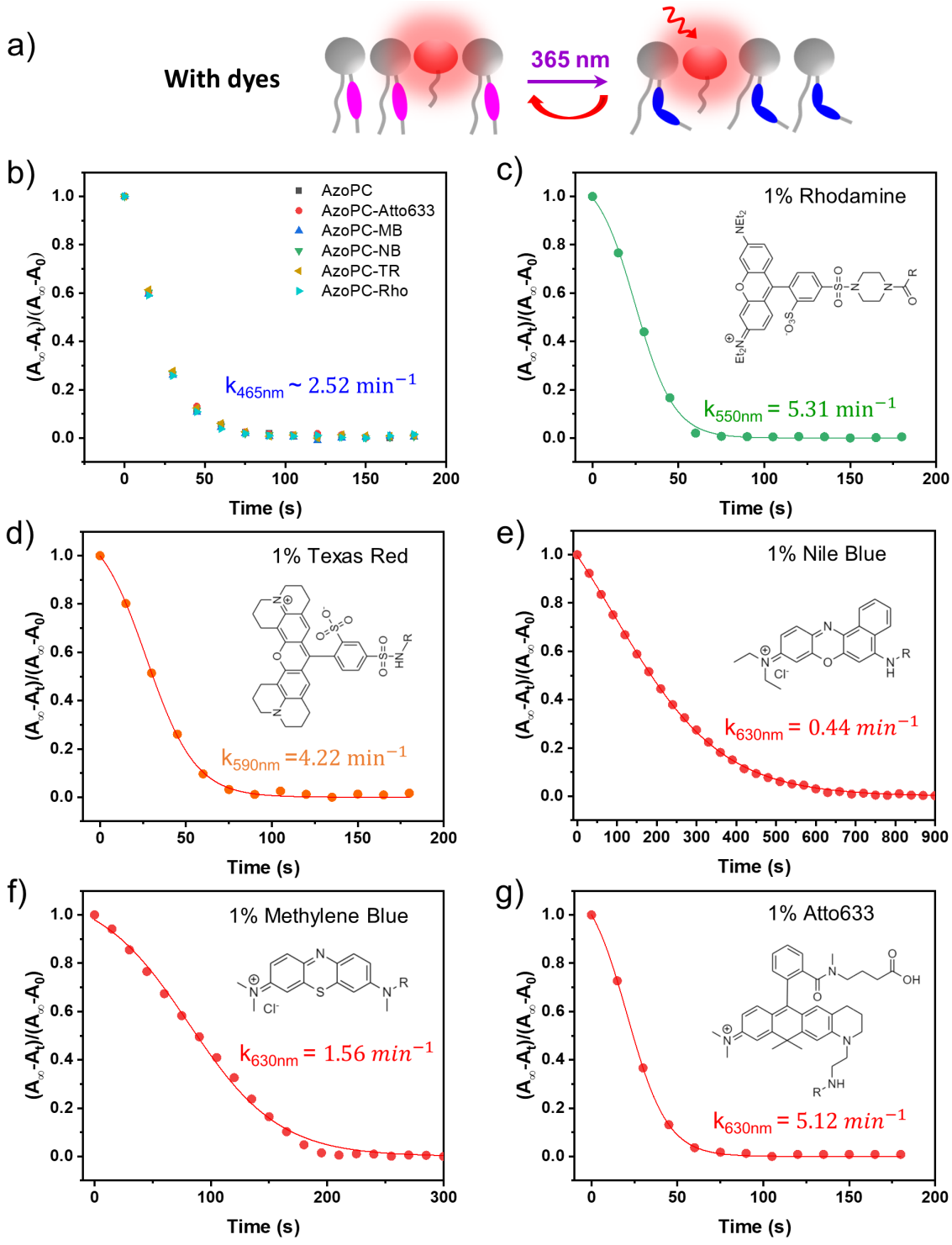

Figure 4.3: Sensitized *cis*-to-*trans* Isomerization of *azo*-PC. (a) Schematic depiction of dye-doped *azo*-**PC** membranes. **(b)** Switching kinetics of pure *azo*-**PC** membranes and dye-doped membranes (doping concentration 1 mol %) by illumination of 465 nm light. the calculated switching rates are all the same, 2.52 min^{-1}. Switching kinetics of **(c)** 1 mol % Rho-doped, **(d)** 1 mol % TR-doped, **(e)** 1 mol % NB-doped, **(f)** 1 mol % MB-doped and **(g)** 1 mol % Atto633-doped *azo*-**PC** membranes under illumination of dye excitation wavelength (550 nm for Rho, 590 nm for TR and 630 nm for MB, NB and Atto633). The normalized absorbance data (dots) were fitted by logistic function (solid curve). Calculated switching rates are 5.31 min^{-1}, 4.22 min^{-1}, 0.44 min^{-1}, 1.56 min^{-1} and 5.12 min^{-1}, respectively.

A 100-fold increase was observed by 1 % of TR doping ($k_{590\text{nm-TR}} = 4.22$ min^{-1}, Figure 4.3d). Only red light can hardly isomerize pure *azo*-**PC** membranes, but with 1 % NB, MB or Atto633, *cis*-to-*trans* switching occurs fast. The calculated switching rates under 630 nm illumination for 1 mol % of MB, NB and Atto633 doped *azo*-**PC** membranes are 0.44 min^{-1}, 1.56 min^{-1} and 5.12 min^{-1} (Figure 4.3e, f, g), which are two to three orders of magnitude faster than that of pure *azo*-**PC** membranes ($k = 3.30 \times 10^{-3}$min^{-1}).

Notably, the switching rate of 1 mol % of Atto633 doped *azo*-**PC** membranes excited by red light ($k = 5.12$ min^{-1}) is even outcompeting compared to pure *azo*-**PC** membranes under blue light illumination ($k = 2.52$ min^{-1}). One possible explanation is that the molar extinction coefficient of Atto633 at 630 nm (130000 M^{-1}cm^{-1}) is approximately a hundred times higher than that of *cis azo*-**PC** at 465 nm (1400 M^{-1}cm^{-1}).[223] That means the absorbance of 1 mol % of Atto633 dye at 630 nm is comparable of 100 mol % of cis *azo*-**PC** at 465 nm.

Table 4.1 shows the comparison of *cis*-to-*trans* switching rates between pure *azo*-**PC** membranes and 1 mol % of dyes doped *azo*-**PC** membranes. It demonstrates that efficient *cis*-to-*trans* switching of *azo*-**PC** membranes excited by different wavelengths from green to red range can be achieved by doping the photolipid membrane with a small amount of dyes.

Table 4.1: *Cis*-to-*trans* switching rate

samples	465 nm(min^{-1})	550 nm(min^{-1})	590 nm(min^{-1})	630 nm(min^{-1})
100 % *azo*-**PC**	2.52	0.36	4.76×10^{-2}	3.30×10^{-3}
1 % Rho	2.52	5.31	/	/
1 % TR	2.52	/	4.22	/
1 % NB	2.52	/	/	0.44
1 % MB	2.52	/	/	1.56
1 % Atto633	2.52	/	/	5.12

For pure *cis azo*-**PC** membranes, lipids are directly excited by 465 nm light and switched. The normalized absorbance change over time can be fitted with a mono-exponential function because the switching rate is only dependent on the concentration change of *cis azo*-**PC** over time. In the presence of the dye molecules, the absorbance curve can not be fitted with the exponential anymore, indicating a different mechanism that triggers the switching process. As shown in Figure 4.3c-g, the data present a sigmoidal characteristic along time, suggesting a fitting by a logistic function. During the isomerization process, the concentration of dyes stays constant. Dyes are excited by illumination, and their energy is then transferred to *cis azo*-**PC**, initiating *cis*-to-*trans* switching. *Cis azo*-**PC** lipids compete with each other to get energy from dyes although the amount of *cis* isomers is reduced over the course of the reaction, which fits the concept of a logistic curve.

4.1.3 Effects of Dye Concentration

Concentration-dependent measurements for Atto633 doped *azo*-**PC** membranes were conducted to get a better understanding on how the dye concentration affects switching rates. *Azo*-**PC** membranes doped with Atto633 of different concentrations from 0.2 to 1.8 mol % were prepared. These dye concentration were chosen since 0.2 and 2 mol % of dye doping in a lipid bilayer does not influence membrane properties significantly according to previous reports.[224,225,226] Figure 4.4 shows the absorption spectrum of *azo*-**PC** SUVs with different doping concentrations of Atto633. Different *cis* PSSs (blue lines) were observed to vary depending on Atto633 concentration. The data indicates that with an increasing amount of Atto633 molecules, photolipid membranes could be less efficiently switched to the *cis* state.

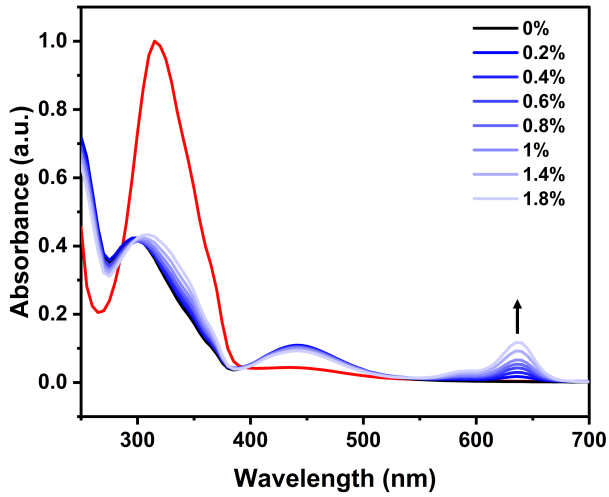

Figure 4.4: The absorption spectrum of *azo*-PC SUVs doped with Atto633 of different concentrations. Red line: samples in dark-adapted state. Black and blue lines: samples in *cis* state. The higher the Atto633 concentration, the less the cis PSS. The arrow indicates increased atto633 absorption.

After analyzing the switching kinetics (Figure 4.5a), a linear relationship was observed between switching rates and dye concentration (Figure 4.5b). Even when the Atto633 concentration is as low as 0.2 mol %, *cis azo*-**PC** membranes could be switched with a high rate ($k = 1.19$ min^{-1}). That means one Atto633 molecule sensitized 499 *cis azo*-**PC** molecules on average, indicating that lipids diffusion plays a role in Atto633-assistant *azo*-**PC** isomerization. Once one Atto633 molecule gets excited, it transfers energy to a nearby *cis azo*-**PC** so that *azo*-**PC** is switched to *trans* state while Atto633 returns to the ground state. Due to membrane diffusion, this Atto633 molecule then moves next to another *cis azo*-**PC**. Next time when the dye is excited, a new *cis azo*-**PC** gets isomerized by it. This process repeats until the *trans*-adapted PSS of the membrane is reached.

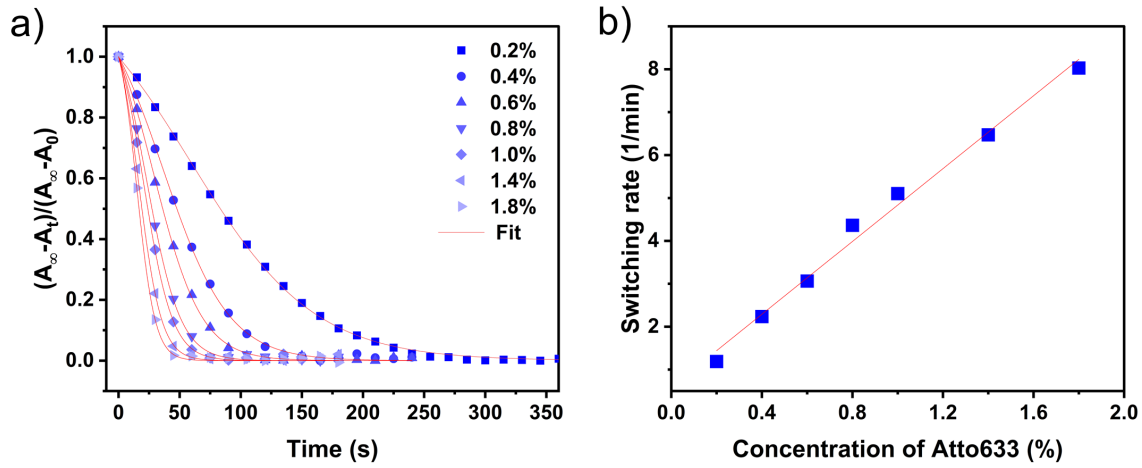

Figure 4.5: Dependence of switching rates on dye concentration. Samples with different doping concentrations of Atto633 (0.2 to 1.8 mol %) were switched by 630 nm and **(a)** switching kinetics were obtained. By fitting with a logistic function, switching rates were calculated. Switching rates are linearly dependent on Atto633 concentration.

4.1.4 Reversibility

One of the most important characteristics of *azo*-**PC** is its reversible switching by direct illumination of UV and blue light. Here the reversibility of sensitized photoisomerization was studied. Three *azo*-**PC** SUV samples doped by 1 mol % Atto633, MB or NB were measured. Samples were exposed to alternating illumination of 365 nm and 630 nm light while their time-resolved absorption spectra were recorded.

By analyzing the intensity of the absorption peak at 315 nm for both *trans* and *cis* PSS, I showed sensitized photoswitching can be repeated for many cycles for all these three samples (left images in Figure 4.6a-c). Even after 8 cycles, the same *trans* PSS as the first cycle was obtained with 630 nm illumination, demonstrating good reversibility.

Absorbance changes over time were further investigated during switching (right images in Figure 4.6a-c). During the first 200 s, 365 nm light was switched on, and the absorption intensity at the 315 nm peak dropped gradually due to *trans*-to-*cis* switching. Then 630 nm light was turned on, initiating *cis*-to-*trans* back isomerization. For Atto633 and NB doped samples, *cis*-to-*trans* switching kinetics of all 8 cycles perfectly coincided. But for the MB-doped sample, a slower *cis*-to-*trans* switching was always observed for later cycles compared to previous cycles. All the measurements were conducted in water under ambient condition. MB is an efficient triplet sensitizer, presenting a high yield of intersystem crossing ($\Phi_{ISC} > 0.50$).[227] The decrease in switching rate along illumination time could therefore be an indication for the degradation of MB by oxygen. This was investigated in more detail in the following section.

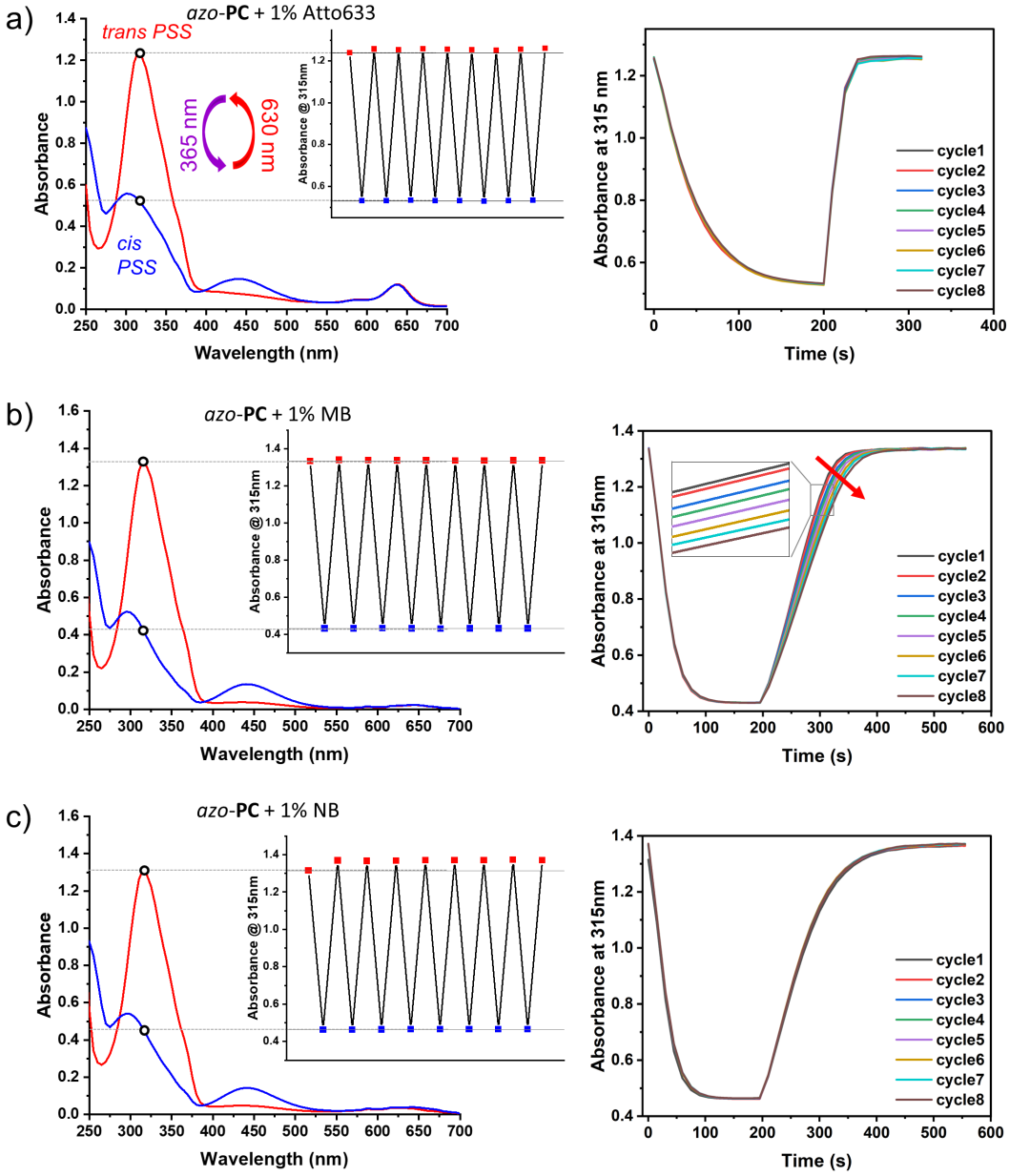

Figure 4.6: Reversibility of sensitized *azo*-PC isomerization. *Azo*-**PC** SUVs doped by **(a)** 1 mol % Atto633, **(b)** 1 mol % MB and **(c)** 1 mol % NB were switched by 365 nm and 630 nm for over 8 cycles. On the left, absorption spectra and 315 nm peak intensity changes over 8 cycles are plotted. On the right, switching kinetics over 8 cycles are plotted (365 nm light on from 0 s to 200 s, 630 nm light on from 200 s to end). The arrow in **(b)** indicates the decreased switching rate.

4.2 *Azo*-PC Protects Methylene Blue from Photobleaching

To gain a better understanding of the effects of oxygen on dyes embedded in *azo*-**PC** membranes, the PL of all dyes upon illumination was measured. Control measurements were performed by assembling dyes in non-switchable DOPC membranes at a concentration of 1 mol %. These dye-doped DOPC samples were illuminated first by 365 nm light for 5-6 min and then at their excitation wavelength (550 nm for Rho, 590 nm for TR, 630 nm for NB, MB and Atto633). The power of all LEDs was fixed at 15 mW to obtain identical illumination conditions. As shown in Figure 4.7, Rho, TR, NB and Atto633 exhibit good photostability. No decrease in their PL emission intensity was observed when irradiating samples with UV light or at their excitation wavelength, meaning that no considerable photobleaching occurred.

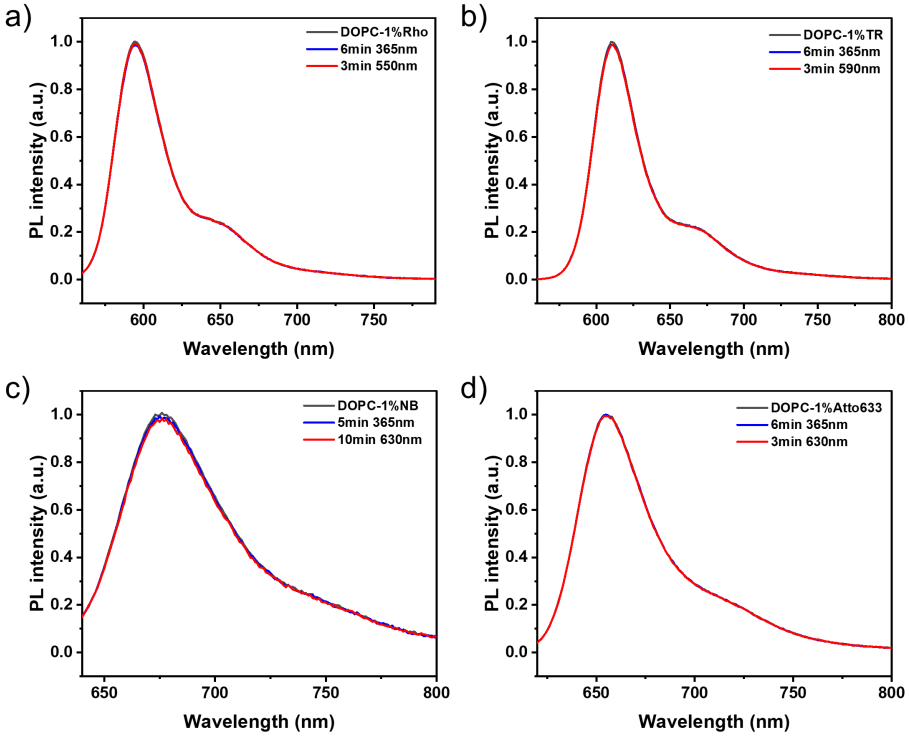

Figure 4.7: Photostability of Rho, TR, NB and Atto633. PL emission of DOPC membranes doped by 1 mol % of **(a)** Rho, **(b)** TR, **(c)** NB and **(d)** Atto633 before any illumination (black line), after UV illumination ((blue line)) and after illumination by their excitation wavelength (red line, 550 nm for Rho, 590 nm for TR, 630 nm for NB and Atto633). Their PL emission intensity did not change, indicating they did not undergo photobleaching.

For MB-doped DOPC membranes, the illumination with 365 nm light for 5 min showed a minimal effect on the MB emission. However, after irradiation of 630 nm light for 10 min, the PL intensity dropped by 50 % (Figure 4.8a). I also measured the time-resolved PL intensity change of MB upon 365 nm and 630 nm illuminations, as shown in Figure 4.8b. The PL intensity dropped linearly during 630 nm illumination since the excited MB got photobleached by oxygen.

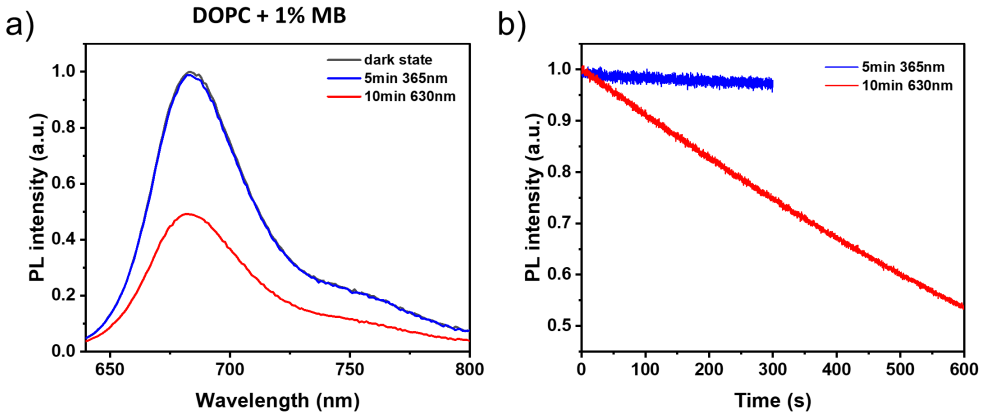

Figure 4.8: Photobleaching of MB doped in DOPC membranes. (a) PL emission of 1 mol % MB doped DOPC membranes before any excitation (black line), after 5 min UV illumination (blue line), and after 10 min 630 nm illumination (red line). PL intensity decreases by 50 % after 10 min 630 nm illumination. **(b)** Real-time PL peak intensity changes upon 365 nm (blue line) and 630 nm illumination (red line).

The same measurements were then conducted on 1 mol % of MB-doped *azo*-**PC** membranes. The PL peak intensity of this sample at the dark-adapted state was normalized to 1 (black line, Figure 4.9a). After 5 min UV light illumination, the PL intensity decreased to 0.72 (solid blue line, Figure 4.9a). As discussed above, 5 min UV illumination does not lead to significant MB bleaching. Therefore, this PL emission decrease may not be attributed to photobleaching. Afterward, the sample was illuminated by 630 nm light for 10 min. The PL recovered to its original intensity (solid red line, Figure 4.9a), instead of decreasing as for DOPC membranes, confirming that MB is not photobleached in this case. The explanation is that UV illumination switched *azo*-**PC** membranes to *cis* state, and MB fluorescence was quenched by *cis azo*-**PC** due to energy transfer. The decrease and increase of MB PL intensity are modulated by *azo*-**PC** states and can be repeated for many cycles (dashed lines and inset, Figure 4.9a). Real-time PL peak intensity changes of MB-doped *azo*-**PC** membranes during *trans*-to-*cis* and *cis*-to-*trans* switching are plotted in Figure 4.9c and Figure 4.9d.

The results demonstrate that in a DOPC membrane, excited MB interacts with triplet oxygen and gets bleached.[228,229] But in an *azo*-**PC** membrane, MB interacts with *cis azo*-**PC** instead of oxygen. *Cis azo*-**PC** efficiently protects MB from photobleaching. This also indicates the interaction between MB and *cis azo*-**PC** is triplet energy transfer. Literature[105,230] show triplet-state energy of MB (32 kcal mol^{-1}) is higher than the triplet-state energy of *cis* azobenzene (30 kcal mol^{-1}), but lower than that of *trans* azobenzene (35.4 kcal mol^{-1}), as shown in Figure 4.9b. Excited MB relaxes to triplet state via ISC and then interacts with *cis azo*-**PC** so that MB goes to ground state and *cis azo*-**PC** is switched to *trans* state. That also means, only *cis azo*-**PC** can protect excited MB from bleaching. This is shown in Figure 4.9d. After 400 s illumination with 630 nm light, the *trans* PSS was already reached. The membrane

was depleted from *cis* lipids and the MB PL emission reached a plateau. A slight intensity decrease was then observed after continuing illumination, indicative of photobleaching. This also explains why the rate decreases after several switching cycles with MB doped samples as shown in Figure 4.6b.

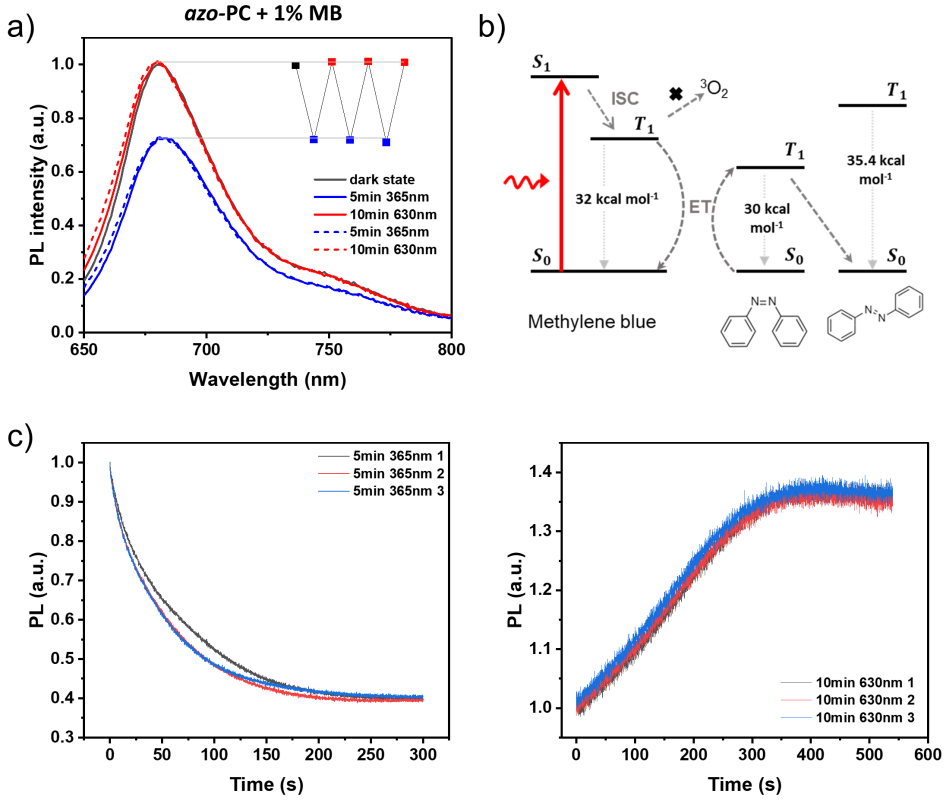

Figure 4.9: Protection of MB from photobleaching in *azo*-PC membranes. (a) PL emission of 1 mol % of MB doped *azo*-**PC** sample at dark-adapted state (black line), after 5 min 365 nm light illumination (blue lines) and after 10 min 630 nm light illumination (red lines). MB PL intensity is photomodulated by *azo*-**PC** states. **(b)** Triplet energy transfer between MB and *cis azo*-**PC** protects MB from Pphotobleaching by oxygen. **(c),(d)** Real-time PL peak intensity changes of MB during illumination by UV light and red light.

4.3 Fluorescence Modulation of Dyes by *Azo*-PC Photoisomerization

It was showed that the fluorescence intensity of MB was quenched by *cis azo*-**PC** compared to *trans azo*-**PC**. That means the fluorescence of MB can be modulated by *azo*-**PC** photoisomerization, which is called photomodulation (PM). The extent of fluorescence modulation can be quantified by PM efficiency E_{PM}.[93]

$$E_{PM} = 1 - \frac{I_{cis}}{I_{trans}}, \tag{4.1}$$

with I_{trans} being the fluorescence intensity of dyes obtained when the *azo*-**PC** membrane is in *trans* state, and I_{cis} being the fluorescence intensity at *cis* state. According to this formula, the PM efficiency of *azo*-**PC** to MB was calculated to be 28 %. The photomodulation of *azo*-**PC** for other dyes (Figure 4.10) was also measured. The fluorescence intensity for all these dyes could be modulated by *azo*-**PC** isomerization. The calculated PM efficiency is 57 % for Rho, 51 % for Atto633, and even 85 % for TR (dye concentration 1 %, Table 4.2).

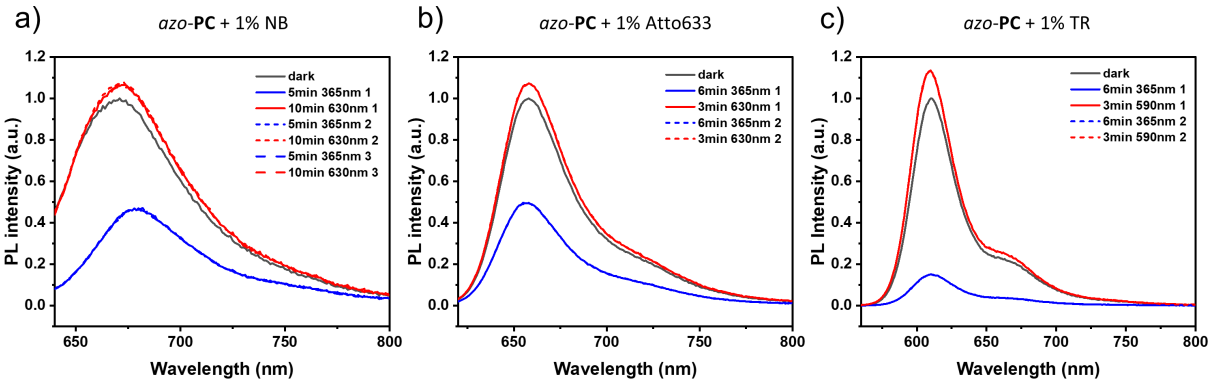

Figure 4.10: Fluorescence modulation of different dyes by *azo*-PC isomerization. PL intensity was measured for **(a)** 1 mol % of NB doped *azo*-**PC** membranes, **(b)** 1 mol % of Atto633 doped *azo*-**PC** membranes and **(c)** 1 mol % of TR doped *azo*-**PC** membranes at dark-adapted state (black lines), *cis* state (blue lines) and *trans* state (red lines). The PL intensity at the *trans* state is higher than that at dark state due to a higher *trans* PSS.

Table 4.2: PM efficiency of *azo*-**PC** to different dyes

dyes	1 % Rho	1 % TR	1 % NB	1 % MB	1 % Atto633
PM efficiency	91 %	85 %	57 %	28 %	51 %

The highest PM efficiency was observed for 1 mol % of Rho-doped *azo*-**PC** membranes, which is up to 91 % (Figure 4.11a). In the *cis* state, fluorescence of Rho is almost turned off. This fluorescence modulation of dyes was reversible over many cycles, which is essential for further applications.

Fluorescence on/off switching has been used for bioimaging, especially super-resolution imaging. For example, in Photoactivated localization microscopy (PALM)[231] and stochastic optical reconstruction microscopy (STORM),[232] photoswitchable fluorophores and fluorescent pairs have been used so that fluorophores display dark and on states. By collecting image sequences each contains isolated fluorophores in on state, image resolution can be improved. I imaged the fluorescence on and off for vesicle sample. Since Rho present highest PM efficiency, and it does not bleach, GUV samples were prepared by doping 1 % Rho into *azo*-**PC** membranes. In the *cis* state, the fluorescence of the vesicle was turned off (Figure 4.12). When

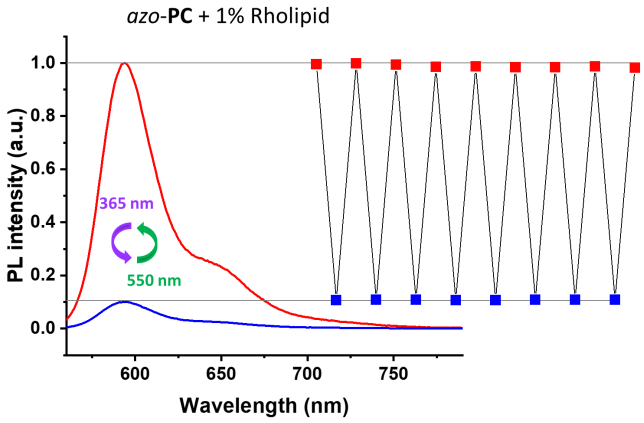

Figure 4.11: Fluorescence modulation of Rho by *azo*-PC isomerization. The PL intensity of 1 mol % of Rho-doped *azo*-**PC** membranes in the *trans* state (red line) and the *cis* state (blue line). This fluorescence modulation is reversible over more than 8 cycles.

switching this vesicle to *trans* state, the gradual turning-on of fluorescence could be observed. This demonstrates the potential of photomodulation between *azo*-**PC** and different dyes for bioimaging.

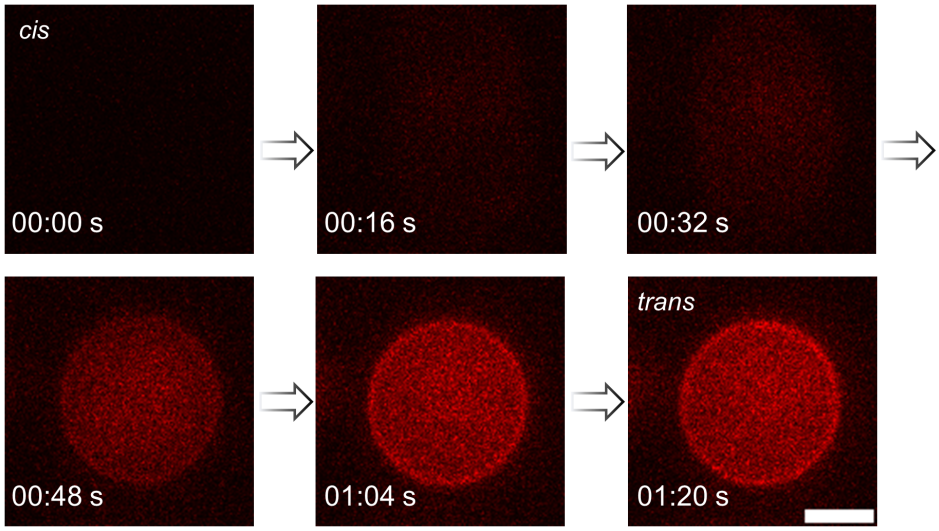

Figure 4.12: Fluorescence on and off of a GUV. The fluorescence of the GUV is off in the *cis* state and turned on when switched to *trans* state. Scale bar: 5 μm.

It was reported that azobenzene is a dark-quencher,[111] which means azobenzene itself does not fluoresce, but is able to quench the fluorescence of other fluorophores. The fluorescence emission of 1 % Rho was measured when doped in a DOPC and an *azo*-**PC** bilayer membrane. Compared to DOPC, *trans azo*-**PC** already quenches the fluorescence of Rho by 51 %, as shown in Figure 4.13.

The quenching efficiency of *azo*-**PC** in the *trans* state and *trans* state can be calculated

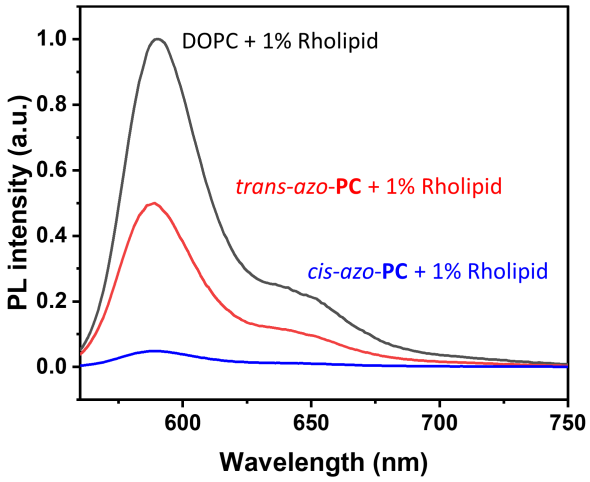

Figure 4.13: *Azo*-PC is a dark-quencher. Not only in *cis* state, but in *trans* state, *azo*-**PC** already quenches fluorescence of Rho.

according to

$$QE_{trans} = 1 - \frac{I_{trans}}{I_{DOPC}}, QE_{cis} = 1 - \frac{I_{cis}}{I_{DOPC}}, \tag{4.2}$$

which is similar to Equation 4.1. The quenching efficiency is dependent on the *azo*-**PC**-to-dye ratio. I then prepared SUV samples in which 1 mol % of Rho was doped in membranes of a mixture of *azo*-**PC** and DOPC lipids. By varying *azo*-**PC** concentration from 1 mol % to 99 mol % but fixing Rho concentration to 1 mol %, samples with various *azo*-**PC**-to-Rho ratios were obtained. Quenching efficiency of these samples in both *trans* and *cis* were then measured and calculated. The quenching efficiencies is exponentially dependent on the photolipid-to-Rho ratio (Figure 4.14,). In the *cis* state, when the *azo*-**PC** concentration is 30 mol %, the quenching efficiency already reaches 80 %.

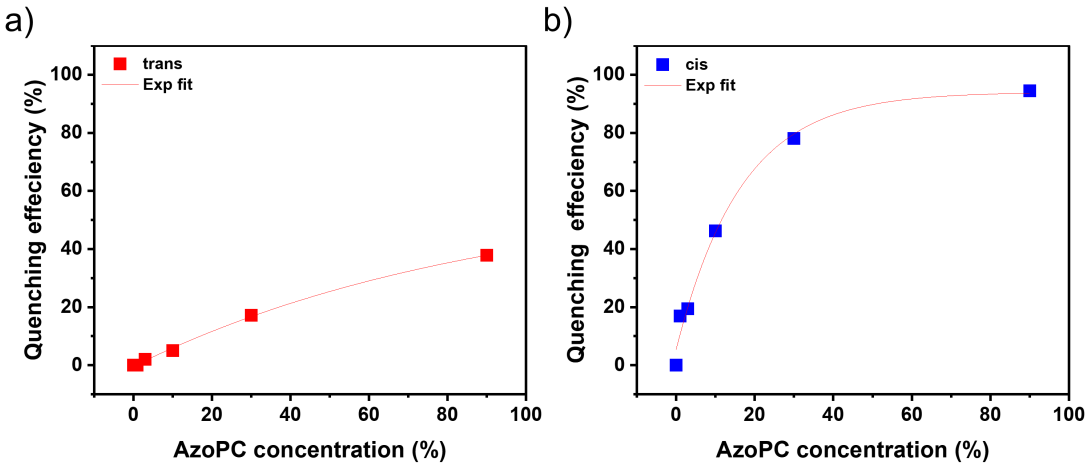

Figure 4.14: Concentration-dependent quenching efficiency of *azo*-PC. Both for **(a)** *trans* and **(b)** *cis azo*-**PC**, quenching efficiency is exponentially dependent on *azo*-**PC** concentration.

4.4 Mechanism Discussions

As discussed in Section 4.2, the interaction mechanism between *azo*-**PC** and MB can be explained by the energy transfer from triplet MB to *azo*-**PC** membrane. This could happen because MB has a high self-ISC efficiency ($\sim$ 0.5).[227] However, other dyes have been reported with very low self-ISC efficiency such as NB ($<$ 0.03),[233] Rho($<$ 0.005).[227] For commercial dyes TR and Atto633, similar experimental results were observed. All these dyes could assist *cis*-to-*trans azo*-**PC** switching with similar rates independent of excitation wavelength and ISC efficiency. This result indicates a general mechanism for interactions between *azo*-**PC** and different dyes. But what is the mechanism? Here, several possibilities are discussed.

Photoredox pathway. Literature[234] reported the ground state oxidation potential of azobenzene is much greater than the excited state reduction potential of dyes (Rho, NB and MB, Table 4.3). Therefore, the calculated ΔG is positive. According to the Rehm-Weller equation (Subsection 2.2.1), photoredox processes can be excluded.

Table 4.3: Redox potential of azobenzene and dyes

Molecules	E^{S0}_{red}[V]	E^{S1}_{red}[V]	E^{S0}_{ox}[V]	E^{S1}_{ox}[V]
azobenzene	-1.78	/	1.59	/
Rho	-1.26	0.93	0.82	-1.37
NB	-0.80	1.10	0.81	-1.09
MB	-0.72	1.15/1.20	0.85	-1.02 /1.08

FRET. As discussed in Subsection 2.2.1, FRET requires a spectral overlap of the acceptor's absorption band and the donor's emission band. However, The emissions of dyes are $\sim$ 200 nm away from the absorption of *cis azo*-**PC** (Figure 4.15). Almost no spectra overlap is observed. Therefore, FRET can be excluded.

Multiphoton processes. All the dyes and *azo*-**PC** molecules were excited with light from LEDs. Furthermore, the excitation intensity was not high. Azobenzene also display a very low two-photon absorption cross section. Multiphoton processes can therefore be excluded.

Recently, a mechanism was proposed by Baumgartner et al.[234] In the study about the intramolecular interaction of chromophore auxiliaries and azobenzenes with the conjugates, they obtained similar results that different chromophores assisted azobenzene photoswitching with red or even NIR light. They proposed the exciplex mechanism. First, auxiliary chromophores are excited to the S_1 state. Since azobenzene and chromophores are close enough, they form an exciplex. Literature reported that azobenzene has very high spin-orbit coupling coefficients,[45] which could force exciplex formation. They argued that exciplex formation

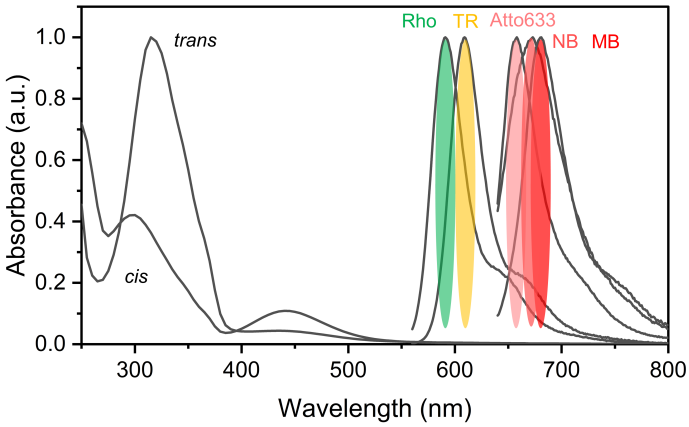

Figure 4.15: Spectra overlap of *azo*-PC's absorption and dyes' emission. The emission of dyes were measured when Rho was excited by 550 nm light, TR was excited by 590 nm light, and Atto633, NB and MB were excited by 630 nm light.

leads to a higher ISC efficiency, and the exciplex triplet is generated. The exciplex finally separates to azobenzene triplet, which returns back to the ground state as a preferable *trans* isomer. In my experiments, *azo*-**PC** is not covalently bound but closely located near the dye molecules. The data suggests that exciplex formation is also a possible reason.

I further did time-resolved PL decay measurements (Figure 4.16). It shows for dye-doped *azo*-**PC** membranes, PL of dyes decays faster when *azo*-**PC** bilayers are in *cis* state. Considering the results of steady as well as time-resolved PL measurements, a question is raised why the *cis azo*-**PC** quenches more fluorescence than *trans azo*-**PC** if the mechanism is exciplex formation.

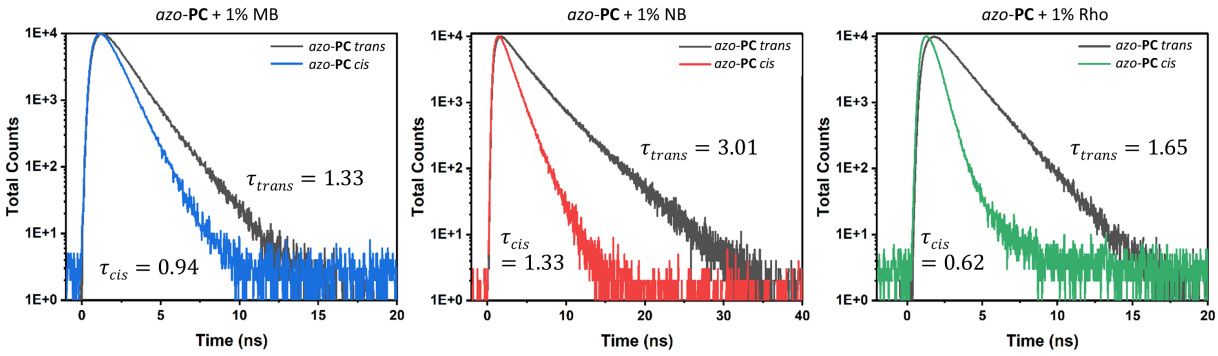

Figure 4.16: Time resolved PL decay of dye-doped *azo*-PC membrane in *trans* and *cis* states. PL of dyes (MB, NB and Rho) decays fast when *azo*-**PC** is in *cis* state.

On one hand, H-aggregates are formed on a *trans azo*-**PC** bilayer membrane.[11] In this case, *azo*-**PC** are assembled to a membrane in a more orderly manner. While in *cis* state, this H-aggregates breaks down so that azobenzene group in the tail could be assembled more closely to dye molecules. On the other hand, It was reported that *cis* azobenzene possesses

higher dipole moment than *trans* isomer,[235] which means *cis azo*-**PC** molecules couple with dyes more easily.[236] Stern-Volmer plots were then performed for a 1 % Rho doped photolipid membrane to investigate the interaction types between dyes and *azo*-**PC** in *trans* and *cis* state. As shown in Figure 4.17, the x axis is the concentration of *azo*-**PC** lipids, and the y axis represent the fluorescence intensity ratio in the absence and in the presence of photolipids. A linear relationship was obtained for *trans azo*-**PC** while a upward deviation was observed for *cis azo*-**PC**. In a Stern-Volmer plot, upward deviation relationship indicates a combination of dynamic and static quenching.[101] The results demonstrate that compared to *trans azo*-**PC**, *cis azo*-**PC** quenches more efficiently because it forms new species together with dye molecules in addition to collisional interaction. The result support the hypothesis of potential exciplex formation.

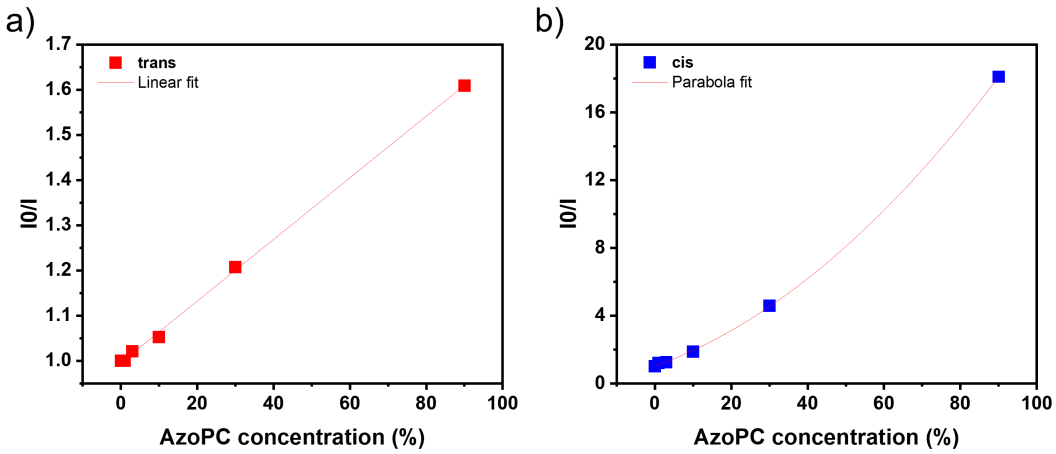

Figure 4.17: Stern-Volmer Plot of % Rho doped photolipid membrane. (a) For dyes on a *trans azo*-**PC** membrane, a linear relationship was observed, indicating a dynamic quenching. **(b)** For dyes on a *cis azo*-**PC** membrane, a upward deviation relationship was observed, indicating a combination of dynamic and static quenching.

4.5 Other Azobenzene-containing Lipids

If the mechanism is exciplex, sensitized switching and fluorescence modulation should also be observed for other azobenzene derivatives. Therefore, I measured the interaction between these dyes and oxy-*azo*-**PC** (Figure 3.1). I observed the same sensitized *cis*-to-*trans* switching of oxy-*azo*-**PC** membrane by doping 1 % of dyes (NB and MB) with red light (Figure 4.18). The switching rates were at a similar level and the switching process can be repeated for many cycles. Compared to the *azo*-**PC**, the PM efficiency of oxy-*azo*-**PC** to dyes is higher. They are 96 %, 84 %,76 % and 68 % for Rho, NB, MB and Atto633, respectively (Figure 4.19 and Table 4.4).

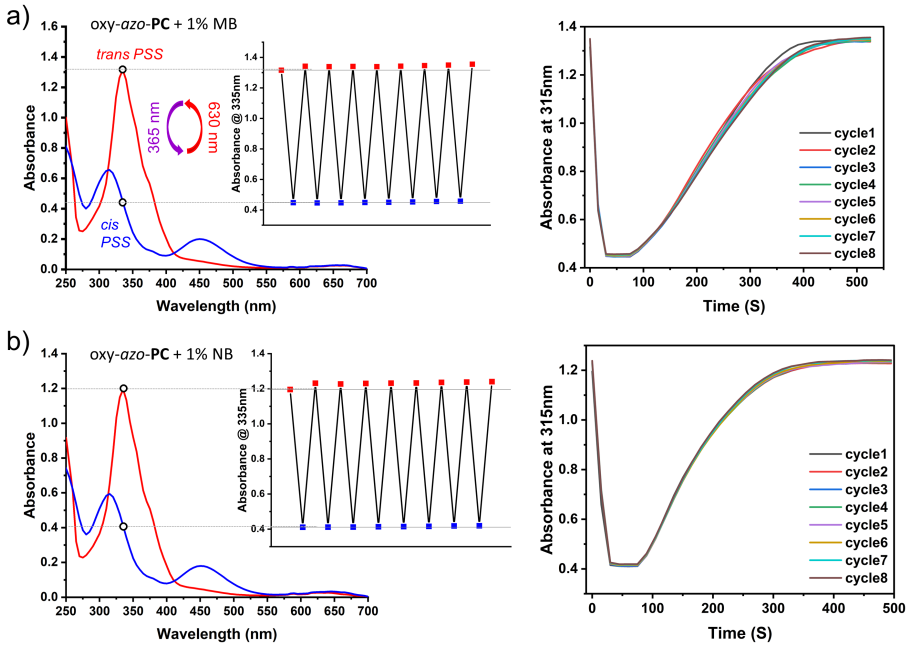

Figure 4.18: Sensitized oxy-*azo*-PC isomerization. Assisted *cis*-to-*trans* switching of oxy-*azo*-**PC** can be realized for over 8 cycles by 1 % of MB and NB doping with illumination of 630 nm light.

Table 4.4: PM efficiency of oxy-*azo*-**PC** to different dyes

dyes	1 % Rho	1 % NB	1 % MB	1 % Atto633
PM efficiency	96 %	84 %	76 %	68 %

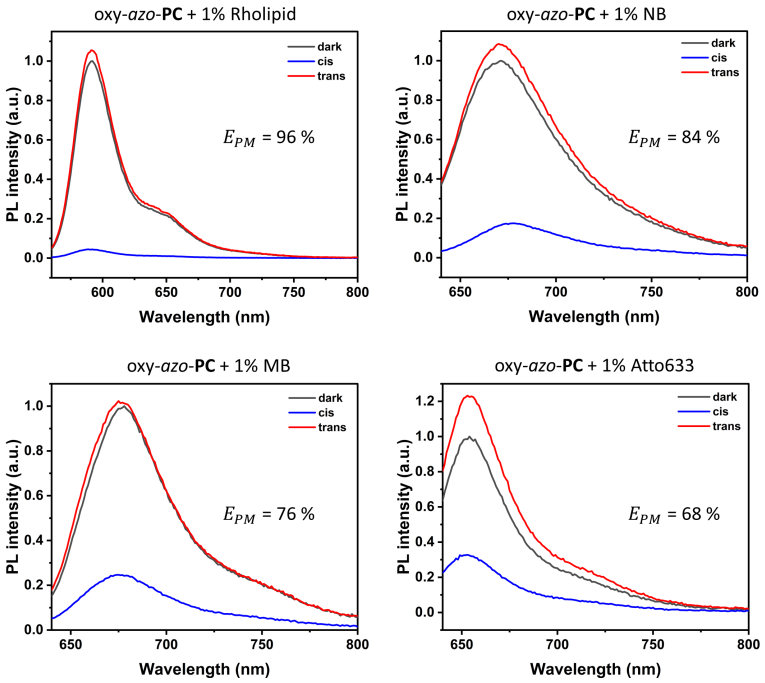

Figure 4.19: Fluorescence modulation of dyes by oxy-*azo*-PC. PM efficiency of oxy-oxy-*azo*-**PC** to Rho, NB, MB and Atto633 are 96 %, 84 %,76 % and 68 %, respectively.

5

Plasmonic Sensing of Photolipid Bilayer Isomerization

As already discussed in the previous chapter, photolipids *azo*-**PC** interact with various dyes through photosensitization and fluorescence modulation. This indicates that it is not ideal to study *azo*-**PC** with fluorescence labeling. Label-free methods for monitoring *azo*-**PC** switching are therefore highly desired. This chapter explores label-free and time-resolved monitoring of *azo*-**PC** bilayer isomerization by single plasmonic AuNRs.

In Section 5.1, the reasons for choosing AuNRs with particular size and shape are introduced. *Azo*-**PC** SLB formation on nanorods was probed by analyzing the plasmon resonance peak shift (Section 5.2). Time-resolved monitoring of *azo*-**PC** SLBs with single AuNRs will be discussed in Section 5.3. Then the measurements conducted on CTAB-coated nanorods and plasma-treated nanorods were compared to explore the effect of the CTAB layer on nanorods' sensing properties, which will be described in Section 5.4. FDTD simulation results are further discussed in Section 5.5 to get a better understanding why *azo*-**PC** bilayer switching leads to the plasmon resonance peak shift of nanorods. In addition, this method is presented to be used to study membrane diffusion and the PSS in Section 5.6. Finally, in Section 5.7, printed AuNR lines show potential in calculating the diffusion coefficient of *azo*-**PC** membranes.

The results presented in this chapter have been published in Advanced Optical Materials as *"Label-Free Time-Resolved Monitoring of Photolipid Bilayer Isomerization by Plasmonic Sensing"*

by J. Zhang, F. Schuknecht, L. Habermann, A. Pattis, J. Heine, S.D. Pritzl, D. Trauner and T. Lohmüller in 2024.[237]

5.1 Nanorods Selction

CTAB-capped AuNRs (Nanopartz Inc., Part# A12-40-650) have been used for the experiments. The nanorods have an average length of 99.1 $\pm$ 3.4 nm and an average diameter of 44.2 $\pm$ 1.2 nm, corresponding to an aspect ratio of 2.2 $\pm$ 0.1, which were calculated from the size distribution data by analyzing the SEM images (Figure 5.1). The AuNRs were chosen for several reasons. Firstly, it is important that the measured lipid membranes cover the AuNRs so that AuNRs can detect the bilayer in the particle's vicinity with high sensitivity. It was reported that the lipid bilayers form pores around particles with a diameter smaller than 22 nm. For particles with a diameter above 22 nm, lipid membranes cover the particle surface.[238,239] Secondly, compared to nanospheres, AuNRs show weaker non-radiative damping[152] and a higher light scattering efficiency, which are more suitable for biosensing applications.

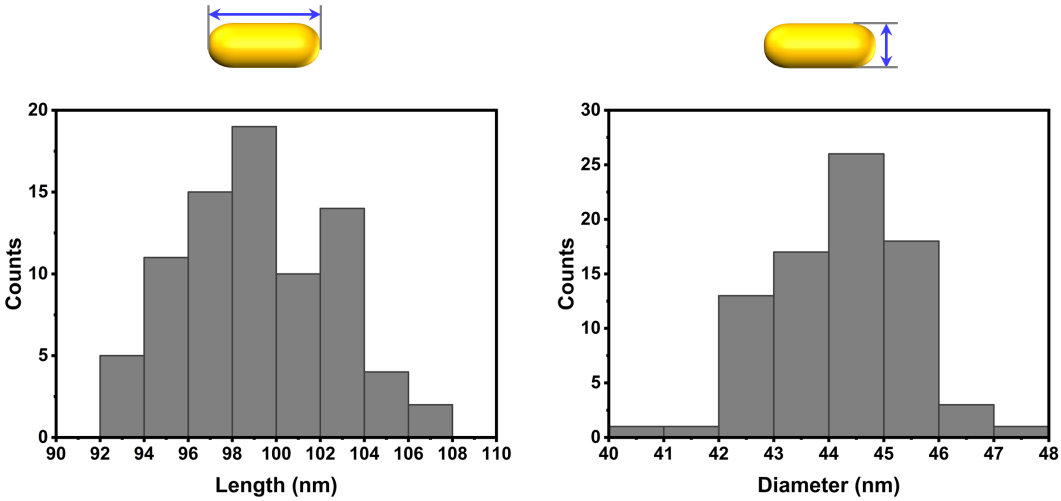

Figure 5.1: Size distribution of used gold nanorods. Average length, diameter and aspect ratio were calculated to be 99.1 $\pm$ 3.4 nm, 44.2 $\pm$ 1.2 nm and 2.2 $\pm$ 0.1, respectively.

Thirdly, the involved plasmon modes of nanorods should not affect the switching behavior of the measured photolipid membranes. Figure 5.2a shows the typical scattering spectrum of the AuNRs, displaying a weak transverse mode at around 530 nm and a strong longitudinal mode at around 660 nm. A 593 nm long-pass filter (LP593) was put between the microscope lamp and the dark-field condenser (Figure 3.12a) to block light below this wavelength. This is to avoid uncontrolled photolipid switching by the light source and via the scattered light by the AuNRs below wavelength 593 nm. The longitudinal plasmon mode is located at the wavelength range where almost no absorption occurs for either *trans* or *cis azo*-**PC**. As shown in Chapter 4, photoswitching by red light illumination is very inefficient. Figure 5.2b presents

the absorption changes of *azo*-**PC** SUVs by illumination with 630 nm light (high power 20 mW). Only minimal cis-to-*trans* switching was observed after 1 h irradiation.

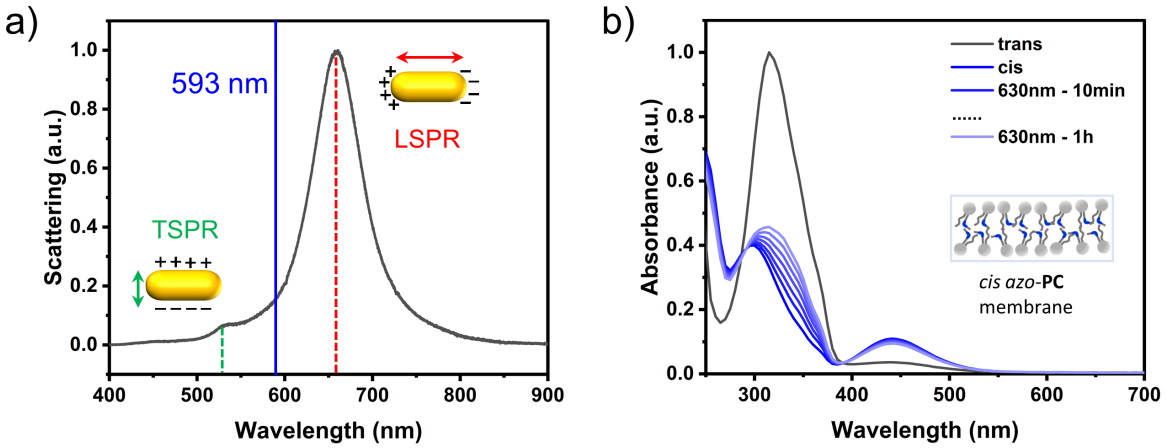

Figure 5.2: Avoiding effects of AuNRs plasmon modes on photolipid switching. (a) The scattering spectrum of single AuNRs exhibits a transverse plasmon mode at around 530 nm and a longitudinal plasmon mode at around 660 nm. A 593 nm long pass filter was used to block the light from the microscope lamp to prevent unwanted *azo*-**PC** isomerization. **(b)** The effects of 630 nm illumination on cis-to-*trans* switching of *azo*-**PC** SUVs. *Trans azo*-**PC** vesicles (black line) were first irradiated with 365 nm light to *cis* state (dark blue line). By illuminating with 630 nm light at 20 mW for 1 hour, only minimal cis-to-*trans* switching was observed.

In addition, the selected nanorods should possess sufficient sensitivity to monitor *azo*-**PC** SLBs isomerization. As discussed in Subsection 2.3.2, the sensitivity factor m in Equation 2.48 depends on size, shape and composition of the nanorods. The size (length 99.1 $\pm$ 3.4 nm, diameter 44.2 $\pm$ 1.2 nm) and aspect ratio (2.2 $\pm$ 0.1) of used nanorods are similar but more monodisperse than the nanorods (size 85.6 $\pm$ 6.6 nm and 39.8 $\pm$ 3.4 nm, aspect ratio 2.2 $\pm$ 0.2) used by Ye et al.[132] They reported a sensitivity factor of approximately 185 $\pm$ 5 nm per RIU towards the refractive index. That means the nanorods can theoretically sense a refractive index change smaller than 0.005. They also calculated the maximum sensing distance ($l_d/2$ in Equation 2.48), which turned out to be 17 nm. This sensing distance is much larger than the thickness of a bilayer membrane ($\sim$ 5 nm), meaning the chosen nanorods are sensitive enough for the bilayer membrane detection.

The obtained scattering spectrum of single nanorods was fitted with a Lorentzian function in energy space (Figure 5.3). Information about the scattering intensity, plasmon resonance peak and plasmon linewidth can be obtained from the fitting, which provides different methods to achieve single-particle plasmonic sensing including detection of the scattering intensity change,[240] plasmon resonance shift and plasmon linewidth broadening.[241] Detection of the plasmon resonance peak shift is the most robust and common approach, which will be used here. The plasmon resonance peak obtained from Lorentzian fitting is in energy space, which needs to be converted to wavelength space.

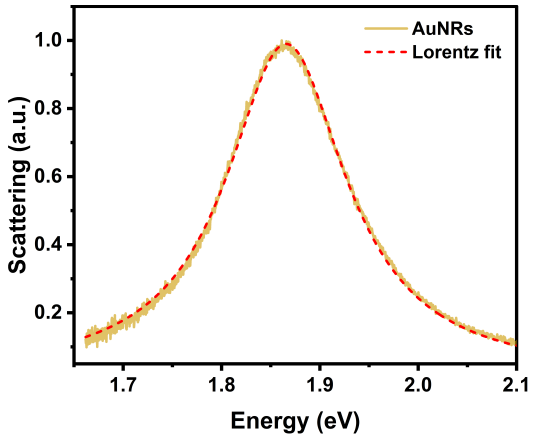

Figure 5.3: Lorentzian fit of the scattering spectrum of single gold nanorods. Plasmon resonance peak could be analyzed from the fitting.

5.2 Plasmonic Sensing of Membrane Deposition

Firstly, membrane formation on single AuNRs was measured via plasmonic sensing. Gold nanorods were dropcasted on a clean glass substrate (Subsection 3.2.1) and *azo*-**PC** SLBs were deposited on top of the nanorods via vesicle fusion of SUVs (Subsection 3.1.2). As shown in Figure 5.4a, the CTAB layer lies in between the nanorods' surface and membrane layer. *Azo*-**PC** SUV samples were in $\sim$ 100 % *trans* state prior to measurements since the sample was dark-adapted for days. The scattering spectrum of single AuNRs was measured with the dark-field microscope equipped with a spectrometer (Figure 3.12).

After *azo*-**PC** bilayer formation, the scattering spectrum of single rods (Figure 5.4b, red line) was red-shifted compared to the spectrum before membrane deposition (Figure 5.4b, gold line). The plasmon resonance shift was calculated by Lorentzian fitting. An average red shift of plasmon resonance due to *azo*-**PC** SLBs deposition was calculated to be 5.49 nm based on statistics from 65 nanorods (Figure 5.4c, blue box). A control measurement was then conducted with non-switchable lipids DOPC and an average red-shift of 5.55 nm was observed (Figure 5.4c, gray box). The results indicate comparable dielectric environment changes induced by both *trans-azo*-**PC** and DOPC bilayer formation. As discussed in Subsection 2.3.2, the plasmon resonance shift depends on the refractive index and the thickness of the adsorbate layer. It was reported that the thickness of a DOPC bilayer is between 3.69[242] and 3.83 nm[243] while the thickness of *azo*-**PC** is dependent on the PSS and solvent. For example, in buffer solution, the head-to-head distance of *trans* and *cis azo*-**PC** bilayer is reported to be 41.9 Å and 34.8 Å, respectively.[12] However, in DI water, this distance decreases to 39 Å for the *trans* bilayer and 34 Å for the *cis* membrane.[11] These literature values demonstrate that DOPC bilayer thickness lies in between the thickness of *trans* and cis *azo*-**PC** bilayer. The refractive index of the membrane is affected by the lipids density. It was reported that

the area per lipid molecule is 72.5 Å^2 for the DOPC membrane.[242] This value of the *azo*-**PC** membrane is between 78.6 Å^2 and 56.6 Å^2 for *cis* and *trans* states.[6]

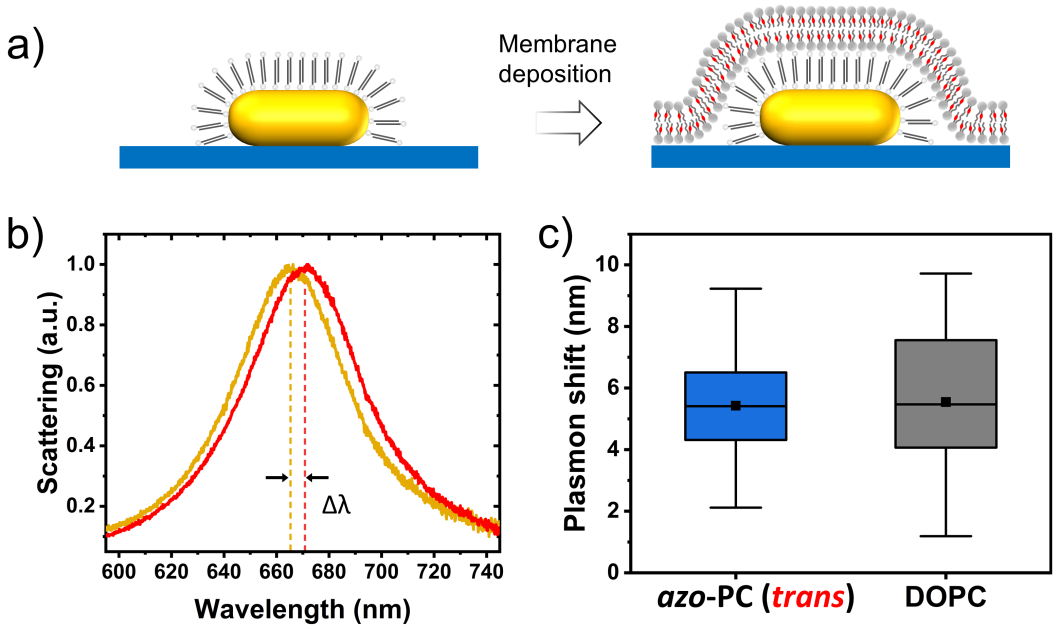

Figure 5.4: Plasmonic sensing of membrane formation. **(a)** Schematic of *trans azo*-**PC** SLBs formation on single CTAB-capped AuNRs. **(b)** Scattering spectra of single AuNRs before (golden line) and after (red line) *trans azo*-**PC** membrane coating. The plasmon resonance red shifts by ~5 nm after membrane deposition. **(c)** Boxplot of the plasmon resonance shift after *trans azo*-**PC** SLBs formation (blue box, statistics based on 65 nanorods) and DOPC formation (gray box, based on 9 nanorods). An average plasmon shift was observed to be 5.49 for *azo*-**PC** and 5.55 nm for DOPC.

5.3 Plasmonic Sensing of *Azo*-PC Bilayer Isomerization

Next, the plasmonic response of gold nanorods was measured while *azo*-**PC** SLBs were switched back and forth between two isomerization states (Figure 5.5a). This photoswitching was achieved via the UV and blue LEDs coupled through the objective (Figure 3.12). Measured AuNRs were aligned into the center of the illumination spot. Figure 5.5b shows an example of measured results. After the trans *azo*-**PC** SLB deposition, the plasmon resonance peak of single nanorods experienced a $\sim$ 6 nm red-shift (yellow square to first red square). By exposure to UV irradiation for 2 min to switch *azo*-**PC** SLBs to *cis* state, a blue shift of plasmon resonance was observed. The following 2 min blue illumination, which induced *cis*-to-*trans* isomerization, made the plasmon resonance peak shift backwards. This reversible shift of plasmon resonance peak can be repeated for many cycles upon alternate illumination of UV and blue light as long as the bilayer membrane was not destroyed.

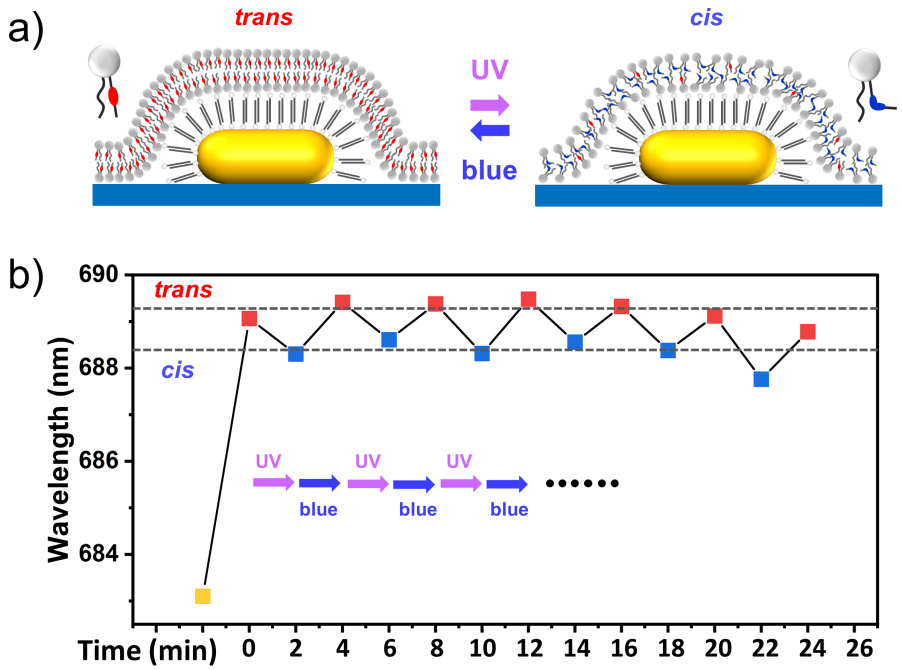

Figure 5.5: Plasmonic sensing of *azo*-PC SLBs isomerization. (a) Schematic of *azo*-**PC** SLBs isomerization on top of single AuNRs. **(b)** Reversible *azo*-**PC** SLBs isomerization measured by monitoring the nanorods' plasmon resonance peak shift. The golden square represents plasmon resonance peak of bare CTAB-coated rods before membrane deposition. Reversible shifts of plasmon resonance peak were observed due to isomerization of *azo*-**PC** membrane between *trans* (red square) *cis* state (blue square) by alternating illumination of UV and blue light.

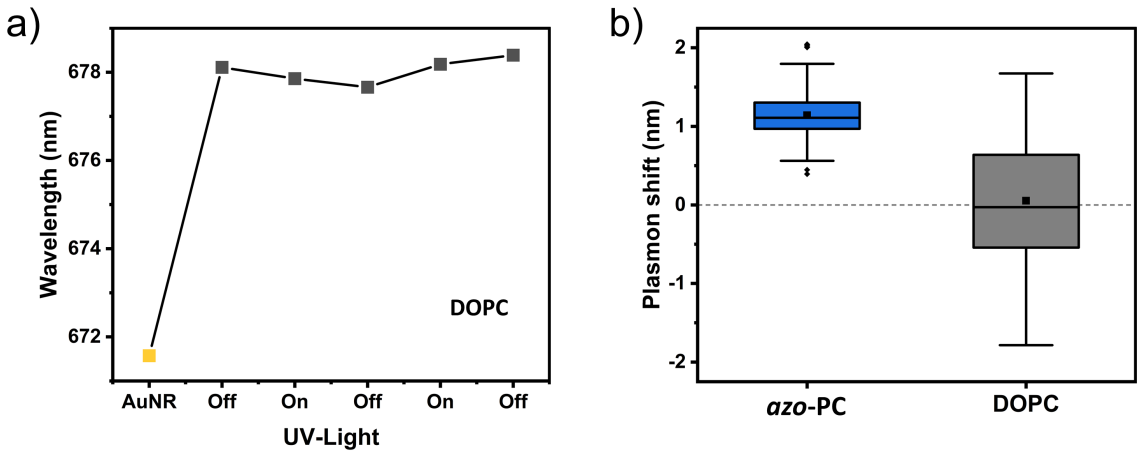

Figure 5.6: Control measurement for DOPC. (a) A stable plasmon resonance peak was observed for DOPC SLBs upon UV illumination for several cycles. Yellow square: plasmon resonance peak of measured AuNRs before DOPC SLBs deposition. It shows a $\sim$ 6 nm red shift after DOPC membrane formation. **(b)** Blue box: An average plasmon resonance peak red shift of 1.14 nm was obtained for *azo*-**PC** SLBs due to isomerization (from measurements on 15 nanorods over 58 illumination cycles). Gray box: No plasmon shift but only small fluctuations are shown for DOPC SLBs upon UV illuminations.

To confirm that this reversible plasmon resonance shift is only induced by *azo*-**PC** isomerization, control measurements were again conducted with DOPC membranes. The plasmon

resonance peak of the measured rods red shifts by $\sim$ 6 nm (yellow square to first gray square, Figure 5.6a) after DOPC SLBs formation. By exposure to UV irradiation, no considerable plasmon resonance shift was observed. This is because the DOPC bilayer does not change upon illumination, and further confirms that the illumination condition does not affect the measurement.

Analyzing data from 15 AuNRs over 58 switching cycles shows an average shift of plasmon resonance peak by 1.14 nm due to *azo*-**PC** isomerization (Figure 5.6b, blue box). For the DOPC membrane, the average fluctuation of plasmon signal due to UV illumination is 0.04 based on data from 9 nanorods measured over 20 illumination cycles (Figure 5.6b, gray box).

Considering the optothermal properties of gold nanorods, control measurements on temperature changes were performed to exclude the possibility of plasmon heating effects on *azo*-**PC** isomerization. Note that nanorods were all measured in water. A temperture probe was immersed in the water, recording temperature changes upon illumination. As illustrated in Figure 5.7, temperature around the membrane stayed stable by illumination of a microscope lamp or UV and blue LEDs.

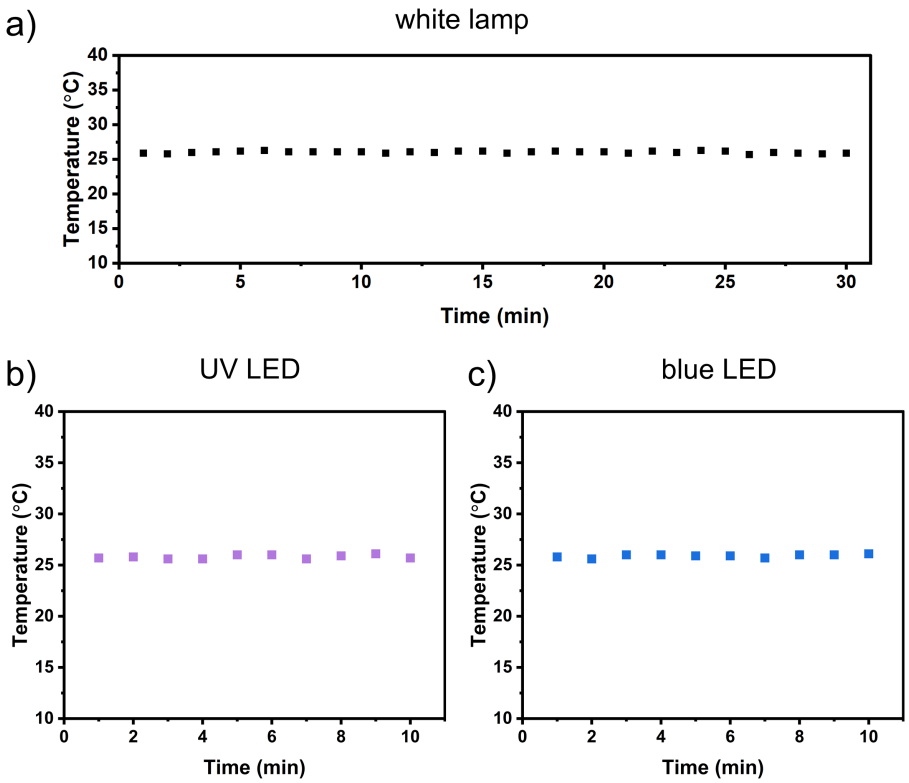

Figure 5.7: Control measurements of temperature changes. No temperature increase was observed when the sample was illumination by **(a)** microscope lamp **(b)** UV LED and **(c)** blue LED.

Time-resolved measurements of the plasmon shift were further conducted to monitor *azo*-**PC** isomerization in real-time by continuously collecting scattering spectra at a rate of 2 spectra per second. As shown in Figure 5.8, the *azo*-**PC** bilayer was initially in a *trans* or *cis* PSS, so that the plasmon resonance stayed stable at the first 10 s. As soon as the UV or blue illumination was switched on at 10 s, the plasmon resonance started to shift, which is an indication of photolipids isomerization. After 10-20 s of illumination, the plasmon resonance reached a plateau, demonstrating that photolipid SLBs covering the nanorod reached a new PSS. From this, the switching rate of *azo*-**PC** bilayer can be determined. It is calculated that the *trans*-to-*cis* switching rate is 0.446 s^{-1}, *cis*-to-*trans* is 0.313 s^{-1}. It was reported that azobenzene switches in picoseconds.[70] An *azo*-**PC** bilayer should also switch fast. This switching rate also depends on the LED power, intensity and wavelength. By applying higher illumination power, a faster switching rate can be achieved.

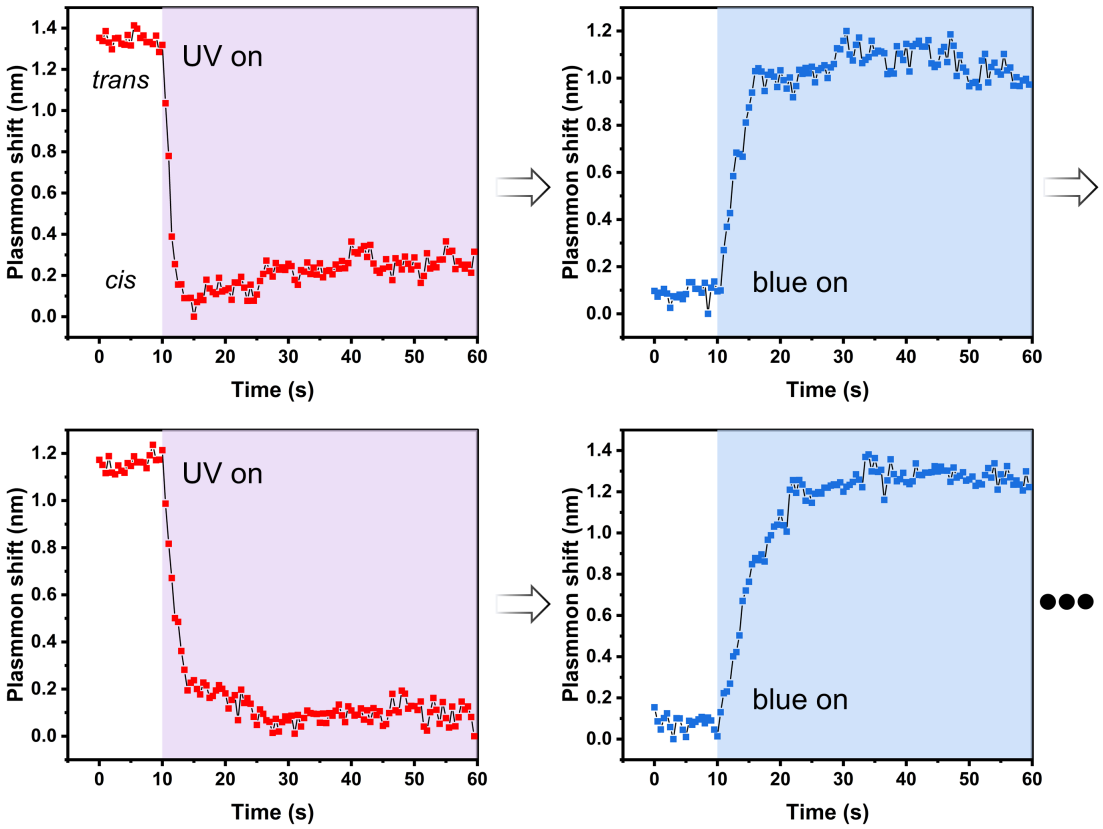

Figure 5.8: Time-resolved monitoring of *azo*-PC SLBs isomerization. The UV or blue illumination was turned on at 10 s. Before any illumination, the plasmon resonance peak stayed stable. Once illumination was on, plasmon resonance started to shift until *azo*-**PC** SLBs reached a PSS. The switching rates are calculated to be 0.446 s^{-1} for *trans*-to-*cis* and 0.313 s^{-1} for *cis*-to-*trans*.

Figure 5.9 shows real-time changes of the plasmonic peak in response to consecutive membrane switching. In Figure 5.9a, the photolipid bilayer was initially in the *trans* state. At 10 s, the UV LED was turned on so that a blue shift of plasmon resonance was observed until a *cis* PSS was reached at $\sim$ 20 s. At 35 s, the UV light was turned off while the blue light was

switched on instantaneously. An immediate red shift occurred indicating the membrane was switched back to the *trans* state. Figure 5.9b presents a monitoring over two switching cycles. The results demonstrate a fast and sensitive plasmonic response of AuNRs to membrane conformational change. Every 0.5 s, an obvious plasmon shift can be observed. Figure 5.9b also shows gradual drift of plasmon resonance due to the off-focus of nanorods. This drift domenstrates the necessity of statistic study.

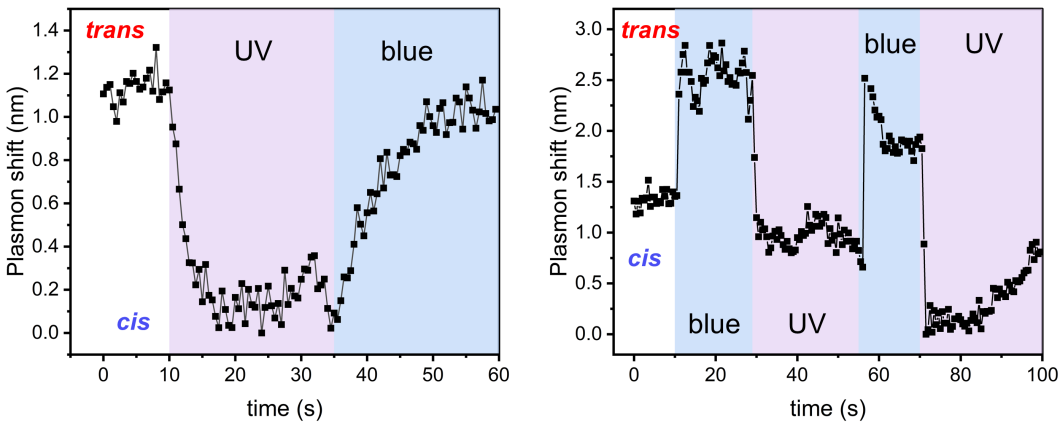

Figure 5.9: Time-resolved switching patterns. (a) The *azo*-**PC** bilayer was initially in the *trans* state. At 10 s, UV light was on to switch the membrane to *cis* state. The plasmon resonance was blue-shifted until *cis* PSS was reached. At 35 s, the UV light was off, and at the same time, the blue light was on so that a back shift of plasmon resonance was observed until a new *trans* PSS was reached. **(b)** The sample was initially in the *cis* state. Blue LED was on at 10 s, off at 25 s, on again at 57 s, and finally off at 65 s. UV LED was on at 25 s, off at 57 s, on again at 65 s. After 1 minute, the measured nanorod was off focus, leading to a fluctuation of plasmon resonance.

Figure 5.10 shows time-resolved measurements on the DOPC membrane. For the same UV or blue illumination conditions, no plasmon resonance shift was observed again, confirming no influence of the illumination condition on the measurement.

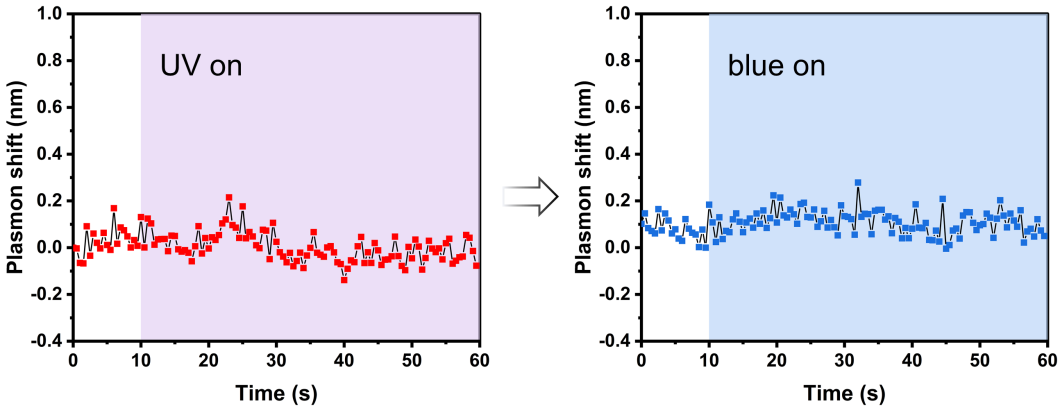

Figure 5.10: Time-resolved measurements for DOPC membranes. The UV or blue light were switched on at 10 s.

5.4 Effects of Ligands on Plasmonic Sensitivity

Until now, all the measurements were conducted on CTAB-coated nanorods. That means AuNRs and measured lipid bilayers are kept at a distance of a CTAB bilayer (3.6 nm). The electromagnetic field decays exponentially from the nanorods' surface. The further lipid bilayers are away from the nanorods' surface, the less sensitivity will be obtained. The presence of a CTAB bilayer is thus expected to decrease the sensitivity of the measurement. As discussed in Subsection 3.2.1, plasma treatment can remove the CTAB layer efficiently. Here measurements were further conducted on plasma-treated nanorods to investigate the impact of ligands on plasmon sensing.

The glass substrates with dropcasted AuNRs were firstly plasma cleaned for 75 s to remove the CTAB layer. Then SUV vesicles were added to form an SLB on CTAB-removed AuNRs (Figure 5.11a, top). An average plasmon shift of 9.59 nm was observed after *azo*-**PC** SLBs formation (Figure 5.11a, bottom, blue box) and 9.35 nm for DOPC SLBs (Figure 5.11a, bottom, gray box), which are larger compared to the shift of 5.49 nm and 5.55 nm for CTAB-coated nanorods. This is an indication of improved sensitivity. Notably, a higher shift of plasmon resonance was obtained for photolipid SLBs compared to the DOPC bilayer, which may be

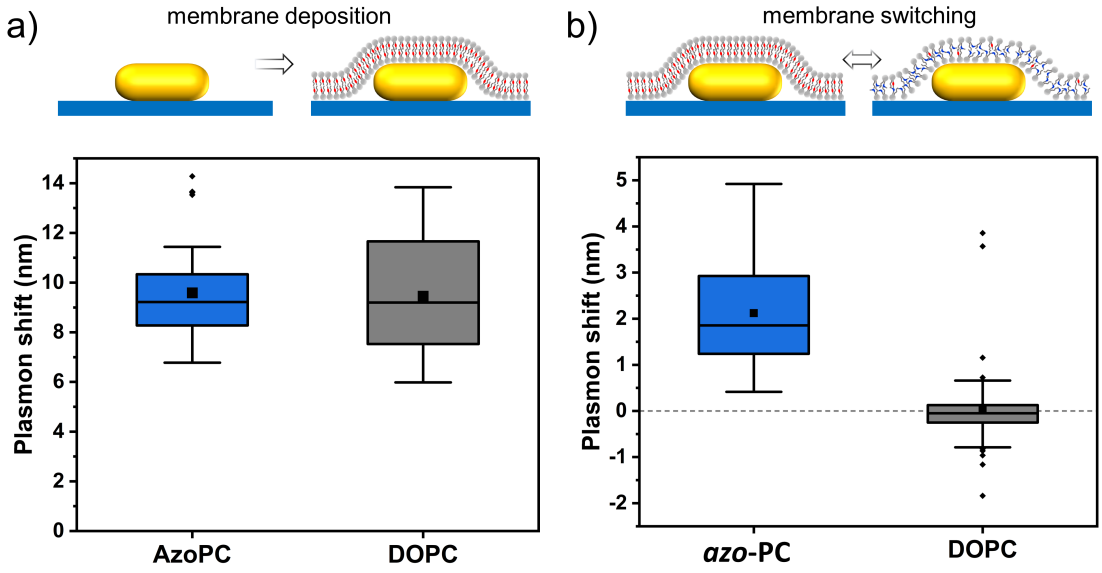

Figure 5.11: Plasmonic sensing on CTAB-removed AuNRs. (a) Top: schematic of *azo*-**PC** SLBs formation on plasma-treated nanorods. Bottom: plasmon resonance shift of plasma-treated AuNRs after membrane deposition. For *azo*-**PC** SLBs, the average shift is 9.59 nm (blue box, measurements on 28 nanorods). For the DOPC membrane, a similar shift of 9.35 nm was obtained based on measurements on 12 nanorods (gray box). **(b)** Top: schematic of *azo*-**PC** bilayer isomerization on plasma-treated nanorods. Bottom: plasmon resonance shift due to *azo*-**PC** photoswitching on plasma-treated AuNRs is 2.12 nm (blue box, measurements of 49 switching cycles on 8 nanorods). Control experiments on DOPC show no plasmon shift (average shift 0.01 nm based on data of 33 switching cycles on 15 nanorods).

because a *trans-azo*-**PC** bilayer is $\sim$ 2 - 3 Å thicker than a DOPC bilayer.[242,11]

Plasmonic sensing of reversible *azo*-**PC** photoisomerization was also performed on plasma-treated AuNRs (Figure 5.11). Based on measurements of 49 switching cycles on 8 nanorods, an average plasmon shift of 2.12 nm was obtained due to *azo*-**PC** switching (Figure 5.11, bottom, blue box). This shift is larger compared to CTAB-coated rods, which again can be explained by a closer proximity between *azo*-**PC** SLBs and the nanorods' surface. Control measurements on the DOPC membrane upon UV and blue illuminations were also conducted for plasma-treated nanorods. No plasmon shift was observed (Figure 5.11, bottom, gray box, 33 switching cycles on 15 nanorods).

5.5 FDTD Simulations of *Azo*-PC Bilayer Photoswitching

As discussed in Subsection 2.1.3, when an *azo*-**PC** membrane is switched between *trans* and *cis* states, changes in photolipid conformation, membrane thickness and lipid density are obtained. These changes may all lead to a plasmon resonance shift of nanorods. To gain a better understanding how the plasmon resonance shift of nanorods is affected by these changes due to photoswitching, FDTD simulations were conducted.

Two scenarios were analyzed, including *azo*-**PC** SLB formation on CTAB-coated nanorods and plasma-treated nanorods. For the CTAB-coated scenario, the nanorods and photolipid bilayers were modeled with a separating distance of 3.6 nm, representing the CTAB bilayer (Figure 5.12a, left figure). The deposited *azo*-**PC** bilayer in the dark-adapted *trans* state was assumed to have a thickness of 4.2 nm. This value of thickness was taken from literature for *azo*-**PC** bilayer in 1X PBS solution.[12] For the plasma-treated scenario, the model was built where a photolipid bilayer formed on the nanorods' surface without any space in between (Figure 5.12b left figure). In reality, a thin water layer is formed separating AuNRs/substrate and SLBs. The thickness of this water layer was reported to be 2 - 8 Å [244] for the glass substrate and $\sim$ 5 Å for the gold substrate,[238] which was neglected in the simulations.

Then different refractive indices from 1.33 to 1.45 were modeled for the 4.2 nm thick *trans azo*-**PC** bilayer. Note that 1.33 is the refractive index of water. In this case, nanorods are surrounded by water and without the formation of a membrane on top. By fitting scattering spectra obtained from FDTD simulation, the plasmon resonance shift can be analyzed. The plasmon shift was found to be linearly dependent on the bilayers' refractive index, shown as the red lines in Figure 5.12a and b. From experiments, an average plasmon shift of 5.49 nm was observed for CTAB-coated nanorods due to the *trans-azo*-**PC** SLB deposition, which corresponds to a change of refractive index from 1.33 (water) to 1.428 (*trans-azo*-**PC** bilayer)

according to simulation results (Figure 5.12a, red line). This refractive index value of 1.428 is quite reasonable, as it is in good agreement with the refractive index of DOPC reported in the literature (1.435 - 1.450).[245] Note that the refractive index of DOPC and *azo*-**PC** should be similar since these two kinds of lipid bilayer cause almost the same plasmon shift and possess similar thickness. For plasma-treated nanorods, the measured plasmon shift after *azo*-**PC** formation is 9.59 nm, corresponding to a refractive index shift from 1.33 to 1.428 as well (Figure 5.12b, red line). The simulation results due to bilayer formation in both models are consistent.

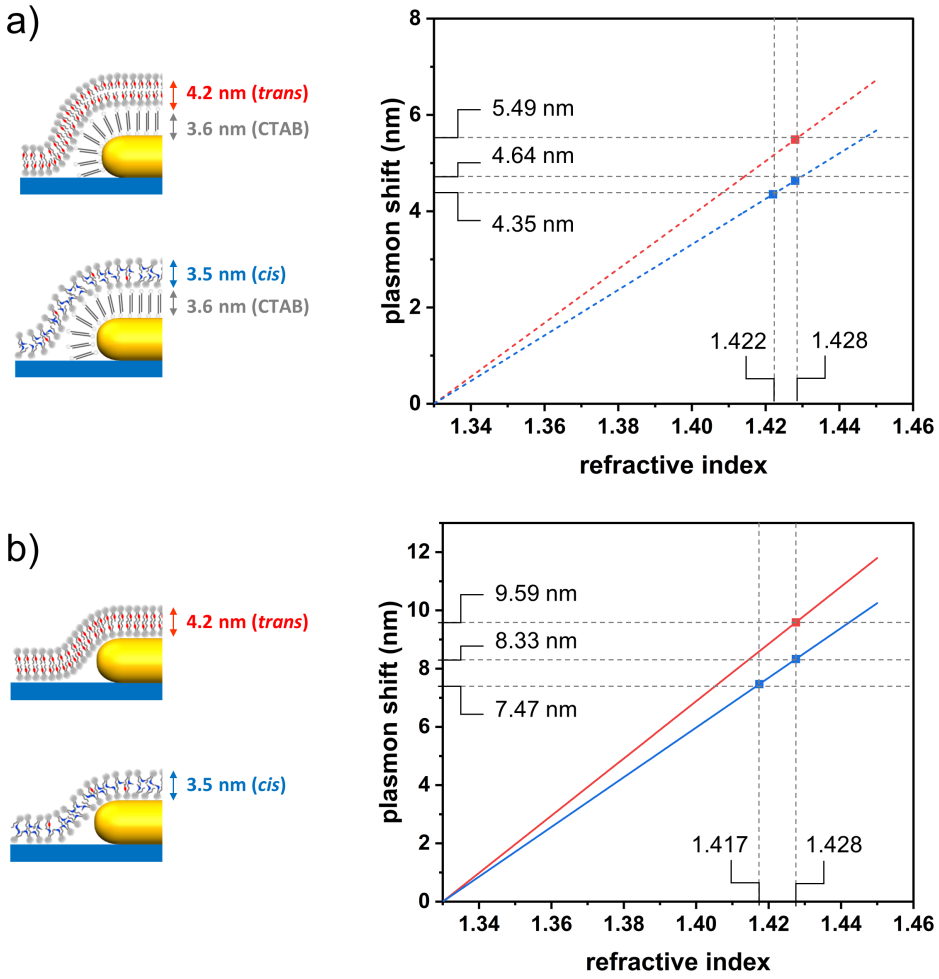

Figure 5.12: FDTD Simulations. (a) CTAB-coated AuNRs. **(b)** Plasma-treated AuNRs. Schematics of the simulated model for both cases are illustrated on the left. The thickness of CTAB layer, *trans* and *cis* *azo*-**PC** were modeled to be 3.6 nm, 4.2 nm and 3.5 nm according to the literature value. The relationship between plasmon shift and refractive index or thickness of bilayer membrane is plotted in the right graphs. Red lines in both graphs show a plasmon shift of 4.2 nm thick bilayer (*trans*-*azo*-**PC** bilayer) dependent on refractive index change, while blue lines represent a plasmon shift of 3.5 nm thick bilayer (*cis*-*azo*-**PC** bilayer). By comparing experimental and simulation results, refractive index and thickness change which lead to plasmon shift after bilayer deposition and *azo*-**PC** photoswitching are analyzed (red and blue squares).

A thickness reduction of 7 Å was assumed after the isomerization of the *azo*-**PC** bilayer

from *trans* to *cis* state based on literature values.[12] The dependence of plasmon resonance shift on refractive index change of a 3.5 nm thick bilayer (*cis*-*azo*-**PC**) was simulated and analyzed as blue lines in Figure 5.12a and b. For CTAB-coated nanorods, the 7 Å thickness reduction results in a blue shift of plasmon resonance of 0.85 nm (from 5.49 nm to 4.64 nm). For plasma-treated nanorods, this shift is 1.26 nm calculated from 9.59 nm to 8.33 nm. Note that the measured plasmon shift due to *azo*-**PC** switching is 1.14 nm for CTAB-coated rods and 2.12 nm for plasma-cleaned rods, which is higher than the shift simulated by bilayer thickness decrease. That means considering only thickness reduction can not completely explain the measured plasmon shift. As shown in Figure 5.12, an additional decrease in refractive index should be taken into account, which is approximately 0.01 for both cases.

At least two changes in *azo*-**PC** bilayer account for this refractive index change. First, the conformational change of azobenzene group leads to a refractive index change of the *azo*-**PC** bilayer. It was reported that the refractive index of azobenzene-functionalized polymer is dependent on the methylene spacer length $(\text{-CH}_2)_x$.[246] For example, the refractive index of azobenzene with 3 methylene groups decreases by 0.036 after UV irradiation. In addition, the lipid density of a *cis* bilayer is less than a *trans* bilayer, which also contributes to the refractive index reduction. Both these two changes lead to a refractive index decrease of *cis azo*-**PC** bilayer compared to *trans*.

5.6 Plasmonic Sensing of Membrane Diffusion

Supported bilayers are fluid on clean glass substrate since a water layer is formed in between. An *azo*-**PC** SLB on glass is found to be fluid in both *trans* and *cis* states. From FRAP measurements, its diffusion coefficient can be determined, which is between 0.4 $\mu m^2 s^{-1}$ (*trans*) and 0.8 $\mu m^2 s^{-1}$ (*cis*). Here, single AuNRs were applied as a plasmonic sensor for the study of *azo*-**PC** membrane fluidity, which allows to investigate membrane fluidity within a small nanoscale area.

To calculate the diffusion coefficient with FRAP, fluorophores in the illumination spot are photobleached and then recovered over time due to the exchange between bleached molecules and non-bleached molecules driven by the lipid diffusion. The idea of applying particle plasmon for the study *azo*-**PC** bilayer diffusion is similar to the concept of FRAP. However, there is an important difference. Firstly, UV light switches *azo*-**PC** lipids in the illumination spot to the *cis* state (the illumination spot is focused on a specific single AuNRs). *Trans* isomers and *cis* isomers then diffuse to mix with each other, which will change the ratio between these two states covering nanorods. By monitoring the plasmon resonance shift over time, lipids mixing can be measured.

Azo-**PC** SLBs fluidity was probed on both CTAB-coated (Figure 5.13a) and plasma-treated single rods (Figure 5.13b) by conducting time-resolved measurements of the plasmon resonance shift. Nanorods were firstly covered by *trans*-adapted *azo*-**PC** SLBs. Before UV illumination, the plasmon resonance stayed stable. Then UV light was on for 5 s (from 10 s to 15 s), where the illumination spot was centered on the measured individual nanorod. A blue shift of the plasmon resonance was observed in both cases. As long as the UV illumination was switched off, the plasmon resonance shifted back gradually. Notably, this back shift of the plasmon resonance was not because of the back switching of the *azo*-**PC** membrane since blue light was not on. An explanation for this observation is shown in Figure 5.14c. In the beginning 10 s, no shift was observed because the whole membrane was in *trans* state. Lipids diffusion did not change the refractive index or thickness of the bilayer on top of nanorods. Once the sample was irradiated with UV light, *azo*-**PC** molecules within the illumination spot switched

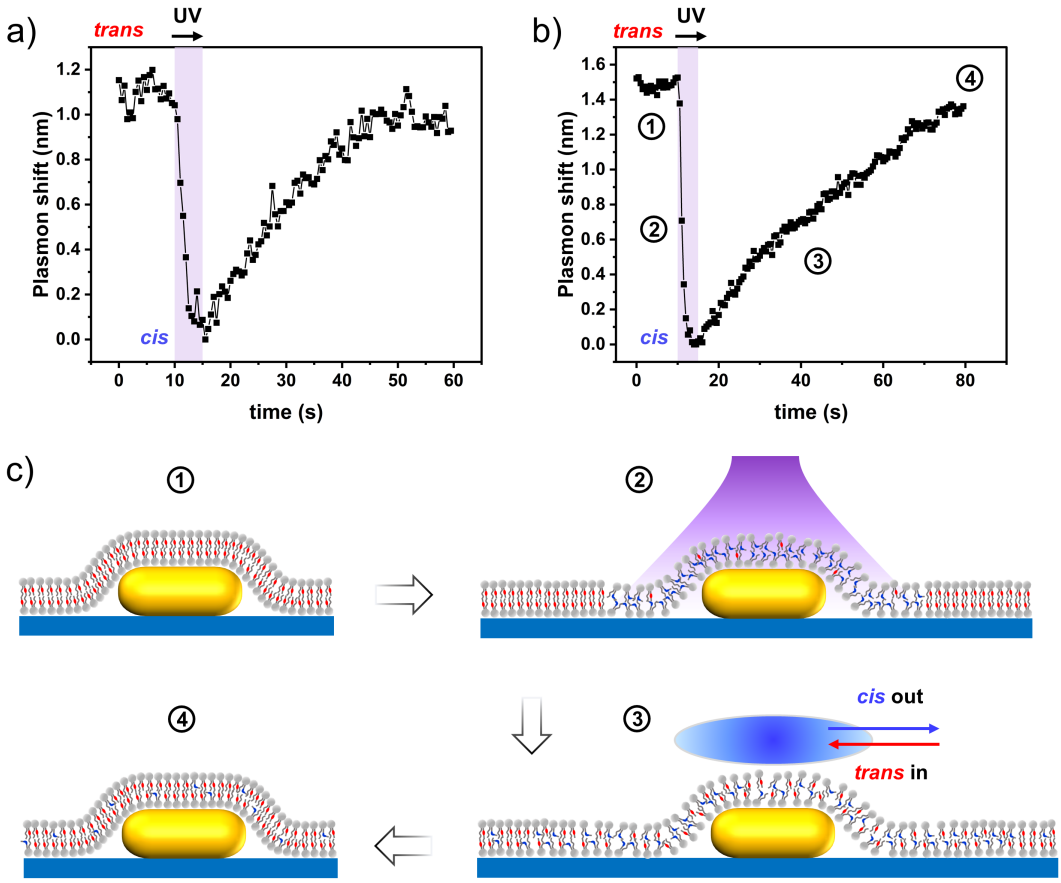

Figure 5.13: Plasmonic sensing of bilayer fluidity. Probing membrane fluidity on **(a)** CTAB-coated nanorods and **(b)** plasma-treated nanorods. The UV illumination spot is centered on the measured nanorods. UV light was on from 10 s to 15 s for both cases. **(c)** An explanation for plasmon shift shown in **(a)** and **(b)**. In the first 10 s, no shift occurred because the whole membrane was in *trans* state. UV illumination switched *azo*-**PC** covering nanorods, thus caused a blue shift of plasmon resonance. After the UV light was off, the exchange between *cis*-*azo*-**PC** inside the illumination spot and *trans*-*azo*-**PC** outside the spot led to a back shift of plasmon resonance. Finally, *cis*-*azo*-**PC** was diluted throughout the whole membrane.

to the *cis* state, leading to a blue shift of the particles' plasmon resonance. However, in the extended SLB area outside of the illumination spot, most of the *azo*-**PC** molecules were still in *trans* state. When UV light was turned off after 15 s, two lipid isomers started to mix, that is, *cis-azo*-**PC** diffused out of the illumination spot, while *trans-azo*-**PC** diffused into this area. This lipid mixing resulted in a change of the *trans*/*cis* ratio covering the nanorod, therefore yielded a back shift of the plasmon resonance. Once the *trans*/*cis* ratio became homogenous throughout the entire membrane, lipid mixing stopped, and the plasmon resonance reached a plateau. The calculated rate of lipid exchange was 0.03 s^{-1} for CTAB-coated rods and 0.02 s^{-1} for CTAB-removed rods.

This method probes lipid diffusion by measuring the change of local *trans*/*cis* ratio over time. The final *trans*/*cis* ratio, that is the PSS, is determined by the UV illumination time. Changing the UV illumination time, different PSSs can be reached. In the next step, single AuNRs were used for the study of *azo*-**PC** bilayer PSS. As shown in Figure 5.14, during the first 10 s, the *azo*-**PC** bilayer covering nanorods was in the *trans*-adapted PSS. At 10 s, the UV light was turned on for different time durations. After the UV illumination was switched off, lipids mixing started until a new PSS was formed. Different PSSs correspond to different plasmon resonance shifts. For this particular nanorods, 1 s of UV illumination induced a

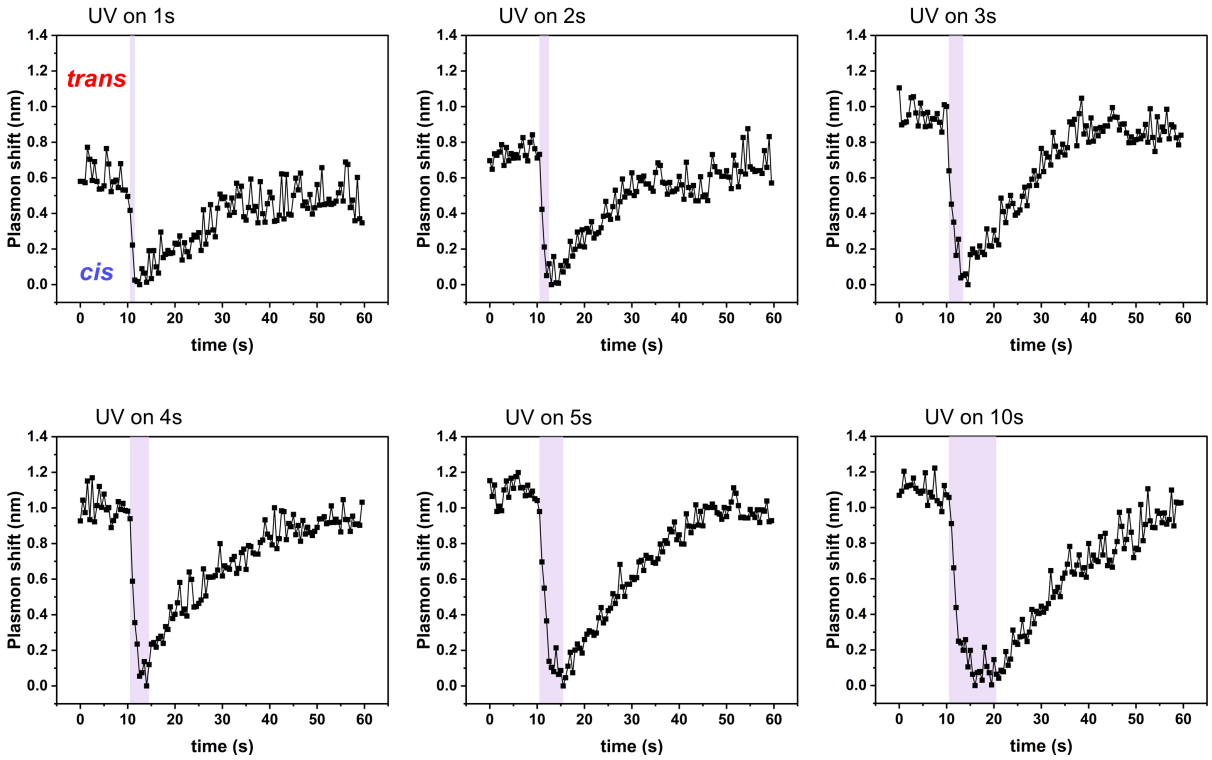

Figure 5.14: Probing photostationary state. *Azo*-**PC** SLBs covering single AuNRs were originally in *trans* state. At 10 s, UV illumination was on but lasted for different times (from 1 s to 10 s). Different PSSs were measured by analyzing the plasmon resonance shift.

plasmon shift of 0.5 nm. This shift increases to 0.7 nm for 2 s illumination, 0.9 nm for 3 s illumination and 1.0 nm for 4 s illumination. Continuing prolonging illumination time to 5 s, the shift rises to 1.1 nm. The plasmon shift does not increase anymore by a prolonged 10 s illumination, that is because all the *azo*-**PC** molecules on top of the nanorod can be switched within 5 s. The results indicate plasmonic sensors can monitor PSS change in a small area.

5.7 Plasmonic Sensing by An AuNRs Array

Another method was further explored to study membrane diffusion in large areas via an AuNR array. First, citrate-capped AuNRs were printed onto a clean substrate in a row. This takes the advantage of optical priting that nanoparticles' position can be controlled. Figure 5.15a shows a line array of 9 nanorods. *Trans-azo*-**PC** SLBs were then formed on a substrate covering the nanorod array. In this case, instead of taking a scattering spectrum of single AuNRs, a spectra image of the whole nanorod array was acquired. Figure 5.15b shows the spectra information of 9 nanorods in Figure 5.15a, where the x-axis of the image represents wavelength, y-axis represents the position of nanorods and brightness displays scattering intensity. From this spectra image, the scattering spectrum of each nanorod can be extracted, so that plasmon resonances were obtained. By taking a series of spectra images, time-resolved plasmon resonance shifts of all 9 nanorods could be analyzed at the same time.

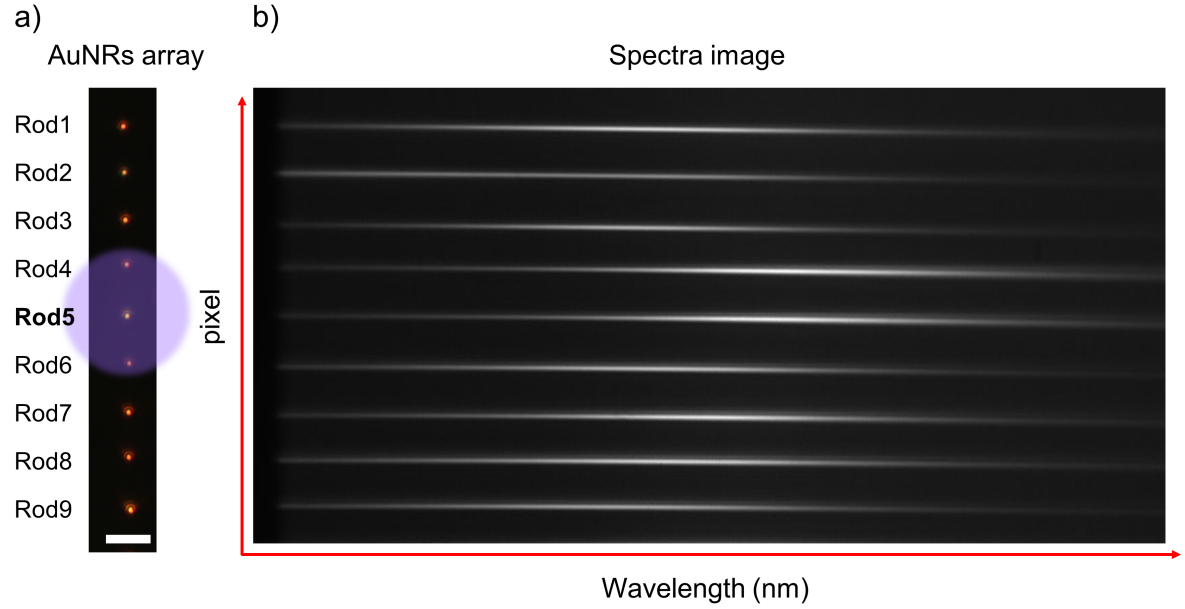

Figure 5.15: AuNRs array. (a) AuNRs array of 9 particles which were printed with a separating distance of 5 μm. UV illumination was centered on Rod5. scale bar: 5 μm. **(b)** Spectra image showing 9 spectra lines corresponding to AuNRs array. The x-axis and y-axis represent the wavelength and pixel position, respectively. The gray value of each point indicates scattering intensity. Scattering spectra of Rod1-Rod9 can be extracted from the spectra image.

Afterwards, the *azo*-**PC** membrane was illuminated by a localized UV light spot, which was

centered on Rod5. The diameter of the illumination spot was analyzed to be ~ 15 μm (Figure 5.16). That means only *azo*-**PC** bilayers covering Rod4, Rod5 and Rod6 will be directly switched to *cis* state by UV light. The switched *cis* lipids then diffuse outside of the illumination spot.

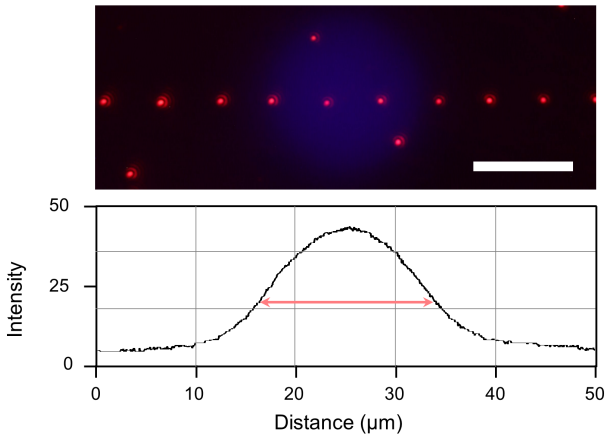

Figure 5.16: Illumination spot. The diameter of LED illumination spot was determined to be ~ 15 μm. Scale bar: 10 μm.

Once the UV light was switched on, *azo*-**PC** lipids in the illumination spot were switched and the plasmon resonance of nanorods shifted. By performing time-resolved measurements, the real-time plasmon resonance shift of AuNRs line was monitored (Figure 5.17). Rod5, at the center of the illumination spot, shows the fastest rate of plasmon shift since the illumination intensity at this position was the highest. For Rod4 and Rod 6, which were away from the illumination center by 5 μm, the plasmon shifted within 3 s. This happens due to a combination of direct switching and diffusion from Rod5. For other nanorods in the line not under the illumination spot, membrane diffusion leads to a gradual plasmon resonance shift. It was found that the rate of the plasmon shift depends on the distance between nanorods and the illumination center. This can be explained since the closer nanorods are away from illumination center, the less time is needed for switched *cis* isomers to diffuse onto the nanorods so that the plasmon resonance shifts faster. The plasmon shift of Rod3 and Rod7 at a distance of 10 μm away from the center occurs within 5 s, while for Rod1 and Rod9 which are 20 μm away from the center, the time needed is more than 10 s.

After conducting 15 time-resolved measurements on this AuNRs line, the average switching rate was calculated, as shown in Figure 5.18. The fastest rate 0.45 s^{-1} was obtained for nanorods at the center (distance 0 μm). At a distance of 5 μm, the rate was 0.30 s^{-1}. For distances above 5 μm, the rate is only determined by diffusion since the nanorods at this distance were outside of the illumination spot. In this case, a linear relationship was shown between rate and distance. This method presents the potential to calculate diffusion coefficients of *azo*-**PC** membrane in a label-free way.

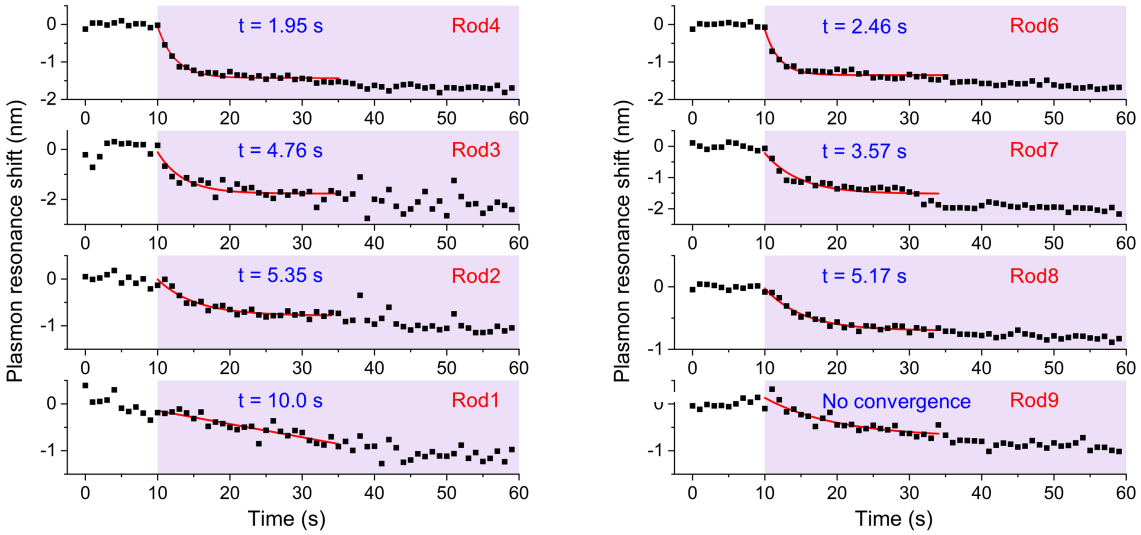

Figure 5.17: Probing diffusion by AuNRs array. Real-time plasmon resonance shift was monitored for AuNRs in the printing line. UV light was on from 10 s to 60 s. Except for Rod4 and Rod6, other rods were outside the illumination spot, for which, plasmon shifts were only affected by membrane diffusion. Plasmon shift times were calculated by fitting the curve with an exponential function.

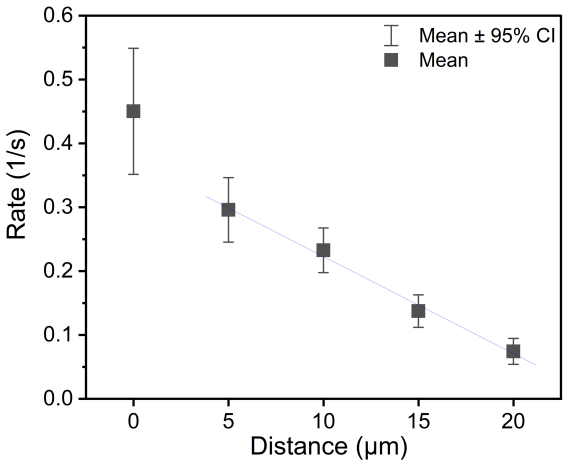

Figure 5.18: Relationship between rate and distance. The plasmon shift rate was calculated from 15 measurements. For distance above 5 μm, the rate is linearly dependent on distance since in this case the rate is only determined by membrane diffusion.

In this chapter, single AuNRs were proposed for the label-free monitoring of photolipid membrane photoisomerization in real time. In the following chapter, another label-free method based on SERS is explored.

6

Optothermal-printed AuNRs for SERS of Photolipid Bilayer Isomerization

In the previous chapter, it was shown that single AuNRs can be used as highly sensitive plasmonic probes for label-free and real-time monitoring of photoisomerization dynamics of *azo*-**PC** membranes. Its potential for the measurements of diffusion and different photostationary states of *azo*-**PC** membranes was also demonstrated. These were achieved by measuring the plasmon resonance shift. However, this does not provide any information about the chemical structure associated with conformational changes of *azo*-**PC** molecules. Plasmonic nanoantennas are also able to provide high electromagnetic field enhancements, which significantly amplify the Raman signal carrying structure information of molecules in the vicinity (SERS, Subsection 2.4.1). It has been reported that SERS can be applied for the characterization of azobenzene structure and its conformational isomerization (Subsection 2.4.3).

For the SERS measurement of *azo*-**PC** membranes, selecting an appropriate SERS substrate is critical. Among all the reported SERS substrates (Subsection 2.4.2), dense periodic nanopatterns produced by lithography or controlled deposition could hinder membrane diffusion. Nanoparticle dimers connected by scaffolds such as DNA origami may not be compatible with membrane formation. Single nanoparticles with sharp tips or edges such as nanostars, bipyramids or nanotriangles show difficulty for the membrane formation as well.

Here, a strategy is presented to reshape single AuNRs into SERS-active nano-ellipsoids

via optical printing and optical heating. These ellipsoid particles are an intermediate step of the nanorod-to-nanosphere melting process. In Section 6.1, all the steps during nanorod-to-sphere transition are introduced. The method to obtain particles in each step will also be discussed. Then in Section 6.2, SERS field enhancements in all steps of the nanorod-to-sphere transition will be compared by anylazing obtained SERS signals of *azo*-**PC** SLBs. The factor resulting in the SERS enhancement will also be presented. The obtained Raman peaks of *azo*-**PC** SLBs will be analyzed compared to that of DOPC membranes (Section 6.3). Finally, photoisomerization of *azo*-**PC** SLBs is measured by analyzing the SERS peak ratio (Section 6.4)

The results presented in this chapter are currently being prepared for publication as *"Optothermal Printing of Gold Nano-Lemons for SERS on Photolipid Bilayer Membranes"* by J. Zhang, P. Vosshage, F. Schuknecht and T. Lohmüller.

6.1 Optical Printing of Gold Nanorods

Citrate-capped AuNRs (Nanopartz Inc., Part# A12-40-650) have been used for optical printing experiments. SEM images (Figure 6.1a) show that the ends of AuNRs are semi-spherical. By analyzing SEM images, the statistics of rods' length and diameter were obtained (Figure 6.1b). The rods show an average length of 99.9 $\pm$ 5.8 nm and an average diameter of 49.6 $\pm$ 2.3 nm, corresponding to an aspect ratio of 2.0 $\pm$ 0.1. Absorption spectra were obtained with UV-vis spectroscopy, displaying a weak transverse mode at around 523 nm and a strong longitudinal mode at around 650 nm (Figure 6.1c).

For optical printing, a droplet of the nanorods solution was dispersed into the water on a clean glass substrate under the microscope (Figure 3.12). Due to electrostatic repulsion, citrate capping prevents nanorods deposition on the substrate. A continuous wave laser (wavelength 671 nm) was used for the optical printing of nanorods. The laser wavelength was chosen to match the longitudinal plasmon mode of AuNRs. As introduced in Subsection 2.3.3, two forces play a role in optical printing. The gradient force pulls the particle to the laser beam focus so that the particle could be trapped. Then the scattering force pushes the particle along the direction of the propagating light beam. The scattering force is proportional to the laser power. However, if the laser power is too low, the particle is trapped but can not be printed onto the substrate since the scattering force is not sufficient to overcome the electrostatic repulsion between AuNRs and the glass substrate. In this case, the lowest power required for a reliable printing was 2 mW (measured after the objective). With this minimum printing power 2mW, AuNRs were printed sequentially with a spatial step of 5 μm. The dark field image of the printed line is shown in Figure 6.2b. Each red spot represents single printed

AuNRs. When checked under SEM (Figure 6.2a), the nanorods retained their shapes except for the slightly sharper ends.

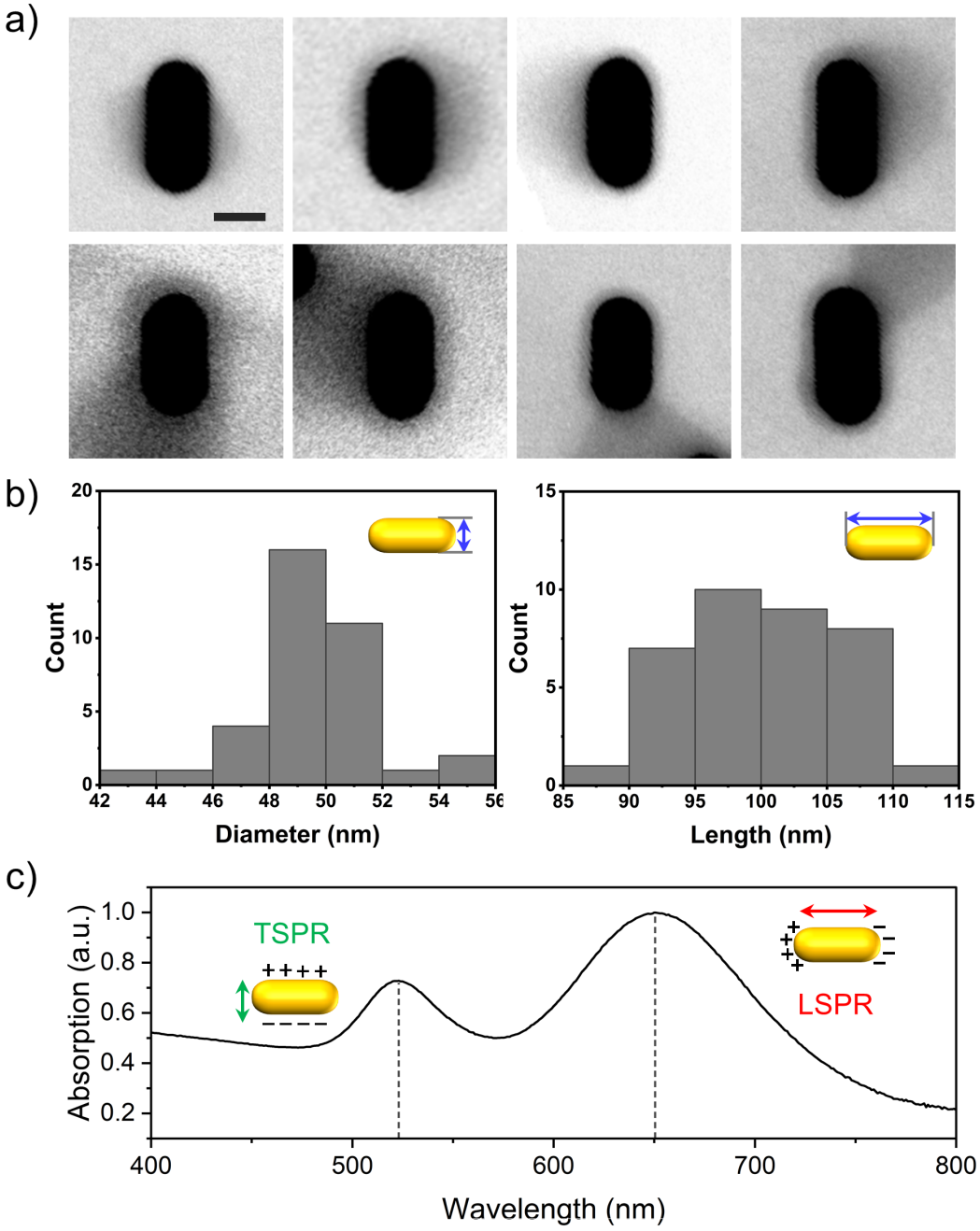

Figure 6.1: Descriptions of AuNRs used. **(a)** SEM images (Scale bar: 40 nm), **(b)** size distribution and **(c)** absorption spectrum of nanorods. Its average length and diameter are 99.9 ± 5.8 nm and 49.6 ± 2.3 nm, respectively, corresponding to an aspect ratio of 2.0 ± 0.1. The absorption spectrum exhibits a transverse mode at 523 nm and a longitudinal mode at 650 nm.

During optical printing, plasmonic heat is also generated, which can cause AuNRs reshaping and melting (Subsection 2.3.4). The results showed that even at the lowest printing power, a slight shape transformation of AuNRs can be observed. The printing power was then

increased to investigate further nanorods reshaping since more plasmonic heating could be obtained with a higher printing power. From dark field images, a color change of printed particles was observed from red spots to yellow spots and then to green spots, when gradually increasing the printing power from 2 mW to 5 mW (Figure 6.2b). This color change indicates gradual nanorods reshaping. From SEM images (Figure 6.2a), it was found that, with a laser power of 3 mW, 50 % of the printed particles presented an ellipsoid shape with sharper tips compared to the initial rods. When increasing printing power to 4 mW, even more short ellipsoid shapes were observed. At 5 mW, particles were printed as spheres with a yield of 44 %, which were identified as green spots in dark field images.

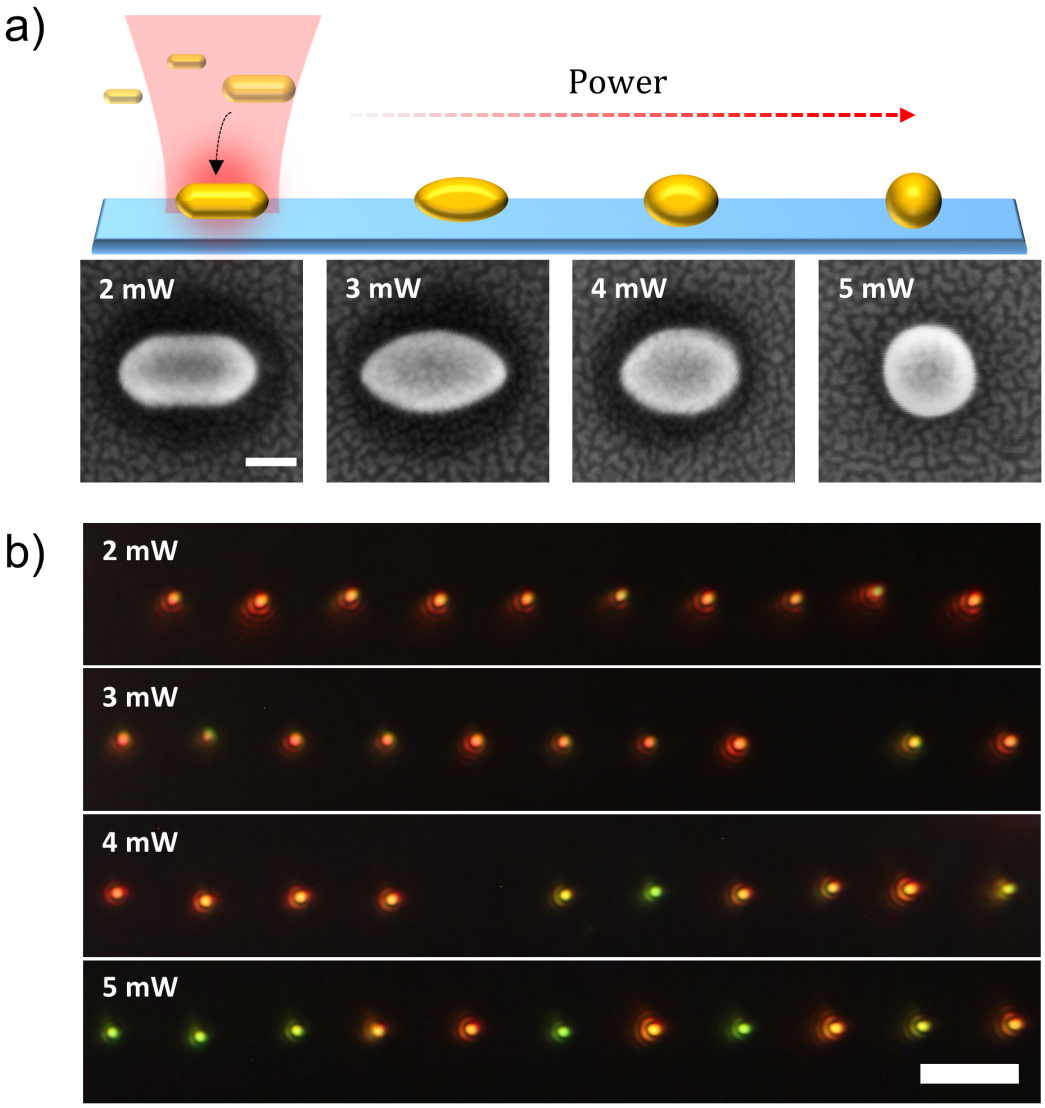

Figure 6.2: Optical printing of AuNRs with increasing laser power. (a) Schematic and SEM images of printed particles with increased printing power. Particle reshaping was observed from nanorods to nanoellipsoids, then short nanoellipsoids, and finally spheres. Scale bar: 40 nm **(b)** dark field image of printed particle lines. A color change was observed for printed spots with increased power. Scale bar: 5 μm.

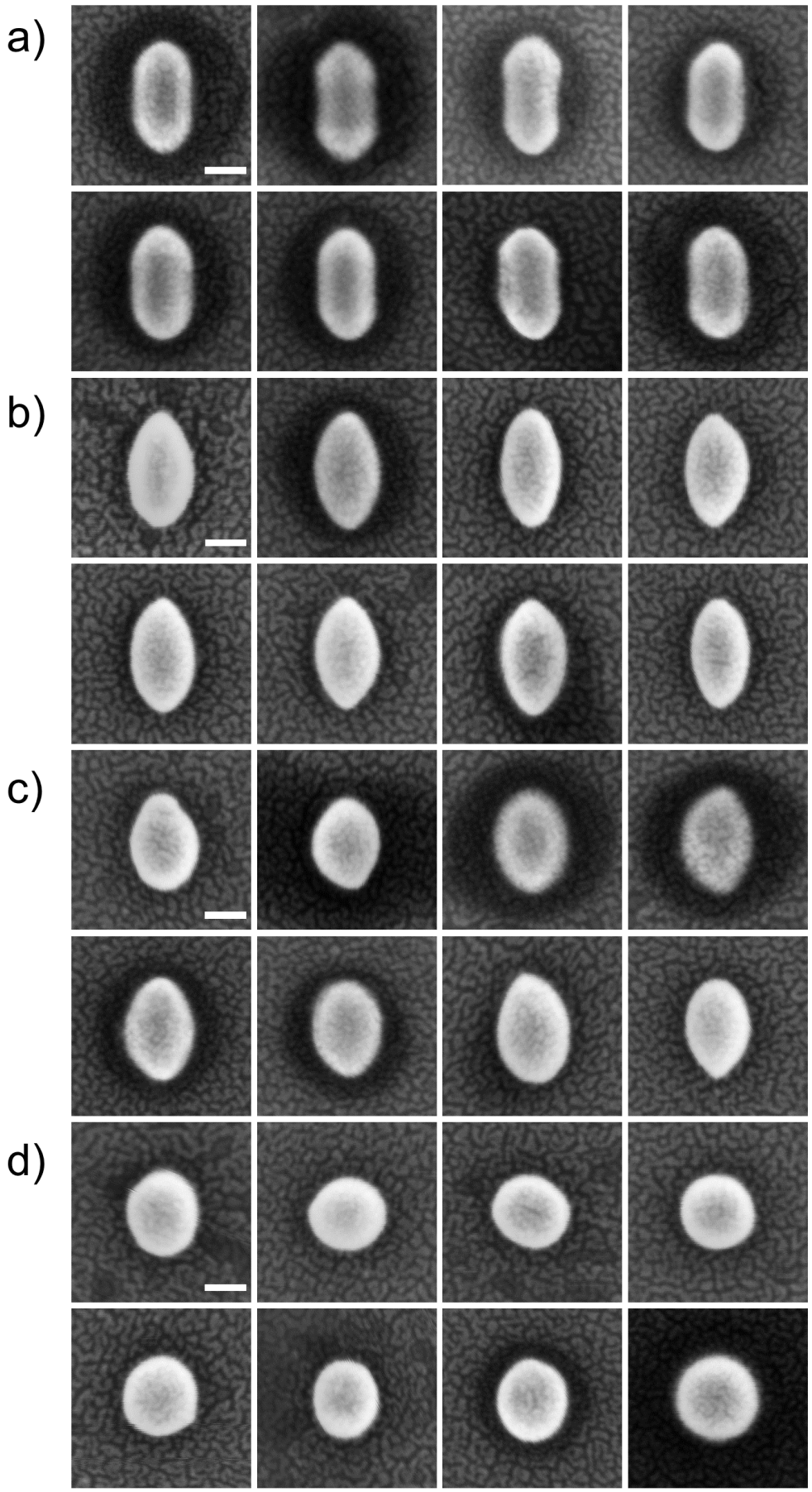

Figure 6.3: The melting process of nanorods to nanospheres. Nanorods melting include intermediate steps of **(a)** sharp-tip nanorods, **(b)** nanoellipsoids, **(c)** short nanoellipsoids to **(d)** nanospheres. Scale bar: 40 nm.

Therefore, three intermediate steps were observed during the melting process of nanorods to nanospheres, which are (1) nanorods with sharp tips, (2) nanoellipsoids (3) short nanoellipsoids (more SEM images are shown in Figure 6.3). This reshaping process is in good agreement with what was reported by Cho et al..[247] They also observed transformation from nanorods to ellipsoids by heating the nanorods sample beyond 180 °C. After heating beyond 300 °C, they also observed the melting of nanorods to nanospheres. The melting mechanism of nanorod to nanosphere has been reported by Link et.al.[156] via the analysis of TEM images, as already discussed in Subsection 2.3.4. The gereration of plasmonic heat leads to the formation of defects and twins in the interior of the rod, followed by atom diffusion from tips to the rod center. Therefore, the rods melts into a intermediate ellipsoid shape with sharped tips before fully transforming into spheres.

This transformation process is affected by nanorods' aspect ratio. For nanorods with an aspect ratio of 3.3, Gordel et al.[157] observed dumbell-shaped and banana-shaped particles. Horiguchi et al.[158] showed ϕ-shaped and bent ϕ-shaped particles during the melting of nanorods with an aspect ratio of 4.4. For longer rods with an aspect ratio of 5.5,[159,160] it was reported that controlled bending and splitting of nanorods can be achieved during optical printing. The nanorods used here have a aspect ratio of ~2, and no bending or splitting was observed. Instead, ellipsoid particles with sharpened tips were formed.

6.2 SERS on Ellipsoid Nanoparticles

Ellipsoids display a higher electromagnetic field enhancement at their ends compared to nanorods since they feature sharper tips. FDTD simulations were conducted to compare the field enhancement of a nanorod, a nanoellipsoid and a nanosphere (Figure 6.4). The simulated nanorod and ellipsoid share the same length and width, but the radius of curvature at the tip of ellipsoid is 3× smaller than that of the rod. Results showed a 2 times higher field

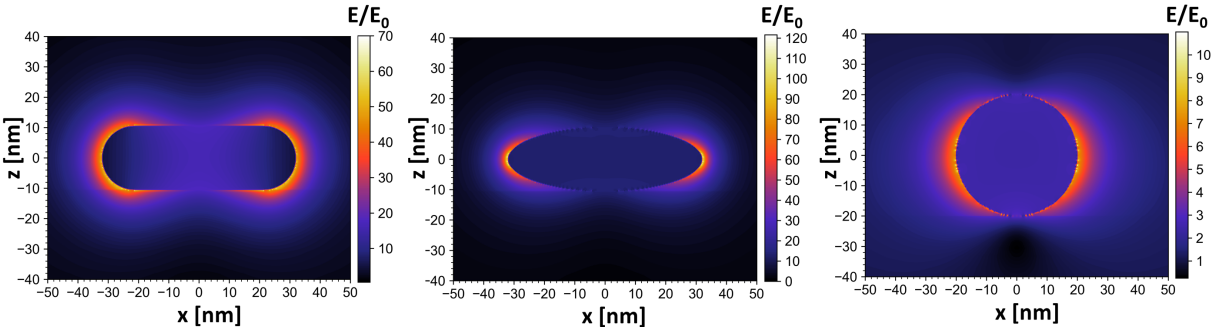

Figure 6.4: Electromagnetic field enhancement comparison between a gold nanorod, an ellipsoid, and a sphere from FDTD simulations. The length and width of the simulated rod and ellipsoid are 60 nm and 20 nm, respectively. The diameter of the sphere is 40 nm.

enhancement of the ellipsoid compared to the rod. Since the Raman signal enhancement is the fourth power of the field enhancement, the SERS intensity of such ellipsoid should increase by a factor of 16. Comparing the ellipsoid shape with a sphere, the field enhancement increased 10 times corresponding to an enhancement of SERS intensity by a factor of 10^4 (Subsection 2.4.1).

Next, SERS measurements of photolipid bilayers were performed on different particle shapes including all intermediate steps involved during the rod-to-sphere melting process. Different shapes were first printed with the respective laser power. Then the substrate with printed particles was plasma treated for 90 s so that contamination was removed and the substrate became hydrophilic for a more reliable SLB formation. Afterward, SUVs of *azo*-**PC** as well as 1×PBS solutions were added to form SLBs on particles. For control measurements, nanorods were dropcasted on a clean substrate and first dried under ambient condition to make the nanorods to adhere the substrate. SERS measurements were conducted with an integration time of 30 s and a laser power of 0.5 mW. This laser power was set to be significantly lower compared to the power required for printing so that no further melting occurs during the SERS measurement. The scattering spectra of each printed particle were also acquired in the same measurement.

For the dropcasted nanorods, only two weak Raman peaks at 1133 cm^{-1} and 1148 cm^{-1} were distinguishable (Figure 6.5a). This indicates that nanorods with spherical ends do not provide sufficient SERS due to a weak e-field at their tips. The results agree with the findings in the literature, which also showed that apherical-end-capped nanorods were not able to provide reliable SERS except for resonant molecules.[184] For the nanorods printed with 2 mW (Figure 6.5b), an improved SERS spectrum could be observed due to the sharper ends. This was also confirmed by taking the scattering spectrum. A small red-shift of plasmon resonance was observed indicating particle reshaping. The highest SERS signal was obtained on nanoellipsoids due to the highest field enhancement at sharp tips (Figure 6.5c). For the next intermediate step, short nanoellipsoids, the SERS signal intensity again decreased since particle ends experience an increase in curvatures. The scattering spectrum also showed a resonance at around 600 nm, which is off resonance with Raman excitation. This blue shift of the plasmon resonance is due to the shortening of nanorods via reshaping. Finally, no Raman was observed on a nanosphere, since the particle plasmon resonance at 555 nm was especially off resonance.

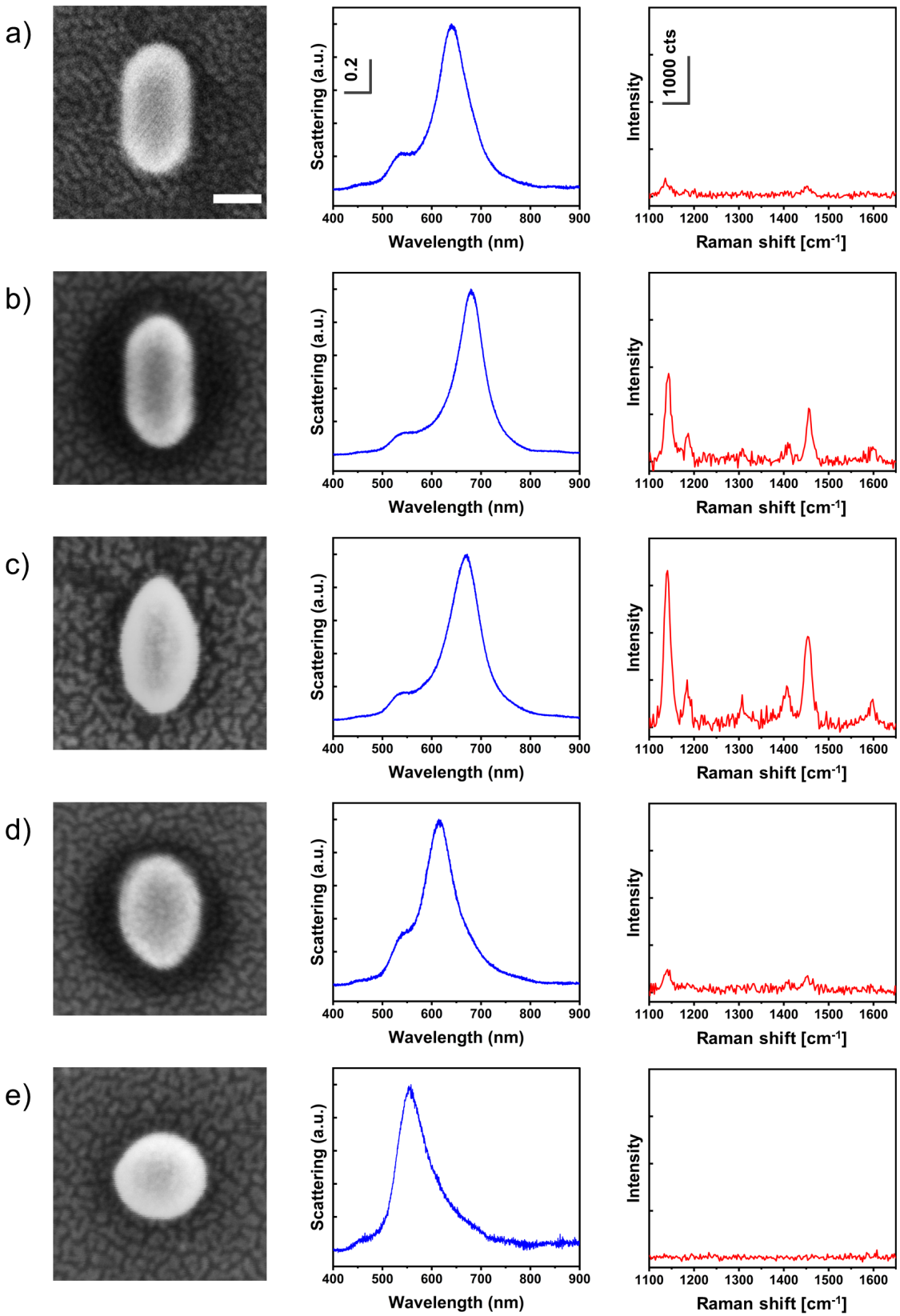

Figure 6.5: SERS spectra of photolipid membranes on **(a)** nanorods, **(b)** sharp-tip nanorods, **(c)** ellipsoids, **(d)** short ellipsoids and **(e)** spheres.

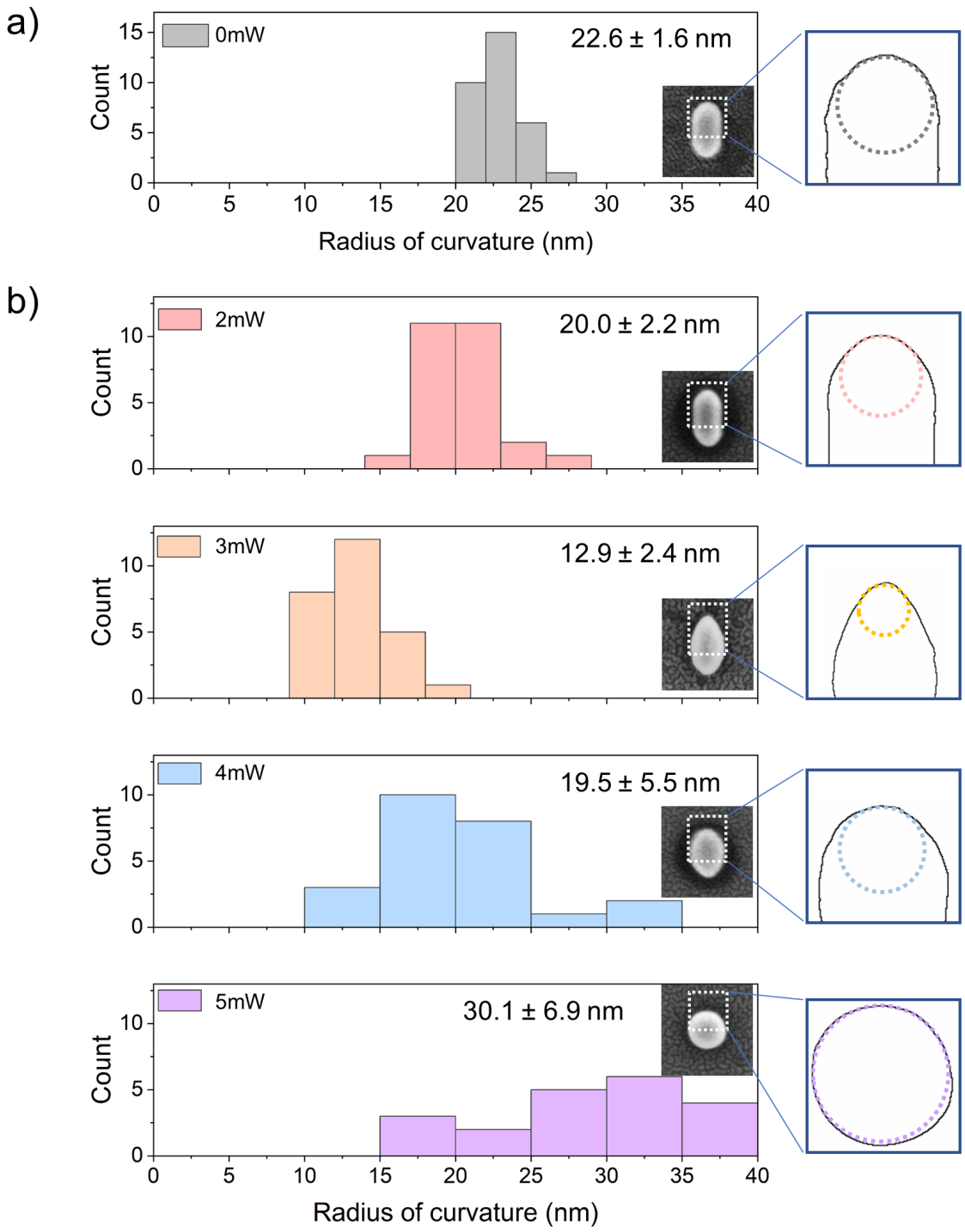

Figure 6.6: Curvature evolution of printed particles with increased laser power. The ROC is 22.6 ± 1.6 nm for deposited nanorods. When the rods are melted to ellipsoids, ROC decreases to 12.9 ± 2.4 nm. During the reshaping from ellipsoids to spheres, ROC increases to 30.1 ± 6.9 nm.

The radius of curvature (ROC) can be applied to describe the extent of sharpness for particle ends. As shown in Figure 6.6, the statistic of curvature changes during the reshaping process was analyzed. For the dropcasted rods, the average ROC was calculated to be 22.6 ± 1.6 nm.

When optical printing is performed with a laser power of 2 mW, this ROC value decreases to 20.0 ± 2.2 nm. The lowest ROC of 12.9 ± 2.4 nm was obtained for particles printed with 3 mW since most were ellipsoidal. Continually increasing the printing power, ROC started to increase again. For a printing power of 5 mW, ROC increases to 30.1 ± 6.9 nm since the rods were completely transformed to nanospheres. These ROC values are consistent with SERS enhancement. The lower the ROC, the shaper the particles' tip, and the higher was the SERS intensity. The ROC values as well as particle size changes during the rod-to-sphere melting process are shown in Table 6.1. The enhancement factor between nanorods and ellipsoids can be compared via

$$EF = \frac{I_{ellipsoid} P_{rod} N_{rod}}{I_{rod} P_{ellipsoid} N_{ellipsoid}}, \tag{6.1}$$

where P is the excitation power, which stays the same for both SERS measurements on rods and ellipsoids. I represents the obtained SERS signal intensity and N is the number of molecules that are involved in SERS, which is the molecules at the particle tips. The SERS intensity ratio $I_{ellipsoid}/I_{rod}$ was calculated by taking into account SERS intensity at peak 1133 cm^{-1} for rods and ellipsoids. The number of molecules was calculated according to

$$\frac{N_{rod}}{N_{ellipsoid}} = \frac{A_{rod}/a_{azo}}{A_{ellipsoid}/a_{azo}}, \tag{6.2}$$

with A calculated by the area of half tips determined by the ROC radius for both shapes. a_{azo} represents area of single *trans-azo*-**PC**, which was assumed to be 1 nm^2 from literature.[8] Finally, an enhancement factor of $\sim$ 13 was estimated between nanorods and ellipsoids, which is within the expected order according to the FDTD simulation.

Table 6.1: Particle size changes during nanorod-to-sphere melting process

shapes	nanorods	sharp-tip rods	ellipsoids	short ellipsoids	spheres
length (nm)	99.9 ± 5.8	110.2 ± 3.9	112.0 ± 3.0	96.8 ± 4.7	74.7 ± 3.3
width (nm)	49.6 ± 2.3	54.8 ± 1.8	61.4 ± 2.0	67.3 ± 2.3	70.2 ± 4.6
ROC (nm)	22.6 ± 1.6	20.0 ± 2.2	12.9 ± 2.4	19.5 ± 5.5	30.1 ± 6.9

6.3 SERS of Photolipid *Azo*-PC

The SERS spectrum of *trans azo*-**PC** SLBs obtained from printed ellipsoids was analyzed (Figure 6.7). Characteristic Raman peaks and corresponding mode descriptions were summarized in Table 6.2, where peaks at 1133 and 1174 cm^{-1} (CN stretching), 1316 cm^{-1} (CC in plane bending), 1399 and 1448 cm^{-1} (NN stretching and in-plane ring bending), and 1590 cm^{-1} (CC stretching) can be observed. This SERS spectrum is almost identical to azobenzene's Raman

spectrum measured in solution reported by Yoon et al..[200] However, in other reports,[197,198] the Raman peak at 1448 cm^{-1} was reported to be the central peak among a triplet peak with another two peaks at $\sim$ 1420 cm^{-1} and $\sim$ 1470 cm^{-1}. A possible reason why only one peak at 1448 cm^{-1} was obtained in this measurements is that *azo*-**PC** SLBs capped the tips of the single ellipsoid. In this case, *azo*-**PC** molecules were arranged with different orientations on the tips, where they can rotate or diffuse within the bilayer. In such works, the SERS spectrum was measured on a self-assembled monolayer of azobenzene-containing molecules, where molecules were fixed at their location and their orientation was more consistent. Another possible explanation could be that Yoon et al. performed SERS on azobenzene derivates with two alkane branches in para position of the phenyl rings, which is similar to the azoPC structure. Different linkers are expected to have an influence on the vibrational modes, which explains the good agreement between the data shown here and that reported by Yoon et al.

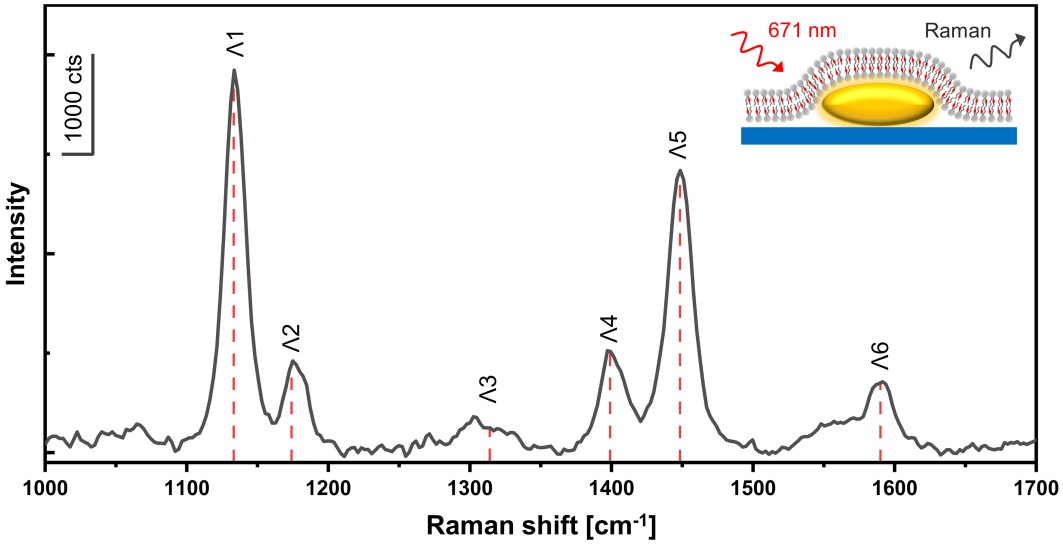

Figure 6.7: SERS spectrum of *azo*-PC bilayer. The spectrum was obtained on an optically printed ellipsoid (inset) with an integration time of 30 s and a laser power of 0.5 mW. Raman peaks at $\Lambda 1$ = 1133^{-1}, $\Lambda 2$ = 1174^{-1}, $\Lambda 3$ = 1316^{-1}, $\Lambda 4$ = 1399^{-1}, $\Lambda 5$ = 1448^{-1} and $\Lambda 6$ = 1590 cm^{-1} were observed.

Table 6.2: Raman peaks for *azo*-PC

Peaks	Raman shifts(cm^{-1})	Assignments[197,198,204]
Λ_1	1133	CN stretching
Λ_2	1174	CN stretching
Λ_3	1316	CC in plane bending
Λ_4	1399	NN stretching, in-plane ring bending
Λ_5	1448	NN stretching, in-plane ring bending
Λ_6	1590	CC stretching

Then optically printed nano-ellipsoids were applied for SERS of the DOPC bilayer. Compared to *azo*-**PC** bilayers, the SERS intensity of DOPC SLBs decreased a lot. This can explain why the Raman spectrum of *azo*-**PC** bilayers was identical to that of azobenzene molecules. The Raman scattering cross section of phospholipids is small and thus is immerged into the Raman signal of azobenzene group. The SERS spectrum of a DOPC bilayer does not overlap with the Raman spectrum of azobenzene.[248,249,250] Typical Raman peaks for DOPC lipids can be observed including peaks at 1040 cm^{-1} (CO stretching),[251] 1262 cm^{-1} (OPO asymmetric stretching)[252] and 1460 cm^{-1} (CH_2 bending).[253] However, the results demonstrate the potential of a single optical printed nano-ellipsoid for the SERS measurements of phospholipid bilayers in water.

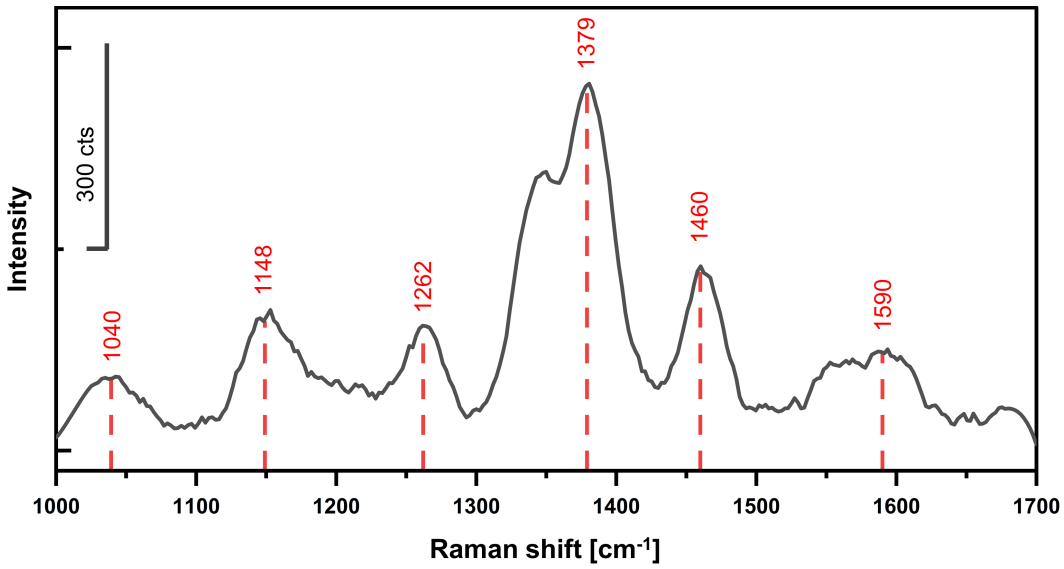

Figure 6.8: SERS spectrum of DOPC bilayer. The spectrum was obtained from an optically printed ellipsoid with an integration time of 30 s and a laser power of 0.5 mW.

Table 6.3: Raman peaks for DOPC

Peaks	Raman shifts(cm^{-1})	Assignments
Λ_1	1040	CO stretching
Λ_2	1148	CC stretching
Λ_3	1262	OPO asymmetric stretching
Λ_4	1379	–
Λ_5	1460	CH_2 bending
Λ_6	1590	CC stretching

6.4 SERS of Photolipid Bilayer Isomerization

It has been shown that high SERS enhancement of the *azo*-**PC** bilayer can be obtained with a single nano-ellipsoid. Next, I tried to investigate photoisomerization of *azo*-**PC** by monitoring SERS spectral changes. The *azo*-**PC** SLB covering the ellipsoid was switched back and forth between *trans* and *cis* states by illumination of UV and blue light sequentially for 5 min. In literature, reversible changes of peak ratio between 1420 and 1450 cm^{-1} were reported due to azobenzene isomerization. In my case, the peak at 1420 cm^{-1} was not observed for *azo*-**PC** bilayers. However, a reversible change of signal intensity at 1448 cm^{-1} normalized to 1133 cm^{-1} was detected. As shown in Figure 6.9, when switched from *trans* to *cis* state, the peak intensity at 1448 cm^{-1} increased by 15 %. As already discussed, the membrane thickness of *azo*-**PC** bilayers is reduced by $\sim$ 17 % (from 4.2 nm to 3.5 nm)[12] in 1x PBS solutions when switched from *trans* to *cis* PSS. This means the *cis*-adapted *azo*-**PC** SLBs are closer to the surface of ellipsoid particles so that stronger enhancement for NN stretching mode (1448 cm^{-1}) can be observed.

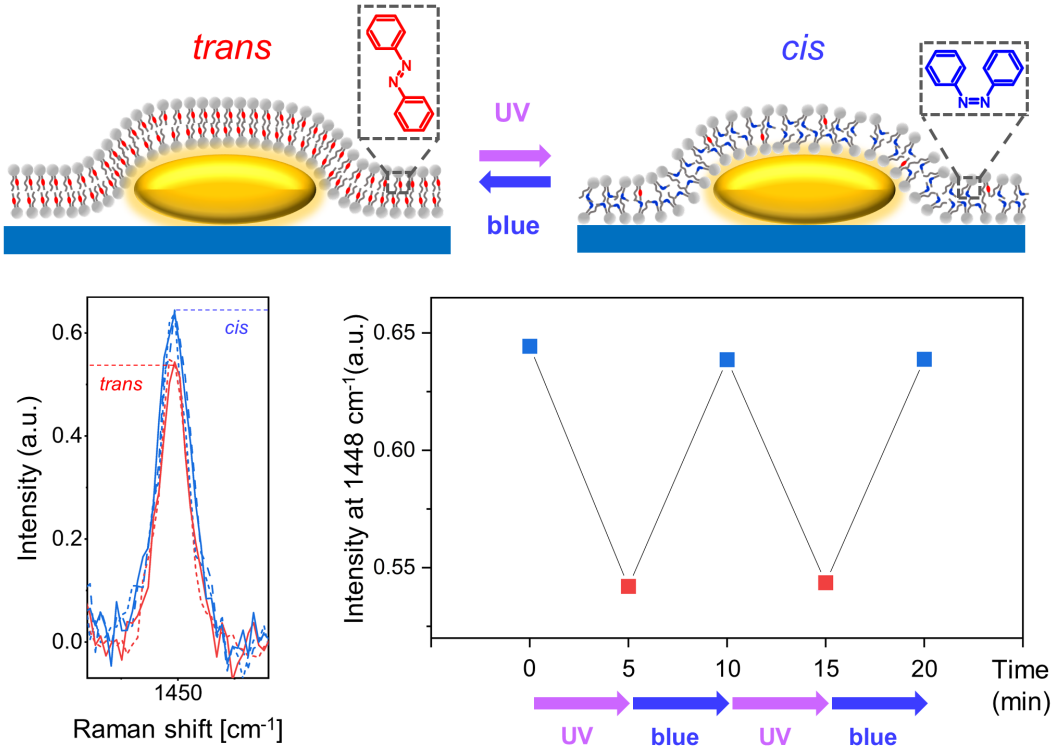

Figure 6.9: Analysis of *azo*-PC photoisomerization via SERS on an ellipsoid. Top: schematic of *azo*-**PC** SLBs photoisomerization on printed ellipsoid. Bottom: Reversible intensity changes at peak 1448 cm^{-1} (normalized to 1133 cm^{-1}) was observed due to *azo*-**PC** SLBs photo-switching.

A control measurement of *azo*-**PC** SLB SERS was performed on a gold nanoparticle aggregate to verify the consistency of the results. This aggregate was formed by printing multiple

AuNPs (diameter of 100 nm) at the same position with the laser beam. The shape of this printed aggregate is irregular, as shown in the inset of Figure 6.10. An *azo*-**PC** SLB was formed on top and the SERS spectrum was measured with the same integration time of 30 s and laser power of 0.5 mW. The obtained SERS spectrum is exactly the same as the one obtained from the printed ellipsoid, which confirms that the SERS spectra are characteristic of the *azo*-**PC** membrane. After switching the *azo*-**PC** SLB by illuminating with blue light for 5 min, the SERS spectrum at *cis* PSS was acquired. An intensity increasing at 1448 cm^{-1} was observed in *cis* PSS compared to in *trans* PSS, which remains the same as measured on the printed ellipsoid. This control measurement confirms the reliability of optothermally printed nanoellipsoids for the detection of *azo*-**PC** bilayer membrane as well as its pfotoisomerization via SERS.

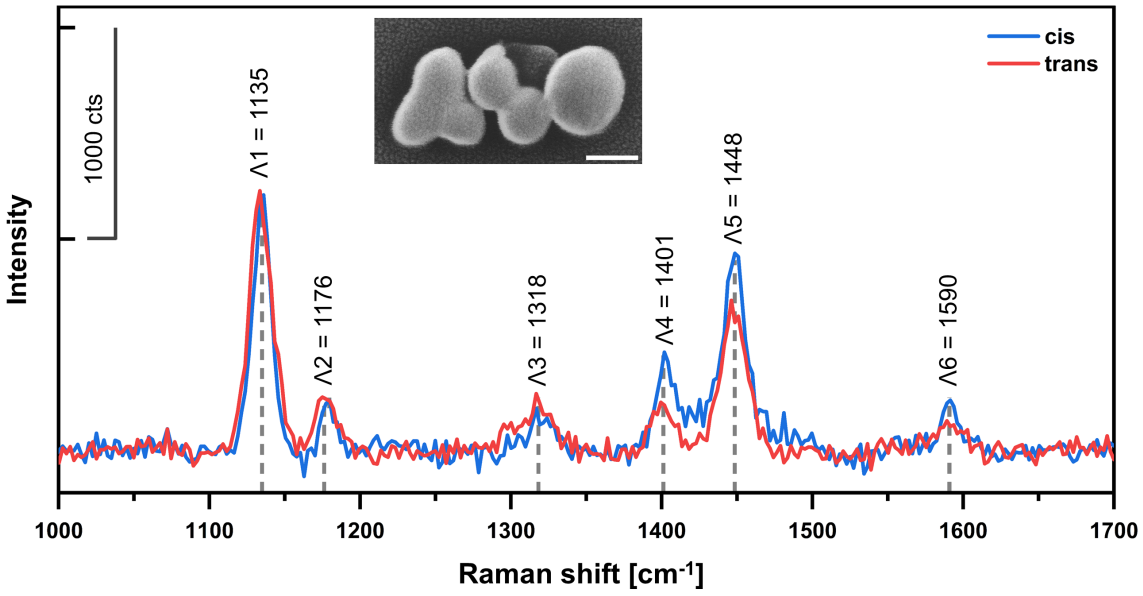

Figure 6.10: Analysis of *azo*-PC photoisomerization via SERS on aggregates. Inset: The undefined nanoparticle aggregate was formed by optical printing. Scale bar: 40 nm. The Raman peaks of trans *azo*-**PC** SLBs measured with this aggregates (red line) are the same as that obtained with printed nano-ellipsoids. When switched to *cis* PSS (blue line), the intensity at peak 1448 cm^{-1} increased.

In this chapter, I successfully developed an method to conduct SERS of *azo*-**PC** bilayer membranes on gold ellipsoids. The gold ellipsoids with sharp ends were generated by optothermally printing, which also enables the SERS measurement of photolipid bilayer isomerization.

7

Conclusions and Outlook

The main aim of this thesis was to use single gold nanoparticles for the label-free and sensitive monitoring of photoisomerization of *azo*-**PC** bilayer membranes at nm scale. Based on this, I successfully developed two methods including single-nanorod plasmonic sensing and SERS on single optothermal-printed nanoellipsoid. The conducted experiments and obtained results are summarized in the following and a brief outlook is given.

In Chapter 4, the interactions between photolipid *azo*-**PC** and dye-labeled lipids were investigated. Dyes are usually applied to image *azo*-**PC** membranes and analyze membrane diffusivity, but the effects of dyes on *azo*-**PC** are typically neglected. By doping different dye-labeled lipids including Rhodamine, Texas Red, Nile blue, methylene blue and Atto633 into photolipid bilayer membranes, fast *cis*-to-*trans* isomerization of *azo*-**PC** can be triggered by illumination of different wavelengths from green to red light, which is not efficient without dye doping. Switching by direct illumination with UV and blue light shows disadvantages in poor penetration depth and biotoxicity, which hinder the biomedical application of *azo*-**PC**. With a small amount of dye doping (1 mol %), this limitation can be overcome. On the other hand, I found the fluorescence intensity of dyes can be controlled by *azo*-**PC** states. For dyes like Rho, their fluorescence can be turned off by *cis azo*-**PC**. In addition, for triplet sensitizers such as MB that are prone to degradation, *cis azo*-**PC** can protect them from photobleaching by oxygen. The results offer different perspectives on the application of photolipids together with dyes in biological systems. Based on the results, I also demonstrated the downsides to use dyes and the necessity to explore label-free methods for the study of *azo*-**PC** photoisomerization.

In Chapter 5, single gold nanorods were applied for the label-free and time-resolved monitoring of *azo*-**PC** SLB photoisomerization. It was shown time-resolved photoswitching of *azo*-**PC** SLBs can be monitored by continuing detecting the plasmon shift over time. Used nanorods were capped by a CTAB layer, which set distance between nanorods' surface and formed *azo*-**PC** SLBs. this CTAB layer can be removed by plasma treating. After removing it, a larger plasmon resonance shift was obtained indicating a higher sensitivity. By FDTD simulations, it was shown that the plasmon resonance shift can be explained by membrane thickness change and refractive index change of SLBs due to lipid density variation and azobenzene isomerization. The results open up opportunities for real-time monitoring of photoswitching process of *azo*-**PC** with plasmon nanosensors and show potentials to the measurement of membrane diffusion and photostationary state at the nanoscale.

In Chapter 6, I presented another label-free method for the detection of *azo*-**PC** SLB photoisomerization via SERS on optothermal-printed single gold nano-ellipsoid. I introduced a very simple and effective way to generate single SERS-active nano-antennae. By varying the optical printing laser power, different intermediate steps can be obtained during the nanorod-to-nanosphere reshaping process due to optical heating. Ellipsoids as one of the intermediate step showed high SERS enhancement of *azo*-**PC** SLB. By detecting the intensity change of the characteristic SERS peak that refers to N=N stretching of azobenzene group, *azo*-**PC** SLB photoisomerization can be measured.

In summary, this thesis showcases different label-free methods for the monitoring of *azo*-**PC** bilayer photoisomerization using plasmonic nanosensors with high accuracy at nm scale. These methods present promising potentials for measuring membrane diffusion and photostationary states and highlights the sensitivity of plasmonic nanoparticles for detecting molecular conformational changes, which could be used for biophysical and chemical applications. Since the proposed two methods were only applied for the study of *azo*-**PC** SLBs in this thesis, their application on *azo*-**PC** vesicles such as GUVs and even lipid nanoparticles could also be investigated which may facilitate their applications in biomedicine. Except for SERS, other IR technologies such as scanning near-field optical microscopy (SNOM)[254] could also be explored for the monitoring of *azo*-**PC** photoisomerization.

References

[1] Johannes Morstein, Anna C. Impastato, and Dirk Trauner. "Photoswitchable lipids." In: *ChemBioChem* 22.1 (2021), pp. 73–83. DOI: 10.1002/cbic.202000449 (cited on pages vii, ix).

[2] Larissa Socrier and Claudia Steinem. "Photo-Lipids: Light-Sensitive Nano-Switches to Control Membrane Properties." In: *ChemPlusChem* 88.11 (2023), e202300203. DOI: 10.1002/cplu.202300203 (cited on pages vii, ix).

[3] Noemi Jiménez-Rojo, Suihan Feng, Johannes Morstein, Stefanie D. Pritzl, Takeshi Harayama, Antonino Asaro, Nynke A. Vepřek, Christopher J. Arp, Martin Reynders, and Alexander J. E. Novak. "Optical control of membrane fluidity modulates protein secretion." In: *bioRxiv* (2022), pp. 2022–02. DOI: 10.1101/2022.02.14.480333 (cited on pages vii, ix, 51).

[4] Abhay Kumar, Archita Maiti, Sahil Verma, and Snehasis Daschakraborty. "How do Photoswitchable Lipids Influence the Intercalation of Anticancer Drug in Lipid Membrane? Investigation using Molecular Dynamics Simulation." In: *Chemistry–An Asian Journal* (2024), e202400416. DOI: 10.1002/asia.202400416 (cited on pages vii, ix).

[5] Archita Maiti and Snehasis Daschakraborty. "Investigating the Influence of Photoswitchable Lipids on the Structure and Dynamics of Lipid Membranes: Fundamentals and Potential Applications." In: *The Journal of Physical Chemistry B* (2024). DOI: 10.1021/acs.jpcb.4c03004 (cited on pages vii, ix).

[6] Carla Pernpeintner, James A. Frank, Patrick Urban, Christian R. Roeske, Stefanie D. Pritzl, Dirk Trauner, and Theobald Lohmüller. "Light-controlled membrane mechanics and shape transitions of photoswitchable lipid vesicles." In: *Langmuir* 33.16 (2017), pp. 4083–4089. DOI: 10.1021/acs.langmuir.7b01020 (cited on pages vii, ix, 1, 9, 14, 73).

[7] Patrick Urban, Stefanie D. Pritzl, Martina F. Ober, Christina F. Dirscherl, Carla Pernpeintner, David B. Konrad, James A. Frank, Dirk Trauner, Bert Nickel, and Theobald Lohmueller. "A lipid photoswitch controls fluidity in supported bilayer membranes." In: *Langmuir* 36.10 (2020), pp. 2629–2634. DOI: 10.1021/acs.langmuir.9b02942 (cited on pages vii, ix, 1, 9, 11–13).

[8] Stefanie D. Pritzl, Patrick Urban, Alexander Prasselsperger, David B. Konrad, James A. Frank, Dirk Trauner, and Theobald Lohmüller. "Photolipid Bilayer Permeability is Controlled by Transient Pore Formation." In: *Langmuir* 36.45 (2020), pp. 13509–13515. DOI: 10.1021/acs.langmuir.0c02229 (cited on pages vii, ix, 1, 9, 13, 96).

[9] Nisha Chander, Johannes Morstein, Jan S. Bolten, Andrej Shemet, Pieter R. Cullis, Dirk Trauner, and Dominik Witzigmann. "Optimized photoactivatable lipid nanoparticles enable red light triggered drug release." In: *Small* 17.21 (2021), p. 2008198. DOI: 10.1002/smll.202008198 (cited on pages vii, ix, 13, 51).

[10] Stefanie D. Pritzl, Johannes Morstein, Sophia Kahler, David B. Konrad, Dirk Trauner, and Theobald Lohmüller. "Postsynthetic photocontrol of giant liposomes via fusion-based photolipid doping." In: *Langmuir* 38.39 (2022), pp. 11941–11949. DOI: 10.1021/acs.langmuir.2c01685 (cited on pages vii, ix, 1).

[11] Patrick Urban, Stefanie D. Pritzl, David B. Konrad, James A. Frank, Carla Pernpeintner, Christian R. Roeske, Dirk Trauner, and Theobald Lohmüller. "Light-controlled lipid interaction and membrane Organization in Photolipid Bilayer Vesicles." In: *Langmuir* 34.44 (2018), pp. 13368–13374. DOI: 10.1021/acs.langmuir.8b03241 (cited on pages vii, ix, 1, 9, 11, 14, 66, 72, 79).

[12] Martina F. Ober, Adrian Müller-Deku, Anna Baptist, Benjamin Ajanović, Heinz Amenitsch, Oliver Thorn-Seshold, and Bert Nickel. "SAXS measurements of azobenzene lipid vesicles reveal buffer-dependent photoswitching and quantitative Z⟶ E isomerisation by X-rays." In: *Nanophotonics* 11.10 (2022), pp. 2361–2368. DOI: 10.1515/nanoph-2022-0053 (cited on pages 1, 13, 72, 79, 81, 99).

[13] Charles A. Day, Lewis J. Kraft, Minchul Kang, and Anne K. Kenworthy. "Analysis of protein and lipid dynamics using confocal fluorescence recovery after photobleaching (FRAP)." In: *Current protocols in cytometry* 62.1 (2012), pp. 2–19. DOI: 10.1002/0471142956.cy0219s62 (cited on page 2).

[14] Veronika Mueller, Alf Honigmann, Christian Ringemann, Rebecca Medda, Günter Schwarzmann, and Christian Eggeling. "FCS in STED microscopy: studying the nanoscale of lipid membrane dynamics." In: *Methods in enzymology*. Vol. 519. Elsevier, 2013, pp. 1–38. DOI: 10.1016/B978-0-12-405539-1.00001-4 (cited on page 2).

[15] Ole G. Mouritsen. *Life-as a matter of fat*. Vol. 537. Springer, 2005. DOI: 10.1007/978-3-319-22614-9 (cited on page 6).

[16] Maddalena Venturoli, Maria Maddalena Sperotto, Marieke Kranenburg, and Berend Smit. "Mesoscopic models of biological membranes." In: *Physics reports* 437.1-2 (2006), pp. 1–54. DOI: 10.1016/j.physrep.2006.07.006 (cited on page 6).

[17] Tibor Hianik. "Structure and physical properties of biomembranes and model membranes." In: *Acta Physica Slovaca* 56.6 (2006), pp. 687–805. DOI: 10.2478/v10155-010-0082-z (cited on page 6).

[18] Helen Watson. "Biological membranes." In: *Essays in biochemistry* 59 (2015), pp. 43–69. DOI: 10.1042/bse0590043 (cited on page 6).

[19] Rob Phillips, Jane Kondev, Julie Theriot, and Hernan Garcia. *Physical biology of the cell*. Garland Science, 2012. DOI: 10.1201/9781134111589 (cited on pages 6, 7).

[20] Anthony G. Lee. "Biological membranes: the importance of molecular detail." In: *Trends in biochemical sciences* 36.9 (2011), pp. 493–500. DOI: 10.1016/j.tibs.2011.06.007 (cited on page 6).

[21] Takeshi Harayama and Howard Riezman. "Understanding the diversity of membrane lipid composition." In: *Nature reviews Molecular cell biology* 19.5 (2018), pp. 281–296. DOI: 10.1038/nrm.2017.138 (cited on page 7).

[22] Yan Shi, Mingjun Cai, Lulu Zhou, and Hongda Wang. "Measurement of mechanical properties of naked cell membranes using atomic force microscope puncture test." In: *Talanta* 210 (2020), p. 120637. DOI: 10.1016/j.talanta.2019.120637 (cited on page 7).

[23] Dmitry A. Los and Norio Murata. "Membrane fluidity and its roles in the perception of environmental signals." In: *Biochimica et Biophysica Acta (BBA)-Biomembranes* 1666.1-2 (2004), pp. 142–157. DOI: 10.1016/j.bbamem.2004.08.002 (cited on page 7).

[24] Kenneth R. Feingold and Peter M. Elias. "Role of lipids in the formation and maintenance of the cutaneous permeability barrier." In: *Biochimica et Biophysica Acta (BBA)-Molecular and Cell Biology of Lipids* 1841.3 (2014), pp. 280–294. DOI: 10.1016/j.bbalip.2013.11.007 (cited on page 7).

[25] Dennis Chapman. "Phase transitions and fluidity characteristics of lipids and cell membranes." In: *Quarterly reviews of biophysics* 8.2 (1975), pp. 185–235. DOI: 10.1017/S0033583500001797 (cited on page 7).

[26] Peter Overath, Lutz Thilo, and Hermann Träuble. "Lipid phase transitions and membrane function." In: *Trends in Biochemical Sciences* 1.3 (1976), pp. 186–189. DOI: 10.1016/0968-0004(76)90204-8 (cited on page 7).

[27] James H. Hurley. "Membrane binding domains." In: *Biochimica et Biophysica Acta (BBA)-Molecular and Cell Biology of Lipids* 1761.8 (2006), pp. 805–811. DOI: 10.1016/j.bbalip.2006.02.020 (cited on page 7).

[28] Sushmita Mukherjee and Frederick R. Maxfield. "Role of membrane organization and membrane domains in endocytic lipid trafficking." In: *Traffic* 1.3 (2000), pp. 203–211. DOI: 10.1034/j.1600-0854.2000.010302.x (cited on page 7).

[29] Arthur A. Spector and Mark A. Yorek. "Membrane lipid composition and cellular function." In: *Journal of lipid research* 26.9 (1985), pp. 1015–1035. DOI: 10.1016/S0022-2275(20)34276-0 (cited on page 7).

[30] Andreas Blicher, Katarzyna Wodzinska, Matthias Fidorra, Mathias Winterhalter, and Thomas Heimburg. "The temperature dependence of lipid membrane permeability, its quantized nature, and the influence of anesthetics." In: *Biophysical journal* 96.11 (2009), pp. 4581–4591. DOI: 10.1016/j.bpj.2009.01.062 (cited on page 7).

[31] Miglena I. Angelova, Anne-Florence Bitbol, Michel Seigneuret, Galya Staneva, Atsuji Kodama, Yuka Sakuma, Toshihiro Kawakatsu, Masayuki Imai, and Nicolas Puff. "pH sensing by lipids in membranes: The fundamentals of pH-driven migration, polarization and deformations of lipid bilayer assemblies." In: *Biochimica et Biophysica Acta (BBA)-Biomembranes* 1860.10 (2018), pp. 2042–2063. DOI: 10.1016/j.bbamem.2018.02.026 (cited on page 7).

[32] Geoffrey M. Geise, Harrison J. Cassady, Donald R. Paul, Bruce E. Logan, and Michael A. Hickner. "Specific ion effects on membrane potential and the permselectivity of ion exchange membranes." In: *Physical Chemistry Chemical Physics* 16.39 (2014), pp. 21673–21681. DOI: 10.1039/C4CP03076A (cited on page 7).

[33] Shadeeb Hossain and Ahmed Abdelgawad. "Analysis of membrane permeability due to synergistic effect of controlled shock wave and electric field application." In: *Electromagnetic biology and medicine* 39.1 (2020), pp. 20–29. DOI: 10.1080/15368378.2019.1706553 (cited on page 7).

[34] Junya Fujimori, Yasuo Yoshihashi, Etsuo Yonemochi, and Katsuhide Terada. "Application of Eudragit RS to thermo-sensitive drug delivery systems: II. Effect of temperature on drug permeability through membrane consisting of Eudragit RS/PEG 400 blend polymers." In: *Journal of controlled release* 102.1 (2005), pp. 49–57. DOI: 10.1016/j.jconrel.2004.09.027 (cited on page 7).

[35] Gülay Bayramoğlu and M. Yakup Arıca. "A novel pH sensitive porous membrane carrier for various biomedical applications based on pHEMA/chitosan: Preparation and its drug release characteristics." In: vol. 203. Wiley Online Library, 2003, pp. 213–218. DOI: 10.1002/masy.200351321 (cited on page 7).

[36] G. Spencer Hartley. "The cis-form of azobenzene." In: *Nature* 140.3537 (1937), pp. 281–281. DOI: 10.1038/140281a0 (cited on page 7).

[37] H. M. Dhammika Bandara and Shawn C. Burdette. "Photoisomerization in different classes of azobenzene." In: *Chemical Society Reviews* 41.5 (2012), pp. 1809–1825. DOI: 10.1039/C1CS15179G (cited on page 8).

[38] Hermann Rau and Erik Lueddecke. "On the rotation-inversion controversy on photoisomerization of azobenzenes. Experimental proof of inversion." In: *Journal of the American Chemical Society* 104.6 (1982), pp. 1616–1620. DOI: 10.1021/ja00370a028 (cited on page 8).

[39] V. Marturano, V. Ambrogi, N. A. G. Bandeira, B. Tylkowski, M. Giamberini, and P. Cerruti. "Modeling of azobenzene-based compounds." In: *Physical Sciences Reviews* 2.11 (2017). DOI: 10.1515/psr-2017-0138 (cited on page 8).

[40] Thomas Schultz, Jason Quenneville, Benjamin Levine, Alessandro Toniolo, Todd J. Martínez, Stefan Lochbrunner, Michael Schmitt, James P. Shaffer, Marek Z. Zgierski, and Albert Stolow. "Mechanism and dynamics of azobenzene photoisomerization." In: *Journal of the American Chemical Society* 125.27 (2003), pp. 8098–8099. DOI: 10.1021/ja021363x (cited on page 8).

[41] H. Satzger, S. Spörlein, C. Root, J. Wachtveitl, W. Zinth, and P. Gilch. "Fluorescence spectra of trans-and cis-azobenzene–emission from the Franck–Condon state." In: *Chemical physics letters* 372.1-2 (2003), pp. 216–223. DOI: 10.1016/S0009-2614(03)00364-6 (cited on page 8).

[42] Tatsuya Fujino and Tahei Tahara. "Picosecond time-resolved Raman study of trans-azobenzene." In: *The Journal of Physical Chemistry A* 104.18 (2000), pp. 4203–4210. DOI: 10.1021/jp992757m (cited on page 8).

[43] Christina R. Crecca and Adrian E. Roitberg. "Theoretical study of the isomerization mechanism of azobenzene and disubstituted azobenzene derivatives." In: *The Journal of Physical Chemistry A* 110.26 (2006), pp. 8188–8203. DOI: 10.1021/jp057413c (cited on page 8).

[44] Josep Casellas, Michael J. Bearpark, and Mar Reguero. "Excited-State Decay in the Photoisomerisation of Azobenzene: A New Balance between Mechanisms." In: *ChemPhysChem* 17.19 (2016), pp. 3068–3079. DOI: 10.1002/cphc.201600502 (cited on page 8).

[45] Alessandro Cembran, Fernando Bernardi, Marco Garavelli, Laura Gagliardi, and Giorgio Orlandi. "On the mechanism of the cis– trans isomerization in the lowest electronic states of azobenzene: S0, S1, and T1." In: *Journal of the American Chemical Society* 126.10 (2004), pp. 3234–3243. DOI: 10.1021/ja038327y (cited on pages 8, 20, 21, 65).

[46] Tatsuya Fujino, Sergei Yu Arzhantsev, and Tahei Tahara. "Femtosecond time-resolved fluorescence study of photoisomerization of trans-azobenzene." In: *The Journal of Physical Chemistry A* 105.35 (2001), pp. 8123–8129. DOI: 10.1021/jp0110713 (cited on page 8).

[47] Yao Xiong and Olga Kuksenok. "Photocontrol of pattern formation and hysteresis loops in polymer gels with host-guest interactions." In: *Iscience* 25.12 (2022). DOI: 10.1016/j.isci.2022.105606 (cited on page 8).

[48] Satoshi Kawata and Yoshimasa Kawata. "Three-dimensional optical data storage using photochromic materials." In: *Chemical reviews* 100.5 (2000), pp. 1777–1788. DOI: 10.1021/cr980073p (cited on page 8).

[49] Rainer Hagen and Thomas Bieringer. "Photoaddressable polymers for optical data storage." In: *Advanced Materials* 13.23 (2001), pp. 1805–1810. DOI: 10.1002/1521-4095(200112)13:23<1805::AID-ADMA1805>3.0.CO;2-V (cited on page 8).

[50] Denis Gindre, Alex Boeglin, Alain Fort, Loïc Mager, and Kokou D. Dorkenoo. "Rewritable optical data storage in azobenzene copolymers." In: *Optics Express* 14.21 (2006), pp. 9896–9901. DOI: 10.1364/OE.14.009896 (cited on page 8).

[51] Rola H. El Halabieh, Ozzy Mermut, and Christopher J. Barrett. "Using light to control physical properties of polymers and surfaces with azobenzene chromophores." In: *Pure and applied chemistry* 76.7-8 (2004), pp. 1445–1465. DOI: 10.1351/pac200476071445 (cited on page 8).

[52] Elango Hrishikesan, Chinnusamy Saravanan, and Palaninathan Kannan. "Bis-triazole-appended azobenzene chromophore for selective sensing of copper (II) ion." In: *Industrial and engineering chemistry research* 50.13 (2011), pp. 8225–8229. DOI: 10.1021/ie200548j (cited on page 8).

[53] Ozge Mermut and Christopher J. Barrett. "Stable sensor layers self-assembled onto surfaces using azobenzene-containing polyelectrolytes." In: *Analyst* 126.11 (2001), pp. 1861–1865. DOI: 10.1039/B105015J (cited on page 8).

[54] Zahid Mahimwalla, Kevin G. Yager, Jun-ichi Mamiya, Atsushi Shishido, Arri Priimagi, and Christopher J. Barrett. "Azobenzene photomechanics: prospects and potential applications." In: *Polymer bulletin* 69 (2012), pp. 967–1006. DOI: 10.1007/s00289-012-0792-0 (cited on page 8).

[55] Oleksandr S. Bushuyev, Thomas A. Singleton, and Christopher J. Barrett. "Fast, reversible, and general photomechanical motion in single crystals of various azo compounds using visible light." In: *Advanced Materials* 25.12 (2013), pp. 1796–1800. DOI: 10.1002/adma.201204831 (cited on page 8).

[56] Jing Sun, Fan Wang, Hongjie Zhang, and Kai Liu. "Azobenzene-Based Photomechanical Biomaterials." In: *Advanced NanoBiomed Research* 1.9 (2021), p. 2100020. DOI: 10.1002/anbr.202100020 (cited on page 8).

[57] Kevin G. Yager and Christopher J. Barrett. "Azobenzene polymers as photomechanical and multifunctional smart materials." In: (2007). DOI: 10.1039/9781847558008-00424 (cited on page 8).

[58] Eric Verploegen, Johannes Soulages, Mariel Kozberg, Tejia Zhang, Gareth McKinley, and Paula Hammond. "Reversible Switching of the Shear Modulus of Photoresponsive Liquid-Crystalline Polymers." In: *Angewandte Chemie International Edition* 48.19 (2009), pp. 3494–3498. DOI: 10.1002/anie.200900583 (cited on page 8).

[59] Maria-Melanie Russew and Stefan Hecht. "Photoswitches: from molecules to materials." In: *Advanced Materials* 22.31 (2010), pp. 3348–3360. DOI: 10.1002/adma.200904102 (cited on page 8).

[60] Jinze Li, Li Ma, Guangxin Chen, Zheng Zhou, and Qifang Li. "A high water-content and high elastic dual-responsive polyurethane hydrogel for drug delivery." In: *Journal of materials chemistry B* 3.42 (2015), pp. 8401–8409. DOI: 10.1039/C5TB01702E (cited on page 8).

[61] Adrianne M. Rosales, Kelly M. Mabry, Eric Michael Nehls, and Kristi S. Anseth. "Photoresponsive elastic properties of azobenzene-containing poly (ethylene-glycol)-based hydrogels." In: *Biomacromolecules* 16.3 (2015), pp. 798–806. DOI: 10.1021/bm501710e (cited on page 8).

[62] Lei Zhang, Sourav Maity, Kai Liu, Qing Liu, Robert Göstl, Giuseppe Portale, Wouter H. Roos, and Andreas Herrmann. "Nematic DNA thermotropic liquid crystals with photoresponsive mechanical properties." In: *Small* 13.34 (2017), p. 1701207. DOI: 10.1002/smll.201701207 (cited on page 8).

[63] Tomiki Ikeda, Makoto Nakano, Yanlei Yu, Osamu Tsutsumi, and Akihiko Kanazawa. "Anisotropic bending and unbending behavior of azobenzene liquid-crystalline gels by light exposure." In: *Advanced Materials* 15.3 (2003), pp. 201–205. DOI: 10.1002/adma.200390045 (cited on page 8).

[64] Yu Yanlei, N. Makoto, and I. Tomiki. "Photomechanics: Directed bending of a polymer film by light." In: *Nature* 425 (2003), p. 145. DOI: 10.1038/425145a (cited on page 8).

[65] Thorsten Hugel, Nolan B. Holland, Anna Cattani, Luis Moroder, Markus Seitz, and Hermann E. Gaub. "Single-molecule optomechanical cycle." In: *Science* 296.5570 (2002), pp. 1103–1106. DOI: 10.1126/science.1069856 (cited on page 8).

[66] Nolan B. Holland, Thorsten Hugel, Gregor Neuert, Anna Cattani-Scholz, Christian Renner, Dieter Oesterhelt, Luis Moroder, Markus Seitz, and Hermann E. Gaub. "Single molecule force spectroscopy of azobenzene polymers: switching elasticity of single photochromic macromolecules." In: *Macromolecules* 36.6 (2003), pp. 2015–2023. DOI: 10.1021/ma021139s (cited on page 8).

[67] Aleksandr Kravchenko, Andriy Shevchenko, Victor Ovchinnikov, Arri Priimagi, and Matti Kaivola. "Optical Interference Lithography Using Azobenzene-Functionalized Polymers for Micro-and Nanopatterning of Silicon." In: *Advanced materials* 23.36 (2011), pp. 4174–4177. DOI: 10.1002/adma.201101888 (cited on page 8).

[68] Takashi Fukuda, Kimio Sumaru, Tatsumi Kimura, Hiro Matsuda, Yoshihito Narita, Tsutomu Inoue, and Fuminori Sato. "Observation of optical near-field as photo-induced surface relief formation." In: *Japanese Journal of Applied Physics* 40.8B (2001), p. L900. DOI: 10.1143/JJAP.40.L900 (cited on page 8).

[69] Andrew A. Beharry and G. Andrew Woolley. "Azobenzene photoswitches for biomolecules." In: *Chemical Society Reviews* 40.8 (2011), pp. 4422–4437. DOI: 10.1039/C1CS15023E (cited on page 8).

[70] Sebastian Spörlein, Heiko Carstens, Helmut Satzger, Christian Renner, Raymond Behrendt, Luis Moroder, Paul Tavan, Wolfgang Zinth, and Josef Wachtveitl. "Ultrafast spectroscopy reveals subnanosecond peptide conformational dynamics and validates molecular dynamics simulation." In: *Proceedings of the National Academy of Sciences* 99.12 (2002), pp. 7998–8002. DOI: 10.1073/pnas.122238799 (cited on pages 8, 76).

[71] Fuzhong Zhang, Arash Zarrine-Afsar, M. Sameer Al-Abdul-Wahid, R. Scott Prosser, Alan R. Davidson, and G. Andrew Woolley. "Structure-based approach to the photocontrol of protein folding." In: *Journal of the American Chemical Society* 131.6 (2009), pp. 2283–2289. DOI: 0.1021/ja807938v (cited on page 8).

[72] Benno Schierling, Ann-Josée Noël, Wolfgang Wende, Le Thi Hien, Eugeny Volkov, Elena Kubareva, Tatiana Oretskaya, Michael Kokkinidis, Andreas Römpp, and Bernhard Spengler. "Controlling the enzymatic activity of a restriction enzyme by light." In: *Proceedings of the National Academy of Sciences* 107.4 (2010), pp. 1361–1366. DOI: 10.1073/pnas.090944410 (cited on page 8).

[73] Mahmoudreza Doroudgar, Johannes Morstein, Johanna Becker-Baldus, Dirk Trauner, and Clemens Glaubitz. "How photoswitchable lipids affect the order and dynamics of lipid bilayers and embedded proteins." In: *Journal of the American Chemical Society* 143.25 (2021), pp. 9515–9528. DOI: 10.1021/jacs.1c03524 (cited on page 8).

[74] James Allen Frank, Henri G. Franquelim, Petra Schwille, and Dirk Trauner. "Optical control of lipid rafts with photoswitchable ceramides." In: *Journal of the American Chemical Society* 138.39 (2016), pp. 12981–12986. DOI: 10.1021/jacs.6b07278 (cited on page 8).

[75] Luckner Ulysse, Juanita Cubillos, and Jean Chmielewski. "Photoregulation of cyclic peptide conformation." In: *Journal of the American Chemical Society* 117.32 (1995), pp. 8466–8467. DOI: 10.1021/ja00137a023 (cited on page 8).

[76] G. Andrew Woolley. "Photocontrolling peptide α helices." In: *Accounts of chemical research* 38.6 (2005), pp. 486–493. DOI: 10.1021/ar040091v (cited on page 8).

[77] Chikara Dohno, Shin-nosuke Uno, and Kazuhiko Nakatani. "Photoswitchable molecular glue for DNA." In: *Journal of the American Chemical Society* 129.39 (2007), pp. 11898–11899. DOI: 10.1021/ja074325s (cited on page 8).

[78] Mingzhe Liu, Hiroyuki Asanuma, and Makoto Komiyama. "Azobenzene-tethered T7 promoter for efficient photoregulation of transcription." In: *Journal of the American Chemical Society* 128.3 (2006), pp. 1009–1015. DOI: 10.1021/ja055983k (cited on page 8).

[79] Oruganti Srinivas, Nivedita Mitra, Avadhesha Surolia, and Narayanaswamy Jayaraman. "Photoswitchable multivalent sugar ligands: synthesis, isomerization, and lectin binding studies of azobenzene–glycopyranoside derivatives." In: *Journal of the American Chemical Society* 124.10 (2002), pp. 2124–2125. DOI: 10.1021/ja0173066 (cited on page 8).

[80] Oruganti Srinivas, Nivedita Mitra, Avadhesha Surolia, and Narayanaswamy Jayaraman. "Photoswitchable cluster glycosides as tools to probe carbohydrate–protein interactions: synthesis and lectin-binding studies of azobenzene containing multivalent sugar ligands." In: *Glycobiology* 15.9 (2005), pp. 861–873. DOI: 10.1093/glycob/cwi069 (cited on page 8).

[81] Charles Tanford. *The hydrophobic effect: formation of micelles and biological membranes 2d ed.* J. Wiley., 1980. DOI: 10.1016/0014-5793(81)80071-3 (cited on page 9).

[82] J. N. Israelachvili, S. Marčelja, and Roger G. Horn. "Physical principles of membrane organization." In: *Quarterly reviews of biophysics* 13.2 (1980), pp. 121–200 (cited on pages 9–11).

[83] Jacob N. Israelachvili, D. John Mitchell, and Barry W. Ninham. "Theory of self-assembly of hydrocarbon amphiphiles into micelles and bilayers." In: *Journal of the Chemical Society, Faraday Transactions 2: Molecular and Chemical Physics* 72 (1976), pp. 1525–1568. DOI: 10.1039/F29767201525 (cited on page 11).

[84] Jacob N. Israelachvili, D. John Mitchell, and Barry W. Ninham. "Theory of self-assembly of lipid bilayers and vesicles." In: *Biochimica et Biophysica Acta (BBA)-Biomembranes* 470.2 (1977), pp. 185–201. DOI: 10.1016/0005-2736(77)90099-2 (cited on page 11).

[85] J. N. Israelachvili and B. W. Ninham. "Intermolecular forces—the long and short of it." In: *Journal of Colloid and Interface Science* 58.1 (1977), pp. 14–25. DOI: 10.1016/0021-9797(77)90367-8 (cited on page 11).

[86] Michael Edidin. "Rotational and translational diffusion in membranes." In: *Annual review of biophysics and bioengineering* 3.1 (1974), pp. 179–201. DOI: 10.1016/s0076-6879(89)72030-9 (cited on page 11).

[87] Paulo F. F. Almeida and Winchil L. C. Vaz. "Lateral diffusion in membranes." In: *Handbook of biological physics* 1.C (1995), pp. 305–357 (cited on pages 11, 12).

[88] Daniel Axelrod, D. E. Koppel, J. Schlessinger, Elliot Elson, and Watt W. Webb. "Mobility measurement by analysis of fluorescence photobleaching recovery kinetics." In: *Biophysical journal* 16.9 (1976), pp. 1055–1069. DOI: 10.1016/S0006-3495(76)85755-4 (cited on page 12).

[89] Hong Qian, Michael P. Sheetz, and Elliot L. Elson. "Single particle tracking. Analysis of diffusion and flow in two-dimensional systems." In: *Biophysical journal* 60.4 (1991), pp. 910–921. DOI: 10.1016/S0006-3495(91)82125-7 (cited on page 12).

[90] S. S. Sandhu, Y. P. Yianni, C. G. Morgan, D. M. Taylor, and B. Zaba. "The formation and Langmuir-Blodgett deposition of monolayers of novel photochromic azobenzene-containing phospholipid molecules." In: *Biochimica et Biophysica Acta (BBA)-Biomembranes* 860.2 (1986), pp. 253–262. DOI: 10.1016/0005-2736(86)90521-3 (cited on page 13).

[91] Christopher G. Morgan, Emrys W. Thomas, Yiannakis P. Yianni, and Shivpal S. Sandhu. "Incorporation of a novel photochromic phospholipid molecule into vesicles of dipalmitoylphosphatidylcholine." In: *Biochimica et Biophysica Acta (BBA)-Biomembranes* 820.1 (1985), pp. 107–114. DOI: 10.1016/0005-2736(85)90221-4 (cited on page 13).

[92] Vasil N. Georgiev, Andrea Grafmüller, David Bléger, Stefan Hecht, Sonja Kunstmann, Stefanie Barbirz, Reinhard Lipowsky, and Rumiana Dimova. "Area increase and budding in giant vesicles triggered by light: behind the scene." In: *Advanced Science* 5.8 (2018), p. 1800432. DOI: 10.1002/advs.201800432 (cited on page 14).

[93] Elizabeth J. Harbron. "Fluorescence intensity modulation in photochromic conjugated polymer systems." In: *Israel Journal of Chemistry* 53.5 (2013), pp. 256–266. DOI: 10.1002/ijch.201300016 (cited on pages 15, 61).

[94] Dojin Kim and Soo Young Park. "Multicolor Fluorescence Photoswitching: Color-Correlated versus Color-Specific Switching." In: *Advanced Optical Materials* 6.20 (2018), p. 1800678. DOI: 10.1002/adom.201800678 (cited on page 15).

[95] Francisco M. Raymo and Massimiliano Tomasulo. "Electron and energy transfer modulation with photochromic switches." In: *Chemical Society Reviews* 34.4 (2005), pp. 327–336. DOI: 10.1039/B400387J (cited on page 15).

[96] Ibrahim Yildiz, Erhan Deniz, and Françisco M. Raymo. "Fluorescence modulation with photochromic switches in nanostructured constructs." In: *Chemical Society Reviews* 38.7 (2009), pp. 1859–1867. DOI: 10.1039/B804151M (cited on page 15).

[97] Masatsugu Shimomura and Toyoki Kunitake. "Fluorescence and photoisomerization of azobenzene-containing bilayer membranes." In: *Journal of the American Chemical Society* 109.17 (1987), pp. 5175–5183. DOI: 10.1021/ja00251a022 (cited on pages 15, 21).

[98] Jacques Ronayette, René Arnaud, and Jacques Lemaire. "Isomérisation photosensibilisée par des colorants et photoréduction de l'azobenzène en solution. II." In: *Canadian Journal of Chemistry* 52.10 (1974), pp. 1858–1867. DOI: 10.1139/v74-265 (cited on pages 15, 21).

[99] René Arnaud and Jacques Lemaire. "Isoméirsation cis–trans de l'azobenzène catalysée par l'iode. III." In: *Canadian Journal of Chemistry* 52.10 (1974), pp. 1868–1871. DOI: 10.1139/v74-266 (cited on page 15).

[100] Alexis Goulet-Hanssens, Clemens Rietze, Evgenii Titov, Leonora Abdullahu, Lutz Grubert, Peter Saalfrank, and Stefan Hecht. "Hole catalysis as a general mechanism for efficient and wavelength-independent Z⟶ E azobenzene isomerization." In: *Chem* 4.7 (2018), pp. 1740–1755. DOI: 10.1016/j.chempr.2018.06.002 (cited on pages 15, 21).

[101] Joseph R. Lakowicz. *Principles of fluorescence spectroscopy*. Springer, 2006. DOI: 10.1007/978-0-387-46312-4 (cited on pages 16, 17, 67).

[102] J. B. Birks. "Quenching of excited singlet and triplet states of aromatic hydrocarbons by oxygen and nitric oxide." In: *Journal of Luminescence* 1 (1970), pp. 154–165. DOI: 10.1016/0022-2313(70)90031-1 (cited on page 16).

[103] Johan Strömqvist, Andriy Chmyrov, Sofia Johansson, August Andersson, Lena Mäler, and Jerker Widengren. "Quenching of triplet state fluorophores for studying diffusion-mediated reactions in lipid membranes." In: *Biophysical Journal* 99.11 (2010), pp. 3821–3830. DOI: 10.1016/j.bpj.2010.09.059 (cited on page 16).

[104] Maria C. DeRosa and Robert J. Crutchley. "Photosensitized singlet oxygen and its applications." In: *Coordination chemistry reviews* 233 (2002), pp. 351–371. DOI: 10.1016/S0010-8545(02)00034-6 (cited on page 16).

[105] Felix Strieth-Kalthoff, Michael J. James, Michael Teders, Lena Pitzer, and Frank Glorius. "Energy transfer catalysis mediated by visible light: principles, applications, directions." In: *Chemical Society Reviews* 47.19 (2018), pp. 7190–7202. DOI: 10.1039/C8CS00054A (cited on pages 16–18, 60).

[106] Nicholas J. Turro, Vaidhyanathan Ramamurthy, and Juan C. Scaiano. *Principles of molecular photochemistry: an introduction*. University science books, 2009 (cited on pages 18, 19).

[107] Felix Strieth-Kalthoff and Frank Glorius. "Triplet energy transfer photocatalysis: unlocking the next level." In: *Chem* 6.8 (2020), pp. 1888–1903. DOI: 10.1016/j.chempr.2020.07.010 (cited on page 18).

[108] Johannes Großkopf, Thilo Kratz, Thomas Rigotti, and Thorsten Bach. "Enantioselective photochemical reactions enabled by triplet energy transfer." In: *Chemical Reviews* 122.2 (2021), pp. 1626–1653. DOI: 10.1021/acs.chemrev.1c00272 (cited on page 18).

[109] Amy F. Grimes, Scott E. Call, Elizabeth J. Harbron, and Douglas S. English. "Wavelength-resolved studies of Förster energy transfer in azobenzene-modified conjugated polymers: the competing roles of exciton migration and spectral resonance." In: *The Journal of Physical Chemistry C* 111.38 (2007), pp. 14257–14265. DOI: 10.1021/jp0743525 (cited on page 19).

[110] Elizabeth J. Harbron, Diego A. Vicente, and Mirth T. Hoyt. "Fluorescence modulation via isomer-dependent energy transfer in an azobenzene-functionalized poly (phenylenevinylene) derivative." In: *The Journal of Physical Chemistry B* 108.49 (2004), pp. 18789–18792. DOI: 10.1021/jp045651m (cited on page 19).

[111] Oxana Kempf, Karl Kempf, Rainer Schobert, and Elisa Bombarda. "Hydrodabcyl: a superior hydrophilic alternative to the dark fluorescence quencher dabcyl." In: *Analytical chemistry* 89.22 (2017), pp. 11893–11897. DOI: 10.1021/acs.analchem.7b03488 (cited on pages 19, 63).

[112] Arnaud Chevalier, Pierre-Yves Renard, and Anthony Romieu. "Azo-Based Fluorogenic Probes for Biosensing and Bioimaging: Recent Advances and Upcoming Challenges." In: *Chemistry–An Asian Journal* 12.16 (2017), pp. 2008–2028. DOI: 10.1002/asia.201700682 (cited on page 19).

[113] David Bléger and Stefan Hecht. "Visible-light-activated molecular switches." In: *Angewandte Chemie International Edition* 54.39 (2015), pp. 11338–11349. DOI: 10.1002/anie.201500628 (cited on page 20).

[114] Lee B. Jones and George S. Hammond. "Mechanisms of Photochemical Reactions in Solution. XXX. 1 Photosensitized Isomerization of Azobenzene." In: *Journal of the American Chemical Society* 87.18 (1965), pp. 4219–4220. DOI: 10.1021/ja01096a059 (cited on page 20).

[115] Pietro Bortolus and Sandra Monti. "Cis-trans photoisomerization of azobenzene. Solvent and triplet donors effects." In: *Journal of Physical Chemistry* 83.6 (1979), pp. 648–652. DOI: 10.1021/j100469a002 (cited on page 21).

[116] Jussi Isokuortti, Kim Kuntze, Matti Virkki, Zafar Ahmed, Elina Vuorimaa-Laukkanen, Mikhail A. Filatov, Andrey Turshatov, Timo Laaksonen, Arri Priimagi, and Nikita A. Durandin. "Expanding excitation wavelengths for azobenzene photoswitching into the near-infrared range via endothermic triplet energy transfer." In: *Chemical Science* 12.21 (2021), pp. 7504–7509. DOI: 10.1039/D1SC01717A (cited on page 21).

[117] Sandra Monti, Enrico Gardini, Pietro Bortolus, and Edmond Amouyal. "The triplet state of azobenzene." In: *Chemical Physics Letters* 77.1 (1981), pp. 115–119. DOI: 10.1016/0009-2614(81)85611-4 (cited on page 21).

[118] Sandra Monti, Sergio Dellonte, and Pietro Bortolus. "The lowest triplet state of substituted azobenzenes: an energy transfer investigation." In: *Journal of photochemistry* 23.2 (1983), pp. 249–256. DOI: 10.1016/0047-2670(83)80065-3 (cited on page 21).

[119] Marc Reimann, Ellen Teichmann, Stefan Hecht, and Martin Kaupp. "Solving the azobenzene entropy puzzle: Direct evidence for multi-state reactivity." In: *The Journal of Physical Chemistry Letters* 13.46 (2022), pp. 10882–10888. DOI: 10.1021/acs.jpclett.2c02838 (cited on page 21).

[120] Alexis Goulet-Hanssens, Manuel Utecht, Dragos Mutruc, Evgenii Titov, Jutta Schwarz, Lutz Grubert, David Bléger, Peter Saalfrank, and Stefan Hecht. "Electrocatalytic Z⟶ E isomerization of azobenzenes." In: *Journal of the American Chemical Society* 139.1 (2017), pp. 335–341. DOI: 10.1021/jacs.6b10822 (cited on page 21).

[121] Mark Fox. *Optical properties of solids*. Vol. 3. Oxford university press, 2010 (cited on pages 22, 23).

[122] Stefan A. Maier. *Plasmonics: fundamentals and applications*. Vol. 1. Springer, 2007. DOI: 10.1007/0-387-37825-1 (cited on pages 22–26, 31, 32).

[123] Mitchell Lee Taylor, Raymond Edward Wilson Jr, Kristopher Daniel Amrhein, and Xiaohua Huang. "Gold nanorod-assisted photothermal therapy and improvement strategies." In: *Bioengineering* 9.5 (2022), p. 200. DOI: 10.3390/bioengineering9050200 (cited on page 26).

[124] Ying Bao and Ayomide Oluwafemi. "Recent advances in surface modified gold nanorods and their improved sensing performance." In: *Chemical Communications* (2024). DOI: 10.1039/D3CC04056A (cited on page 26).

[125] Jeffrey M. McMahon, Stephen K. Gray, and George C. Schatz. "Calculating nonlocal optical properties of structures with arbitrary shape." In: *Physical Review B* 82.3 (2010), p. 035423. DOI: 10.1103/PhysRevB.82.035423 (cited on page 27).

[126] Vlastimil Křápek, Rostislav Řepa, Michael Foltýn, Tomáš Šikola, and Michal Horák. "Plasmonic lightning-rod effect." In: *arXiv preprint arXiv:2407.09454* (2024). DOI: 10.48550/arXiv.2407.09454 (cited on page 27).

[127] Alexander Al-Zubeidi, Lauren A. McCarthy, Ali Rafiei-Miandashti, Thomas S. Heiderscheit, and Stephan Link. "Single-particle scattering spectroscopy: fundamentals and applications." In: *Nanophotonics* 10.6 (2021), pp. 1621–1655. DOI: 10.1515/nanoph-2020-0639 (cited on page 27).

[128] Jeffrey N. Anker, W. Paige Hall, Olga Lyandres, Nilam C. Shah, Jing Zhao, and Richard P. Van Duyne. "Biosensing with plasmonic nanosensors." In: *Nature materials* 7.6 (2008), pp. 442–453. DOI: 10.1038/nmat2162 (cited on page 27).

[129] Adam B. Taylor and Peter Zijlstra. "Single-molecule plasmon sensing: current status and future prospects." In: *ACS sensors* 2.8 (2017), pp. 1103–1122. DOI: 10.1021/acssensors.7b00382 (cited on page 27).

[130] Christina Rosman, Janak Prasad, Andreas Neiser, Andreas Henkel, Jonathan Edgar, and Carsten Sönnichsen. "Multiplexed plasmon sensor for rapid label-free analyte detection." In: *Nano letters* 13.7 (2013), pp. 3243–3247. DOI: 10.1021/nl401354f (cited on page 27).

[131] Christina Lambertz, Ariadna Martos, Andreas Henkel, Andreas Neiser, Torben-Tobias Kliesch, Andreas Janshoff, Petra Schwille, and Carsten Sönnichsen. "Single particle plasmon sensors as label-free technique to monitor minde protein wave propagation on membranes." In: *Nano Letters* 16.6 (2016), pp. 3540–3544. DOI: 10.1021/acs.nanolett.6b00507 (cited on page 27).

[132] Weixiang Ye, Sirin Celiksoy, Arpad Jakab, Alena Khmelinskaia, Tamara Heermann, Ana Raso, Seraphine V. Wegner, German Rivas, Petra Schwille, and Ruben Ahijado-Guzman. "Plasmonic nanosensors reveal a height dependence of MinDE protein oscillations on membrane features." In: *Journal of the American Chemical Society* 140.51 (2018), pp. 17901–17906. DOI: 10.1021/jacs.8b07759 (cited on pages 27, 71).

[133] W. Paige Hall, Jeffrey N. Anker, Yao Lin, Justin Modica, Milan Mrksich, and Richard P. Van Duyne. "A calcium-modulated plasmonic switch." In: *Journal of the American Chemical Society* 130.18 (2008), pp. 5836–5837. DOI: 10.1021/ja7109037 (cited on page 27).

[134] Tian Ming, Lei Zhao, Manda Xiao, and Jianfang Wang. "Resonance-Coupling-Based Plasmonic Switches." In: *small* 6.22 (2010), pp. 2514–2519. DOI: 10.1002/smll.201000920 (cited on page 27).

[135] Soumyadyuti Samai, Tina Lok Yee Choi, Kathryn N. Guye, Yunqi Yan, and David S. Ginger. "Plasmonic nanoparticle dimers with reversibly photoswitchable interparticle distances linked by DNA." In: *The Journal of Physical Chemistry C* 122.25 (2017), pp. 13363–13370. DOI: 10.1021/acs.jpcc.7b10181 (cited on page 27).

[136] Lei Shi, Chao Jing, Wei Ma, Da-Wei Li, Jonathan E. Halls, Frank Marken, and Yi-Tao Long. "Plasmon resonance scattering spectroscopy at the single-nanoparticle level: real-time monitoring of a click reaction." In: *Angewandte Chemie International Edition* 52.23 (2013), pp. 6011–6014. DOI: 10.1002/anie.201301930 (cited on page 27).

[137] G. Raschke, S. Kowarik, T. Franzl, C. Sönnichsen, T. A. Klar, J. Feldmann, A. Nichtl, and K. Kürzinger. "Biomolecular recognition based on single gold nanoparticle light scattering." In: *Nano letters* 3.7 (2003), pp. 935–938. DOI: 10.1021/nl034223+ (cited on page 27).

[138] Chanda Ranjit Yonzon, Eunhee Jeoung, Shengli Zou, George C. Schatz, Milan Mrksich, and Richard P. Van Duyne. "A comparative analysis of localized and propagating surface plasmon resonance sensors: the binding of concanavalin A to a monosaccharide functionalized self-assembled monolayer." In: *Journal of the American Chemical Society* 126.39 (2004), pp. 12669–12676. DOI: 10.1021/ja047118q (cited on page 27).

[139] Ruben Ahijado-Guzman, Julia Menten, Janak Prasad, Christina Lambertz, German Rivas, and Carsten Sönnichsen. "Plasmonic nanosensors for the determination of drug effectiveness on membrane receptors." In: *ACS Applied Materials and Interfaces* 9.1 (2017), pp. 218–223. DOI: 10.1021/acsami.6b14013 (cited on page 27).

[140] Ruben Ahijado-Guzman, Janak Prasad, Christina Rosman, Andreas Henkel, Lydia Tome, Dirk Schneider, German Rivas, and Carsten Sönnichsen. "Plasmonic nanosensors for simultaneous quantification of multiple protein–protein binding affinities." In: *Nano letters* 14.10 (2014), pp. 5528–5532. DOI: 10.1021/nl501865p (cited on page 27).

[141] Cristina L. Baciu, Jan Becker, Andreas Janshoff, and Carsten Sönnichsen. "Protein–membrane interaction probed by single plasmonic nanoparticles." In: *Nano Letters* 8.6 (2008), pp. 1724–1728. DOI: 10.1021/nl080805l (cited on page 27).

[142] Jeffrey N. Anker, W. Paige Hall, Olga Lyandres, Nilam C. Shah, Jing Zhao, and Richard P. Van Duyne. "Biosensing with plasmonic nanosensors." In: *Nature materials* 7.6 (2008), pp. 442–453. DOI: 10.1038/nmat2162 (cited on page 28).

[143] Erik Martinsson, Mohammad M. Shahjamali, Nicolas Large, Negin Zaraee, Yu Zhou, George C. Schatz, Chad A. Mirkin, and Daniel Aili. "Influence of surfactant bilayers on the refractive index sensitivity and catalytic properties of anisotropic gold nanoparticles." In: *Small* 12.3 (2016), pp. 330–342. DOI: 10.1002/smll.201502449 (cited on pages 28, 47).

[144] Katherine A. Willets and Richard P. Van Duyne. "Localized surface plasmon resonance spectroscopy and sensing." In: *Annu. Rev. Phys. Chem.* 58.1 (2007), pp. 267–297. DOI: 10.1146/annurev.physchem.58.032806.104607 (cited on page 28).

[145] Arthur Ashkin. "Applications of laser radiation pressure." In: *Science* 210.4474 (1980), pp. 1081–1088. DOI: 10.1126/science.210.4474.10 (cited on page 28).

[146] Alexander S. Urban, Andrey A. Lutich, Fenando D. Stefani, and Jochen Feldmann. "Laser printing single gold nanoparticles." In: *Nano letters* 10.12 (2010), pp. 4794–4798. DOI: 10.1021/nl1030425 (cited on page 28).

[147] Jaekwon Do, Michael Fedoruk, Frank Jäckel, and Jochen Feldmann. "Two-color laser printing of individual gold nanorods." In: *Nano letters* 13.9 (2013), pp. 4164–4168. DOI: 10.1021/nl401788w (cited on page 28).

[148] Spas Nedev, Alexander S. Urban, Andrey A. Lutich, and Jochen Feldmann. "Optical force stamping lithography." In: *Nano letters* 11.11 (2011), pp. 5066–5070. DOI: 10.1021/nl203214n (cited on page 28).

[149] Maria Dienerowitz, Michael Mazilu, and Kishan Dholakia. "Optical manipulation of nanoparticles: a review." In: *Journal of nanophotonics* 2.1 (2008), p. 021875. DOI: 10.1117/1.2992045 (cited on page 28).

[150] Alexander S. Urban, Sol Carretero-Palacios, Andrey A. Lutich, Theobald Lohmüller, Jochen Feldmann, and Frank Jäckel. "Optical trapping and manipulation of plasmonic nanoparticles: fundamentals, applications, and perspectives." In: *Nanoscale* 6.9 (2014), pp. 4458–4474. DOI: 10.1039/C3NR06617G (cited on page 29).

[151] Alexander O. Govorov and Hugh H. Richardson. "Generating heat with metal nanoparticles." In: *Nano today* 2.1 (2007), pp. 30–38. DOI: 10.1016/S1748-0132(07)70017-8 (cited on page 29).

[152] C. Sönnichsen, T. Franzl, Tv Wilk, Gero von Plessen, J. Feldmann, O. V. Wilson, and Paul Mulvaney. "Drastic reduction of plasmon damping in gold nanorods." In: *Physical review letters* 88.7 (2002), p. 077402. DOI: 10.1103/PhysRevLett.88.077402 (cited on pages 29, 70).

[153] Stephan Link, Clemens Burda, M. B. Mohamed, B. Nikoobakht, and Mostafa A. El-Sayed. "Laser photothermal melting and fragmentation of gold nanorods: energy and laser pulse-width dependence." In: *The Journal of Physical Chemistry A* 103.9 (1999), pp. 1165–1170. DOI: 10.1021/jp983141k (cited on page 30).

[154] S. Link, C. Burda, B. Nikoobakht, and M. A. El-Sayed. "How long does it take to melt a gold nanorod?: A femtosecond pump–probe absorption spectroscopic study." In: *Chemical Physics Letters* 315.1-2 (1999), pp. 12–18. DOI: 10.1016/S0009-2614(99)01214-2 (cited on page 30).

[155] Zhong L. Wang, Janet M. Petroski, Travis C. Green, and Mostafa A. El-Sayed. "Shape transformation and surface melting of cubic and tetrahedral platinum nanocrystals." In: *The Journal of Physical Chemistry B* 102.32 (1998), pp. 6145–6151. DOI: 10.1021/jp981594j (cited on page 30).

[156] Stephan Link, Zhong L. Wang, and Mostafa A. El-Sayed. "How does a gold nanorod melt?" In: *The Journal of Physical Chemistry B* 104.33 (2000), pp. 7867–7870. DOI: 10.1021/jp0011701 (cited on pages 30, 92).

[157] Marta Gordel, Joanna Olesiak-Banska, Katarzyna Matczyszyn, Claude Nogues, Malcolm Buckle, and Marek Samoc. "Post-synthesis reshaping of gold nanorods using a femtosecond laser." In: *Physical Chemistry Chemical Physics* 16.1 (2014), pp. 71–78. DOI: 10.1039/C3CP53457J (cited on pages 30, 92).

[158] Yukichi Horiguchi, Kanako Honda, Yuichi Kato, Naotoshi Nakashima, and Yasuro Niidome. "Photothermal reshaping of gold nanorods depends on the passivating layers of the nanorod surfaces." In: *Langmuir* 24.20 (2008), pp. 12026–12031. DOI: 10.1021/la800811j (cited on pages 30, 92).

[159] Anastasia Babynina, Michael Fedoruk, Paul Kühler, Alexander Meledin, Markus Döblinger, and Theobald Lohmüller. "Bending gold nanorods with light." In: *Nano letters* 16.10 (2016), pp. 6485–6490. DOI: 10.1021/acs.nanolett.6b03029 (cited on pages 30, 92).

[160] Francis Schuknecht, Christoph M. Maier, Paul Vosshage, Verena A. Hintermayr, Markus Döblinger, and Theobald Lohmüller. "Single-Step Plasmonic Dimer Printing by Gold Nanorod Splitting with Light." In: *Nano Letters* 23.11 (2023), pp. 4762–4769. DOI: 10.1021/acs.nanolett.2c04954 (cited on pages 30, 35, 92).

[161] Judith Langer, Dorleta Jimenez de Aberasturi, Javier Aizpurua, Ramon A. Alvarez-Puebla, Baptiste Auguié, Jeremy J. Baumberg, Guillermo C. Bazan, Steven E. J. Bell, Anja Boisen, and Alexandre G. Brolo. "Present and future of surface-enhanced Raman scattering." In: *ACS nano* 14.1 (2019), pp. 28–117. DOI: 10.1021/acsnano.9b04224 (cited on page 31).

[162] Eric Le Ru and Pablo Etchegoin. *Principles of Surface-Enhanced Raman Spectroscopy: and related plasmonic effects*. Elsevier, 2008 (cited on page 31).

[163] Shuping Xu. "Experimental aspects of surface-enhanced Raman scattering for biological applications." In: *Principles and Clinical Diagnostic Applications of Surface-Enhanced Raman Spectroscopy*. Elsevier, 2022, pp. 81–124. DOI: 10.1016/B978-0-12-821121-2.00010-X (cited on page 31).

[164] Augusto Marcelli, Antonio Cricenti, Wojciech M. Kwiatek, and Cyril Petibois. "Biological applications of synchrotron radiation infrared spectromicroscopy." In: *Biotechnology advances* 30.6 (2012), pp. 1390–1404. DOI: 10.1016/j.biotechadv.2012.02.012 (cited on page 32).

[165] Gregory W. Auner, S. Kiran Koya, Changhe Huang, Brandy Broadbent, Micaela Trexler, Zachary Auner, Angela Elias, Katlyn Curtin Mehne, and Michelle A. Brusatori. "Applications of Raman spectroscopy in cancer diagnosis." In: *Cancer and Metastasis Reviews* 37 (2018), pp. 691–717. DOI: 10.1007/s10555-018-9770-9 (cited on page 32).

[166] Zhiyun Li, M. Jamal Deen, Shiva Kumar, and P. Ravi Selvaganapathy. "Raman spectroscopy for in-line water quality monitoring—Instrumentation and potential." In: *Sensors* 14.9 (2014), pp. 17275–17303. DOI: 10.3390/s140917275 (cited on page 32).

[167] Katrin Kneipp, Harald Kneipp, Irving Itzkan, Ramachandra R. Dasari, and Michael S. Feld. "Surface-enhanced Raman scattering and biophysics." In: *Journal of Physics: Condensed Matter* 14.18 (2002), R597. DOI: 10.1088/0953-8984/14/18/202 (cited on pages 32, 33).

[168] Alan Campion and Patanjali Kambhampati. "Surface-enhanced Raman scattering." In: *Chemical society reviews* 27.4 (1998), pp. 241–250. DOI: 10.1039/A827241Z (cited on page 33).

[169] M. Grant Albrecht and J. Alan Creighton. "Anomalously intense Raman spectra of pyridine at a silver electrode." In: *Journal of the american chemical society* 99.15 (1977), pp. 5215–5217. DOI: 10.1021/ja00457a071 (cited on page 33).

[170] T. E. Furtak and S. H. Macomber. "Voltage-induced shifting of charge-transfer excitations and their role in surface-enhanced Raman scattering." In: *Chemical Physics Letters* 95.4-5 (1983), pp. 328–332. DOI: 10.1016/0009-2614(83)80568-5 (cited on page 33).

[171] Patanjali Kambhampati, C. M. Child, Michelle C. Foster, and Alan Campion. "On the chemical mechanism of surface enhanced Raman scattering: experiment and theory." In: *The Journal of chemical physics* 108.12 (1998), pp. 5013–5026. DOI: 10.1063/1.475909 (cited on page 33).

[172] Lucas A. Lane, Ximei Qian, and Shuming Nie. "SERS nanoparticles in medicine: from label-free detection to spectroscopic tagging." In: *Chemical reviews* 115.19 (2015), pp. 10489–10529. DOI: 10.1021/acs.chemrev.5b00265 (cited on pages 33, 34).

[173] Katrin Kneipp, Yang Wang, Harald Kneipp, Lev T. Perelman, Irving Itzkan, Ramachandra R. Dasari, and Michael S. Feld. "Single molecule detection using surface-enhanced Raman scattering (SERS)." In: *Physical review letters* 78.9 (1997), p. 1667. DOI: 10.1103/PhysRevLett.78.1667 (cited on page 34).

[174] Shuming Nie and Steven R. Emory. "Probing single molecules and single nanoparticles by surface-enhanced Raman scattering." In: *science* 275.5303 (1997), pp. 1102–1106. DOI: 10.1126/science.275.5303.110 (cited on page 34).

[175] Janina Kneipp, Harald Kneipp, and Katrin Kneipp. "SERS—a single-molecule and nanoscale tool for bioanalytics." In: *Chemical Society Reviews* 37.5 (2008), pp. 1052–1060. DOI: 10.1039/B708459P (cited on page 34).

[176] Cristiano Matricardi, Christoph Hanske, Juan Luis Garcia-Pomar, Judith Langer, Agustín Mihi, and Luis M. Liz-Marzán. "Gold nanoparticle plasmonic superlattices as surface-enhanced Raman spectroscopy substrates." In: *ACS nano* 12.8 (2018), pp. 8531–8539. DOI: 10.1021/acsnano.8b04073 (cited on page 34).

[177] Yunqing Wang, Bing Yan, and Lingxin Chen. "SERS tags: novel optical nanoprobes for bioanalysis." In: *Chemical reviews* 113.3 (2013), pp. 1391–1428. DOI: 10.1021/cr300120g (cited on page 34).

[178] Yuying Zhang, Xue Mi, Xiaoyue Tan, and Rong Xiang. "Recent progress on liquid biopsy analysis using surface-enhanced Raman spectroscopy." In: *Theranostics* 9.2 (2019), p. 491. DOI: 10.7150/thno.29875 (cited on page 34).

[179] Hui Wang, Carly S. Levin, and Naomi J. Halas. "Nanosphere arrays with controlled sub-10-nm gaps as surface-enhanced Raman spectroscopy substrates." In: *Journal of the American Chemical Society* 127.43 (2005), pp. 14992–14993. DOI: 10.1021/ja055633y (cited on page 34).

[180] Jian Feng Li, Yi Fan Huang, Yong Ding, Zhi Lin Yang, Song Bo Li, Xiao Shun Zhou, Feng Ru Fan, Wei Zhang, Zhi You Zhou, and De Yin Wu. "Shell-isolated nanoparticle-enhanced Raman spectroscopy." In: *nature* 464.7287 (2010), pp. 392–395. DOI: 10.1038/nature08907 (cited on page 34).

[181] John C. Hulteen, David A. Treichel, Matthew T. Smith, Michelle L. Duval, Traci R. Jensen, and Richard P. Van Duyne. "Nanosphere lithography: size-tunable silver nanoparticle and surface cluster arrays." In: *The Journal of Physical Chemistry B* 103.19 (1999), pp. 3854–3863. DOI: 10.1021/jp9904771 (cited on page 34).

[182] T. Lohmuller, L. Iversen, M. Schmidt, C. Rhodes, H. L. Tu, W. C. Lin, and J. T. Groves. "Single molecule tracking on supported membranes with arrays of optical nanoantennas." In: *Nano letters* 12.3 (2012), pp. 1717–1721. DOI: 10.1021/nl300294b (cited on page 34).

[183] Paul Kühler, Max Weber, and Theobald Lohmüller. "Plasmonic nanoantenna arrays for surface-enhanced Raman spectroscopy of lipid molecules embedded in a bilayer membrane." In: *ACS applied materials and interfaces* 6.12 (2014), pp. 8947–8952. DOI: 10.1021/am5023418 (cited on page 34).

[184] Kai-Qiang Lin, Jun Yi, Jin-Hui Zhong, Shu Hu, Bi-Ju Liu, Jun-Yang Liu, Cheng Zong, Zhi-Chao Lei, Xiang Wang, and Javier Aizpurua. "Plasmonic photoluminescence for recovering native chemical information from surface-enhanced Raman scattering." In: *Nature communications* 8.1 (2017), p. 14891. DOI: 10.1038/ncomms14891 (cited on pages 34, 93).

[185] Leonardo Scarabelli, Marc Coronado-Puchau, Juan J. Giner-Casares, Judith Langer, and Luis M. Liz-Marzán. "Monodisperse gold nanotriangles: size control, large-scale self-assembly, and performance in surface-enhanced Raman scattering." In: *ACS nano* 8.6 (2014), pp. 5833–5842. DOI: 10.1021/nn500727w (cited on page 35).

[186] Rongchao Jin, YunWei Cao, Chad A. Mirkin, K. Lance Kelly, George C. Schatz, and J. G. Zheng. "Photoinduced conversion of silver nanospheres to nanoprisms." In: *science* 294.5548 (2001), pp. 1901–1903. DOI: 10.1126/science.106654 (cited on page 35).

[187] L. Osinkina, T. Lohmuller, F. Jackel, and J. Feldmann. "Synthesis of gold nanostar arrays as reliable, large-scale, homogeneous substrates for surface-enhanced Raman scattering imaging and spectroscopy." In: *The Journal of Physical Chemistry C* 117.43 (2013), pp. 22198–22202. DOI: 10.1021/jp312149d (cited on page 35).

[188] Emren Nalbant Esenturk and A. R. Hight Walker. "Surface-enhanced Raman scattering spectroscopy via gold nanostars." In: *Journal of Raman Spectroscopy: An International Journal for Original Work in all Aspects of Raman Spectroscopy, Including Higher Order Processes, and also Brillouin and Rayleigh Scattering* 40.1 (2009), pp. 86–91. DOI: 10.1002/jrs.2084 (cited on page 35).

[189] Christopher G. Khoury and Tuan Vo-Dinh. "Gold nanostars for surface-enhanced Raman scattering: synthesis, characterization and optimization." In: *The Journal of Physical Chemistry C* 112.48 (2008), pp. 18849–18859. DOI: 10.1021/jp8054747 (cited on page 35).

[190] Dong-Kwon Lim, Ki-Seok Jeon, Jae-Ho Hwang, Hyoki Kim, Sunghoon Kwon, Yung Doug Suh, and Jwa-Min Nam. "Highly uniform and reproducible surface-enhanced Raman scattering from DNA-tailorable nanoparticles with 1-nm interior gap." In: *Nature nanotechnology* 6.7 (2011), pp. 452–460. DOI: 10.1038/nnano.2011.79 (cited on page 35).

[191] Mihir Dass, Fatih N. Gür, Karol Kołątaj, Maximilian J. Urban, and Tim Liedl. "DNA origami-enabled plasmonic sensing." In: *The Journal of Physical Chemistry C* 125.11 (2021), pp. 5969–5981 (cited on page 35).

[192] Saeideh Mehmandoust, Vahid Eskandari, and Elaheh Karooby. "A review of fabrication of DNA origami plasmonic structures for the development of surface-enhanced Raman scattering (SERS) platforms." In: *Plasmonics* 19.3 (2024), pp. 1131–1143 (cited on page 35).

[193] Wenjing Yan, Liguang Xu, Chuanlai Xu, Wei Ma, Hua Kuang, Libing Wang, and Nicholas A. Kotov. "Self-assembly of chiral nanoparticle pyramids with strong R/S optical activity." In: *Journal of the American Chemical Society* 134.36 (2012), pp. 15114–15121 (cited on page 35).

[194] Paul Kühler, Eva-Maria Roller, Robert Schreiber, Tim Liedl, Theobald Lohmüller, and Jochen Feldmann. "Plasmonic DNA-origami nanoantennas for surface-enhanced Raman spectroscopy." In: *Nano letters* 14.5 (2014), pp. 2914–2919. DOI: 10.1021/nl5009635 (cited on page 35).

[195] Vivek V. Thacker, Lars O. Herrmann, Daniel O. Sigle, Tao Zhang, Tim Liedl, Jeremy J. Baumberg, and Ulrich F. Keyser. "DNA origami based assembly of gold nanoparticle dimers for surface-enhanced Raman scattering." In: *Nature communications* 5.1 (2014), p. 3448. DOI: 10.1038/ncomms4448 (cited on page 35).

[196] Taishi Zhang, Nengyue Gao, Shuang Li, Matthew J. Lang, and Qing-Hua Xu. "Single-particle spectroscopic study on fluorescence enhancement by plasmon coupled gold nanorod dimers assembled on DNA origami." In: *The journal of physical chemistry letters* 6.11 (2015), pp. 2043–2049. DOI: 10.1021/acs.jpclett.5b00747 (cited on page 35).

[197] Yue Bing Zheng, John L. Payton, Choong-Heui Chung, Rong Liu, Sarawut Cheunkar, Bala Krishna Pathem, Yang Yang, Lasse Jensen, and Paul S. Weiss. "Surface-enhanced Raman spectroscopy to probe reversibly photoswitchable azobenzene in controlled nanoscale environments." In: *Nano letters* 11.8 (2011), pp. 3447–3452. DOI: 10.1021/nl2019195 (cited on pages 35, 36, 97).

[198] Gayatri K. Joshi, Karl N. Blodgett, Barry B. Muhoberac, Merrell A. Johnson, Kimberly A. Smith, and Rajesh Sardar. "Ultrasensitive photoreversible molecular sensors of azobenzene-functionalized plasmonic nanoantennas." In: *Nano Letters* 14.2 (2014), pp. 532–540. DOI: 10.1021/nl403576c (cited on pages 35, 36, 97).

[199] Lili Sun, Changshun Wang, Yujia Pan, Tianyu Chen, and Ziyao Lv. "Enhanced trans-to-cis photoisomerization quantum yield of azobenzene spatially confined in silver nanoparticle aggregates." In: *Journal of Raman Spectroscopy* 51.5 (2020), pp. 756–763. DOI: 10.1002/jrs.5847 (cited on page 35).

[200] Jun Hee Yoon and Sangwoon Yoon. "Photoisomerization of azobenzene derivatives confined in gold nanoparticle aggregates." In: *Physical Chemistry Chemical Physics* 13.28 (2011), pp. 12900–12905. DOI: 10.1039/C0CP02588G (cited on pages 35, 97).

[201] Nicholas Tallarida, Laura Rios, Vartkess A. Apkarian, and Joonhee Lee. "Isomerization of one molecule observed through tip-enhanced Raman spectroscopy." In: *Nano Letters* 15.10 (2015), pp. 6386–6394. DOI: 10.1021/acs.nanolett.5b01543 (cited on page 35).

[202] Li-Qing Zheng, Xing Wang, Feng Shao, Martin Hegner, and Renato Zenobi. "Nanoscale chemical imaging of reversible photoisomerization of an azobenzene-thiol self-assembled monolayer by tip-enhanced raman spectroscopy." In: *Angewandte Chemie* 130.4 (2018), pp. 1037–1041. DOI: 10.1002/ange.201710443 (cited on pages 35, 36).

[203] Markus Döbbelin, Artur Ciesielski, Sébastien Haar, Silvio Osella, Matteo Bruna, Andrea Minoia, Luca Grisanti, Thomas Mosciatti, Fanny Richard, and Eko Adi Prasetyanto. "Light-enhanced liquid-phase exfoliation and current photoswitching in graphene–azobenzene composites." In: *Nature communications* 7.1 (2016), p. 11090. DOI: 10.1038/ncomms11090 (cited on pages 35, 36, 43).

[204] Christina M. Stuart, Renee R. Frontiera, and Richard A. Mathies. "Excited-state structure and dynamics of cis-and trans-azobenzene from resonance Raman intensity analysis." In: *The Journal of Physical Chemistry A* 111.48 (2007), pp. 12072–12080. DOI: 10.1021/jp0751460 (cited on pages 35, 36, 97).

[205] Wan-Chen Lin, Cheng-Han Yu, Sara Triffo, and Jay T. Groves. "Supported membrane formation, characterization, functionalization, and patterning for application in biological science and technology." In: *Current protocols in chemical biology* 2.4 (2010), pp. 235–269. DOI: 10.1002/9780470559277.ch100131 (cited on page 40).

[206] Dan A. Klaerke, Maria de los Angeles Tejada, Vibeke Grøsfjeld Christensen, Mette Lassen, Per Amstrup Pedersen, and Kirstine Calloe. "Reconstitution and electrophysiological characterization of ion channels in lipid bilayers." In: *Current Protocols in Pharmacology* 81.1 (2018), e37. DOI: 10.1002/cpph.37 (cited on page 40).

[207] Edward T. Castellana and Paul S. Cremer. "Solid supported lipid bilayers: From biophysical studies to sensor design." In: *Surface science reports* 61.10 (2006), pp. 429–444. DOI: 10.1016/j.surfrep.2006.06.001 (cited on page 40).

[208] Stefanie D. Pritzl, David B. Konrad, Martina F. Ober, Alexander F. Richter, James A. Frank, Bert Nickel, Dirk Trauner, and Theobald Lohmüller. "Optical membrane control with red light enabled by red-shifted photolipids." In: *Langmuir* 38.1 (2021), pp. 385–393. DOI: 10.1021/acs.langmuir.1c02745 (cited on page 41).

[209] Christopher Weber, Tobias Liebig, Manuel Gensler, Anton Zykov, Linus Pithan, Jürgen P. Rabe, Stefan Hecht, David Bléger, and Stefan Kowarik. "Cooperative switching in nanofibers of azobenzene oligomers." In: *Scientific reports* 6.1 (2016), p. 25605. DOI: 10.1038/srep25605 (cited on pages 43, 44).

[210] Zonglin Chu, Yanxiao Han, Tong Bian, Soumen De, Petr Král, and Rafal Klajn. "Supramolecular control of azobenzene switching on nanoparticles." In: *Journal of the American Chemical Society* 141.5 (2018), pp. 1949–1960. DOI: 10.1021/jacs.8b09638 (cited on page 43).

[211] Pooja Arya, Joachim Jelken, Nino Lomadze, Svetlana Santer, and Marek Bekir. "Kinetics of photoisomerization of azobenzene containing surfactants." In: *The Journal of Chemical Physics* 152.2 (2020). DOI: 10.1063/1.5135913 (cited on page 44).

[212] Joseph R. Lakowicz. *Principles of fluorescence spectroscopy*. Springer, 2006 (cited on page 44).

[213] Alexander Florian Richter. "Charge carrier dynamics in nontoxic semiconductor quantum dots." In: (2020). DOI: 10.5282/edoc.27359 (cited on page 45).

[214] Hyunho Kang, Joseph T. Buchman, Rebeca S. Rodriguez, Hattie L. Ring, Jiayi He, Kyle C. Bantz, and Christy L. Haynes. "Stabilization of silver and gold nanoparticles: preservation and improvement of plasmonic functionalities." In: *Chemical reviews* 119.1 (2018), pp. 664–699. DOI: 10.1021/acs.chemrev.8b00341 (cited on page 46).

[215] Jonathan G. Mehtala, Dmitry Y. Zemlyanov, Joann P. Max, Naveen Kadasala, Shou Zhao, and Alexander Wei. "Citrate-stabilized gold nanorods." In: *Langmuir* 30.46 (2014), pp. 13727–13730. DOI: 10.1021/la5029542 (cited on page 46).

[216] Jon S. Donner, Guillaume Baffou, David McCloskey, and Romain Quidant. "Plasmon-assisted optofluidics." In: *Acs nano* 5.7 (2011), pp. 5457–5462. DOI: 10.1021/nn200590u (cited on page 46).

[217] Michael J. A. Hore, Xingchen Ye, Jamie Ford, Yuzhi Gao, Jiayang Fei, Qiong Wu, Stuart J. Rowan, Russell J. Composto, Christopher B. Murray, and Boualem Hammouda. "Probing the structure, composition, and spatial distribution of ligands on gold nanorods." In: *Nano letters* 15.9 (2015), pp. 5730–5738. DOI: 10.1021/acs.nanolett.5b03088 (cited on page 46).

[218] Magdalena Stobiecka, Kaitlin Coopersmith, and Maria Hepel. "Resonance elastic light scattering (RELS) spectroscopy of fast non-Langmuirian ligand-exchange in glutathione-induced gold nanoparticle assembly." In: *Journal of colloid and interface science* 350.1 (2010), pp. 168–177. DOI: 10.1016/j.jcis.2010.06.010 (cited on page 47).

[219] Geun Wan Kim and Ji Won Ha. "Single-particle study: Effects of oxygen plasma treatment on structural and spectral changes of anisotropic gold nanorods." In: *Physical Chemistry Chemical Physics* 22.21 (2020), pp. 11767–11770. DOI: 10.1039/D0CP00996B (cited on page 47).

[220] Maria Alba, Nicolas Pazos-Perez, Belén Vaz, Pilar Formentin, Moritz Tebbe, Miguel A. Correa-Duarte, Pedro Granero, Josep Ferré-Borrull, Rosana Alvarez, and Josep Pallares. "Macroscale plasmonic substrates for highly sensitive surface-enhanced Raman scattering." In: *Angewandte Chemie International Edition* 52.25 (2013), pp. 6459–6463. DOI: 10.1002/anie.201302285 (cited on page 47).

[221] Viktor Myroshnychenko, Jessica Rodríguez-Fernández, Isabel Pastoriza-Santos, Alison M. Funston, Carolina Novo, Paul Mulvaney, Luis M. Liz-Marzán, and F. Javier García De Abajo. "Modelling the optical response of gold nanoparticles." In: *Chemical Society Reviews* 37.9 (2008), pp. 1792–1805. DOI: 10.1039/B711486A (cited on page 50).

[222] Kane Yee. "Numerical solution of initial boundary value problems involving Maxwell's equations in isotropic media." In: *IEEE Transactions on antennas and propagation* 14.3 (1966), pp. 302–307. DOI: 10.1109/TAP.1966.1138693 (cited on page 50).

[223] K. Stranius and K. Börjesson. "Determining the photoisomerization quantum yield of photoswitchable molecules in solution and in the solid state." In: *Scientific reports* 7.1 (2017), pp. 1–9. DOI: 10.1038/srep41145 (cited on page 55).

[224] Hélène Bouvrais, Tanja Pott, Luis A. Bagatolli, John H. Ipsen, and Philippe Méléard. "Impact of membrane-anchored fluorescent probes on the mechanical properties of lipid bilayers." In: *Biochimica et Biophysica Acta (BBA)-Biomembranes* 1798.7 (2010), pp. 1333–1337. DOI: 10.1016/j.bbamem.2010.03.026 (cited on page 56).

[225] Hammad A. Faizi, Cody J. Reeves, Vasil N. Georgiev, Petia M. Vlahovska, and Rumiana Dimova. "Fluctuation spectroscopy of giant unilamellar vesicles using confocal and phase contrast microscopy." In: *Soft Matter* 16.39 (2020), pp. 8996–9001. DOI: 10.1039/D0SM00943A (cited on page 56).

[226] Andrew F. Loftus, Sigrid Noreng, Vivian L. Hsieh, and Raghuveer Parthasarathy. "Robust measurement of membrane bending moduli using light sheet fluorescence imaging of vesicle fluctuations." In: *Langmuir* 29.47 (2013), pp. 14588–14594. DOI: 10.1021/la403837d (cited on page 56).

[227] Nathan A. Romero and David A. Nicewicz. "Organic photoredox catalysis." In: *Chemical reviews* 116.17 (2016), pp. 10075–10166. DOI: 10.1021/acs.chemrev.6b00057 (cited on pages 57, 65).

[228] Wilker Caetano, Paula S. Haddad, Rosangela Itri, Divinomar Severino, Vinicius C. Vieira, Mauricio S. Baptista, André P. Schröder, and Carlos M. Marques. "Photo-induced destruction of giant vesicles in methylene blue solutions." In: *Langmuir* 23.3 (2007), pp. 1307–1314. DOI: 10.1021/la061510v (cited on page 60).

[229] Omar Mertins, Isabel O. L. Bacellar, Fabrice Thalmann, Carlos M. Marques, Maurício S. Baptista, and Rosangela Itri. "Physical damage on giant vesicles membrane as a result of methylene blue photoirradiation." In: *Biophysical journal* 106.1 (2014), pp. 162–171. DOI: 10.1016/j.bpj.2013.11.4457 (cited on page 60).

[230] Marco Montalti, Alberto Credi, Luca Prodi, and M. Teresa Gandolfi. *Handbook of photochemistry*. CRC press, 2006. DOI: 10.1201/9781420015195 (cited on page 60).

[231] Eric Betzig, George H. Patterson, Rachid Sougrat, O. Wolf Lindwasser, Scott Olenych, Juan S. Bonifacino, Michael W. Davidson, Jennifer Lippincott-Schwartz, and Harald F. Hess. "Imaging intracellular fluorescent proteins at nanometer resolution." In: *science* 313.5793 (2006), pp. 1642–1645. DOI: 10.1126/science.112734 (cited on page 62).

[232] Michael J. Rust, Mark Bates, and Xiaowei Zhuang. "Stochastic optical reconstruction microscopy (STORM) provides sub-diffraction-limit image resolution." In: *Nature methods* 3.10 (2006), p. 793. DOI: 10.1038/nmeth929 (cited on page 62).

[233] Ralph S. Becker, Sankar Chakravorti, and Suresh Das. "The photosensitizers benzophenoxazine and thiazines: comprehensive investigation of photophysical and photochemical properties." In: *Photochemistry and photobiology* 51.5 (1990), pp. 533–538. DOI: 10.1111/j.1751-1097.1990.tb01962.x (cited on page 65).

[234] Benedikt Baumgartner, Viktorija Glembockyte, Alberto J. Gonzalez-Hernandez, Abha Valavalkar, Robert J. Mayer, Lucy L. Fillbrook, Adrian Müller-Deku, Jinhua Zhang, Florian Steiner, Christoph Gross, Martin Reynders, Hermany Munguba, Anisul Arefin, Armin Ofial, Jonathon E Beves, Theobald Lohmueller, Benjamin Dietzek-Ivanšic, Johannes Broichhagen, Philip Tinnefeld, Joshua Levitz, and Oliver Thorn-Seshold. "A general method for near-infrared photoswitching in biology, demonstrated by the> 700 nm photocontrol of GPCR activity in brain slices." In: (2024). DOI: 10.26434/chemrxiv-2024-vm4n3 (cited on page 65).

[235] G. S. Hartley and R. J. W. Le Fevre. "The dipole moments of cis-and trans-azobenzenes and of some related compounds." In: *Journal of the Chemical Society (Resumed)* (1939), pp. 531–535. DOI: 10.1039/JR9390000531 (cited on page 67).

[236] Holger A. Scheidt, Katja Kolocaj, David B. Konrad, James A. Frank, Dirk Trauner, Dieter Langosch, and Daniel Huster. "Light-induced lipid mixing implies a causal role of lipid splay in membrane fusion." In: *Biochimica et Biophysica Acta (BBA)-Biomembranes* 1862.11 (2020), p. 183438. DOI: 10.1016/j.bbamem.2020.183438 (cited on page 67).

[237] Jinhua Zhang, Francis Schuknecht, Ludwig Habermann, Alexander Pattis, Jonathan Heine, Stefanie D. Pritzl, Dirk Trauner, and Theobald Lohmüller. "Label-Free Time-Resolved Monitoring of Photolipid Bilayer Isomerization by Plasmonic Sensing." In: *Advanced Optical Materials* 12.10 (2024), p. 2302266. DOI: 10.1002/adom.202302266 (cited on page 70).

[238] Yuri Roiter, Maryna Ornatska, Aravind R. Rammohan, Jitendra Balakrishnan, David R. Heine, and Sergiy Minko. "Interaction of nanoparticles with lipid membrane." In: *Nano letters* 8.3 (2008), pp. 941–944. DOI: 10.1021/nl080080l (cited on pages 70, 79).

[239] Claudia Contini, James W. Hindley, Thomas J. Macdonald, Joseph D. Barritt, Oscar Ces, and Nick Quirke. "Size dependency of gold nanoparticles interacting with model membranes." In: *Communications chemistry* 3.1 (2020), p. 130. DOI: 10.1038/s42004-020-00377-y (cited on page 70).

[240] Sirin Celiksoy, Weixiang Ye, Karl Wandner, Katharina Kaefer, and Carsten Sonnichsen. "Intensity-based single particle plasmon sensing." In: *Nano Letters* 21.5 (2021), pp. 2053–2058. DOI: 10.1021/acs.nanolett.0c04702 (cited on page 71).

[241] Benjamin Foerster, Vincent A. Spata, Emily A. Carter, Carsten Sönnichsen, and Stephan Link. "Plasmon damping depends on the chemical nature of the nanoparticle interface." In: *Science advances* 5.3 (2019), eaav0704. DOI: 10.1126/sciadv.aav0704 (cited on page 71).

[242] John F. Nagle and Stephanie Tristram-Nagle. "Structure of lipid bilayers." In: *Biochimica et Biophysica Acta (BBA)-Reviews on Biomembranes* 1469.3 (2000), pp. 159–195. DOI: 10.1016/S0304-4157(00)00016-2 (cited on pages 72, 73, 79).

[243] Petteri Parkkila, Mohamed Elderdfi, Alex Bunker, and Tapani Viitala. "Biophysical characterization of supported lipid bilayers using parallel dual-wavelength surface plasmon resonance and quartz crystal microbalance measurements." In: *Langmuir* 34.27 (2018), pp. 8081–8091. DOI: 10.1021/acs.langmuir.8b01259 (cited on page 72).

[244] Bernd W. König, S. Krueger, W. J. Orts, Charles F. Majkrzak, Norm F. Berk, J. V. Silverton, and Klaus Gawrisch. "Neutron reflectivity and atomic force microscopy studies of a lipid bilayer in water adsorbed to the surface of a silicon single crystal." In: *Langmuir* 12.5 (1996), pp. 1343–1350. DOI: 10.1021/la950580r (cited on page 79).

[245] Zdzislaw Salamon, Savitha Devanathan, Isabel D. Alves, and Gordon Tollin. "Plasmon-waveguide resonance studies of lateral segregation of lipids and proteins into microdomains (rafts) in solid-supported bilayers." In: *Journal of biological chemistry* 280.12 (2005), pp. 11175–11184. DOI: 10.1074/jbc.M411197200 (cited on page 80).

[246] Ryohei Yagi, Hideki Katae, Yutaka Kuwahara, Sun-Nam Kim, Tomonari Ogata, and Seiji Kurihara. "On-off switching properties of one-dimensional photonic crystals consisting of azo-functionalized polymer liquid crystals having different methylene spacers and polyvinyl alcohol." In: *Polymer* 55.5 (2014), pp. 1120–1127. DOI: 10.1016/j.polymer.2014.01.018 (cited on page 81).

[247] Hoduk Cho, Jae Won Shin, and Ryong Ryoo. "Atomic scale mechanisms underlying thermal reshaping of anisotropic gold nanocrystals revealed by in situ electron microscopy." In: *The Journal of Physical Chemistry C* 124.23 (2020), pp. 12855–12863. DOI: 10.1021/acs.jpcc.0c04281 (cited on page 92).

[248] Daniel P. Cherney, John C. Conboy, and Joel M. Harris. "Optical-trapping Raman microscopy detection of single unilamellar lipid vesicles." In: *Analytical chemistry* 75.23 (2003), pp. 6621–6628. DOI: 10.1021/ac034838r (cited on page 98).

[249] Paul Kühler, Max Weber, and Theobald Lohmüller. "Plasmonic nanoantenna arrays for surface-enhanced Raman spectroscopy of lipid molecules embedded in a bilayer membrane." In: *ACS applied materials interfaces* 6.12 (2014), pp. 8947–8952. DOI: 10.1021/am5023418 (cited on page 98).

[250] Yu V. Zaytseva, I. V. Zaytseva, and N. V. Surovtsev. "Conformational state diagram of DOPC/DPPCd62/cholesterol mixtures." In: *Biochimica et Biophysica Acta (BBA)-Biomembranes* 1864.4 (2022), p. 183869. DOI: 10.1016/j.bbamem.2022.183869 (cited on page 98).

[251] Bruce P. Gaber and Warner L. Peticolas. "On the quantitative interpretation of biomembrane structure by Raman spectroscopy." In: *Biochimica et Biophysica Acta (BBA)-Biomembranes* 465.2 (1977), pp. 260–274. DOI: 10.1016/0005-2736(77)90078-5 (cited on page 98).

[252] Robert C. Spiker Jr and Ira W. Levin. "Raman spectra and vibrational assignments for dipalmitoyl phosphatidylcholine and structurally related molecules." In: *Biochimica et Biophysica Acta (BBA)-Lipids and Lipid Metabolism* 388.3 (1975), pp. 361–373. DOI: 10.1016/0005-2760(75)90095-8 (cited on page 98).

[253] Kenneth G. Brown, Warner L. Peticolos, and Ellen Brown. "Raman studies of conformational changes in model membrane systems." In: *Biochemical and biophysical research communications* 54.1 (1973), pp. 358–364. DOI: 10.1016/0006-291X(73)90930-3 (cited on page 98).

[254] Thorsten Gölz, Enrico Baù, Jinhua Zhang, Korbinian Kaltenecker, Dirk Trauner, Stefan A. Maier, Fritz Keilmann, Theobald Lohmüller, and Andreas Tittl. "Transient infrared nanoscopy resolves the millisecond photoswitching dynamics of single lipid vesicles in water." In: *arXiv preprint arXiv:2406.02513* (2024). DOI: 10.48550/arXiv.2406.02513 (cited on page 102).

List of Figures

2.1 Phospholipids are building blocks of cell membranes . . . 6
2.2 Azobenzene isomerizations and their absorption spectra . . . 7
2.3 Photoswitchable lipid *azo*-**PC** . . . 9
2.4 Self-assembly of phospholipids . . . 10
2.5 GUVs . . . 11
2.6 Diffusion of *azo*-**PC** SLBs . . . 13
2.7 Controlling membrane properties with photolipids . . . 14
2.8 A system combining azobenzene and fluorophore molecules . . . 15
2.9 Fluorescence quenching by intersystem crossing . . . 16
2.10 Förster resonance energy transfer . . . 17
2.11 Dexter energy transfer . . . 18
2.12 Electron transfer and hole transfer . . . 19
2.13 *cis*-to-*trans* isomerization of azobenzene by TET . . . 20
2.14 *cis*-to-*trans* isomerization of azobenzene via electron or hole transfer . . . 21
2.15 Formation of localized particle plasmons . . . 24
2.16 Principle of plasmonic sensing with single nanoparticles . . . 27
2.17 Illustration of optical forces . . . 28
2.18 Internal non-radiative plasmonic decay lead to heating of AuNPs. . . . 29
2.19 Melting process from a gold nanorod to nanodot. . . . 30
2.20 Illustration of IR absorption, Rayleigh scattering, Raman scattering and fluorescence. . . . 32
2.21 Schematic to calculate the field enhancement of SERS . . . 33
2.22 Typical SERS substrates . . . 34
2.23 Typical Raman spectra of azobenzene molecules . . . 35

3.1 Chemical structure of lipid molecules . . . 38
3.2 PL/PLE spectra and chemical structure of dye-labeled lipids . . . 39
3.3 Preparation of SUVs by tip sonication . . . 40
3.4 Preparation of GUVs by electroformation . . . 41
3.5 Preparation of SLBs by vesicle fusion . . . 41
3.6 Fluorescence microscopy . . . 42
3.7 UV-vis absorption spectroscopy . . . 43
3.8 Calculating switching rate through time-lapse absorption spectra . . . 43
3.9 Principle of TCSPC . . . 45
3.10 AuNRs stabilized with different ligands . . . 46
3.11 Dropcasted and printed AuNRs . . . 47
3.12 Dark field microscope base setup . . . 48
3.13 Scanning electron microscopy . . . 49
3.14 Finite-difference time-domain methods . . . 50

4.1 Emission specification of used LEDs . . . 52
4.2 *Cis*-to-*trans* isomerzation of *azo*-**PC** by direct illumination . . . 53
4.3 Sensitized *cis*-to-*trans* Isomerization of *azo*-**PC** . . . 54
4.4 The absorption spectrum of Atto633-doped *azo*-**PC** SUVs . . . 56
4.5 Dependence of switching rates on dye concentration . . . 57
4.6 Reversibility of sensitized *azo*-**PC** isomerization . . . 58
4.7 Photostability of Rho, TR, NB and Atto633 . . . 59
4.8 Photobleaching of MB doped in DOPC membranes . . . 60
4.9 Protection of MB from photobleaching in *azo*-**PC** membranes . . . 61
4.10 Fluorescence modulation of different dyes by *azo*-**PC** isomerization . . . 62
4.11 Fluorescence modulation of Rho by *azo*-**PC** isomerization . . . 63
4.12 Fluorescence on and off of a GUV . . . 63
4.13 *Azo*-**PC** is a dark-quencher . . . 64
4.14 Concentration-dependent quenching efficiency . . . 64
4.15 Spectra overlap of *azo*-**PC**'s absorption and dyes' emission . . . 66
4.16 Time resolved PL decay . . . 66
4.17 Stern-Volmer Plot of % Rho doped photolipid membrane . . . 67
4.18 Sensitized oxy-*azo*-**PC** isomerization . . . 68
4.19 Fluorescence modulation of dyes by oxy-*azo*-**PC** . . . 68

5.1 Size distribution of used AuNRs . . . 70
5.2 Avoiding effect of AuNRs plasmon modes on photolipid switching . . . 71
5.3 Lorentzian fit of the scattering spectrum of AuNRs . . . 72
5.4 Plasmonic sensing of membrane formation . . . 73
5.5 Plasmonic sensing of *azo*-**PC** SLBs isomerization . . . 74
5.6 Control measurement for DOPC . . . 74
5.7 Control measurements of temperature changes . . . 75
5.8 Time-resolved monitoring of *azo*-**PC** SLBs isomerization . . . 76
5.9 Time-resolved switching patterns . . . 77
5.10 Time-resolved measurements for DOPC membranes . . . 77
5.11 Plasmonic sensing on CTAB-removed AuNRs . . . 78
5.12 FDTD Simulations . . . 80
5.13 Plasmonic sensing of bilayer fluidity . . . 82
5.14 Probing photostationary state . . . 83
5.15 AuNRs array . . . 84
5.16 Illumination spot . . . 85
5.17 Probing diffusion by AuNRs array . . . 86
5.18 Relationship between rate and distance . . . 86

6.1 Descriptions of used AuNRs . . . 89
6.2 Optical printing of AuNRs with increasing laser power . . . 90
6.3 The melting process of nanorods to nanospheres . . . 91
6.4 Field enhancements of nanorods, ellipsoids and spheres . . . 92
6.5 SERS spectra of photolipid membranes for different particles shapes . . . 94
6.6 Curvature evolution of printed particles with increased laser power . . . 95
6.7 SERS spectrum of *azo*-**PC** bilayer . . . 97

6.8 SERS spectrum of DOPC bilayer 98
6.9 Analysis of *azo*-**PC** bilayer photoisomerization via SERS 99
6.10 Analysis of *azo*-**PC** photoisomerization via SERS on aggregate 100

List of Tables

2.1 Raman peaks for azobenzne 36

3.1 Filter cubes 42

4.1 *Cis*-to-*trans* switching rate 55
4.2 PM efficiency of *azo*-**PC** to different dyes 62
4.3 Redox potential of azobenzene and dyes 65
4.4 PM efficiency of oxy-*azo*-**PC** to different dyes 68

6.1 Particle size changes during nanorod-to-sphere melting process 96
6.2 Raman peaks for *azo*-**PC** 97
6.3 Raman peaks for DOPC 98

List of Abbreviations

UV ultraviolet

FCS fluorescence correlation spectroscopy

PC phosphatidylcholine

PS phosphatidylserine

PE phosphatidylethanolamine

DOPC 1,2-dioleoyl-sn-glycero-3-phosphocholine

PSSs photostationary states

SPT single particle tracking

SLBs supported lipid bilayers

GUVs giant unilamellar vesicles

SUVs small unilamellar vesicles

LB Langmuir–Blodgett

DPhPC 1,2-diphytanoyl-sn-glycero-3-phosphocholine

FDTD Finite difference time domain

AuNPs gold nanoparticles

AuNRs gold nanorods

TEM transmission electron microscopy

SERS surface enhanced Raman scattering

RRS resonance Raman scattering

ET energy transfer

PET photoinduced electron transfer

IC internal conversion

ISC intersystem crossing

DET Dexter energy transfer

FRET Förster resonance energy transfer

LUMO lowest unoccupied molecular orbital

HOMO highest occupied molecular orbital

TET triplet energy transfer

PES potential energy surface

SEM scanning electron microscopy

PL photoluminescence

PLE photoluminescence excitation

TCSPC time-correlated single photon counting

PBS phosphate-buffered saline

ITO Indium-Tin-Oxide

LEDs light-emitting diodes

CTAB cetyltrimethylammonium bromide

DI deionized

AFM atomic force microscopy

DFM dark field microscope

DFC dark field condenser

CCD charge-coupled diode

ROI regions of interest

SEM scanning electron microscopy

Rho Rhodamine

TR Texas Red

NB Nile blue

MB Methylene blue

PM photomodulation

PALM Photoactivated localization microscopy

STORM stochastic optical reconstruction microscopy

ROC radius of curvature

Acknowledgments

Looking back to the past four years, I always feel grateful. In October 2020, during COVID-19 pandemic, I traveled to this country. At that time, everything seemed uncertain to me, both for living and research. It was a hard time, but an important span of my life where I grew a lot scientifically and personally. It would not have been possible without the support and help of people who shared the path with me, to whom I want to express my gratitude.

First, I would like to thank PD. Dr. **Theo Lohmüller** for supervising and supporting me. Thank you for introducing me to the study of photoswitchable lipids and plasmonic nanoparticles and guiding me to work on three projects which I was really interested in. Discussions with you were always fruitful, and your solid understanding of observations and great ideas encouraged me to think deeply and try new things. You taught me a lot about scientific writing and presentation. Thank for your patience to listen to me, especially at the beginning when I cannot express myself fluently. Thank you for your help from the very beginning when I applied the scholarship.

I want to thank Prof. Dr. **Jochen Feldmann** for giving me the opportunity to do research in the PHOG group, and providing scientific atmosphere to present, share and discuss my results.

Many thanks to my collaborators from our biophotonics group - **Francis Schuknecht**, **Paul Vossage**, **Dominik Kammerer**, Dr. **Stefanie Pritzl**, **Ashwin Vadlamani**, **Ludwig Habermann**, **Alexander Pattis** and **Jonathan Heine**. I appreciate all the discussions with you, from which I gained a deeper physical understanding of the projects. Thank you Francis for helping me with the setups whenever I got problems. Thank you Paul for always willing to support me technically and especially helping me with Latex for my thesis writing. I am thankful to accompany you Ludwig, Alex and Jonathan during your bachelor thesis. It was a great experience to work with you, and from you I learned a lot. I further want to thank Dr. **Benedikt Baumgartner** and Dr. **Oliver Thorn-Seshold** for fruitful collaborations. Thank you for providing great samples and scientific discussions. In addition, I want to thank **Thorsten Gölz**, **Enrico Baù**, Dr. **Fritz Keilmann** and Prof. Dr. **Andreas Tittl** for the pleasant collaboration. The discussions with you were always exciting and productive. Definitely, I want to thank Prof. Dr. **Dirk Trauner** for providing me reliable photolipid samples.

Thanks to my former and current colleagues at the chair with whom I had lots of wonderful memories: **Anja Barfüßer**, **Mariam Kurashvili**, **Fei He**, Dr. **Huayang Zhang**,

Philip Bootz, Dr. **Anithadevi Sekar**, **Julian Mann**, **Matthias Kestler**, **Lena Stickel**, Dr. **Ilka Vinçon**, Dr. **Quinten Akkerman**, Dr. **Yiou Wang**, Dr. **Sebastian Rieger**, Dr. **Amrita Dey**, Dr. **Jiawen Fang**, Dr. **Linzhong Wu**, Dr. **Nicola Kerschbaumer**, Dr. **Tushar Debnath**. Thank you for all your help when I encountered problems. Thank you Anja for always taking care of me. Mariam, it is great to have you at the chair. Thank you since every time I asked for you help, you took it seriously. Thank you Fei for sharing life and each process. I am thankful we could accompany, listen to and encourage each other. Thank you Huayang for always giving pertinent advice and your encouragement. Special thanks to Diminik, Anja, Mariam, Paul and Francis for helping proof read this thesis.

Thanks goes to **Gerlinde Adam** for the administrative support, **Talee Barghouti** and **Stefan Niedermaier** for the technique support. Thank you also for the daily conversations, which always make me warm-hearted.

Last but not least, I want to thank my parents **Jiaming Zhang** and **Cuilan Cheng** and my brother **Wen Zhang** for always supporting me. Especially I want to thank my husband Dr. **Tao Yuan**. I always feel so lucky to meet and marry you. Every day together with you was sweet. Thank you for keeping loving me!